الجمهورية الجزائرية الديمقراطية الشعبية
People's Democratic Republic of Algeria
وزارة التعليم العالي و البحث العلمي
Ministry of Higher Education and Scientific Research

جامعة ابي بكر بلقايد - تلمسان
Abou Bekr Belkaid University – Tlemcen
كلية التكنولوجيا
Faculty of Technology



THESIS

Presented for the **degree** of **Doctorate 3rd Cycle**

In : Electronics

Specialty : Electronic Instrumentation

By *:* Mohammed Anes BELBACHIR

Topic

Simulation and Design of Solar Cells Based on Inorganic/Organic Materials

Defended publicly on 04/06/2026 , before the examination committee composed of :

Mrs.BOUAZZA born Ahlam GUEN	-Professor	-Univ. of Tlemcen	-President
Mr.Salim KERAI	-Professor	-Univ. of Tlemcen	-Director
Mr.Abderrahmane Zakarya DJENNATI	-Associate Professor	-Univ. of Tlemcen	-Co-Director
Mr.Mousaab BELARBI	-Associate Professor	-ENP Oran	-Examiner
Mr.Nabil ZOUGAGH	-Associate Professor	-Univ. of Tlemcen	-Examiner
Mr.Mohammed KHAOUANI	-Associate Professor	-Univ. of Ain Temouchent	-Guest

Academic Year : 2025/2026

Dedication

“

TO the man — my most precious gift from God — to whom I owe my life, my success, and my deepest respect: my beloved father, ***Omar****.*

TO the woman who has endured every hardship so that I would never have to, who never refused my needs and spared no effort to make me happy: my loving mother, ***Hayet****.*

TO a kind soul who believed in me.

TO my brother, ***Mouad****, and my dear sisters,* ***Chaimaa*** *and* ***Alaa****, whose constant encouragement and unconditional support have accompanied me throughout my studies. May God bless them with lasting happiness and success.*

TO my dear uncle, ***Bouziane****, and his wife,* ***Hbiba****, whom I consider my second mother. This work is a token of my deep gratitude for your kindness, support, and encouragement through every step of my journey.*

TO my dear friends and colleagues, ***Oussama Ammour*** *and* ***Hichem Rouigueb****, for your unwavering support, patience, and friendship throughout this journey. Your constant encouragement, collaboration, and understanding have made every stage of this work both meaningful and rewarding.*

Thank you all.

”

- Mohammed Anes

Acknowledgements

First and foremost, I would like to express my deepest gratitude to Almighty Allah for granting me the strength, perseverance, and determination to bring this work to completion.

I extend my sincere appreciation to my thesis director, **Pr.Salim Kerai**, whose invaluable guidance, insightful advice, and constant encouragement have been fundamental throughout the development of this research. His scientific rigor, patience, and continuous support have profoundly shaped the quality and direction of this work.

My heartfelt thanks also go to my co-director, **Dr.Abderrahmane Zakarya Djennati**, for his generous assistance, constructive feedback, and continuous motivation. His expertise and availability have been a great source of inspiration and progress at every stage of this thesis.

I would also like to express my deep gratitude to **Dr.Mohammed Khaouni** for his unfailing support, valuable guidance, and for accompanying me step by step throughout this journey. His practical insights and encouragement have been instrumental in overcoming many challenges along the way.

My sincere thanks are also extended to **Pr.Bouazza born Guen Ahlam**, President of the jury, for the honor she has done me by presiding over my thesis defense, as well as to **Dr.Mousaab Belarbi** and **Dr.Nabil Zougagh**, Examiners of this work, for their careful reading, pertinent remarks, and valuable contributions to improving this manuscript.

Finally, I wish to express my profound appreciation to all those who, in one way or another, have contributed to the realization of this work. Their support and encouragement have been truly invaluable.

Abstract

This thesis establishes a validated computational framework for the design and optimization of perovskite-based photovoltaic devices using Silvaco Atlas TCAD software.

Single-junction FTO/TiO_2/$MAPbI_3$/HTM perovskite solar cells achieved simulated efficiencies of 12.68 %, closely matching experimental values of 13.15 %. Systematic exploration of hole transport layers revealed CuSCN as a promising alternative to Spiro−OMeTAD, exhibiting superior open-circuit voltage and short-circuit current density despite transport limitations.

Two-terminal monolithic perovskite–silicon tandems achieved 28.03 % efficiency through precise optimization of a 3 nm FTO recombination layer and a 15 nm intrinsic silicon absorber thickness.

Three-terminal tandems further improved performance to 28.99 % efficiency with fill factors exceeding 89 % by decoupling voltage extraction and enabling independent operation of subcells. Temperature studies identified 25 °C as optimal for maximizing power output, while stability investigations demonstrated that compositional alloying and surface passivation preserve over 90 % of initial efficiency after accelerated aging.

The validated simulation platform provides actionable design guidelines for wide-bandgap perovskites, advanced light management, and techno-economic optimization, establishing a clear pathway toward commercially viable high-efficiency perovskite-based solar energy systems.

Keywords : Perovskite solar cells; Tandem photovoltaics; TCAD simulation; Hole transport materials; Device optimization; Three-terminal architecture.

الملخص

تُقدّم هذه الأطروحة إطارًا حسابيًا معتمدًا لتصميم وتحسين الأجهزة الكهروضوئية المعتمدة على البيروفسكايت باستخدام برنامج Silvaco ATLAS TCAD .

حققت الخلايا الشمسية أحادية الوصلة $FTO/TiO_2/MAPbI_3/HTM$ كفاءة محاكاة بلغت 12.68%، وهي قريبة جدًا من القيمة التجريبية البالغة 13.15%. أظهرت الدراسة المنهجية لطبقات نقل الثقوب أن مركب CuSCN يُعد بديلاً واعدًا لمادة Spiro-OMeTAD، حيث أظهر فرق جهد أعلى في الدائرة المفتوحة وكثافة تيار أكبر رغم محدودية النقل.

أما الخلايا الشمسية ثنائية الأطراف من نوع بيروفسكايت–سيليكون فقد حققت كفاءة قدرها 28.03% من خلال تحسين دقيق لطبقة إعادة التركيب المصنوعة من FTO بسماكة 3 نانومتر وطبقة السيليكون الجوهرية بسماكة 15 نانومتر.

كما حسّنت البنى ثلاثية الأطراف الأداء لتصل إلى كفاءة 28.99% مع عامل امتلاء يتجاوز 89%، وذلك بفضل الفصل بين استخراج الجهد وتمكين التشغيل المستقل لكل خلية فرعية. أظهرت دراسات درجة الحرارة أن 25 درجة مئوية تمثل الحالة المثلى لتحقيق أقصى إنتاج للطاقة، في حين أثبتت اختبارات الاستقرار أن المزج التركيبي ومعالجات التمرير السطحي تحافظ على أكثر من 90% من الكفاءة الأصلية بعد اختبارات التقادم السريع.

يوفّر هذا النموذج الحسابي المعتمد إرشادات عملية لتصميم بيروفسكايتات ذات فجوة نطاق واسعة، وتحسين الإدارة الضوئية، وتحليل الجوانب التقنية والاقتصادية، مما يمهّد الطريق نحو أنظمة طاقة شمسية عالية الكفاءة وقابلة للتطبيق التجاري.

الكلمات المفتاحية: الخلايا الشمسية البيروفسكايتية؛ الخلايا ثنائية ومتعددة الأطراف؛ محاكاة TCAD؛ مواد نقل الثقوب؛ تحسين أداء الأجهزة؛ البنية ثلاثية الأطراف.

Résumé

Cette thèse établit un cadre de modélisation validé pour la conception et l'optimisation des dispositifs photovoltaïques à base de pérovskite à l'aide du logiciel Silvaco Atlas TCAD.

Les cellules solaires à jonction unique FTO/TiO_2/$MAPbI_3$/HTM ont atteint une efficacité simulée de 12.68 %, en bon accord avec la valeur expérimentale de 13.15 %. L'étude systématique des couches de transport de trous a révélé que le CuSCN constitue une alternative prometteuse au Spiro−OMeTAD, offrant une tension en circuit ouvert et une densité de courant de court-circuit supérieures malgré certaines limitations de transport.

Les tandems pérovskite–silicium à deux terminaux ont atteint une efficacité de 28.03 % grâce à l'optimisation d'une couche de recombinaison en FTO de 3 nm et d'une couche intrinsèque de silicium de 15 nm.

Les structures à trois terminaux ont encore amélioré les performances jusqu'à 28.99 % d'efficacité avec un facteur de remplissage supérieur à 89 %, en permettant une extraction de tension indépendante pour chaque sous-cellule. Les études thermiques ont identifié 25 °C comme température optimale pour la puissance maximale, tandis que les tests de stabilité ont montré qu'un alliage compositionnel et une passivation de surface permettent de conserver plus de 90 % de l'efficacité initiale après vieillissement accéléré.

Cette plateforme de simulation validée fournit des recommandations concrètes pour la conception des pérovskites à large bande interdite, la gestion optique avancée et l'optimisation technico-économique, ouvrant la voie à des systèmes photovoltaïques à pérovskite performants et commercialement viables.

Mots clés : Cellules solaires à pérovskite; Photovoltaïque tandem; Simulation TCAD; Matériaux de transport de trous; Optimisation des dispositifs; Architecture à trois terminaux.

Contents

Dedication . . . . . **I**

Acknowledgements . . . . . **II**

Abstract . . . . . **III**

الملخص . . . . . **IV**

Résumé . . . . . **V**

Introduction **1**

1 Semiconductor physics and the photovoltaic effect **4**
1.1 Introduction 5
1.2 History 5
1.3 Semiconductors materials: proprieties and types 5
1.3.1 Energy bands 6
1.3.2 Fermi energy 7
1.3.3 Semiconductors types 8
1.4 Conductivity in semiconductors 10
1.4.1 Conductivity of intrinsic semiconductors 10
1.4.2 Conductivity of extrinsic semiconductors 11
1.5 Photovoltaic fundamentals: the p-n junction 12
1.5.1 P-N junction: concept and operation 12
1.5.2 Energy band diagram and formation of the pn junction 13
1.6 Biasing of the pn junction 14
1.6.1 Forward bias 14
1.6.2 Reverse bias 15
1.7 Current expression 15
1.8 The photovoltaic effect and carrier generation 16
1.8.1 Photovoltaic effect 16
1.8.2 Quantum efficiency 18
1.8.3 Recombination and carrier extraction 19
1.9 Solar cells: principles and performance metrics 20
1.9.1 Solar radiation 20
1.9.2 Solar cell equivalent circuit model 21
1.9.3 Performance parameter of solar cells 23
1.9.4 Solar cell operation 24

1.9.5 Classification of solar cells . . . 25
1.10 Conclusion . . . 28

2 Inorganic materials and perovskite solar cells . . . 29
2.1 Introduction . . . 30
2.2 Perovskites materials . . . 30
2.2.1 Crystallographic structure of perovskites . . . 30
2.2.2 Perovskites materials classifications . . . 31
2.3 Hybrid organic-inorganic and all-inorganic perovskite : similarities and differences . . . 35
2.3.1 Hybrid organic–inorganic perovskites . . . 35
2.3.2 All-inorganic perovskites . . . 35
2.3.3 Comparison between hybrid organic-inorganic and all-inorganic perovskites 37
2.3.4 Inorganic perovskites: physical properties . . . 38
2.4 Solar cells based on perovskite . . . 42
2.4.1 Emergence of perovskite photovoltaics . . . 42
2.4.2 Working principle of perovskite solar cells . . . 44
2.4.3 Device architectures . . . 45
2.4.4 Advantages of perovskite cells . . . 46
2.4.5 Limitation of PSCs . . . 46
2.5 Tandem solar cell . . . 48
2.5.1 Tandem solar cells: overcoming the Shockley–Queisser limit . . . 48
2.5.2 Tandem architectures . . . 49
2.5.3 Materials and candidates . . . 53
2.6 Conclusion . . . 55

3 Simulation and design of perovskite solar cells using Silvaco ATLAS TCAD . . . 56
3.1 Introduction . . . 57
3.2 Presentation of Silvaco . . . 57
3.2.1 Silvaco TCAD and ATLAS simulator . . . 57
3.2.2 Device structure under Silvaco . . . 58
3.3 Validation of the structure . . . 63
3.3.1 Energy band diagram at equilibrium . . . 63
3.3.2 Device under forward bias . . . 64
3.3.3 Device under reverse bias . . . 64
3.4 Perovskite single-junction cell structure . . . 65
3.4.1 Methodology . . . 65
3.4.2 Device fabrication . . . 66
3.4.3 Device structure . . . 66
3.4.4 Device modeling . . . 67
3.5 Results and discussion . . . 68
3.5.1 Performance characterization . . . 68
3.5.2 EQE and IQE spectra of FTO/TiO_2/$MAPbI_3$/HTM single-junction solar sell . . . 69

3.5.3 Absorption and transmission spectra of FTO/TiO_2/$MAPbI_3$/HTM single-junction perovskite solar cell . . . 70
3.5.4 Energy band alignment and carrier transport in FTO/TiO_2/$MAPbI_3$/HTM single-junction perovskite solar cell . . . 71
3.6 Impact of hole transport layer selection on device characteristics . . . 72
3.6.1 J–V characteristics of FTO/TiO_2/$MAPbI_3$ with different HTLs . . 73
3.6.2 EQE and IQE of FTO/TiO_2/$MAPbI_3$ with different HTLs . . . 75
3.7 Tandem perovskite/silicon solar cell study . . . 76
3.7.1 Methodology . . . 76
3.7.2 Simulation details . . . 77
3.8 Results and discussion . . . 79
3.8.1 J–V characteristics of FTO/TiO_2/$MAPbI_3$/HTM and tandem solar cells . . . 79
3.8.2 IQE and EQE analysis . . . 80
3.8.3 Optical absorption and transmission properties . . . 81
3.8.4 Energy band alignment and carrier transport pathways . . . 82
3.9 Comprehensive study of tandem solar cell performance: investigating the effects of temperature and intrinsic silicon thickness . . . 83
3.9.1 Effect of intrinsic silicon thickness on tandem cell efficiency . . . 83
3.9.2 Temperature dependence of tandem solar cell performance . . . 85
3.10 Validation of results: experimental precision and comparative analysis . . . 88
3.10.1 Comparison of tandem solar cell configurations . . . 88
3.10.2 Experimental validation and reproducibility . . . 89
3.10.3 Error analysis and performance stability . . . 89
3.11 Conclusion . . . 90

4 Advanced three-terminal perovskite/silicon tandem solar cell architecture 91
4.1 Introduction . . . 92
4.2 Introduction to the three-terminal tandem structure . . . 92
4.2.1 Overview of the three-terminal tandem structure . . . 92
4.3 Advantages of the 3T structure over the 2T structure (Chapter 3) . . . 93
4.3.1 Why the 3T structure is beneficial for this study . . . 94
4.4 The 3T under Silvaco . . . 94
4.4.1 Methodology . . . 95
4.4.2 Simulation details . . . 95
4.4.3 Material selection and structural design for the bottom cell . . . 96
4.4.4 Models . . . 98
4.5 Results and discussion . . . 99
4.5.1 J-V curve overview . . . 99
4.5.2 EQE spectra of the top and bottom cells in the 3T tandem configuration 101
4.5.3 Absorption and transmission for the 3T tandem cell . . . 103
4.5.4 Band diagram for the 3T tandem cell . . . 105
4.5.5 Performance mapping of the 3T tandem solar Cell . . . 107
4.5.6 Performance comparison between 3T and 2T tandem cells . . . 108
4.5.7 J-V characteristics . . . 109
4.5.8 EQE comparison between 3T and 2T tandem cells . . . 111

4.5.9 Absorption and transmission spectra comparison between 3T and 2T tandem cells . . . 112
4.5.10 Band diagram energy comparison between 3T and 2T tandem cells 113
4.6 Comparative analysis with reported literature . . . 114
4.6.1 Key insights . . . 116
4.7 Conclusion . . . 117

Conclusion . . . **119**

List of Figures

1.1 Common semiconductor materials. 6
1.2 Band diagram. 6
1.3 Semiconductor at room temperature showing fermi energy level. 7
1.4 n-type semiconductor. 8
1.5 Conduction in n-type semiconductor. 9
1.6 p-type semiconductor. 9
1.7 Conduction in p-type semiconductor. 10
1.8 p-n junction semiconductor. 13
1.9 Energy band diagram of p-n junction, (a) Carrier diffusion and recombination at the junction before equilibrium, (b) Band bending and built-in potential barrier formation at thermal equilibrium. 14
1.10 Forward-biased p–n junction. 15
1.11 Reverse-biased p–n junction. 15
1.12 Energy band diagram showing photon absorption ($h_v > E_g$) and carrier relaxation to band edges. 17
1.13 Direct and indirect bandgap semiconductor excitation processes. 17
1.14 Shockley–Queisser efficiency limit vs bandgap energy. 19
1.15 Solar irradiance spectrum for different air masses. 20
1.16 J–V Curves of an Ideal Solar Cell in Dark and Illuminated Conditions. . . 22
1.17 Equivalent circuits for a) an ideal solar cell and b) ideal solar cell with parasitic losses. 23
1.18 Typical J–V and power density curves of a solar cell, showing the Jsc, Voc, mpp, and fill factor. 23
1.19 Cross section of solar cell. 24
1.20 Types of photovoltaic solar cells. 25

2.1 Crystal structure of ABX_3 perovskite: (A) Cubic unit cell centred on the A-site cation, (B) Corner-sharing BX_6 octahedra stabilized by the central A-site cation. 30
2.2 Four representative perovskite structures as described in the text. 32
2.3 Examples of layered Ruddlesden–Popper perovskites with $n = 1, 2$ and 3, showing quasi-2D butylammonium (BA) methylammonium lead iodide phases. 33
2.4 Structural diversity in 1D and quasi-2D perovskite-related compounds. A) $MAPbI_3$ δ-phase (2H polytype). B) 4H polytype with alternating connectivity. C) $(MA)_3PbI_5 \cdot DMF$, a Pb-deficient 1D phase. D) $(Gua)_2PbI_4$, a quasi-2D corrugated sheet structure. E) $MAPbI_3 \cdot H_2O$ monohydrate degradation phase. F) $(MA)_2Pb_3I_8 \cdot {}_2DMSO$ intermediate. 34

2.5 Comparative bandgap diagrams and stability profiles for hybrid ($MAPbI_3$) and inorganic ($CsPbI_3$) perovskites, highlighting phase transitions, degradation pathways under moisture/heat, and temperature-dependent stability curves derived from thermogravimetric analysis (TGA) and X-ray diffraction (XRD) data. . . . 36
2.6 (A) Absorption and photoluminescence (PL) spectra of $CsPbX_3$ (X = Cl, Br, I) inorganic perovskites, showing bandgap tuning with halide composition; (B) Bandgap energy (E_g) and corresponding emission wavelength of $CsPb(Cl_xBr_{1-x})_3$ and $CsPb(Br_xI_{1-x})_3$ alloys as a function of halide concentration (x). . . . 39
2.7 Electronic band structure of $CsPbI_3$ inorganic perovskite calculated via DFT, showing direct bandgap and spin-orbit coupling effects. . . . 40
2.8 Mechanical stress-strain curves and thermal decomposition profiles for selected inorganic perovskites (e.g., $CsPbBr_3$ and $CsPbI_3$) . . . 41
2.9 Conversion efficiencies of best research solar cells (NREL). . . . 43
2.10 Schematic energy level alignment of PSC layers: FTO/TiO_2/$MAPbI_3$/spiro-OMeTAD with various metal contacts. . . . 44
2.11 Schematic diagrams of n-i-p and p-i-n perovskite solar cell architectures. . 45
2.12 Simplified schematics of: (A) single-junction, (B) multi-junction solar cells illustrating the reduction of thermalization losses. . . . 49
2.13 Schematic representations of various tandem solar cell architectures, namely two-terminal, three-terminal, and four-terminal configurations. . . . 49
2.14 Schematic representation of a two-terminal tandem solar cell structure. . . 50
2.15 Schematic representation of a four-terminal tandem solar cell structure. . . 51
2.16 Efficiency response of: (A) 2T and (B) 4T configurations to deviations from ideal bandgap pairs. . . . 51
2.17 Schematic representation of a three-terminal tandem solar cell structure. . 52
2.18 Shockley–Queisser limits of Si-based tandem solar cells (2T, 3T type A/B, 4T) versus top-cell bandgap. . . . 52

3.1 Atlas inputs and outputs. . . . 57
3.2 General workflow of device simulation using Silvaco Atlas TCAD. . . . 58
3.3 ATLAS mesh creation. . . . 59
3.4 Defined device: (A) Regions and (B) Doping profiles. . . . 60
3.5 Electrode configuration in the perovskite solar cell. . . . 61
3.6 Energy band diagram of the FTO/TiO_2/$MAPbI_3$/HTM solar cell at equilibrium. . . . 63
3.7 Energy band diagram of the FTO/TiO_2/$MAPbI_3$/HTM solar cell under forward bias. . . . 64
3.8 Energy band diagram of the FTO/TiO_2/$MAPbI_3$/HTM solar cell under reverse bias. . . . 65
3.9 Experimental route for each layer of a perovskite solar cell development. Deposition of: (a) compact and mesoporous TiO_2, (b) PbI_2, (c) CH_3NH_3I (formation of perovskite film), (d) Spiro-OMeTAD and (e) final perovskite solar cell . . . 66

3.10 Cross-sectional schematic of a solar cell with the FTO/TiO_2/$MAPbI_3$/HTM configuration . . . 67
3.11 J–V characteristics of the FTO/TiO_2/$MAPbI_3$/HTM solar cell (simulated and experimental). . . . 68
3.12 (A) EQE (B) IQE spectra of FTO/TiO_2/$MAPbI_3$/HTM solar cell. . . . 69
3.13 Absorption and transmission spectra of the FTO/TiO_2/$MAPbI_3$/HTM configuration. . . . 70
3.14 Energy band diagram of the FTO/TiO_2/$MAPbI_3$/HTM configuration. . . . 71
3.15 Cross-sectional diagram of FTO/TiO_2/$MAPbI_3$ solar cells with different HTLs . . . 72
3.16 J–V characteristics of FTO/TiO_2/$MAPbI_3$ solar cells employing different HTLs (Spiro-OMeTAD, CuI, CuSCN, and NiO_x). . . . 73
3.17 EQE and IQE of FTO/TiO_2/$MAPbI_3$ solar cells with HTLs. . . . 75
3.18 A cross-sectional schematic of the tandem solar cell. . . . 77
3.19 J–V characteristics of tandem and single-junction solar cells (simulated and experimental). . . . 79
3.20 (A) IQE, (B) EQE spectra of tandem and FTO/TiO_2/$MAPbI_3$/HTM solar cells. . . . 80
3.21 Absorption and transmission spectra of the tandem solar cell compared to the FTO/TiO_2/$MAPbI_3$/HTM configuration. . . . 81
3.22 Energy band diagram of the tandem solar cell and FTO/TiO_2/$MAPbI_3$/HTM configuration. . . . 82
3.23 J–V characteristics of the tandem solar cell for different intrinsic silicon layer thicknesses. . . . 84
3.24 Effect of intrinsic silicon layer thickness on short-circuit current density and maximum power in tandem solar cell configuration. . . . 85
3.25 J–V characteristics of the tandem solar cell for different operating temperatures. . . . 86
3.26 Effect of temperature on short-circuit current density and maximum power in tandem solar cell configuration. . . . 87

4.1 Schematic representation of the 3T tandem solar cell cathode–anode–anode configuration. . . . 93
4.2 Cross sectional schematic of: (A) the top perovskite solar cell with the FTO/TiO_2/$MAPbI_3$/HTM/ITO configuration, and (B) the bottom silicon IBC solar cell with the a−Si:H(n^+)/a−Si:H(i)/c−Si(i)/a−Si:H(p^{++})-a−Si:H(n^{++})/ITO/Ag configuration. . . . 95
4.3 J–V characteristics of the top cell, bottom cell, and 3T tandem cell. . . . 99
4.4 EQE spectra of the top perovskite cell and bottom silicon cell in the 3T tandem configuration. . . . 102
4.5 Absorption and transmission spectra of the 3T tandem cell. . . . 103
4.6 Band diagram of the 3T tandem solar cell showing conduction and valence band energies across the device structure. . . . 105

4.7 Performance map of the (A) perovskite top sub-cell showing PCE as a function of V_{tz} and V_{rz} (max = 18.47 %), (B) silicon bottom sub-cell showing PCE as a function of V_{tz} and V_{rz} (max = 10.53 %), (C) 3T tandem cell showing PCE as a function of V_{tz} and V_{rz} (max = 28.99 %). 107
4.8 J–V curve comparison between 3T and 2T tandem solar cells. 109
4.9 EQE spectra for the 3T and 2T tandem cells. 111
4.10 Absorption and transmission spectra comparison between 3T and 2T tandem solar cells. 112
4.11 Band diagram energy for: (A) 3T tandem cell, (B) 2T tandem cell. 113

List of Tables

1.1 Summary of different generations of solar cells. 27

2.1 Comparison between hybrid and all-inorganic perovskites. 37

3.1 Parameters used for simulating the perovskite solar cell. 67
3.2 Input parameters of different HTLs used in the simulation. 73
3.3 Parameters of silicon layers in the tandem solar cell structure. 77
3.4 Comparative performance metrics for these different tandem solar cell architectures. 89

4.1 Material parameters for the layers of the bottom silicon IBC subcell in the 3T tandem solar cell. 96
4.2 Performance summary of top cell, bottom cell, and 3T tandem cell. 100
4.3 Performance summary of the 3T and 2T tandem cells. 110
4.4 Comparison of simulated 2T and 3T tandem solar cells with reported literature. 115

List of abbreviations and acronyms

ABX3 *Perovskite crystal structure formula*

AIP *All-Inorganic Perovskite*

AM1.5G *Air Mass 1.5 Global (standard solar spectrum)*

a-Si:H *Hydrogenated Amorphous Silicon*

BA *Butylammonium*

BIPV *Building-Integrated Photovoltaics*

CaTiO3 *Calcium Titanate*

c-Si *Crystalline Silicon*

CBM *Conduction Band Minimum*

CIGS *Copper Indium Gallium Selenide*

CZTSSe *Copper Zinc Tin Sulfur Selenide (Kesterite)*

DFT *Density Functional Theory*

DMF *N,N-Dimethylformamide*

DMSO *Dimethyl Sulfoxide*

DSSC *Dye-Sensitized Solar Cell*

Eg *Bandgap Energy*

EHP *Electron-Hole Pair*

EQE *External Quantum Efficiency*

ETL *Electron Transport Layer*

FA *Formamidinium ($HC(NH_2)_2^+$)*

FDTD *Finite-Difference Time-Domain*

FF *Fill Factor*

FTO *Fluorine-doped Tin Oxide*

GaAs *Gallium Arsenide*

GBL *Gamma-Butyrolactone*

HOIP *Hybrid Organic-Inorganic Perovskite*

HTL *Hole Transport Layer*

HTM *Hole Transport Material*

IBC *Interdigitated Back Contact*

IQE *Internal Quantum Efficiency*

ITO *Indium Tin Oxide*

Jsc *Short-Circuit Current Density*

LCOE *Levelized Cost of Electricity*

LED *Light-Emitting Diode*

MA *Methylammonium ($CH_3NH_3^+$)*

MAPbI3 *Methylammonium Lead Iodide*

MPP *Maximum Power Point*

n-i-p *n-type / intrinsic / p-type (device structure)*

OPV *Organic Photovoltaic*

p-i-n *p-type / intrinsic / n-type (device structure)*

PCE *Power Conversion Efficiency*

PCBM *Phenyl-C_{61}-Butyric Acid Methyl Ester*

PEDOT:PSS *Poly(3,4-ethylenedioxythiophene):Polystyrene Sulfonate*

PL *Photoluminescence*

PLQY *Photoluminescence Quantum Yield*

Pmax *Maximum Power Output*

PSC *Perovskite Solar Cell*

PTAA *Poly(triaryl amine)*

PV *Photovoltaic*

QD *Quantum Dot*

QE *Quantum Efficiency*

RH *Relative Humidity*

SAM *Self-Assembled Monolayer*

SHJ *Silicon Heterojunction*

SRH *Shockley-Read-Hall (recombination)*

TCAD *Technology Computer-Aided Design*

TCE *Transparent Conductive Electrode*

TCO *Transparent Conductive Oxide*

TGA *Thermogravimetric Analysis*

TMM *Transfer-Matrix Method*

UV *Ultraviolet*

UVO *Ultraviolet-Ozone*

VBM *Valence Band Maximum*

Voc *Open-Circuit Voltage*

XRD *X-Ray Diffraction*

2T *Two-Terminal (tandem configuration)*

3T *Three-Terminal (tandem configuration)*

4T *Four-Terminal (tandem configuration)*

Introduction

The accelerating global energy demand and mounting environmental concerns have positioned photovoltaic technology as a cornerstone of the renewable energy transition. Solar energy emerged as the fastest-growing renewable technology, with over 655 GW of new capacity installed in 2024, contributing significantly to global carbon emission reductions [1]. Photovoltaic systems directly convert sunlight into electricity, offering a clean and sustainable alternative to conventional energy sources. Despite this remarkable progress, the solar sector confronts persistent challenges in achieving cost-competitive, high-efficiency, and scalable solutions capable of surpassing the limitations inherent in first- and second-generation solar technologies [2].

Crystalline silicon has dominated the photovoltaic market for decades, representing approximately 95 % of global installations. Monocrystalline silicon solar cells have achieved laboratory efficiencies exceeding 27 %, approaching the theoretical Shockley–Queisser limit of approximately 33.7 % for single-junction devices [3]. However, silicon-based photovoltaics are constrained by fundamental and practical limitations. Silicon is an indirect bandgap semiconductor with a bandgap of approximately 1.12 eV, requiring thick absorber layers exceeding 200 µm to achieve adequate photon absorption. This necessitates high-purity crystalline wafers produced via energy-intensive processes such as the Czochralski method, with processing temperatures exceeding 1000 °C [1, 2]. Silicon exhibits substantial thermalization losses, where photons with energies significantly above the bandgap generate hot carriers that rapidly relax to the band edge, dissipating excess energy as heat. Additionally, silicon's relatively low absorption coefficient in the near-infrared necessitates advanced light-trapping architectures such as textured surfaces and anti-reflection coatings, adding complexity and cost. The efficiency plateau observed in commercial silicon modules, typically 20 % to 22 %, underscores the difficulty of translating laboratory-scale advances into mass production [4]. Given these intrinsic limitations, the photovoltaic research community has intensified efforts to identify alternative absorber materials. The ideal next-generation photovoltaic material should exhibit a direct bandgap with high absorption coefficient exceeding 10^4 cm^{-1}, bandgap tunability across 1.2 eV to 2.3 eV for spectral optimization and tandem integration, low-temperature solution-based processability to reduce manufacturing energy and cost, high carrier mobilities exceeding $10\,\mathrm{cm}^2\,\mathrm{V}^{-1}\,\mathrm{s}^{-1}$ and long diffusion lengths exceeding 1 µm, defect tolerance to minimize non-radiative recombination, and compatibility with flexible substrates. Metal-halide perovskites have demonstrated unprecedented progress in addressing these criteria. Perovskite solar cells, first reported with 3.8 % efficiency in 2009, have achieved certified laboratory efficiencies exceeding 26.7 % for single-junction devices and 34.85 % for perovskite–silicon tandem architectures as of 2024 [5]. This rapid effi-

ciency trajectory, unmatched in photovoltaic history, has been enabled by the unique optoelectronic properties of metal-halide perovskites, including tunable direct bandgaps, strong visible-light absorption, ambipolar charge transport, and remarkable tolerance to structural defects [6, 7].

Metal-halide perovskites belong to a versatile family of compounds with the general formula ABX_3, where A is a monovalent cation such as methylammonium, formamidinium, or cesium, B is a divalent metal cation typically lead or tin, and X is a halide anion. Perovskite absorbers exhibit absorption coefficients exceeding 10^5 cm^{-1} in the visible spectrum, enabling complete photon harvesting in films as thin as 300 nm to 500 nm, drastically reducing material consumption compared to silicon's 200 µm requirement. All-inorganic perovskites, such as $CsPbI_3$ and $CsPbBr_3$, replace the volatile organic A-site cations with inorganic cesium or rubidium, significantly enhancing thermal stability exceeding 300 °C and resistance to moisture-induced degradation [8]. While all-inorganic perovskites sacrifice some optoelectronic performance of hybrid organic–inorganic perovskites like $MAPbI_3$, they offer markedly improved long-term operational stability, a critical requirement for commercial deployment. $CsPbI_3$-based devices have achieved efficiencies exceeding 21 %, demonstrating the viability of inorganic compositions for high-performance photovoltaics [9].

The transition from hybrid organic–inorganic to all-inorganic perovskite compositions represents a strategic pathway to address the primary limitation of perovskite solar cells: operational stability. Hybrid organic–inorganic perovskites such as $MAPbI_3$ undergo rapid degradation when exposed to moisture, oxygen, elevated temperatures exceeding 85 °C, and prolonged UV irradiation. The hygroscopic methylammonium cation volatilizes at temperatures below 200 °C, leading to irreversible decomposition. In contrast, all-inorganic perovskites retain their crystalline integrity at temperatures exceeding 400 °C and demonstrate superior resistance to environmental stressors. $CsPbI_3$-based devices have maintained over 90 % of initial efficiency under damp-heat conditions at 85 °C and 85 % relative humidity for prolonged durations. Furthermore, all-inorganic perovskites exhibit reduced ion migration, a key mechanism underlying hysteresis and voltage-scan-direction-dependent performance degradation. However, the photoactive black α-phase of $CsPbI_3$ is metastable at room temperature, spontaneously converting to a non-perovskite yellow δ-phase with poor photovoltaic properties, necessitating compositional alloying or surface passivation strategies [8].

The rapid ascent of perovskite solar cells has positioned them as the most viable alternative to silicon photovoltaics for next-generation energy conversion. Perovskite solar cells combine the efficiency of crystalline silicon with low-cost, solution-processable fabrication. Perovskite absorbers can be deposited via spin-coating, blade-coating, inkjet printing, or slot-die coating at temperatures below 150 °C, enabling compatibility with flexible polymer substrates and roll-to-roll manufacturing. The tunable bandgap of perovskites makes them uniquely suited for tandem solar cell architectures, which surpass the Shockley–Queisser limit by stacking multiple absorbers with complementary bandgaps. Perovskite–silicon tandems, wherein a wide-bandgap perovskite top cell with a bandgap of approximately 1.6 eV to 1.7 eV captures high-energy photons and a silicon bottom cell absorbs near-infrared radiation, have achieved certified efficiencies of 34.85 %. All-perovskite tandems, pairing wide-bandgap perovskites with narrow-bandgap tin–lead alloys, have

reached efficiencies of 31.38 % [10, 11].

Despite the remarkable experimental progress in perovskite solar cells, further efficiency optimization and commercialization require systematic computational modeling to guide material selection, device architecture design, and fabrication parameter optimization. The primary objective of this thesis is the design, simulation, and optimization of perovskite-based photovoltaic devices using advanced numerical modeling frameworks, with particular emphasis on single-junction perovskite solar cells and two-terminal and three-terminal tandem architectures integrating perovskite and silicon subcells. The study leverages Silvaco ATLAS TCAD software, a physics-based semiconductor device simulator, to solve the coupled Poisson, carrier continuity, and drift-diffusion transport equations governing photovoltaic operation. The simulation platform incorporates wavelength-dependent optical generation via transfer-matrix methods, Shockley–Read–Hall and Langevin recombination mechanisms, Poole–Frenkel field-dependent mobility, and realistic material parameters derived from experimental literature.

Chapter 1 establishes the theoretical foundation by reviewing the fundamental physics of semiconductors, *p*-*n* junctions, photovoltaic operation, solar radiation, and the classification of solar cell technologies from first-generation crystalline silicon to third-generation perovskite and tandem systems.

Chapter 2 focuses on perovskite materials and perovskite solar cells, covering the crystallographic structure and classification of metal-halide perovskites, the distinctions between hybrid organic–inorganic and all-inorganic compositions, their optical and electronic properties, device architectures, and the advantages and limitations shaping their practical deployment. The chapter concludes with an introduction to tandem solar cell architectures, including two-terminal, three-terminal, and four-terminal designs.

Chapter 3 presents the computational methodology employed for simulating and optimizing perovskite-based photovoltaic devices using Silvaco ATLAS TCAD software. This chapter details the device structure definition, mesh refinement, physical models, optical generation under AM1.5G illumination, and validation against experimental single-junction perovskite solar cells. The chapter then investigates the effect of hole transport layer selection on device performance and presents the design, simulation, and optimization of a two-terminal monolithic perovskite–silicon tandem solar cell.

Chapter 4 explores the design and performance evaluation of a three-terminal perovskite–silicon tandem solar cell, highlighting its structural definition, physical modeling, and voltage decoupling advantages over conventional two-terminal designs. The chapter includes two-dimensional voltage mapping to identify optimal operating points and comparative analysis with two-terminal tandems.

Chapter 1

Semiconductor physics and the photovoltaic effect

1.1 Introduction

Photovoltaic technology converts sunlight directly into electricity using semiconductor materials, providing a clean and sustainable alternative to conventional energy sources. Rooted in the photovoltaic effect discovered in the 19th century, PV science has evolved from simple experimental cells to highly efficient, advanced solar devices driving today's renewable energy transition [12].

This chapter outlines the fundamental principles governing solar cell operation, starting with the essential properties of semiconductors—their band structures, carrier dynamics, and doping mechanisms that give rise to n-type and p-type materials. The formation and behavior of the p–n junction, along with its current–voltage characteristics and the photovoltaic effect, are examined as the basis of energy conversion in PV devices. Further sections discuss solar radiation, charge generation, recombination, and quantum efficiency, followed by an overview of key performance parameters. Finally, the chapter highlights the evolution of solar cell technologies—from first-generation silicon devices to emerging perovskite and tandem architectures—emphasizing their role in enhancing efficiency, reducing costs, and enabling large-scale deployment of solar energy.

1.2 History

Historically, the concept dates back to 1839 when Alexandre-Edmond Becquerel first observed the photovoltaic effect in a metal–electrolyte system [13]. Subsequent milestones include Willoughby Smith's discovery of selenium photoconductivity in 1873 [14], Charles Fritts's fabrication of the first selenium-based solar cell in 1883 (efficiency $< 1\,\%$), and Russell Shoemaker Ohl's accidental creation of a silicon p–n junction in 1940, yielding $\approx$1 % efficiency [15]. A pivotal moment occurred in 1954 when Daryl Chapin, Gerald Pearson, and Calvin Fuller at Bell Laboratories produced the first practical silicon solar cell with $\approx$6 % efficiency, demonstrated by powering small electrical devices [16].

By the 1960s, solar cells found their first major application in space, powering satellites [17]. Over the decades, improvements in materials, surface passivation, and optical management have raised silicon cell efficiencies beyond 27 % in laboratories [18], while tandem architectures—such as perovskite/silicon—have achieved record efficiencies of 34.85 % [19]. Today, PV technology is the fastest-growing renewable energy source, with roughly 600 GW to 655 GW added in 2024 and global capacity surpassing about 2.2 TW. In 2025, it remains on an approximately 20 % growth trajectory, with dozens of countries installing more than 1 GW annually, collectively avoiding on the order of hundreds of millions to billions of tons of CO_2 each year [20, 21].

1.3 Semiconductors materials: proprieties and types

Semiconductors are a group of elements that show electrical conductivity between that of insulators and conductors. It is a characteristic due to their band gap—the narrow energy gap between the valence band (occupied by electrons) and the conduction band (where

electrons are mobile) [22]. Pure or intrinsic semiconductors have an unfilled conduction band at absolute zero (0 K), while the valence band is completely filled. As temperature increases, thermal energy excites some electrons over the narrow forbidden band gap into the conduction band, thereby facilitating electrical conductivity. The conductivity is a temperature-dependent property, as opposed to metals, where conductivity tends to decrease with temperature increase [23].

Semiconductor materials can be elemental, for example, silicon (Si) and germanium (Ge), or compounds, for example, gallium arsenide (GaAs), indium phosphide (InP), and cadmium telluride (CdTe). Ternary alloys such as $Al_xGa_{1-x}As$ or Si_xGe_{1-x} are also widely used for fine-tuning electronic properties. They are normally formed by atoms that possess four valence electrons, facilitating covalent bonding within a crystal lattice [24]. Figure 1.1 provides a pictorial account of some widely seen semiconductor materials, covering elements within group IV and compound semiconductors within groups III–V and II–VI.

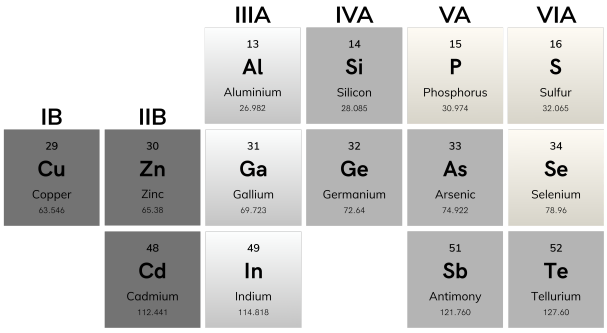


Figure 1.1: Common semiconductor materials.

1.3.1 Energy bands

To better understand their electrical behavior, semiconductors are often compared to conductors and insulators using energy band diagrams. As shown in Figure 1.2, conductors have overlapping valence and conduction bands, allowing free movement of electrons without any external energy [25]. Insulators, on the other hand, have a very wide band gap, preventing electron flow under normal conditions.

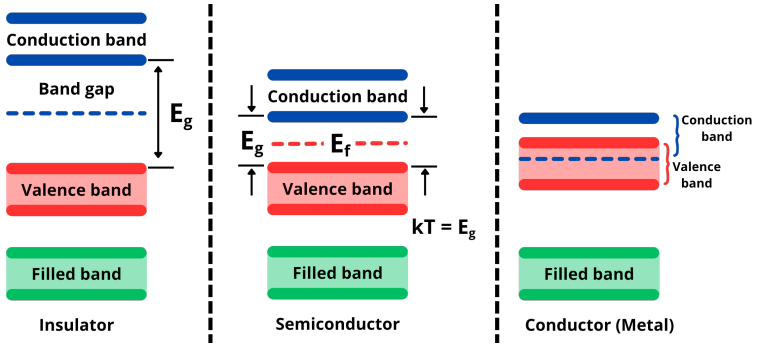


Figure 1.2: Band diagram.

Semiconductors sit between these extremes, with a moderate band gap that allows electrons to be thermally or optically excited into the conduction band. When an electron makes this transition, it leaves behind a "hole" in the valence band—an absence of an electron that behaves as a positive charge carrier. The flow of current in semiconductors is thus governed by both electrons and holes, and their concentrations increase with temperature [26].

1.3.2 Fermi energy

In semiconductor materials, both the concept of Fermi energy (E_f) and the presence of holes are fundamental for understanding electrical behavior [27]. At room temperature (300 K), neither the conduction band nor the valence band is entirely full or completely empty [28]. The conduction band—typically sparsely populated at its lower edge—is called so because it allows electrons to move freely, enabling electrical conduction. In contrast, the valence band, though almost fully occupied, still contains a few vacant energy states near its top, which also contribute to conduction [29].

The electrons within the valence band, referred to as valence electrons, are generally bound in covalent bonds. However, when they gain sufficient energy—either thermally or optically—they can jump across the band gap (E_g) to the conduction band. This transition leaves behind an empty state in the valence band, known as a hole [30]. Both the excited electrons in the conduction band and the holes in the valence band act as charge carriers and contribute to current flow [31]. The E_f level lies somewhere within the E_g and represents a statistical threshold: it is the energy at which the probability of an electron occupying a state is exactly 50 %. States below E_f are more likely to be filled, while those above it are more likely to be empty [31]. In intrinsic (pure) semiconductors, the Fermi level is typically located near the center of the E_g.

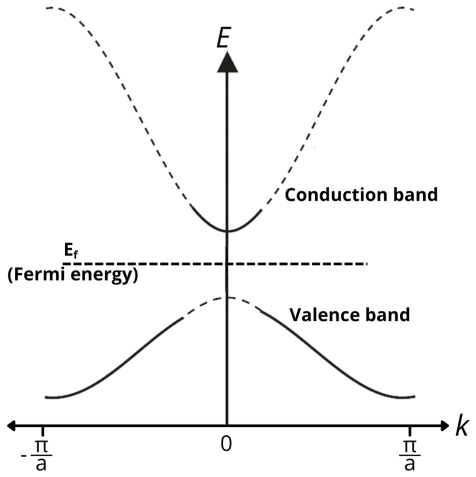


Figure 1.3: Semiconductor at room temperature showing fermi energy level.

As shown in Figure 1.3, a semiconductor in thermal equilibrium at room temperature exhibits partial filling in the conduction band and some empty states in the valence band. When an electron gains enough energy to leave its covalent bond, it creates an electron–hole pair (EHP). The energy required for this transition must be at least equal to the

material's bandgap energy [32]. Once free, the electron can move through the lattice via the conduction band, while the hole can migrate through the valence band as surrounding electrons jump to fill it [33]. This dual mechanism of conduction—by electrons and holes—is essential in semiconductor physics [27]. To assess a semiconductor's electrical conductivity, one must determine the concentration of electrons (n) and holes (p) per unit volume. For intrinsic semiconductors, these concentrations are equal, denoted by $n_\mathrm{i} = p_\mathrm{i}$ [34].

1.3.3 Semiconductors types

There are two main types of semiconductors: intrinsic and extrinsic. In its pure form, an intrinsic semiconductor has very low electrical conductivity because it has a high resistivity. However, this conductivity can be significantly modified by deliberately introducing small amounts of foreign atoms into the lattice, a process known as doping. When such impurities are incorporated, the material is termed an extrinsic semiconductor [35]. Compared with intrinsic types, extrinsic semiconductors demonstrate enhanced conductivity and are therefore widely employed in the fabrication of electronic components, including diodes and transistors.

The dopants used for this purpose are typically either pentavalent or trivalent elements. Pentavalent atoms, such as phosphorus (P), arsenic (As), or antimony (Sb), possess five valence electrons in their outer shell. In contrast, trivalent elements—such as boron (B), aluminum (Al), gallium (Ga), or indium (In)—contain only three valence electrons. Depending on whether pentavalent or trivalent impurities are introduced, extrinsic semiconductors are classified into two main types [34]:

N-type

An n-type semiconductor is created by adding pentavalent atoms—such as phosphorus, arsenic, or antimony—to an intrinsic semiconductor like silicon. These atoms contain five valence electrons, one more than the four required to form stable covalent bonds with neighboring silicon atoms [22], as illustrated in Figure 1.4.

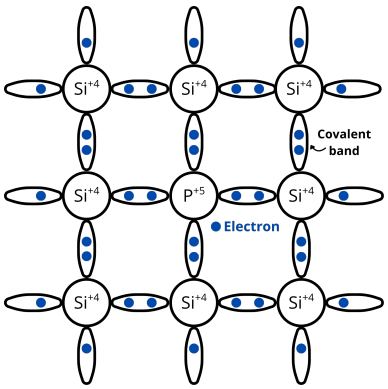


Figure 1.4: n-type semiconductor.

The fifth electron remains unbound and free to move throughout the lattice, contributing to electrical conduction. This process is known as doping, and the pentavalent

atoms are called donor impurities because they ”donate” free electrons to the conduction band.

As a result, electrons become the majority carriers in the n-type material, while holes exist in smaller numbers and act as minority carriers. When an external voltage is applied, these free electrons flow toward the positive terminal, enabling efficient current conduction, as shown in Figure 1.5. From a band structure perspective, doping introduces a donor energy level just below the conduction band, requiring minimal energy to excite electrons into the conduction band [36]. This characteristic makes n-type semiconductors essential for the formation of the p–n junction in solar cells, where electron transport dominates and supports current generation under illumination [37].

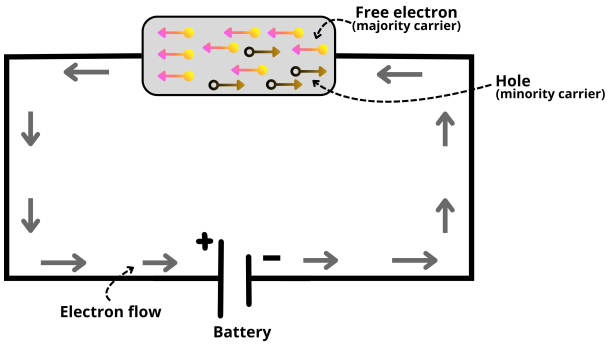


Figure 1.5: Conduction in n-type semiconductor.

P-type

A p-type semiconductor is obtained by introducing a small concentration of trivalent atoms—such as boron, aluminum, or gallium—into a pure semiconductor material like silicon [22]. These atoms possess only three valence electrons, which means when they replace a silicon atom in the crystal lattice, one covalent bond remains incomplete, as illustrated in Figure 1.6.

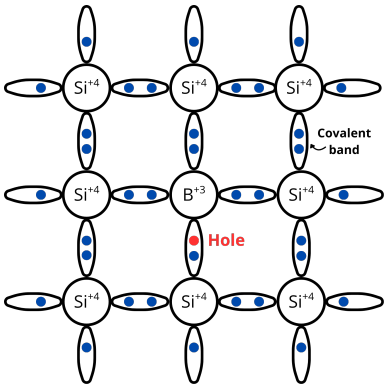


Figure 1.6: p-type semiconductor.

This absence of an electron creates what is known as a “hole”, which behaves like a positive charge carrier. Since trivalent atoms readily accept electrons to complete their bonding structure, they are referred to as acceptor impurities. As more of these atoms

are introduced, the number of holes increases, making them the majority charge carriers in the material, while electrons become the minority carriers [38].

The movement of these holes under an electric field—from the positive to the negative terminal—enables current flow, as shown in Figure 1.7. In terms of band theory, p-type doping introduces an energy level just above the valence band called the acceptor level, allowing electrons from the valence band to be thermally excited into this level, leaving behind mobile holes [37]. This mechanism underpins the functionality of p-type materials in devices like diodes and solar cells, where hole transport plays a crucial role.

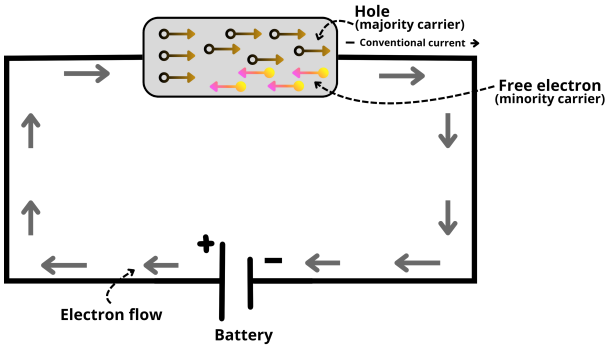


Figure 1.7: Conduction in p-type semiconductor.

1.4 Conductivity in semiconductors

1.4.1 Conductivity of intrinsic semiconductors

Intrinsic semiconductors, such as pure silicon or germanium, are characterized by an equal concentration of electrons in the conduction band and holes in the valence band. Under the influence of an external electric field, these charge carriers move in opposite directions—electrons towards the positive terminal and holes towards the negative terminal—producing an electric current [30, 34]. The total current I in an intrinsic semiconductor is the sum of the electron current I_e and the hole current I_h [39]. These are given by:

$$I_e = n_i e \nu_e A \tag{1.1}$$

$$I_h = p_i e \nu_h A \tag{1.2}$$

where $n_i = p_i$ is the intrinsic carrier concentration, e is the elementary charge, ν_e and ν_h are the drift velocities of electrons and holes, respectively, and A is the cross-sectional area [30].

Since drift velocity v is proportional to the electric field E, we use the relation [40]:

$$\nu_e = \mu_e E \tag{1.3}$$

$$\nu_h = \mu_h E \tag{1.4}$$

where μ_e and μ_h are the mobilities corresponding to electrons and holes, respectively [41].

Substituting these expressions into the total current gives [42]:

$$I = n_i e(\mu_e + \mu_h)EA \tag{1.5}$$

By Ohm's law $V = IR$, and considering a material of length l, we get:

$$E = \frac{V}{l} \quad \Rightarrow \quad I = n_i e(\mu_e + \mu_h)\frac{V}{l}A \tag{1.6}$$

The intrinsic resistivity ρ_i is then defined as [43]:

$$\rho_i = \frac{1}{n_i e(\mu_e + \mu_h)} \tag{1.7}$$

and the corresponding conductivity becomes:

$$\sigma_i = n_i e(\mu_e + \mu_h) \quad \text{(S/m)} \tag{1.8}$$

This shows that the conductivity increases with both carrier mobility and intrinsic carrier concentration, both of which are temperature-dependent. Notably, n_i increases exponentially with temperature due to thermal excitation, making intrinsic semiconductors significantly more conductive at higher temperatures [44].

1.4.2 Conductivity of extrinsic semiconductors

In extrinsic semiconductors, doping introduces additional carriers into the system, drastically altering the conductivity [45]. The total current density J in an extrinsic semiconductor is given by:

$$J = e\left(n\mu_e + p\mu_h\right)E \tag{1.9}$$

leading to a conductivity of:

$$\sigma = e\left(n\mu_e + p\mu_h\right) \tag{1.10}$$

where n and p are the carrier concentrations of electrons and holes, respectively [45].

N-type semiconductors

In n-type materials, donor atoms introduce free electrons into the conduction band. Assuming a doping level where $N_D \gg n_i$, the electron concentration n_n becomes significantly greater than the hole concentration p_n. Therefore, the conductivity simplifies to:

$$\sigma_n \approx e n_n \mu_e \tag{1.11}$$

indicating that conductivity is primarily determined by the electron mobility and the concentration of donor electrons [46].

P-type semiconductors

In p-type semiconductors, acceptor atoms introduce holes by capturing electrons from the valence band. For $N_A \gg n_i$, the hole concentration p_p is much greater than the electron concentration n_p, and the conductivity becomes:

$$\sigma_p \approx e p_p \mu_h \tag{1.12}$$

Here, conductivity is primarily governed by the hole mobility and the number of holes injected via acceptor doping [46].

At very low temperatures, extrinsic semiconductors experience carrier freeze-out, where dopant atoms are not fully ionized, significantly reducing conductivity [47]. In the intermediate temperature range (extrinsic region), mobility typically decreases with increasing temperature due to enhanced phonon scattering, causing the conductivity to drop. However, at high temperatures, intrinsic carrier generation becomes dominant again, leading to an exponential increase in conductivity—similar to the behavior of intrinsic materials [42, 48].

Understanding the p–n junction, the essential component of photovoltaic devices, is based on these theoretical concepts of intrinsic and extrinsic semiconductor behavior. The p–n junction is a crucial component of solar cell function because it combines p-type and n-type regions into a single structure, allowing charge separation and current generation under illumination.

1.5 Photovoltaic fundamentals: the p-n junction

1.5.1 P-N junction: concept and operation

A p-n junction is formed by introducing p-type and n-type dopants into specific regions of a single semiconductor crystal, as illustrated in Figure 1.8. The area where these two doped regions meet is known as the junction interface. At this boundary, it is theoretically assumed that the concentrations of donor and acceptor atoms are equal [49].

To avoid the creation of grain boundaries—which would occur if the junction were formed by physically combining two separate materials—the p-n junction is typically realized within a monocrystalline semiconductor through a controlled doping process [49, 50]. Upon forming this junction, three fundamental phenomena occur at the interface:

- A depletion region (also called the space charge or transition region) forms across the junction.

- A potential barrier develops between the p-type and n-type regions.
- The presence of this depletion region results in the emergence of both junction capacitance and diffusion capacitance.

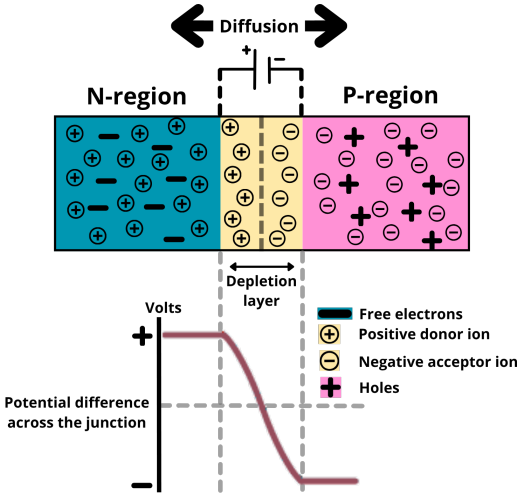


Figure 1.8: p-n junction semiconductor.

Immediately after the formation of a p-n junction, the electrons predominantly remain in the n-type region, while holes are concentrated in the p-type region [29]. Because the electron concentration is significantly higher in the n-region than in the p-region, electrons act as minority carriers in the p-region. Likewise, the p-region contains a much greater number of holes compared to the n-region, making holes the minority carriers in the n-region [51]. Upon the junction's formation, electrons begin to diffuse from the n-region into the p-region, leaving behind positively charged donor ions near the interface. Concurrently, holes diffuse from the p-region into the n-region, resulting in the presence of negatively charged acceptor ions near the junction. This separation of charges leads to the creation of a built-in electric field, forming a barrier potential V_B [32], also referred to as the depletion region, as depicted in Figure 1.8.

This depletion region establishes itself very rapidly and is relatively thin compared to the overall p- and n-type regions. The potential barrier it creates inhibits further movement of charge carriers across the junction unless external energy—typically from an applied voltage—is supplied. Under standard conditions, the built-in potential is around 0.7 V for Si and 0.3 V for Ge [52].

1.5.2 Energy band diagram and formation of the pn junction

The energy band diagram of a p-n junction is illustrated in Figure 1.9. At the moment the junction is created, the p-type region—doped with trivalent atoms—exhibits impurity energy levels that are slightly higher than those in the n-type region [53], which is doped with pentavalent atoms. This difference arises because trivalent atoms have valence electrons that are less tightly bound to the nucleus compared to pentavalent atoms. As a result, the valence electrons in the p-region occupy higher energy states [53]. This leads to

a partial overlap between the energy bands of the two regions. As a consequence, electrons in the higher-energy conduction band of the n-region tend to move, or diffuse, into the lower-energy conduction band of the p-region. Upon entering the p-region, these electrons recombine rapidly with holes present in the valence band, as shown in Figure 1.9(a). This process continues, causing the development of a depletion region near the junction [53].

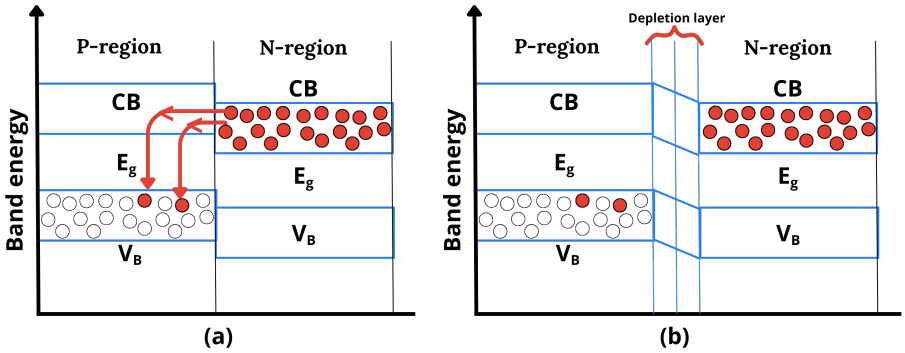


Figure 1.9: Energy band diagram of p-n junction, (a) Carrier diffusion and recombination at the junction before equilibrium, (b) Band bending and built-in potential barrier formation at thermal equilibrium.

As electrons leave the n-region, the overall energy level in that region decreases, effectively shifting the energy bands downward. This band bending continues until the conduction band edge of the n-region aligns with that of the p-region [54]. At this point, thermal equilibrium is established, as depicted in Figure 1.9(b). The resulting potential difference forms a barrier—often described as a steep energy "hill"—that prevents further spontaneous electron diffusion [54]. Electrons can only overcome this potential barrier if external energy, such as a forward bias voltage, is supplied.

1.6 Biasing of the pn junction

A p–n junction is a two-terminal electronic component consisting of a p-type and n-type semiconductor joined together. These terminals are known as the anode and cathode. One of the defining characteristics of the p–n junction is its unidirectional behavior—it allows current to pass readily in one direction (forward) while significantly resisting flow in the opposite direction (reverse) [55]. To control the behavior of the p–n junction, it is connected to a DC voltage source, a process known as biasing. The response of the p–n junction to this external voltage depends on the type of biasing applied: either forward or reverse [32].

1.6.1 Forward bias

In a forward-biased configuration, the positive terminal of the voltage source is connected to the anode (p-type region), and the negative terminal to the cathode (n-type region). This setup reduces the potential barrier at the junction, thereby allowing charge carriers—holes from the p-side and electrons from the n-side—to move toward the junction. As

they meet, recombination occurs, enabling a significant current to flow through the device [51]. This movement of carriers leads to a reduction in the width of the depletion region, effectively lowering the junction's resistance. The result is a substantial increase in current, provided the applied voltage exceeds the material's threshold [56].

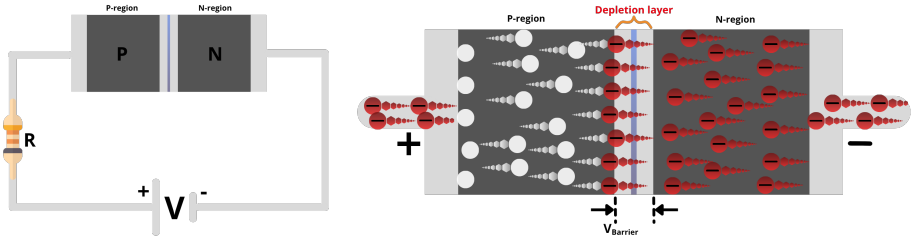


Figure 1.10: Forward-biased p–n junction.

1.6.2 Reverse bias

Conversely, in reverse bias, the p–n junction is connected such that the negative terminal of the voltage source is attached to the p-type region, and the positive terminal to the n-type region. This orientation pulls holes away from the junction toward the battery's negative terminal [57], and electrons toward the positive terminal, causing both types of charge carriers to move away from the junction. As a result, recombination at the junction ceases, and current flow is essentially blocked. The depletion layer becomes wider, and the barrier potential increases, creating a high-resistance path [32].

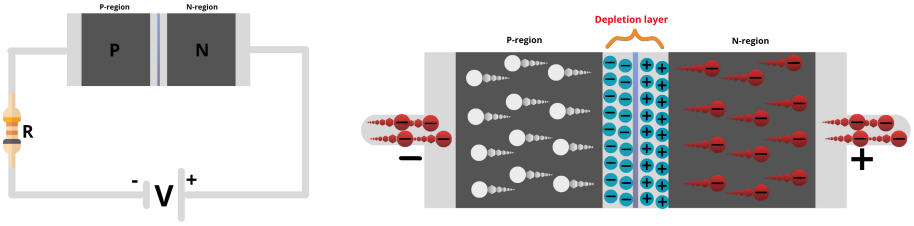


Figure 1.11: Reverse-biased p–n junction.

1.7 Current expression

The current–voltage (I–V) relationship of an ideal p–n junction is governed by Shockley's diode equation, which accurately models the general characteristics in both the forward-bias and reverse-bias operating regions [58, 59]. Mathematically, the equation is expressed as:

$$I = I_0 \left[\exp\left(\frac{V_D}{\eta V_T} \right) - 1 \right] \tag{1.13}$$

where I is the instantaneous p–n junction current, I_0 is the reverse saturation current, V_D is the applied voltage across the p–n junction, η is the ideality factor (also referred to as the semiconductor constant), which depends on the material properties, device construction,

and operating conditions (typically in the range $1 \leq \eta \leq 2$, with $\eta = 1$ for an ideal diode), and V_T is the thermal voltage [60], defined as:

$$V_T = \frac{kT}{q} \tag{1.14}$$

Here, k is Boltzmann's constant ($1.3810^{-23}\,\mathrm{J\,K^{-1}}$), T is the absolute temperature in kelvin, and q is the elementary charge of an electron ($1.610^{-19}\,\mathrm{C}$). Substituting the expression for V_T into equation 1.13 yields the widely used form of Shockley's equation [60]:

$$I = I_0 \left[\exp\left(\frac{qV_D}{\eta kT} \right) - 1 \right] \tag{1.15}$$

This equation indicates that in forward bias ($V_D > 0$), the exponential term dominates, leading to an exponential increase in current once V_D exceeds the threshold voltage. Conversely, in reverse bias ($V_D < 0$), the current is approximately equal to $-I_0$, corresponding to the small leakage current due to thermally generated minority carriers. The V_T plays a crucial role in determining the slope of the exponential region and is approximately 25.85 mV at room temperature [58, 60]. Importantly, this current equation also serves as the foundation for understanding the photovoltaic effect. An extra photocurrent term is added to the Shockley equation when a p–n junction is exposed to light, changing the p–n junction I–V relationship. Essential performance parameters like short-circuit current, open-circuit voltage, fill factor, and overall conversion efficiency are derived from the characteristic I–V curve of a solar cell, which is defined by the balance between the p–n junction's dark current and the light-generated photocurrent.

1.8 The photovoltaic effect and carrier generation

1.8.1 Photovoltaic effect

Light-absorbing semiconductors lie at the heart of PV technology. In essence, these materials capture sunlight and transform it into electrical energy by transferring energy from photons to electrons—a phenomenon first reported by Edmond Becquerel in 1839 [61]. For this process to occur efficiently, the material must absorb incoming photons, generating either excitons or immediately separated electron–hole pairs, and then transport these charge carriers to their respective selective contacts while minimizing energy losses [62].

Each photon, despite having no rest mass, carries an energy E inversely proportional to its wavelength λ, given by [63]:

$$E = \frac{hc}{\lambda} = h\nu = pc \tag{1.16}$$

where h is Planck's constant, c is the speed of light, ν is the photon frequency ($\nu = \frac{c}{\lambda}$), and p is the photon momentum. In semiconductors, electrons mainly occupy the valence band. When a photon with energy $h\nu$ greater than the bandgap E_g is absorbed, an electron can be promoted from the valence band to the conduction band, leaving behind a hole. Any energy in excess of E_g is quickly dissipated as heat through thermalization, as excited carriers relax within femtoseconds to the band edges E_c and E_v, as depicted in Figure 1.12.

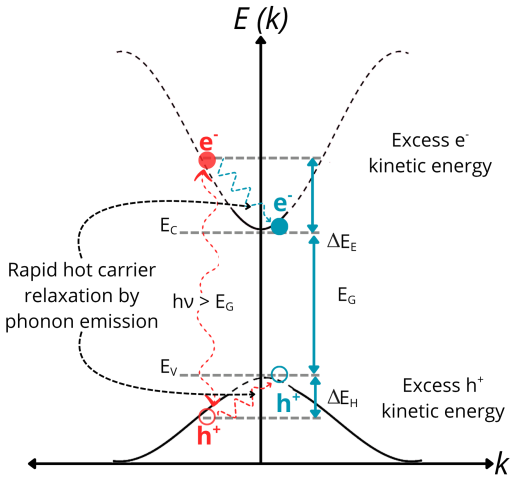


Figure 1.12: Energy band diagram showing photon absorption (h_v>E_g) and carrier relaxation to band edges.

For the situation illustrated in Figure 1.13, the conduction and valence bands are aligned in momentum space. This configuration allows photons with energies above E_g to be readily absorbed, producing a sharp absorption edge—characteristic of direct bandgap semiconductors. In contrast, in an indirect bandgap material, the conduction band minimum is shifted in momentum space relative to the valence band maximum. Because photons have negligible momentum ($p = \frac{h}{\lambda}$), a phonon must participate in the transition to conserve momentum. This additional requirement lowers the absorption probability for photons with $h\nu > E_g$, leading to a more gradual absorption onset. As a result, indirect bandgap materials such as silicon must be much thicker (around 200 µm) to absorb the same photon flux that a direct bandgap material, like a halide perovskite, can absorb in layers only 500 nm thick [17, 64]. On the other hand, this phonon requirement also suppresses radiative recombination, since electron–hole recombination across an indirect gap must likewise be phonon-assisted [65].

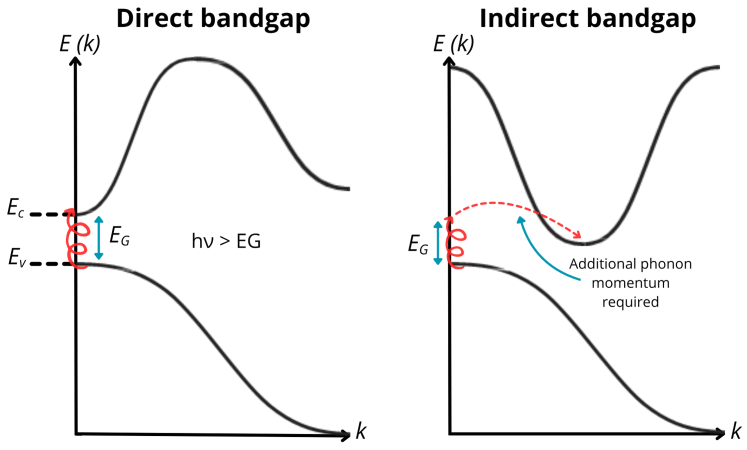


Figure 1.13: Direct and indirect bandgap semiconductor excitation processes.

This process is directly analogous to the operation of a p–n junction under illumination. In the dark, a p–n junction naturally forms a depletion region with a built-in electric

field that drives electrons toward the n-side and holes toward the p-side. This same inherent field separates the electron-hole pairs created when light is absorbed, sweeping electrons into the n-region's conduction band and holes into the p-region's valence band. By allowing the carriers to flow to external contacts and preventing instantaneous recombination, this separation creates a current. To put it another way, the p–n junction functioning in illumination can be thought of as the photovoltaic effect. In this case, the same junction physics that controls p–n junction conduction in the dark also controls how much photocurrent a solar cell generates.

Mathematically, this is expressed by the modified Shockley diode equation under illumination:

$$I(V) = I_{\text{ph}} - I_0 \left[\exp\left(\frac{qV}{\eta k T} \right) - 1 \right] \tag{1.17}$$

where I_{ph} is the photocurrent generated by absorbed light, I_0 is the reverse saturation current, q is the elementary charge, k is Boltzmann's constant, T is the absolute temperature, and η is the diode ideality factor. This equation highlights that the solar cell behaves like a diode with an added photocurrent source, and all key photovoltaic parameters—including I_{sc}, V_{oc}, fill factor, and conversion efficiency—are derived from this relationship.

1.8.2 Quantum efficiency

The performance of a solar cell is fundamentally governed by its ability to convert incident photons into free charge carriers that contribute to the external current. This ability is quantitatively described by the quantum efficiency (QE), which provides a spectral measure of the device's photoresponse. The quantum efficiency at a given wavelength, $QE(\lambda)$, is defined as the ratio between the number of charge carriers collected at the electrodes and the number of incident photons of that wavelength. Mathematically:

$$QE(\lambda) = \frac{N_{\text{collected carriers}}}{N_{\text{incident photons}}} \tag{1.18}$$

An ideal solar cell would exhibit a unitary quantum efficiency ($QE = 1$) for all photons with energies exceeding the bandgap ($h\nu > E_g$), implying that each absorbed photon generates one collected electron–hole pair. In practice, however, various loss mechanisms—including reflection, incomplete absorption, and carrier recombination—reduce the measured QE below this ideal value.

Quantum efficiency can be evaluated in two complementary forms. The EQE accounts for all incident photons, thus including optical losses such as reflection and transmission through the device. It therefore represents the overall probability that a photon striking the cell surface will result in a collected charge carrier. In contrast, the IQE considers only the absorbed photons, providing a more intrinsic measure of how effectively the device converts absorbed light into electrical current. IQE is typically obtained by correcting EQE for reflection and transmission losses according to the relation:

$$IQE(\lambda) = \frac{EQE(\lambda)}{1 - R(\lambda) - T(\lambda)} \tag{1.19}$$

where $R(\lambda)$ and $T(\lambda)$ denote the wavelength-dependent reflectance and transmittance, respectively.

Spectral variations in QE reflect underlying physical processes within the solar cell. At short wavelengths (blue region), photons are absorbed near the surface, where inadequate passivation can lead to surface recombination losses. At intermediate wavelengths (green region), limited carrier diffusion lengths or bulk recombination can diminish carrier collection. At long wavelengths (red and infrared regions), photons may traverse the absorber without being fully absorbed if its thickness or absorption coefficient is insufficient. Consequently, the QE spectrum serves as a powerful diagnostic tool for evaluating the optical and electronic quality of each layer in the photovoltaic device and for identifying loss mechanisms that limit its overall efficiency.

While achieving high quantum efficiency—maximising the number of absorbed photons and their conversion into charge carriers—is essential, it is equally important to extract these carriers with the highest possible energy. Materials with larger E_g absorb fewer photons, but the energy retained per photon is higher, leading to smaller thermalisation losses [66].

This inherent trade-off between carrier energy (favoured by a wider bandgap) and the number of carriers generated (favoured by a narrower bandgap), combined with unavoidable intrinsic losses, determines the detailed balance limit (Figure 1.14). This theoretical framework sets the upper limit for the power conversion efficiency of an ideal single-junction solar cell operating under the AM1.5G spectrum [3, 67]. It accounts for spectral losses (sub-bandgap transmission and thermalisation) and radiative recombination losses. In real devices, additional non-ideal effects in the absorber and at the selective contacts further lower the practical efficiency compared to this theoretical maximum [68].

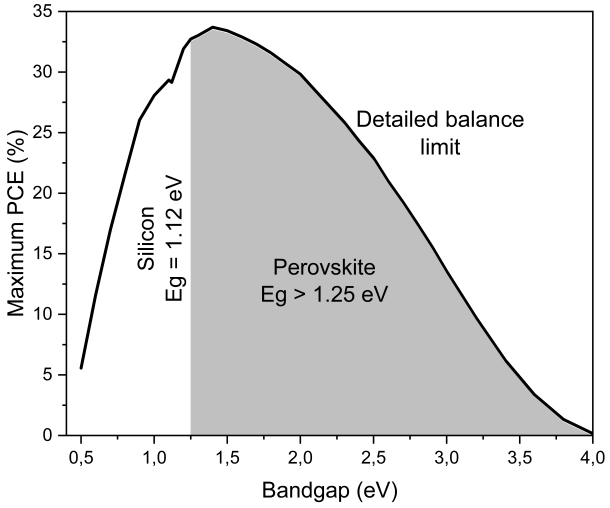


Figure 1.14: Shockley–Queisser efficiency limit vs bandgap energy [3].

1.8.3 Recombination and carrier extraction

When a semiconductor absorbs a photon, it can generate a bound electron–hole pair called an exciton. In materials with strong dielectric screening, these excitons usually separate

quickly into free carriers. Once free, electrons and holes may follow different pathways depending on the carrier density and the electronic structure of the material.

One pathway is radiative recombination, where an electron recombines with a hole and emits a photon. This process results in the release of light, and the photon produced might be reabsorbed by the material [69]. Another pathway is non-radiative recombination, often described by the Shockley-Read-Hall (SRH) mechanism. Here, electrons and holes recombine through defect states or traps within the bandgap, releasing energy as heat rather than light. This energy loss reduces the efficiency of devices like solar cells [70].

A third recombination type is Auger recombination, a non-radiative process where the recombination energy from an electron and hole is transferred to a third carrier (electron or hole), which is excited to a higher energy state instead of emitting a photon [71]. This process typically occurs at high carrier densities and also dissipates energy as heat.

The central goal in solar cell design is to extract these carriers before they recombine. A classic approach is the p–n junction, in which p-type (hole-rich) and n-type (electron-rich) semiconductors are joined. Their contact establishes an internal electric field—known as the built-in potential—that drives electrons and holes in opposite directions.

1.9 Solar cells: principles and performance metrics

1.9.1 Solar radiation

The solar spectrum, originating from the Sun's photosphere at an effective temperature of approximately 5778 K, closely resembles that of a blackbody radiator. As shown in Figure 1.15, most of the solar irradiance is concentrated within the visible range (approximately 400–700 nm), with a substantial contribution also extending into the near-infrared and a smaller portion in the ultraviolet region.

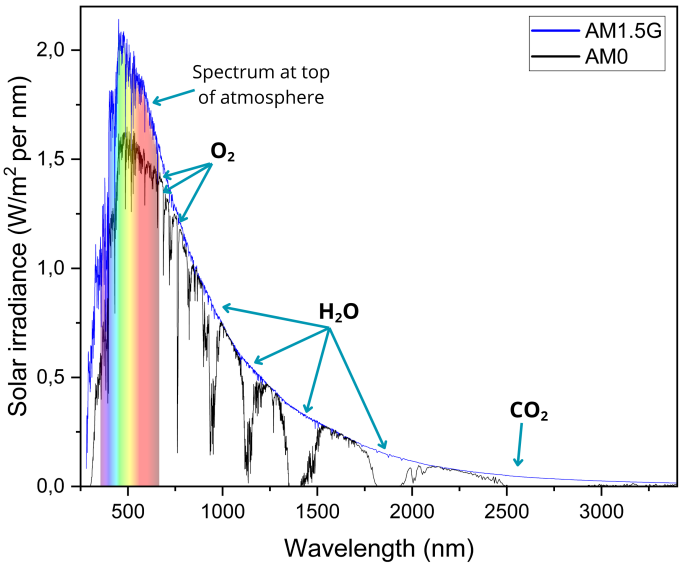


Figure 1.15: Solar irradiance spectrum for different air masses [72].

When this radiation reaches the top of the Earth's atmosphere (AM0 spectrum), it

retains its near-blackbody shape. However, after passing through the atmosphere, the resulting AM1.5G terrestrial spectrum exhibits multiple absorption bands primarily due to atmospheric gases such as O_2, H_2O, and CO_2. These gases selectively absorb specific wavelength ranges, reducing the photon flux available for photovoltaic conversion at those regions.

Each semiconductor material is characterized by a specific E_g, corresponding to a threshold wavelength $\lambda_g = \frac{hc}{E_g}$, beyond which photons no longer possess sufficient energy to generate electron–hole pairs. Only photons with wavelengths shorter than this threshold (i.e., higher photon energies) can be absorbed to produce electrical carriers. Under idealized conditions, the maximum theoretical power conversion of a solar cell can be visualized as the area under the solar spectrum to the left of the bandgap wavelength.

For instance, a material with a bandgap corresponding to $\lambda = 2500$ nm (approximately $E_g \approx 0.5$ eV) could, in principle, absorb almost the entire solar photon spectrum. However, after carrier thermalization, the excess energy of high-energy photons is lost as heat, and the recoverable electrical energy per photon remains limited to the bandgap value. Consequently, despite the apparent advantage of a low bandgap in capturing more photons, the overall conversion efficiency is reduced due to thermal losses. This trade-off between photon absorption range and energy conversion efficiency fundamentally determines the optimal bandgap range for photovoltaic materials [72].

1.9.2 Solar cell equivalent circuit model

To fully understand how a photovoltaic device works, its electrical behavior under operating conditions must be examined. For a semiconductor with a given bandgap energy, the J_{sc} represents the total extractable current. It is calculated by integrating the incident photon flux across the spectrum, weighted by the device's EQE at each wavelength:

$$J_{sc} = -q \int_{\lambda_1}^{\lambda_2} \mathrm{EQE}(\lambda) \Phi_{\mathrm{AM1.5G}}(\lambda)\, d\lambda \tag{1.20}$$

Here, q is the elementary charge, and $\Phi_{\mathrm{AM1.5G}}(\lambda)$ is the photon flux spectrum under standard AM1.5G sunlight. In photovoltaic convention, photocurrent is generally reported as a positive quantity [52, 73].

In the absence of illumination, a solar cell behaves similarly to a diode as illustrated in Figure 1.16: when a forward bias is applied, the current increases exponentially. This dark current is described by the ideal diode equation:

$$J_{\mathrm{dark}}(V) = J_0 \left(e^{\frac{qV}{kT}} - 1 \right) \tag{1.21}$$

where J_0 is the dark saturation current (leakage in the absence of light), V is the applied voltage, k is Boltzmann's constant, and T is the temperature. In practice, an ideality factor n (typically between 1 and 2) is included to account for recombination pathways, such as trap-assisted processes in the bulk or at interfaces [51]:

$$J_{\text{dark}}(V) = J_0 \left(e^{\frac{qV}{nkT}} - 1 \right) \tag{1.22}$$

Under illumination, the total current density combines the photocurrent and the dark current:

$$J(V) = J_{sc} - J_{\text{dark}}(V) = J_{sc} - J_0 \left(e^{\frac{qV}{nkT}} - 1 \right) \tag{1.23}$$

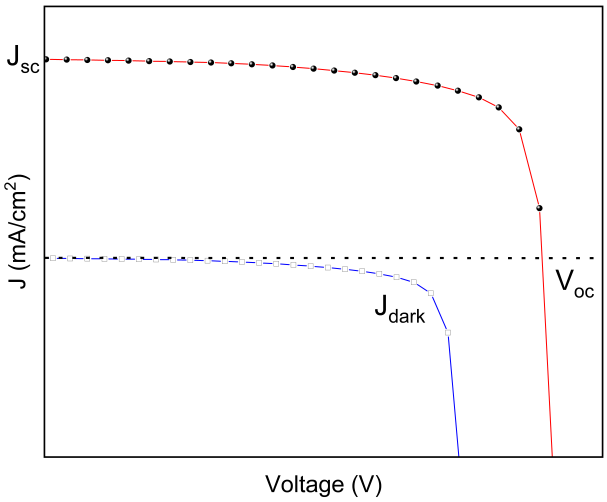


Figure 1.16: J–V Curves of an Ideal Solar Cell in Dark and Illuminated Conditions.

Parasitic losses are an important factor limiting the performance of solar cells. To maintain efficient charge transport, the series resistance (R_S) should be kept as low as possible. High R_S values can arise from excessively thick transport layers, which hinder carrier mobility and increase the likelihood of recombination, or from inefficient charge transfer across an interface [74].

In the ideal diode model, current flows only in the forward direction, with no reverse saturation current, meaning the diode is effectively in parallel with an infinite resistance. However, in real devices, imperfections such as pinholes in a layer or other leakage paths create "shunting" effects, reducing the shunt resistance (R_{sh}). This leads to deviations from the ideal current–voltage behavior and lowers the cell efficiency [74].

The practical J–V characteristics of a solar cell deviate from the ideal diode behavior due to parasitic resistive effects that arise during fabrication and operation. These non-idealities are captured by the modified *p*-*n* junction equation:

$$J(V) = J_{sc} - J_0 \left[\exp\left(\frac{q(V + JAR_S)}{nkT} \right) - 1 \right] - \frac{V + JAR_S}{R_{sh}} \tag{1.24}$$

where J_{sc} is the short-circuit current density, J_0 is the reverse saturation current density, q is the elementary charge, n is the diode ideality factor, k is the Boltzmann constant, and T is the absolute temperature. In this expression, A represents the active area of the solar cell, over which the total current is generated. Since the equation is written in terms of current density (J) rather than total current (I), the term JAR_S

corresponds to the voltage drop across the series resistance R_S when the total current $I = JA$ flows through the device. Thus, the product JAR_S ensures that the resistive voltage loss is properly expressed in volts, maintaining dimensional consistency with V.

An equivalent circuit model incorporating both series and shunt resistances is illustrated in Figure 1.17b.

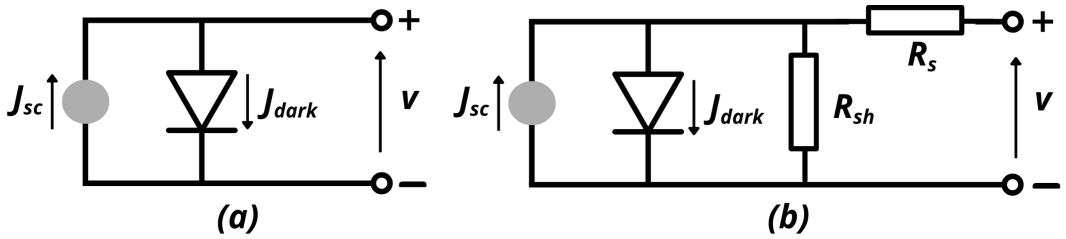


Figure 1.17: Equivalent circuits for a) an ideal solar cell and b) ideal solar cell with parasitic losses.

1.9.3 Performance parameter of solar cells

The electrical performance of a solar cell is typically evaluated through its J–V characteristics under standard illumination conditions. As shown in Figure 1.18, the device behavior is represented by the red J–V curve, from which several critical parameters can be extracted—each providing valuable insight into the physical mechanisms governing photovoltaic operation. The generated power density ($P = JV$) is plotted alongside the current–voltage response, highlighting the point of maximum electrical output.

The J_{sc} represents the maximum current density that the solar cell can deliver when the external circuit is shorted ($V = 0$). It depends on the number of absorbed photons, the carrier collection efficiency, and the optical and electronic quality of the active layers. Thus, J_{sc} provides information on the device's light absorption capability and charge transport efficiency.

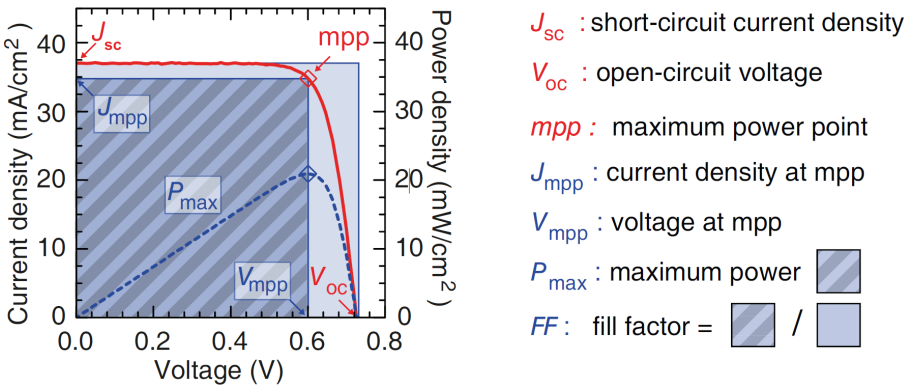


Figure 1.18: Typical J–V and power density curves of a solar cell, showing the Jsc, Voc, mpp, and fill factor [75].

The V_{oc}, also indicated in Figure 1.18, corresponds to the maximum voltage produced by the device when no external current is drawn ($J = 0$). It is primarily determined by the

difference between the quasi-Fermi levels of electrons and holes under illumination and is strongly affected by recombination processes within the device. A higher recombination rate lowers V_{oc}, making this parameter a sensitive indicator of material and interface quality.

The MPP defines the operating condition at which the product of current density and voltage ($J_{\mathrm{mpp}}V_{\mathrm{mpp}}$) is maximized, yielding P_{max}. This point, labeled *mpp* in Figure 1.18, reflects the optimal trade-off between current and voltage that allows the solar cell to deliver its peak efficiency.

The fill factor is a dimensionless quantity that describes the "squareness" of the J–V curve and quantifies how closely the cell approaches its ideal rectangular shape. It is given by:

$$FF = \frac{J_{\mathrm{mpp}}V_{\mathrm{mpp}}}{J_{sc}V_{oc}} \tag{1.25}$$

A higher FF indicates lower resistive losses and better diode quality, while reductions in FF are typically associated with high series resistance or leakage (shunt) currents.

Finally, the PCE, denoted by η, expresses the fraction of incident solar power converted into electrical energy and is calculated as:

$$\eta = \frac{J_{sc}V_{oc}FF}{P_s} \tag{1.26}$$

where P_s is the incident solar power density (typically $1000\,\mathrm{W/m^2}$ under AM1.5G conditions). The simultaneous maximization of J_{sc}, V_{oc}, and FF is therefore essential for achieving high-efficiency photovoltaic devices.

1.9.4 Solar cell operation

A solar cell, or PV cell, is a semiconductor device that directly converts sunlight into electrical energy through the photovoltaic effect. When photons are absorbed in the active layer, they excite electrons from the valence band to the conduction band, generating electron–hole pairs.

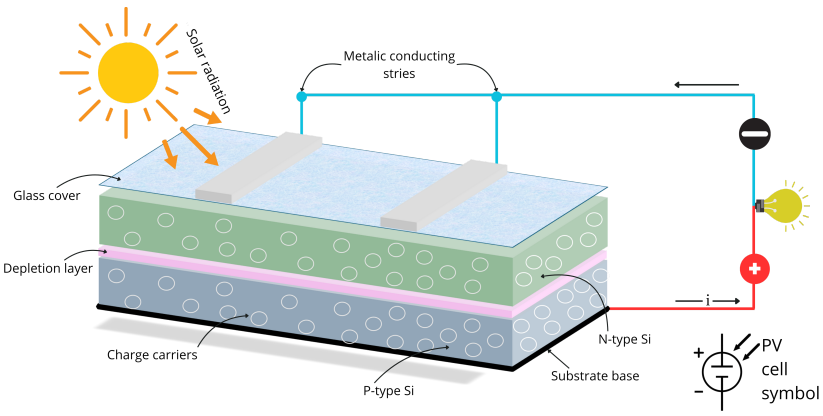


Figure 1.19: Cross section of solar cell.

These carriers are then separated by the built-in electric field of a p-n junction and collected at the front and back metal contacts, producing a current [76]. The fundamental components of a conventional silicon-based solar cell include a p-type absorber layer, an n-type window layer, anti-reflection coatings to minimize optical losses, and rear passivation layers to suppress recombination [76].

1.9.5 Classification of solar cells

Solar cells are generally classified according to their material composition, efficiency, cost, and scalability. Traditionally, photovoltaic technologies have been divided into three generations, illustrating the evolution from mature, wafer-based devices to emerging thin-film and hybrid structures [2, 77].

The first generation is dominated by crystalline silicon wafers, which remain the industrial standard due to their high efficiency and long-term reliability [78]. The second generation comprises thin-film solar cells, developed to reduce material consumption and production costs [79]. The third generation introduces innovative materials and architectures, such as perovskites and tandem designs, aiming for efficiencies beyond 30 % [80, 81].

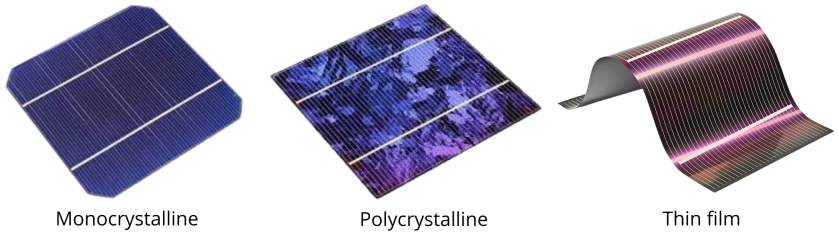


Figure 1.20: Types of photovoltaic solar cells.

By 2025, the global PV industry is expected to exceed $200 billion, with silicon accounting for approximately 95 %, thin films for around 4 %, and emerging technologies for about 1 % of total installations [82].

First-generation solar cells

First-generation solar cells are based on crystalline silicon wafers (monocrystalline and polycrystalline). They exhibit high efficiency (15 % to 25 %), excellent stability (25–30 years lifespan), and dominate the PV market due to mature manufacturing technologies. However, they require high-purity materials and energy-intensive processing [83].

- **Monocrystalline silicon solar cells**

Monocrystalline cells are fabricated from single-crystal silicon ingots grown via the Czochralski process. Their uniform lattice structure minimizes recombination losses, enabling commercial efficiencies of 22 % to 27.8 %, with laboratory results nearing the Shockley–Queisser limit for silicon [84]. Recent innovations such as bifacial designs capture sunlight from both sides, increasing energy yield by 10 % to 20 %. The main drawback remains the high energy cost of crystal growth [85].

- **Polycrystalline silicon solar cells**

Polycrystalline cells are produced by casting molten silicon into blocks and slicing them into wafers containing multiple grains. Although less efficient (18 % to 22 %) due to grain boundary recombination, they are cheaper to manufacture and widely used in large-scale installations [85].

- **Amorphous silicon solar cells**

Amorphous silicon cells represent the thin-film form of silicon technology. They consist of a non-crystalline silicon layer deposited on glass, plastic, or metal substrates. Typical efficiencies range from 10 % to 13.8 %, and they are known for flexibility and low manufacturing costs. However, they suffer from the Staebler–Wronski effect, causing degradation during initial light exposure [86]. Applications include building-integrated photovoltaics, portable devices, and low-power electronics [87].

Second-generation solar cells

Second-generation cells aim to reduce material usage and production costs by employing thin-film deposition instead of bulk wafers. Their semiconductor layers are typically a few micrometers thick. Efficiencies range from 10–23%, and leading technologies include CdTe, CIGS, a−Si, and kesterite (CZTSSe) [88].

- **Cadmium telluride solar cells**

CdTe solar cells are among the most commercially successful thin-film technologies, with record efficiencies of 22.1 %. They feature a high absorption coefficient and perform well in hot or low-light conditions. The main limitations are cadmium toxicity and recycling challenges [89].

- **Copper indium gallium selenide solar cells**

CIGS solar cells achieve record efficiencies of 23.35% and offer excellent low-light performance and mechanical flexibility. However, the scarcity of indium and gallium limits large-scale deployment [90].

- **Kesterite solar cells**

Kesterite-based solar cells use earth-abundant, non-toxic elements (Cu, Zn, Sn, S, Se) and achieve efficiencies around 12–13%. Although less efficient than CdTe or CIGS, they are environmentally benign and suitable for sustainable large-scale production [79].

- **Amorphous silicon thin-film cells**

While also part of the silicon family, a-Si thin-film devices are often categorized within the second generation due to their thin-film architecture and low-cost deposition methods. They are particularly suited for flexible and portable applications [87].

Third-generation solar cells

Third-generation technologies encompass emerging and hybrid systems that aim to surpass the theoretical efficiency limits of single-junction devices ($\approx 33\,\%$). These include perovskite, organic, quantum dot, dye-sensitized, and tandem solar cells. They emphasize high efficiency (>30%), low-cost fabrication, and flexible substrates [91, 92].

- **Perovskite solar cells**

Perovskite solar cells represent the most promising third-generation technology. They have achieved 26.7 % efficiency for single-junctions and 34.85 % for perovskite–silicon tandems as of 2025. Their solution processability, low-temperature fabrication, and tunable bandgap make them ideal for tandem integration and scalable roll-to-roll manufacturing [91]. Challenges remain in long-term stability and lead toxicity, but progress in encapsulation and lead-free perovskites continues rapidly [93].

- **Organic and polymer solar cells**

Organic photovoltaic cells use conjugated polymers or small molecules as active layers. They are lightweight, flexible, and can be fabricated via printing techniques, but efficiencies remain around 19 % to 20 %, and operational stability is limited [91].

- **Quantum dot and dye-sensitized solar cells**

Quantum dot and dye-sensitized solar cells use nanostructured semiconductors to absorb light and facilitate charge separation. Though their efficiencies (13 % to 15 %) are modest, they offer tunability, transparency, and potential for low-cost applications such as building-integrated PV and indoor energy harvesting [87, 94].

Table 1.1: Summary of different generations of solar cells [83–94].

Generation	**Main Materials / Types**	**Efficiency Range**	**Key Features**	**Limitations**
1st	Monocrystalline Si, Polycrystalline Si, a−Si	15 %–27.8 %	High stability, mature technology	Energy-intensive, high cost
2nd	CdTe, CIGS, a−Si (thin film), CZTSSe	10 %–23 %	Low material use, flexible	Toxic/scarce materials, lower stability
3rd	Perovskite, Tandem, Organic, QD, DSSC	20 %–35 %	High efficiency, low cost potential	Stability and scalability issues

The Table 1.1 compares the three generations of solar cells based on their materials, efficiency, key features, and limitations. The first generation features silicon-based cells, known for their high stability and mature technology, though they are energy-intensive and costly. The second generation introduces thin-film technologies, which reduce material use and offer flexibility but face challenges with toxic materials and lower stability. The third generation includes advanced materials like perovskite and tandem cells, offering high efficiency and potential for low-cost manufacturing, yet still struggles with issues related to stability and scalability.

1.10 Conclusion

In this chapter, we have reviewed the fundamental concepts underlying photovoltaic technology, from the physical principles of the photovoltaic effect to the operation of semiconductor junctions and the performance parameters that define solar cell efficiency. These foundations provide the essential understanding required to analyze and design modern photovoltaic devices. Building on this theoretical background, the next chapter will focus on inorganic materials, with particular attention to perovskite compounds and their application in perovskite-based solar cells. We will explore the advantages offered by this emerging technology, as well as the different architectures, ranging from single-junction to tandem structures, that have positioned perovskites at the forefront of next-generation photovoltaic research.

Chapter 2

Inorganic materials and perovskite solar cells

2.1 Introduction

The growing demand for sustainable energy has accelerated research into advanced photovoltaic technologies, with perovskite materials emerging as leading candidates for next-generation solar cells. Owing to their exceptional optoelectronic properties, structural versatility, and low-cost processing, perovskites have achieved remarkable efficiency improvements within just over a decade of development [95, 96].

This chapter first outlines the crystallographic structure and classification of perovskite materials, focusing on the fundamental ABX_3 lattice and the distinctions between HOIPs and AIPs. Their similarities, differences, and relevant physical properties are compared to clarify the role of composition in determining material performance and stability. Subsequently, the chapter examines PSCs—covering their emergence, working principles, and device architectures—alongside the advantages and limitations that shape their practical deployment. Finally, attention is given to tandem solar cells, designed to surpass the Shockley–Queisser efficiency limit of single-junction devices. Different tandem architectures (2T, 3T, and 4T) are discussed, along with promising materials and candidates that enable higher efficiency and improved stability in next-generation photovoltaic systems.

2.2 Perovskites materials

2.2.1 Crystallographic structure of perovskites

Perovskites belong to a family of ionic crystals that can be described by the general chemical formula ABX_3, where A and B are cations of different sizes, and X is an anion. The first material identified with this crystal arrangement was calcium titanate ($CaTiO_3$), discovered by Gustav Rose in the Ural Mountains in 1839. Rose named it after his colleague, the Russian mineralogist Lev Aleksevich von Perovski [97]. In $CaTiO_3$, titanium and oxygen atoms assemble into BX_6 octahedra, while calcium cations occupy the central positions, surrounded by twelve oxygen atoms (Figure 2.1). Since this discovery, a vast number of natural and synthetic perovskites have been reported. In fact, silicate perovskites, particularly bridgmanite, represent the most abundant crystal structure in the Earth's mantle [98].

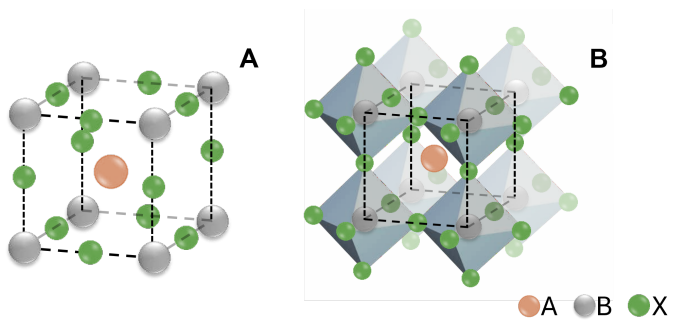


Figure 2.1: Crystal structure of ABX_3 perovskite: (A) Cubic unit cell centred on the A-site cation, (B) Corner-sharing BX_6 octahedra stabilized by the central A-site cation.

V. M. Goldschmidt's proposal of geometric rules governing the formation of cubic perovskites based on ionic radii in 1926 marked a significant advancement in our understanding of perovskite stability [99]. He introduced the so-called tolerance factor (t), expressed as:

$$t = \frac{r_A + r_X}{\sqrt{2}(r_B + r_X)} \tag{2.1}$$

where r_A, r_B, and r_X correspond to the ionic radii of the A-, B-, and X-site ions, respectively. According to this rule, when $0.8 < t < 1.0$, a stable perovskite structure is typically expected, with $t = 1.0$ denoting the ideal cubic case. However, especially in halide-based perovskites, the tolerance factor by itself does not always accurately predict structural stability [100].

To further assess the feasibility of perovskite formation, an additional condition known as the octahedral factor (μ) is considered:

$$\mu = \frac{r_B}{r_X} \tag{2.2}$$

For BX_6 octahedra to form, the criterion $\mu \geq 0.41$ must be satisfied. Nevertheless, beyond these geometric restrictions, variations in ionic sizes and the competition between A–X and B–X bonding interactions allow for a wide range of structural distortions. In 1972, A. M. Glazer proposed a framework to describe potential octahedral tilting patterns in perovskites, and he systematically classified these distortions, which alter the B–X–B bond angle away from the ideal 180° [101].

2.2.2 Perovskites materials classifications

Metal halide perovskites

In the case of metal-halide perovskites with the general formula ABX_3, the A-site is occupied by a monovalent cation, the B-site by a divalent cation, and the X-site by a halide anion. This differs from oxide perovskites, where the X-site anion is divalent. In photoactive hybrid organic–inorganic PSCs, the A-site cation is often organic—commonly methylammonium ($CH_3NH_3^+$, MA) or formamidinium ($HC(NH_2)_2^+$, FA)—though inorganic cations such as Cs^+ can also be used. The B-site typically hosts Pb_2^+ or Sn_2^+, while the halide site is filled by I^-, Br^-, Cl^-, or mixtures of these. The first examples of alkali lead halides in this structural family were synthesized in 1893 by H. L. Wells, who prepared cesium- and potassium-based variants such as $CsPbI_3$, $CsPbBr_3$, and $CsPbCl_3$ [102]. Later, in 1966, Christiaan Møller carried out the first detailed crystallographic study on cesium-based perovskites, observing photoconductivity—a clear indication of semiconductor-like behaviour [103].

Hybrid organic–inorganic compounds such as methylammonium lead and tin halide perovskites were first reported by Dieter Weber in 1978, who also noted that their colour depended on composition [104]. In the 1990s and 2000s, David Mitzi and his colleagues

at IBM advanced this field considerably, exploring their optoelectronic characteristics and developing several of the synthesis methods still in use today [105–110].

The term 3D perovskites refers to a fully connected framework of corner-sharing BX_6 octahedra. Due to variations in ionic radii and octahedral tilting, multiple structural phases can exist. Figure 2.2 illustrates four representative cases. The simplest is the ideal cubic structure (space group $Pm\bar{3}m$) shown in Figure 2.2A, with no octahedral tilts (Glazer notation $a^0a^0a^0$). An example is room-temperature $MAPbBr_3$, which has a tolerance factor of $t = 0.927$ from equation 2.1. When octahedra tilt within one plane, two different tetragonal variants appear, depending on whether the tilts alternate ($a^0a^0c^-$, Figure 2.2B) or align ($a^0a^0c^+$, Figure 2.2C) along the c-axis. $MAPbI_3$, for instance, crystallizes in the I4/mcm symmetry at room temperature with $t = 0.912$ [111, 112]. Another distortion mode involves tilts along different axes, as in $CsPbI_3$ (Figure 2.2D). This phase, with $t = 0.807$, only stabilizes at high temperatures above 550 K, adopting the orthorhombic Pnma space group.

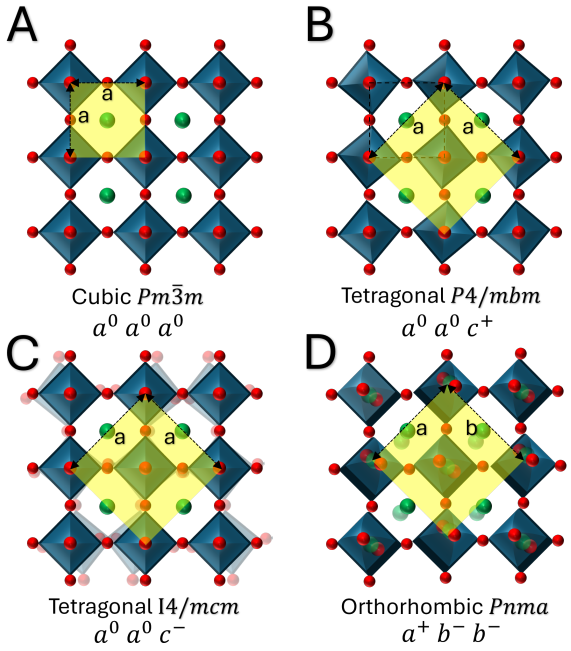


Figure 2.2: Four representative perovskite structures as described in the text.

Although the Goldschmidt tolerance factor is still frequently applied, improvements have been spurred by its limitations for halide perovskites. The region of perovskite stability has been reduced by combining both Goldschmidt and octahedral factors [113], while another improvement entails adjusting the Shannon ionic radii [114, 115]. In order to improve phase formation prediction, Bartel and colleagues recently proposed a new metric called the Bartel tolerance factor (τ). Its expression is

$$\tau = \frac{1}{\mu} - n_A \left(n_A - \frac{\frac{r_A}{r_B}}{\ln\left(\frac{r_A}{r_B}\right)} \right) \tag{2.3}$$

and includes the oxidation state of the A-site cation (n_A) as well as the octahedral factor.

This model predicts that compounds with $\tau < 4.18$ will form perovskite phases with a 91% reliability rate [100].

Related materials

The structural flexibility of perovskites is not limited to the 3D framework. The enormous chemical versatility of this family has given rise to a wide range of low-dimensional and layered derivatives, which significantly expand their physical and electronic properties. Among the most studied are the quasi-2D perovskite-like compounds, such as the Ruddlesden–Popper, Dion–Jacobson, and Aurivillius series [116]. These materials consist of extended layers of corner-sharing metal-halide octahedra stacked along one direction, separated by bulky organic or inorganic spacer cations. This architecture naturally forms multiple quantum wells, in which the thickness of the inorganic slabs (denoted by the n value, where $n = 1, 2, 3, \ldots$) determines the dimensionality of the system [117, 118].

Because the organic spacers confine the electronic states within the inorganic layers, these 2D systems exhibit strong excitonic effects, tunable through both the choice of spacer molecules and their rigidity, as well as the thickness of the inorganic layers [119, 120]. Figure 2.3 illustrates examples of quasi-2D Ruddlesden–Popper phases with $n = 1, 2, 3$ in butylammonium (BA) methylammonium lead iodide. These structures are of particular interest because mixed 2D–3D perovskite films can be prepared with relative ease. Such composites have been widely investigated not only for novel optoelectronic applications but also as an efficient means of grain-boundary and interface passivation, improving device stability and efficiency [121, 122]. However, while fabrication is straightforward, the long-term structural stability of these mixed phases remains an open question.

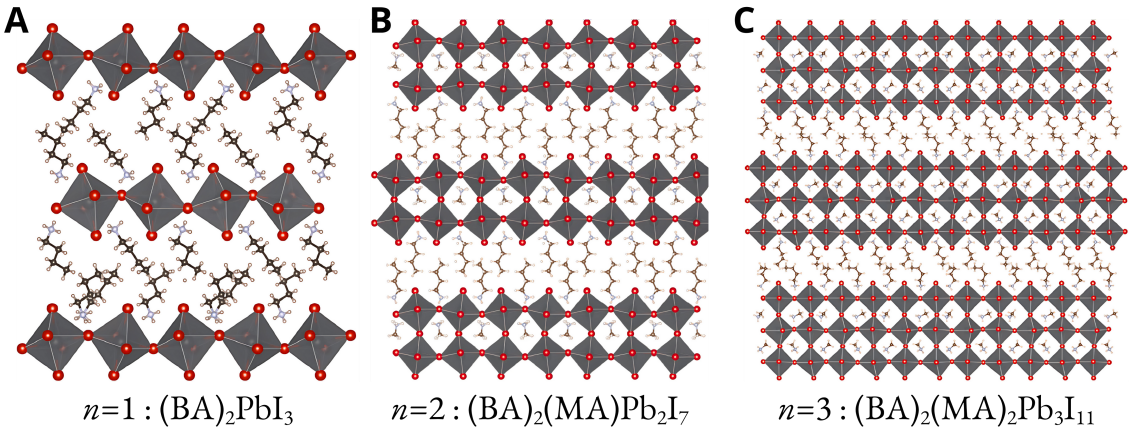


Figure 2.3: Examples of layered Ruddlesden–Popper perovskites with $n = 1, 2$ and 3, showing quasi-2D butylammonium (BA) methylammonium lead iodide phases. Renderings from crystallographic data in [119, 123, 124].

Low-dimensional perovskite-related phases, including one-dimensional (1D) and zero-dimensional (0D) compounds, have also been reported in addition to quasi-2D structures. These phases are frequently regarded as undesirable secondary phases that arise during film degradation or incomplete crystallization, even though they can occasionally be helpful intermediates during crystal growth or contribute to novel electronic properties [125–

128]. For instance, during synthesis, solvent molecules may intercalate to form metastable 1D or 0D complexes [129, 130].

Figure 2.4 presents representative examples of such phases. The δ-phase of $MAPbI_3$ (2H polytype) is a 1D system built from face-sharing PbI_6 octahedra stabilized by organic cations [131]. A related 4H polytype combines alternating corner- and face-sharing octahedra [131]. Pb-deficient 1D intermediates are represented by solvent-intercalated structures like $(MA)_3PbI_5 \cdot DMF$ [129], whereas $(Gua)_2PbI_4$ exhibits a quasi-2D structure supported by guanidinium cations [132]. Common degradation products include the monohydrate phase $MAPbI_3 \cdot H_2O$, which contains a mixture of octahedra that share faces and edges [133]. Finally, $(MA)_2Pb_3I_8 \cdot {}_2DMSO$ forms during solution processing when dimethyl sulfoxide intercalates between ribbons of octahedra, leading to a distinctive intermediate phase [129].

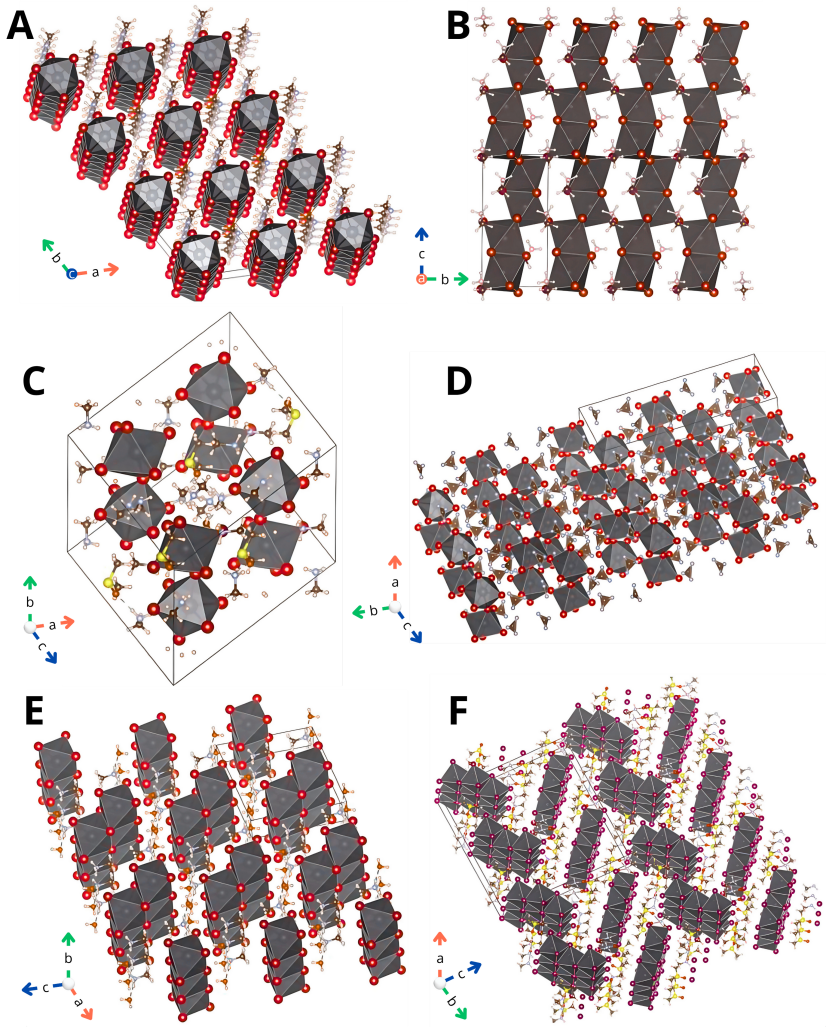


Figure 2.4: Structural diversity in 1D and quasi-2D perovskite-related compounds. A) $MAPbI_3$ δ-phase (2H polytype). B) 4H polytype with alternating connectivity. C) $(MA)_3PbI_5 \cdot DMF$, a Pb-deficient 1D phase. D) $(Gua)_2PbI_4$, a quasi-2D corrugated sheet structure. E) $MAPbI_3 \cdot H_2O$ monohydrate degradation phase. F) $(MA)_2Pb_3I_8 \cdot {}_2DMSO$ intermediate. Structures rendered from crystallographic data in [129, 131–133].

2.3 Hybrid organic-inorganic and all-inorganic perovskite : similarities and differences

2.3.1 Hybrid organic–inorganic perovskites

Depending on the type of A-site cation, perovskites can be broadly categorized into HOIPs and AIPs. In HOIPs, the A-site contains organic cations such as methylammonium (MA^+, $CH_3NH_3^+$) or formamidinium (FA^+, $HC(NH_2)_2^+$), while the B-site hosts inorganic divalent metals (e.g., Pb^{2+} or Sn^{2+}), and the X-site is occupied by halide anions (I^-, Br^-, Cl^-, or mixtures thereof). The hybrid nature of HOIPs introduces molecular dynamics—notably rotational freedom of the organic cations—which enhances dielectric screening and defect tolerance [134]. The benchmark HOIP, ($MAPbI_3$), is extensively studied due to its well-established processing routes, high power conversion efficiencies, and rapid early-stage performance improvements [135, 136]. $MAPbI_3$ exhibits a direct bandgap of approximately 1.55 eV, which can be tuned up to 1.7 eV through halide substitution (e.g., $MAPbI_2Br$). Its absorption coefficient exceeds 10^5 cm^{-1}, allowing thin films of 300 nm to 500 nm to absorb over 90 % of incident photons above the bandgap [134].

The material also demonstrates balanced electron and hole mobilities (20 $cm^2\,V^{-1}\,s^{-1}$ to 100 $cm^2\,V^{-1}\,s^{-1}$), long carrier diffusion lengths ($>$ 1 µm in polycrystalline films, up to 100 µm in single crystals), and low trap densities ($\sim 10^{15} - 10^{16}$ cm^{-3})—all of which contribute to high open-circuit voltages ($V_{oc} > 1.1$ V) and fill factors $>$ 80 % in efficient solar cells [136]. HOIPs like $MAPbI_3$ are typically fabricated through low-temperature solution processing, such as one-step spin-coating of methylammonium iodide (MAI) and lead iodide (PbI_2) in solvents like DMF or GBL, often assisted by antisolvent dripping (e.g., chlorobenzene) to promote uniform crystallization [135]. Additives like DMSO form intermediate adducts ($MAI \cdot PbI_2 \cdot DMSO$), slowing crystallization and promoting larger grains (>500 nm) with fewer grain boundaries, thus reducing non-radiative recombination [134]. Other methods, such as two-step sequential deposition or vapor-assisted conversion, offer better stoichiometric control and reduced defect formation [135].

Despite these merits, HOIPs suffer from moisture-induced degradation—for instance, $MAPbI_3$ rapidly decomposes into PbI_2 and volatile organic by-products ($MAI/CH_3NH_2/HI$) under humid conditions, leading to >50 % efficiency loss after 100 hours at 85 % RH without encapsulation [135]. In addition, phase transitions between the tetragonal β-phase (I4/mcm) and cubic α-phase ($Pm\bar{3}m$) around 55 °C cause bandgap fluctuations and ion migration [137]. Furthermore, the toxicity of lead has prompted interest in lead-free alternatives such as $MASnI_3$, though these often suffer from Sn^{2+} oxidation and limited efficiencies ($\approx$ 10 %) [138]. These limitations have motivated a shift toward all-inorganic perovskites, which retain the same ABX_3 structure but offer greater thermal and environmental stability [139, 140].

2.3.2 All-inorganic perovskites

AIPs replace the volatile organic A-site cations with inorganic monovalent ions, typically Cs^+ or Rb^+, resulting in a more rigid lattice and superior thermal endurance [136]. This

absence of organic components eliminates volatility and significantly enhances mechanical robustness, thermal resilience, and moisture resistance—key advantages for long-term operation in photovoltaics, LEDs, and detectors [137, 141]. Although both HOIPs and AIPs share the corner-sharing BX_6 octahedral framework, their different A-site chemistries impart distinct material behaviors. As shown in Figure 2.1, $CsPbI_3$ demonstrates a comparable bandgap (1.7 eV) to $MAPbI_3$ but exhibits markedly improved thermal stability, maintaining its crystalline integrity above 300 °C, whereas $MAPbI_3$ decomposes below 200 °C due to organic sublimation [142]. Additionally, inorganic A-site cations are less prone to hydrolysis, granting enhanced resistance to oxygen and humidity, as confirmed by durability tests under 85 °C and 85 % RH (IEC standards) [139]. However, AIPs face challenges related to phase instability—for instance, the photoactive black α-phase of $CsPbI_3$ tends to revert to the non-perovskite yellow δ-phase at room temperature, thereby reducing efficiency [136]. As of 2025, state-of-the-art $CsPbI_3$-based solar cells achieve around 21 % PCE, while HOIP devices exceed 25 % under certified conditions [143]. To counteract these drawbacks, researchers are exploring halide alloying (e.g., $CsPbI_2Br$) to stabilize the cubic phase, as well as defect passivation via additives or surface functionalization to suppress non-radiative losses [138].

Overall, Figure 2.5 summarizes the key differences in bandgap energies, phase evolution, and thermal/structural stability between $MAPbI_3$ and $CsPbI_3$. The results highlight the fundamental trade-off between the superior optoelectronic performance of HOIPs and the robust stability of AIPs, emphasizing the latter's potential for commercialization under realistic operating environments.

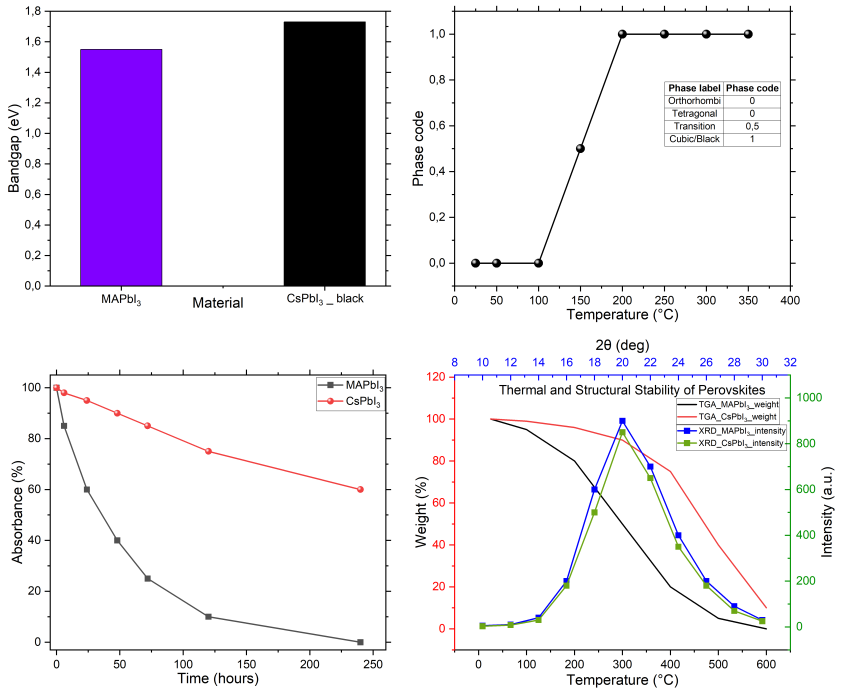


Figure 2.5: Comparative bandgap diagrams and stability profiles for hybrid ($MAPbI_3$) and inorganic ($CsPbI_3$) perovskites, highlighting phase transitions, degradation pathways under moisture/heat, and temperature-dependent stability curves derived from thermogravimetric analysis (TGA) and X-ray diffraction (XRD) data.

2.3.3 Comparison between hybrid organic-inorganic and all-inorganic perovskites

With single-junction AIP solar cells reaching efficiencies of up to 26.1 % in specialized configurations (e.g., indoor photovoltaics at 41.21 % under low light), recent developments have further highlighted the stability advantages of AIPs. Meanwhile, HOIPs continue to lead in overall efficiency, reaching certified 26.7 % for single-junction devices [144]. In contrast to HOIPs' susceptibility to organic decomposition below 200 °C [145], AIPs exhibit superior operational stability and superior thermal decomposition thresholds above 400 °C, maintaining over 90 % efficiency under humid conditions for prolonged periods of time [139]. With efficiencies of 15 % to 20 %, lead-free AIPs—like Sn-based compositions—have made headway in addressing toxicity issues more successfully than HOIPs [146]. After 1500 h of damp-heat testing, mutual stabilization techniques such as hybrid/inorganic bilayers have maintained 93.5 % efficiency, improving HOIP stability [147].

The Table 2.1 below compares key aspects of hybrid organic-inorganic and all-inorganic perovskites, including material composition, bandgap, thermal stability, and power conversion efficiency, highlighting their advantages and trade-offs.

Table 2.1: Comprehensive comparison between hybrid organic–inorganic and all-inorganic perovskite materials.

Aspect	**Hybrid Organic–Inorganic Perovskites (e.g., $MAPbI_3$, $FAPbI_3$)**	**All-Inorganic Perovskites (e.g., $CsPbI_3$, $CsPbBr_3$)**
Materials Composition	A-site: organic cations (MA^+, FA^+) introduce molecular dynamics and hydrogen bonding; B-site: Pb^{2+}/Sn^{2+}; X-site: halides (I^-, Br^-, Cl^-). Prone to volatility of organic components, leading to decomposition under heat or humidity [139].	A-site: inorganic cations (Cs^+, Rb^+) provide a rigid lattice; B-site: Pb^{2+}/Sn^{2+}; X-site: halides. Lead-free options (e.g., Ge^{2+}, Sn^{2+}) reduce toxicity, with recent Sn-containing AIPs showing improved stability [148, 149].
Bandgap (eV)	Tunable 1.2–2.3; e.g., $MAPbI_3$ ≈1.55 eV (direct), while quantum-dot variants such as $FAPbI_3$ reach ≈1.5 eV for improved absorption [150].	Tunable 1.7–3.0; e.g., $CsPbI_3$ ≈1.73 eV (direct), wider for Br/Cl substitution (2.3 eV for $CsPbBr_3$); pressure-induced narrowing enhances spectral matching [150].
Carrier Mobility ($cm^2V^{-1}s^{-1}$)	High (10–100); long diffusion lengths (> 1 µm), enabling efficiencies up to 26.7 % in single-junction cells [144].	Comparable (20–100); slightly lower due to ionic scattering, but optimized in $CsPbI_2Br$ for tandem architectures [151].
Exciton Binding Energy (meV)	Low (10–50); efficient carrier dissociation enhances performance under low-light conditions [152].	Similar (15–60); dependent on dielectric constant; passivation treatments reduce binding energy and improve LED operation [152].

Continued on next page

Table 2.1 – continued from previous page

Aspect	Hybrid Organic–Inorganic Perovskites (e.g., $MAPbI_3$, $FAPbI_3$)	All-Inorganic Perovskites (e.g., $CsPbI_3$, $CsPbBr_3$)
Thermal Stability	Poor; decomposition below 200 °C due to volatile organics, though bilayer engineering extends lifetime up to 1500 h at 85 °C/85 % RH [147].	Excellent; stable above 400 °C, free from organic degradation; $CsPbI_2Br$ retains ≈90 % of PCE after multiple thermal cycles [153, 154].
Moisture Stability	Highly sensitive; hydrolysis of organic cations causes degradation, partly mitigated by encapsulation but typically <1000 h in humid conditions [155].	Improved; retains 90 % of efficiency at 60 % RH for 30 min; further enhanced by dopants and space-confinement effects [153, 155].
Phase Stability	Multiple phases (e.g., α, β, δ in $MAPbI_3$); low-temperature transitions (≈55 °C) lead to hysteresis [156].	Phase transitions (e.g., α-$CsPbI_3$ stable only above 300 °C); stabilized via doping/alloying (e.g., Br incorporation). Recent studies show >91 % retention after aging [153, 156].
Optical Absorption Coefficient (cm^{-1})	$> 10^5$ in the visible range; sharp absorption edge, with QDs yielding PLQY >90 % [157].	Similar ($> 10^5$); tunable via halide composition; zwitterion-capped nanocrystals exhibit reduced blinking and enhanced stability [148].
Defect Tolerance	High; dominated by shallow trap states minimizing non-radiative recombination, but ion migration remains an issue [158].	High; ion migration suppressed in mixed-halide AIPs; non-centrosymmetric distortions improve defect stability [159, 160].
Synthesis	Low-temperature solution processing (<150 °C); scalable; additive-assisted methods achieve up to 26.1 % PCE [161].	Higher temperatures required for phase control; vapor and dual-source deposition common; air-processed n–i–p tandems surpass 23 % PCE [162].
PCE (%)	Up to 26.7 % (single-junction, certified 25.51 %); tandems exceeding 34 % with silicon [144, 163].	Up to 26.1 % (single-junction); modules reach 20.7 %; indoor >41 %; tandems between 23–31 % in all-perovskite designs [139].

This comparison underscores the trade-offs: HOIPs offer easier processing and slightly better optoelectronic properties, with efficiencies surpassing 26 % in lab settings, but at the cost of stability under environmental stress [135, 139]. AIPs provide robustness for practical applications, with recent ion migration suppression and defect engineering enabling >90 % retention after prolonged exposure, albeit with challenges in phase control and slightly lower peak efficiencies [147, 153].

2.3.4 Inorganic perovskites: physical properties

Optical properties

The remarkable optical properties of inorganic perovskites, like $CsPbX_3$ (X = Cl, Br, I), make them ideal for photovoltaic and optoelectronic applications. Even in thin films

(300–500 nm thick), they can efficiently capture photons due to their high absorption coefficients, which typically exceed 10^5 cm^{-1} in the visible spectrum [164]. By substituting the halide anion, the bandgap can be greatly adjusted, ranging from about 1.2 eV to 3.0 eV. For example, compositions rich in iodides have narrower bandgaps (≈1.5 eV for $CsPbI_3$) and compositions rich in chlorides have wider bandgaps (≈3.0 eV for $CsPbCl_3$) [165].

This tunability is demonstrated in Figure 2.6(A), where the absorption and photoluminescence (PL) spectra of $CsPbX_3$ (X = Cl, Br, I) compositions show how the bandgap changes with halide composition. Moreover, as shown in Figure 2.6(B), the bandgap energy (E_g) and corresponding emission wavelength of $CsPb(Cl_xBr_{1-x})_3$ and $CsPb(Br_xI_{1-x})_3$ alloys can be finely tuned with varying halide concentration, enabling the optimization of the material's spectral response for various applications.

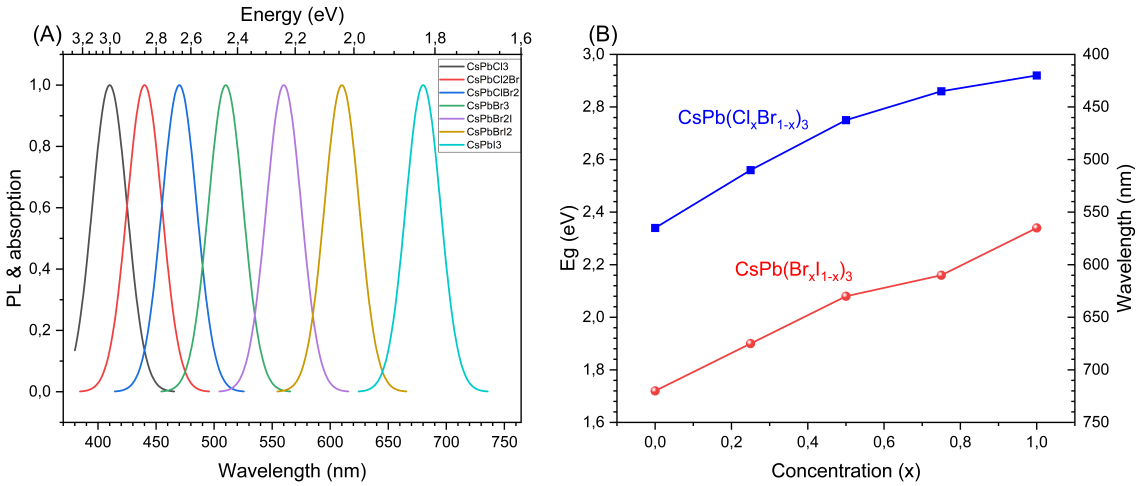


Figure 2.6: (A) Absorption and photoluminescence (PL) spectra of $CsPbX_3$ (X = Cl, Br, I) inorganic perovskites, showing bandgap tuning with halide composition; (B) Bandgap energy (E_g) and corresponding emission wavelength of $CsPb(Cl_xBr_{1-x})_3$ and $CsPb(Br_xI_{1-x})_3$ alloys as a function of halide concentration (x).

These materials show low Urbach energies (<20 meV) and strong photoluminescence quantum yields (up to 90 % in quantum dots), suggesting low disorder and excellent optical quality [165]. These characteristics can be further altered by pressure effects. For instance, $GaGeX_3$ (X = Cl, Br, I) perovskites bandgap decreases under hydrostatic pressure (up to 10 GPa), which enhances red-shift in absorption spectra [166]. Passivation techniques reduce the impact of defects like halide vacancies, which can introduce trap states that impair optical performance.

Electronic properties

Ambipolar charge transport characterizes the electronic behavior of inorganic perovskites, with balanced electron and hole mobilities frequently reaching 10–100 $cm^2V^{-1}s^{-1}$ in single crystals [167]. Devices with effective charge collection and negligible recombination losses are made possible by carrier diffusion lengths greater than 1 µm [167]. In contrast to higher values in organic semiconductors, low exciton binding energies (usually 10–50 meV) enable quick dissociation into free carriers at room temperature [165].

Density functional theory calculations of electronic band structures show direct bandgaps in many variations, including Mg_3SbX_3 (1.2–2.5 eV), which promote strong optical transitions [165]. Figure 2.7 displays the electronic band structure of $CsPbI_3$ inorganic perovskite, calculated via DFT, highlighting the direct bandgap and spin–orbit coupling effects. Lead-based perovskites exhibit band splitting due to spin–orbit coupling and Rashba effects, which may allow for spintronic applications [165].

Electronic characteristics also change under pressure; for $InGeF_3$, conductivity improves when the bandgap transitions from indirect to direct at about 5 GPa [168]. Compositional alloying (e.g., $CsPbI_2Br$) can mitigate hysteresis caused by ion migration [169]. Although defect densities are low ($\approx 10^5$ cm^{-3}), surface states must still be engineered for optimal performance [170].

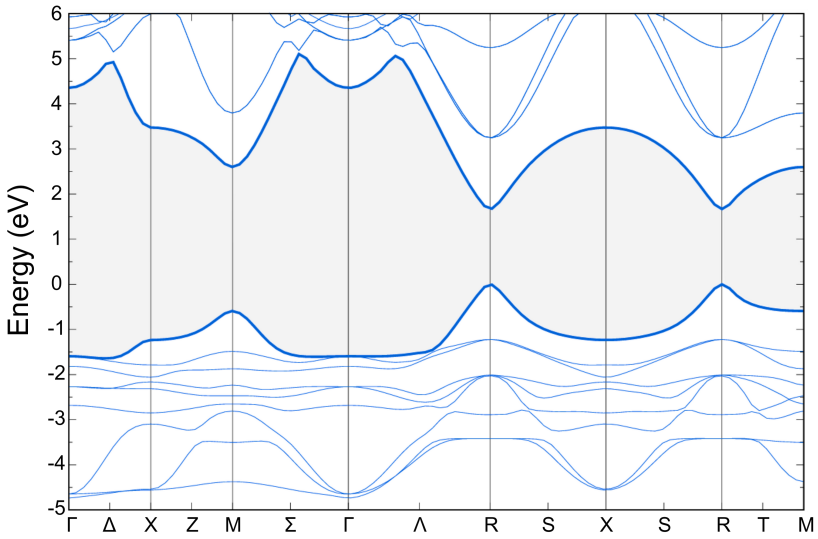


Figure 2.7: Electronic band structure of $CsPbI_3$ inorganic perovskite calculated via DFT, showing direct bandgap and spin-orbit coupling effects.

Mechanical and thermal properties

With Young's moduli between 10–30 GPa, inorganic perovskites exhibit strong mechanical characteristics that make them flexible enough for bendable devices [164]. Pugh's ratio ($B/G > 1.75$) in compounds such as Sr_3AsI_3 indicates that they are frequently ductile, allowing for strain tolerance without brittle failure [168]. Cubic phases exhibit isotropic behavior, while distorted phases (such as orthorhombic) show direction-dependent stiffness, indicating the prevalence of anisotropic elasticity [168]. Figure 2.8 shows the thermal decomposition profiles (A) and mechanical stress–strain curves (B) for selected inorganic perovskites, including $CsPbBr_3$ and $CsPbI_3$, highlighting their significant thermal stability and stress response. With a decomposition onset above 300–400 °C for $CsPbBr_3$, they provide better thermal stability than hybrid analogs [164].

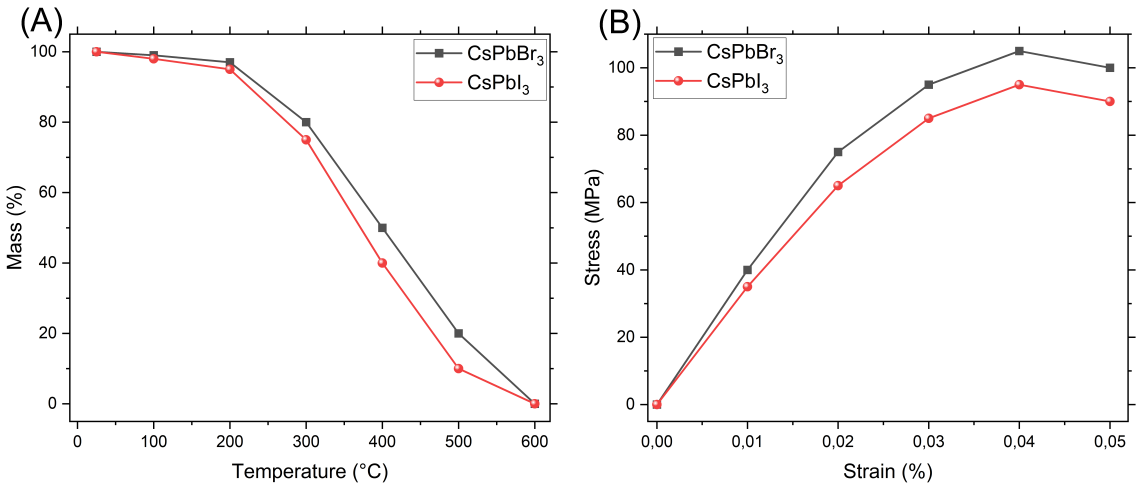


Figure 2.8: Mechanical stress-strain curves and thermal decomposition profiles for selected inorganic perovskites (e.g., $CsPbBr_3$ and $CsPbI_3$) [171].

While specific heat capacities adhere to Debye models, thermal conductivity is low ($\approx$ 0.5 $m^{-1}K^{-1}$), which is advantageous for thermoelectric applications [165]. Pressure enhances mechanical stability; for instance, $GaGeX_3$ resists compression by increasing its bulk modulus from 20 GPa to 50 GPa [166]. Encapsulation helps to reduce moisture-induced degradation, which remains a challenge [172]. Soft vibrational modes contributing to phase transitions are revealed by studying phonon properties using Raman spectroscopy [165]. A recent advancement involves $CsPbI_3$ capping layers for mutual stabilization, which has increased LED lifetimes beyond 180 000 min [173].

Structural variants

Beyond the archetypal 3D ABX_3 cubic structure, inorganic perovskites include diverse variants. Two-dimensional layered structures, such as Ruddlesden–Popper phases (A_2PbX_4), feature inorganic sheets separated by larger cations, enhancing environmental stability but reducing dimensionality and charge transport [173]. Zero-dimensional quantum dots (e.g., $CsPbBr_3$ QDs) offer size-tunable properties for LED applications [174]. Distorted phases arise from Goldschmidt tolerance factors ($t \approx 0.8$–1.0); for $t < 0.9$, orthorhombic or tetragonal symmetries dominate, as in γ-$CsPbI_3$ [175].

Novel cubic A_3BX_3 types, such as Mg_3NX_3 (X = F, Br, I), exhibit stable cubic lattices with direct bandgaps [164]. Pressure induces phase transitions, for example, from cubic to tetragonal in $InGeF_3$ at 2–4 GPa [166]. Defect engineering, such as B-site doping (Pb $\rightarrow$ Sn/Ge), reduces toxicity while maintaining structural integrity [170].

These characteristics make inorganic perovskites attractive candidates for sensors, LEDs, and photovoltaic applications. Their long-term stability continues to be investigated through compositional engineering and defect passivation [176].

2.4 Solar cells based on perovskite

2.4.1 Emergence of perovskite photovoltaics

Perovskite materials, characterized by their classic ABX_3 crystal lattice exhibit exceptional optoelectronic properties such as tunable direct bandgaps, high absorption coefficients exceeding 10^5 cm^{-1}, ambipolar charge carrier mobilities in the range of 10–100 $cm^2V^{-1}s^{-1}$, and carrier diffusion lengths greater than 1 µm [177].

These intrinsic characteristics have enabled a paradigm shift from fundamental materials science to their integration in high-performance photovoltaic devices, marking a revolutionary era in solar energy conversion technologies [178]. This transition began with the pioneering work of Kojima *et al.* in 2009, who reported the first perovskite-sensitized solar cell using $CH_3NH_3PbI_3$ ($MAPbI_3$) as a sensitizer in a liquid-electrolyte-based architecture similar to DSSCs, achieving an initial PCE of approximately 3.8 % under standard AM1.5G illumination [179]. Early challenges such as iodide oxidation and the hygroscopic nature of liquid electrolytes were overcome by 2012 through the introduction of solid-state hole transport materials (e.g., spiro-OMeTAD), which raised the PCE to nearly 9.7 % and triggered exponential growth in research activity [180].

The efficiency evolution of PSCs has been unprecedented in the history of photovoltaics: from 3.8 % in 2009 to 10 % by 2012 via compositional refinements, 15 % in 2013 through interface engineering, 20 % in 2014 using mixed-halide strategies, and surpassing 25 % by 2021 with defect passivation techniques—reaching certified records of 26.7–26.9 % for single-junction cells as of 2025. Concurrently, tandem architectures have further extended these performance boundaries.

By mid-2025, perovskite–silicon tandems and all-perovskite tandems have achieved certified efficiencies of 33.1 % and 31.38 %, respectively, surpassing the Shockley–Queisser limit for single-junction devices (≈33 % under standard conditions) [181]. In the wider photovoltaic space, perovskites compete with established technologies such as second-generation thin films (e.g., $Cu(In,Ga)Se_2$ (CIGS) at ≈23 % and CdTe at ≈22 %, both limited by material scarcity and toxicity) and crystalline silicon (c−Si, with module efficiencies of 22–27 % but burdened by energy-intensive wafer production exceeding 1000 °C) [182]. Perovskites disruptive potential stems from their facile, low-temperature solution-based fabrication processes (e.g., spin-coating or inkjet printing below 150 °C), inherent defect tolerance enabling high PCE despite polycrystalline morphologies, bandgap tunability across 1.2–2.3 eV via anion/cation alloying for spectral optimization, and adaptability to flexible, lightweight substrates. These features could potentially reduce the levelized cost of electricity (LCOE) to below 0.03 $/kWh, compared with 0.04–0.05 $/kWh for silicon-based technologies [183].

This dramatic increase in efficiency—more than an order of magnitude in only ten years, compared to silicon's gradual improvement over five decades—positions perovskites not merely as rivals but as complementary enhancers, particularly in tandem configurations that extend silicon's spectral utilization beyond 30 % while minimizing thermalization losses [184].

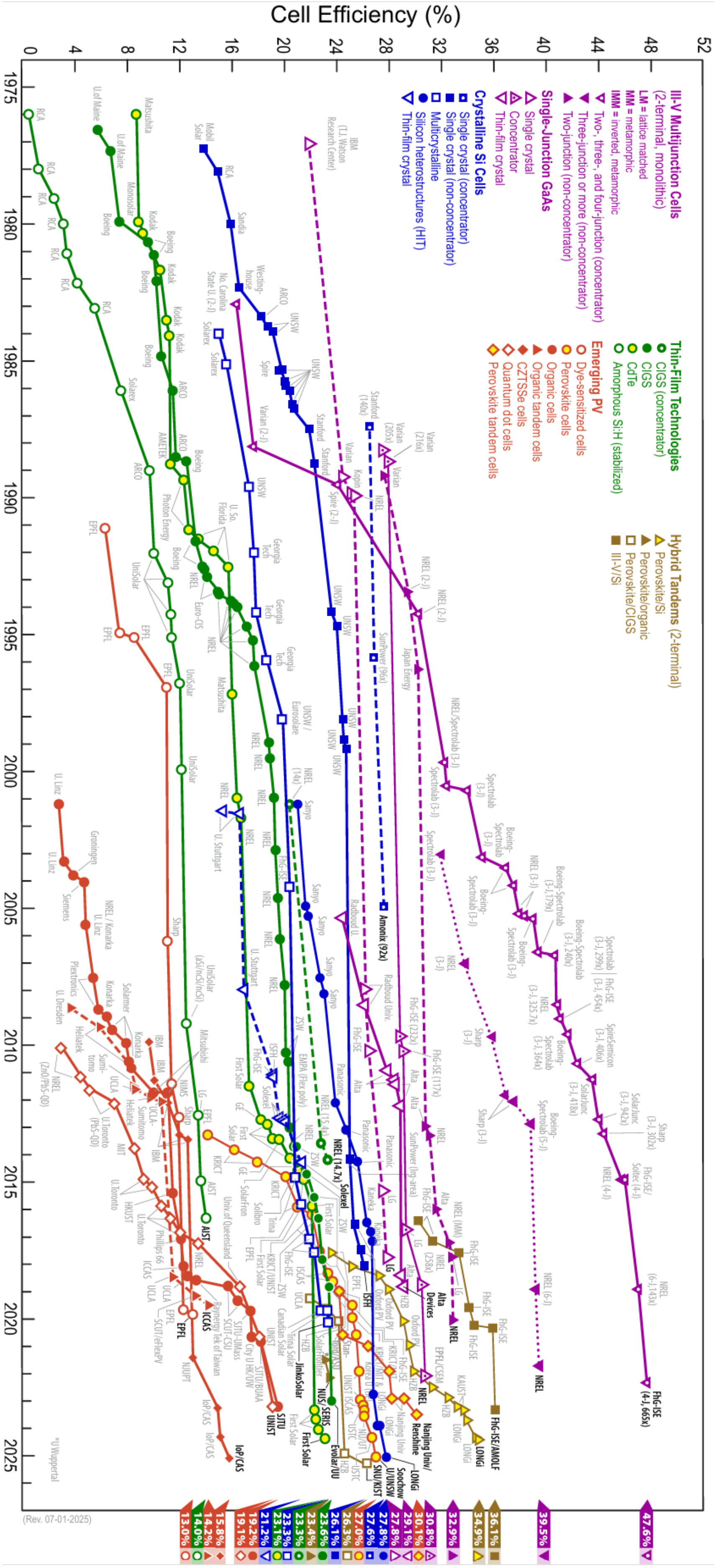


Figure 2.9: Conversion efficiencies of best research solar cells (NREL) [185].

2.4.2 Working principle of perovskite solar cells

Using the semiconductor qualities of the perovskite absorber layer, PSCs work by effectively converting incident solar photons into extractable electrical charge carriers [186]. Incident photons with energies (hv) greater than the direct optical bandgap of the material (E_g, usually $\approx 1.5 - 1.7$ eV for $MAPbI_3$) drive electrons from the valence band maximum to the conduction band minimum, producing electron-hole pairs or loosely bound excitons controlled by the Wannier-Mott model [187]. At room temperature ($kT \approx 25$ meV), the exciton binding energy ($E_b \approx 10 - 50$ meV) promotes thermal dissociation, producing free carriers with little recombination. This is much lower than in organic semiconductors because of the high dielectric constants $\varepsilon_r \approx 20 - 70$ [188]. At asymmetric heterojunction interfaces, charge separation is orchestrated: holes are directed to the hole transport layer (HTL, e.g., spiro-OMeTAD with VBM ≈ -5.2 eV), while electrons are selectively funneled to the electron transport layer (ETL, e.g., TiO_2 with CBM ≈ -4.0 eV vs. vacuum) [189]. This selectivity results from band alignment, where the Fermi level of the perovskite ($E_F \approx -4.6$ eV) creates inherent potentials ($V_{bi} \approx 0.8 - 1.2$ V) that propel carrier drift. These potentials are enhanced by diffusion gradients from high carrier concentrations in the absorber ($\approx 10^{15} - 10^{17}$ cm^{-3} under illumination) [190].

In order to mitigate non-radiative recombination pathways like SRH processes at defect states, an archetypal FTO/TiO_2/perovskite/HTL/Metal device's energy band diagram shows upward bending at the perovskite/HTL junction (facilitating hole transfer) and downward band bending at the TiO_2/perovskite interface (Schottky-like barrier $\approx 0.2 - 0.4$ eV for electron extraction) [188]. Figure 2.10 illustrates the schematic energy level alignment of PSC layers: FTO/TiO_2/$MAPbI_3$/spiro−OMeTAD with various metal contacts, showing the band alignment and its impact on charge separation and transport.

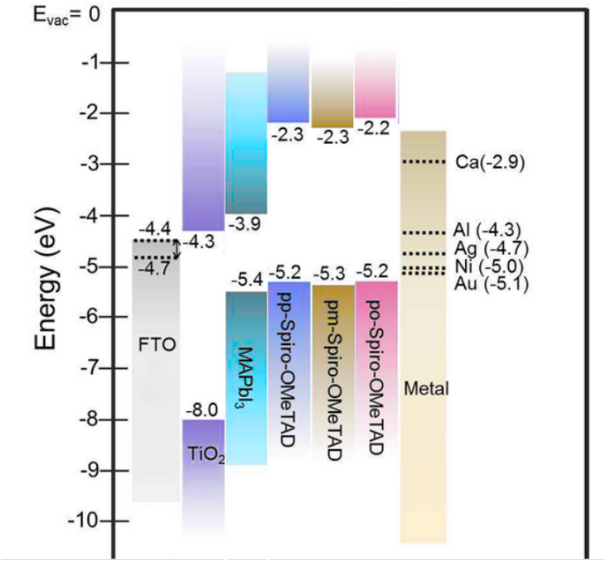


Figure 2.10: Schematic energy level alignment of PSC layers: FTO/TiO_2/$MAPbI_3$/spiro-OMeTAD with various metal contacts [191].

Thin absorber films ($300 - 500$ nm) can harvest >90 % of above-bandgap photons thanks to the device's high absorption coefficient ($\alpha > 10^5$ cm^{-1} in the visible regime), and

efficient transport before recombination is ensured by extended carrier diffusion lengths ($L_d > 1$ µm, governed by $L_d = \sqrt{D\tau}$, where D is diffusivity $\approx 1-10$ cm^2/s and τ lifetime $\approx 100 - 1000$ ns) [186]. Moreover, quasi-Fermi level splitting near the radiative limit is facilitated by the material's defect tolerance, which results from shallow trap states within the bandgap rather than deep mid-gap levels. In optimized devices, this leads to fill factors >80 % and V_{oc} up to 1.2 V [187].

2.4.3 Device architectures

Device architectures for PSCs are primarily categorized into three main types: mesostructured n-i-p, planar n-i-p, and planar p-i-n (inverted). Figure 2.11 shows schematic diagrams of the three main types of perovskite solar cell architectures.

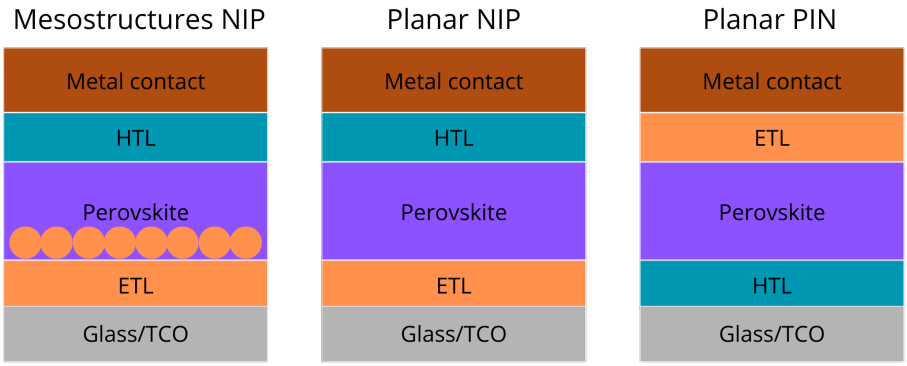


Figure 2.11: Schematic diagrams of n-i-p and p-i-n perovskite solar cell architectures.

- **Mesostructured n-i-p structure:** This design uses a TCO substrate, such as FTO, as the ETL and a mesoporous scaffold, usually TiO_2 or Al_2O_3 [192]. The perovskite penetrates the mesoporous layer's pores, increasing the surface area available for charge extraction. A hole transport layer (HTL, such as spiro-OMeTAD) and back electrode (Au/Ag) come next [193]. It developed from dye-sensitized solar cells and provides up to 25 % more stability and PCEs, but the scaffold needs to be processed at high temperatures [194].

- **Planar n-i-p structure:** This simplified version substitutes a compact planar ETL (such as TiO_2 or SnO_2) for the mesoporous layer that is deposited on the TCO substrate. The electrode, perovskite, and HTL (such as PTAA) come next [195, 196]. Recent improvements in interface passivation have reduced recombination, and it circumvents pore-filling problems, allowing for simpler fabrication and PCEs exceeding 26 % [197].

- **Planar p-i-n structure (inverted):** This inverted design begins with the HTL (like PEDOT:PSS or NiO_x) on the substrate, followed by the electrode, perovskite, and ETL (like PCBM or C_{60}) [178]. It achieves PCEs between 24–26 % with reduced hysteresis via fullerene ETLs and supports low-temperature processing (below 100 °C), which is ideal for flexible devices [144].

2.4.4 Advantages of perovskite cells

Perovskite solar cells offer several compelling advantages over traditional silicon-based photovoltaics, driving their potential for commercialization [198].

- **Superior performance and efficiency:** PSCs have quickly attained PCEs >27 % for single-junction and >34 % for perovskite-silicon tandems, coming close to or surpassing crystalline silicon (≈27 %) [194]. With theoretical limits of up to 43 % in tandems, tunable bandgaps allow for improved spectral utilization [192]. In contrast to silicon's drop-off, they function well in diffuse light [193].

- **Scalability and low cost:** Compared to silicon's high-temperature (>1000 °C) processes, solution-based fabrication at low temperatures (<150 °C) uses about half as much energy [194]. Compared to silicon's 0.50 $/W, abundant materials (such as PbI_2 at <1 $/g) and printing techniques allow module costs to be less than 0.30 $/W [195, 196, 199]. Scalable through slot-die coating to large areas [197].

- **Flexibility and versatility:** Unlike rigid silicon wafers, thin-film absorbers (≈500 nm) enable lightweight (<1 kg/m^2) flexible cells on plastics [178]. Fit for wearables, cars, or building-integrated photovoltaics [144]. Windows versions that are semi-transparent [200].

- **Sustainability and quick development:** Potential recyclability and lower embodied energy (10–20 MJ/m^2 compared to 100–200 MJ/m^2 for silicon) lessen the environmental impact [198]. Lead-free alternatives advanced, and efficiency doubled in ten years [194].

2.4.5 Limitation of PSCs

Despite the numerous advantages, there are several key limitations that still need to be addressed for the widespread adoption of PSCs [192]. While progress is being made in overcoming these challenges, they remain critical to the technology's commercialization and long-term reliability.

- **Lead toxicity and environmental concerns**

  One of the major challenges with PSCs is the toxicity of lead, which is commonly used in the perovskite materials (e.g., $MAPbI_3$). The potential for lead leakage into the environment during production, usage, or disposal poses a significant concern, particularly in large-scale applications. Although encapsulation techniques have been developed to minimize lead leakage, concerns about the environmental impact persist. Several efforts are underway to develop lead-free alternatives, such as tin-based (Sn) perovskites, which are less toxic but still face challenges in terms of stability and efficiency. Further research is needed to ensure that these lead-free perovskites can achieve performance on par with their lead-based counterparts without sacrificing longevity or efficiency.

- **Stability under environmental conditions**

  Perovskite materials, especially those used in PSCs, are inherently unstable under exposure to moisture, oxygen, UV light, and temperature fluctuations. The perovskite layer can degrade when exposed to environmental stressors, leading to a loss of efficiency and potentially failure of the device over time. This degradation is exacerbated by the presence of lead, which not only affects environmental safety but also the material's robustness. While encapsulation techniques, such as the use of barrier layers and hermetic sealing, have shown to enhance stability, the issue of long-term durability remains a significant hurdle. Moisture and thermal stability are especially concerning in real-world outdoor applications, and ongoing efforts aim to improve the material's resistance to such stressors.

- **Hysteresis and ion migration**

  Another issue limiting the efficiency and reliability of PSCs is hysteresis, the phenomenon where the performance of the device depends on the scanning direction of the voltage, leading to inconsistencies in the current-voltage characteristics. This is often associated with ion migration within the perovskite layer, where ions (particularly halides) move under an applied electric field, causing shifts in the electronic properties of the material. This can lead to performance losses, reduced efficiency, and instability over time. While advancements in passivation techniques, interface engineering, and the use of mixed cation and halide perovskites have reduced hysteresis, complete mitigation is still an ongoing challenge.

- **Scalability and manufacturing challenges**

  While PSCs offer a significant reduction in manufacturing costs compared to traditional silicon-based solar cells, the scalability of production remains an area of concern. The solution-based fabrication methods used for PSCs, such as spin coating or inkjet printing, are suitable for small-area devices but face challenges when scaling up for large-area production. Achieving uniformity and consistency over large areas while maintaining high efficiency is a significant hurdle. Moreover, the long-term performance of large-area PSCs has yet to be fully validated, and further optimization is required for scalable and economically viable commercial production.

- **Long-term stability and aging**

  The long-term stability of PSCs remains one of the most significant obstacles. Even with advances in encapsulation and material modifications, the efficiency of PSCs tends to degrade over time due to factors such as moisture exposure, UV radiation, and high operating temperatures. Recent studies have shown that while encapsulation can significantly extend the lifespan of these cells, they still exhibit degradation over periods of months to a few years. This is a stark contrast to silicon-based cells, which typically have lifespans exceeding 20 years. Thus, achieving decade-long stability remains a key focus of research, as the commercial success of PSCs will depend on their ability to maintain performance over extended periods.

- **Cost of materials and processing techniques**

  While PSCs have the potential to be much cheaper to produce than silicon-based solar cells due to the low-temperature solution processing techniques, certain materials used in the fabrication of PSCs, such as the HTMs like spiro-OMeTAD, are still relatively expensive. Moreover, the optimization of the deposition techniques for scalable production is ongoing, and while printing technologies like slot-die coating show promise for large-area manufacturing, they still need to be refined to ensure consistent performance at a commercial scale. Moreover, the use of rare or expensive materials in some of the alternative formulations (such as in Sn-based or other non-lead alternatives) could increase costs, potentially reducing the economic advantage of PSCs in the long run.

2.5 Tandem solar cell

Tandem solar cells, constituting a specialized class within multi-junction photovoltaic architectures, embody a paramount methodology for transcending the SQ detailed-balance efficiency ceiling inherent to single-junction devices. The SQ formalism, based on thermodynamic principles of radiative recombination and black-body spectral assumptions under AM1.5G insolation, shows that the best bandgap is about 1.34 eV, which gives an efficiency limit of about 33.7 %. This is mostly due to carrier thermalization (the loss of supra-bandgap photon energy through phonon interactions) and sub-bandgap transmission losses [3]. By using either monolithic or hybrid integration of two sub-cells with carefully chosen complementary bandgaps, tandem configurations make it possible to separate the spectrum, which reduces entropic losses and raises the theoretical efficiency limit to about 47 % for unconcentrated light in idealized double-junction systems [201].

Recent research has caused a major change in tandem photovoltaics. This is because there is a need to lower the LCOE by improving power conversion efficiencies and making manufacturing processes that can be scaled up. Certified efficiencies for tandem prototypes have surpassed 34 %, as demonstrated by perovskite–silicon hybrids. Continuous improvements in defect passivation, interfacial engineering, and compositional tweaking are paving the way for impending commercial feasibility [18, 202].

2.5.1 Tandem solar cells: overcoming the Shockley–Queisser limit

The fundamental principle of tandem solar cells is dichromatic spectral bifurcation: high-energy photons are preferentially absorbed by a wide-bandgap superior sub-cell, while infra-bandgap photons pass through unhindered to be collected by an inferior sub-cell with a smaller bandgap. This layered vertical structure, going from the incident (heliotropic) side to the opposite side, reduces thermalization inefficiencies.

This concept is visually depicted in Figure 2.12, which shows simplified energy-band diagrams for both single-junction and multi-junction solar cells, illustrating how excess kinetic energy is reduced compared to monolithic counterparts. In solitary-junction solar cells, spectral exploitation is significantly inferior. For example, crystalline silicon (with a bandgap of approximately 1.12 eV) suffers from thermalization losses, where ultravio-

let/visible photons induce extensive lattice heating, while near-infrared photons bypass absorption altogether. Tandem strategies mitigate this through bandgap complementarity, with optima ranging from 1.5 eV to 1.7 eV for the upper sub-cell and 0.9 eV to 1.1 eV for the lower sub-cell [201, 203].

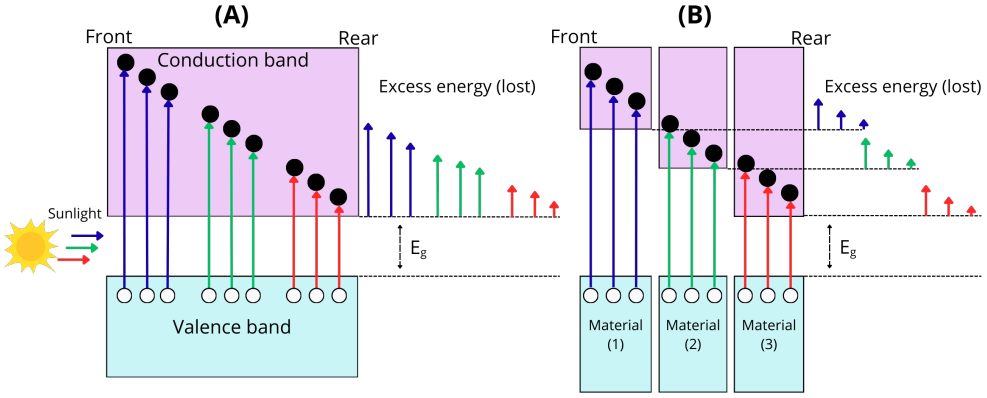


Figure 2.12: Simplified schematics of: (A) single-junction, (B) multi-junction solar cells illustrating the reduction of thermalization losses.

The thermodynamic limit of efficiency for tandem cells is 86.8 % under maximum solar concentration, where entropic dissipation is minimized by using infinite-junction laminates. However, practical double-junction implementations offer a balanced trade-off between efficiency enhancement and fabrication requirements [3, 204]. Efficiency isocontours for tandem assemblies emphasize the vulnerability to bandgap misalignment, where deviations from the ideal alignment cause significant performance degradation. Modern bandgap modulation techniques, such as halide alloying in perovskites, have successfully circumvented these limitations, enabling laboratory efficiencies exceeding 30 % by achieving precise spectral alignment.

2.5.2 Tandem architectures

Tandem solar cells come in three main types, each with different designs that impact how they manage light, charge carriers, and performance.

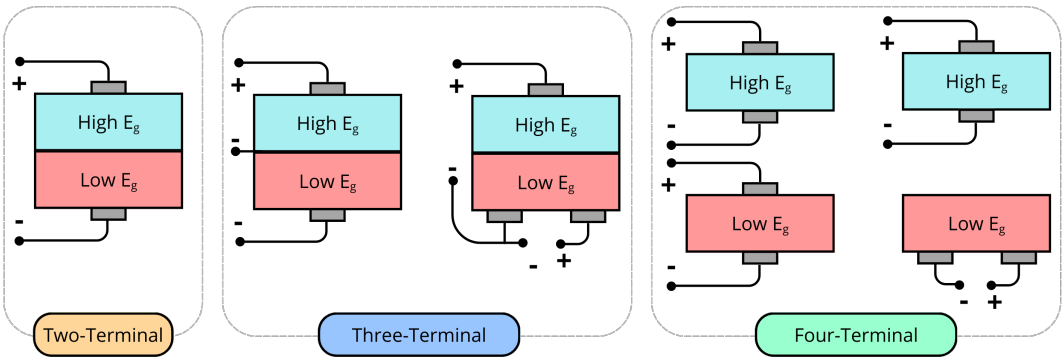


Figure 2.13: Schematic representations of various tandem solar cell architectures, namely two-terminal, three-terminal, and four-terminal configurations.

These architectures include two-terminal configurations, where all components are connected in series, making it a simpler design. In three-terminal systems, the sub-cells are connected to separate electrical contacts, giving more control over voltage and current. Four-terminal designs have the sub-cells stacked separately, each with its own electrical contact, offering the most flexibility. Figure 2.13 shows the schematic representations of these three types of tandem solar cell architectures: 2T, 3T, and 4T configurations [205, 206].

Two-terminal (monolithic) tandem

In the 2T monolithic configuration (Figure 2.14), the sub-cells—sharing identical front and rear polarity (p/n or n/p)—are sequentially fabricated atop one another and electronically connected in series through a tunnel heterojunction or recombination interlayer.

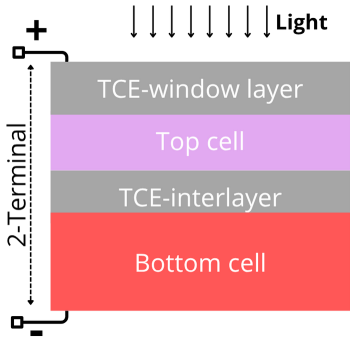


Figure 2.14: Schematic representation of a two-terminal tandem solar cell structure.

The result of this integration is an additive open-circuit voltage ($V_{\mathrm{oc,total}} \approx V_{\mathrm{oc,top}} + V_{\mathrm{oc,bottom}}$), whereas the lowest-performing sub-cell ($J_{\mathrm{sc,total}} = \min J_{\mathrm{sc,top}}, J_{\mathrm{sc,bottom}}$) limits the short-circuit current [207, 208]. Therefore, accurate photocurrent matching is essential, which is usually accomplished by modifying the superior absorber's bandgap and thickness, as well as by modifying the window layers' optical characteristics or by utilizing cutting-edge photonic management techniques like anti-reflective coatings, nanostructures, or photonic crystals. With its simplified encapsulation, reduced parasitic absorption from fewer transparent electrodes, and compatibility with well-established single-junction module fabrication [209], this architecture is very appealing for industrial deployment; however, it also places strict requirements on process compatibility. The upper sub-cell must be deposited without causing harm to the underlying layers, which calls for low-temperature or plasma-mitigated methods like atomic layer deposition or organometallic vapor-phase epitaxy. Furthermore, spectral variability due to diurnal or atmospheric changes can aggravate current mismatch, leading to fill-factor losses and reinforcing the need for adaptive maximum power point tracking algorithms [210]. Notwithstanding these difficulties, the 2T paradigm still controls both terrestrial and space photovoltaics: perovskite–silicon monolithic tandems are setting records for efficiency on Earth, while epitaxial III–V tandems continue to be the standard for power generation in space. Subsequent developments in defect passivation and interfacial engineering are driving the technology closer to commercialization [18].

Four-terminal tandem

As shown in Figure 2.15, each sub-cell in a 4T tandem configuration has its own front and rear electrodes and is mechanically stacked after being independently manufactured. Without requiring current matching or polarity alignment, this structural configuration guarantees that the two sub-cells stay electronically isolated while mechanically coupled, enabling both to function at their respective maximum power points [205, 207]. Consequently, the overall device efficiency is equal to the arithmetic sum of the individual sub-cell efficiencies, providing significant bandgap selection flexibility and removing the spectral and entropic penalties that are typical of monolithic integration.

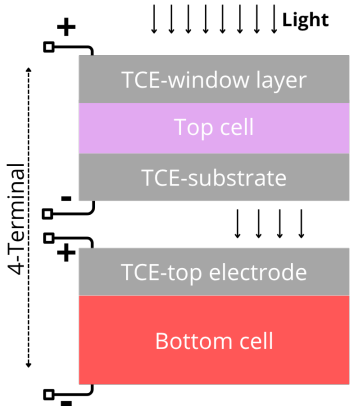


Figure 2.15: Schematic representation of a four-terminal tandem solar cell structure.

The 4T approach is especially beneficial for research because of its inherent configurational freedom, which allows for the independent design, characterization, and optimization of disparate material systems [205, 207]. However, there are a number of barriers to practical deployment. The need for at least three transparent conductive electrodes—two front electrodes plus the top cell's rear contact—increases ohmic losses, parasitic absorption, and Auger recombination. It also raises the cost of fabrication using deposition methods like sputtering or chemical vapor deposition (CVD) [208]. Large-scale photovoltaic installations may become less competitive as a result of increased balance-of-system costs brought on by complex module-level interconnections.

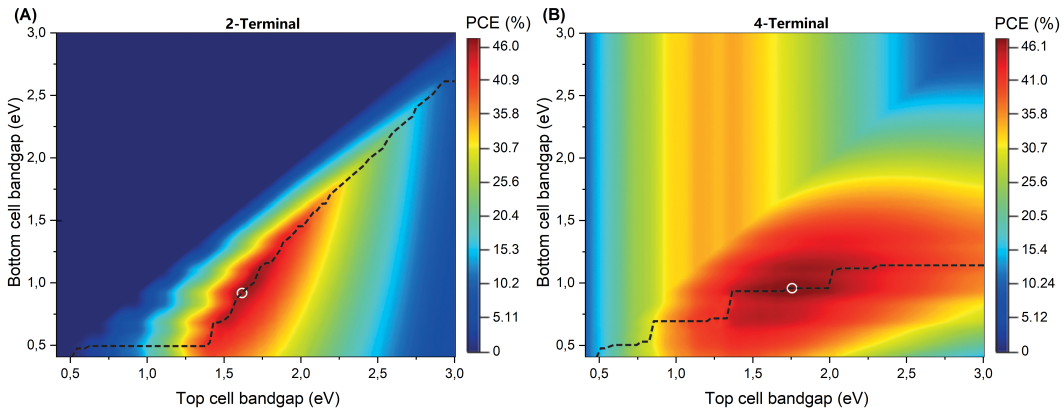


Figure 2.16: Efficiency response of: (A) 2T and (B) 4T configurations to deviations from ideal bandgap pairs [211].

Recent developments show the potential of the 4T architecture in spite of these obstacles. Using elastomeric substrates and strain-tolerant interlayers, flexible versions of perovskite–silicon tandem stacks have been shown to achieve efficiencies of over 30 % [212, 213]. A partnership between CEA and 3SUN reported 30.8 % efficiency for large-area prototypes that used bifacial silicon substrates to take advantage of albedo gains, marking a significant milestone [214].

Three-terminal tandem

The 3T tandem architecture is generally divided into two distinct configurations: Type A and type B [205, 206]. Type A closely resembles a 2T monolithic tandem but incorporates an additional electrode within the recombination layer, as illustrated in Figure 2.17. This supplementary terminal alleviates the strict requirements of current matching and identical polarity that constrain conventional monolithic tandems, since both sub-cells are effectively connected in parallel. Consequently, the overall V_{oc} is dictated by the sub-cell with the lower potential—typically the silicon bottom cell—while the short-circuit current remains essentially fixed under theoretical efficiency limit calculations.

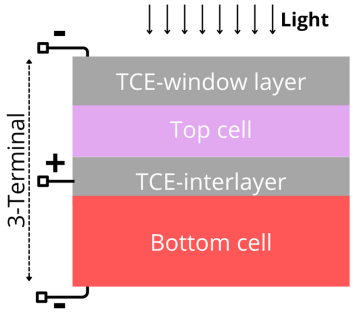


Figure 2.17: Schematic representation of a three-terminal tandem solar cell structure.

As shown in Figure 2.16 and Figure 2.18, this results in an efficiency profile that is nearly independent of the top-cell bandgap, yielding constant plateaus but lower maxima compared to 2T and 4T configurations.

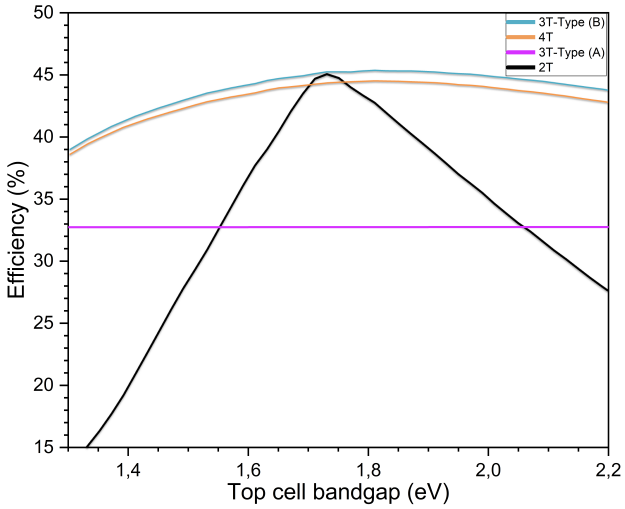


Figure 2.18: Shockley–Queisser limits of Si-based tandem solar cells (2T, 3T type A/B, 4T) versus top-cell bandgap [215].

For this reason, type A structures have attracted limited research attention, despite proof-of-concept reports in the literature [205, 206, 216–218]. By contrast, type B integrates a monolithic top sub-cell with an IBC bottom cell that features a conductive front surface [205, 206]. In this configuration, both cells are fabricated monolithically, with a third electrode connected at the rear side of the IBC bottom cell. This additional contact allows quasi-independent operation of the two sub-cells at their respective maximum power points, thereby reducing sensitivity to spectral variations and top-cell bandgap fluctuations. Although some degree of current matching is still required, the base electrode enables extraction of excess current from the bottom cell, mitigating mismatch-related losses. As a result, the theoretical efficiency limit of type B structures approaches that of 4T tandems, as depicted in Figure 2.18. Originally proposed by Nagashima et al [219], type B has gained momentum in recent years, particularly for III–V/Si and perovskite/Si tandems, owing to the rapid development and commercialization of IBC silicon technology [219–224].

2.5.3 Materials and candidates

The performance of tandem solar cells fundamentally depends on the judicious choice and combination of absorber materials. Key requirements include tunable bandgaps, strong optical absorption, low Urbach energies (minimizing sub-bandgap losses), and thermal as well as mechanical compatibility between stacked layers. Equally important are low defect densities (10^{15} cm^{-3}, balanced carrier mobilities ($10\,cm^2V^{-1}s^{-1}$), and fabrication processes that avoid phase segregation or interdiffusion of elements. These parameters are crucial to suppress Shockley–Read–Hall recombination and interfacial trap states, thereby maintaining long-term device stability across operational temperature ranges (−40 °C to 85 °C) and under accelerated stress testing following IEC 61215 standards [205, 206].

Silicon as the benchmark bottom cell

The most common material platform for bottom sub-cells is still c−Si, which has an indirect bandgap of about 1.12 eV at room temperature. It is an essential part of tandem architectures due to its large-scale production, extensive industrial infrastructure, and low module costs (≈0.3 $/Wp in 2025). For effective coverage of the AM1.5G solar spectrum, silicon is especially well-suited to pair with top absorbers in the 1.5–1.7 eV range [7, 208]. The most efficient single-junction silicon cells, which are based on SHJ and passivated emitter rear cell technologies, have an efficiency of 26.7 %. Advanced surface passivation techniques, such as poly-SiO_x or Al_2O_3 layers, together with optimized texturing, can suppress surface recombination velocities below $10\,cm\,s^{-1}$ and yield internal quantum efficiencies above 95 % in the near-infrared region (900–1100 nm). Recent progress has established silicon as the backbone of high-performance tandems. LONGi reported 34.85 % efficiency for a perovskite–silicon monolithic tandem.

By June 2025, large-area ($260.9\,cm^2$) devices had achieved 33 % efficiency, in part because of bifacial designs that take advantage of ground albedo [18, 225]. Compatibility problems with perovskite top cells, which necessitate efficient encapsulation techniques (e.g., polyolefin or EVA) to prevent halide migration and reduce potential-induced degra-

dation, and limited absorption at wavelengths > 1100 nm due to indirect transitions are the remaining obstacles.

Perovskite–silicon tandems

By tuning the halide composition or A-site cation mixing, metal-halide perovskites (ABX_3, where A is Cs^+, FA^+, MA^+; B is Pb^{2+}, Sn^{2+}; and X is I^-, Br^-, Cl^-) have tunable bandgaps from 1.2–2.3 eV. Perovskites are inexpensive, have suitable optoelectronic characteristics, and are solution-processable at comparatively reduced temperatures (below 100 °C). The use of defect passivation techniques, including self-assembled monolayers, and band-edge engineering have led to efficiencies above 25 % in a single junction [226]. Perovskites have demonstrated great potential not only for absorbing the visible, but in fact, in parts of the blue region of the solar spectrum, not effectively addressed by silicon alone, particularly when used as upper cells in conjunction with silicon. The most recent defect passivation developments, leveraging additives such as piperidinium and dimethylammonium iodide, have decreased non-radiative recombination and have facilitated efficiency gains in tandems as high as 33.1 % in conjunction with record-shattering open-circuit voltages of approximately 2.01 V. Even flexible tandem structures based on PET substrates have achieved 30 % efficiency by leveraging strain-relief layers [202, 212], whereas monolithically integrated perovskite-silicon tandem configurations only recently achieved an impressive level of 34.9 % efficiency (Fraunhofer ISE/AMOLF, 2025). Stability, too, has been improved, as demonstrated by Qcells, who reported that devices have over 90 % of their performance remaining after 1000 h at 85 °C and 85 % relative humidity damp-heat stress [227].

All-perovskite tandems

Fully perovskite tandems combine wide-bandgap (≈1.8 eV, e.g., $CsPbI_2Br$ or mixed-halide alloys) and narrow-bandgap (≈1.2 eV, e.g., Sn–Pb perovskites) absorbers. With scalable techniques like roll-to-roll slot-die coating or vapor-phase deposition, this method promises low production costs (<0.5 $/Wp) and substrate flexibility (either rigid glass or flexible polymers) [194, 228]. SolaEon achieved a certified 31.38 % efficiency with a graded Sn–Pb composition that suppressed Sn^{2+} oxidation and enhanced radiative recombination. Theoretical limits suggest efficiencies up to ≈42 % are possible under one-sun conditions for such dual-junction designs.

Other material combinations

Other material pairings have also been explored. III–V/Si tandems (e.g., GaAsP/Si or InGaP/GaAs/Si) have achieved >38 % under AM1.5G illumination, making them the standard for space applications. However, their terrestrial use is limited to concentrator photovoltaics due to the high cost of epitaxial growth, which is approximately 100 higher than silicon [229]. Using CIGS's bandgap tunability (1.0–1.7 eV) and robust defect tolerance, perovskite–CIGS tandems are another promising route; in 2025, HZB/Humboldt University Berlin demonstrated a certified 24.6 % efficiency [230]. The percentage of perovskite–

organic tandems, which combine halide perovskites with organic semiconductors like Y6 or ITIC derivatives, has surpassed 26.4 % (SERIS/NUS, June 2025). These tandems provide lightweight, semi-transparent modules with broad spectral absorption [213].

2.6 Conclusion

In summary, this chapter provided a comprehensive overview of perovskite materials and their growing significance in photovoltaic research. The discussion covered their crystallographic structure, material classifications, and the distinctions between hybrid organic–inorganic and all-inorganic perovskites, emphasizing how compositional and structural variations influence their optoelectronic behavior and stability. The fundamentals of PSCs were then reviewed, including their working principles, architectures, and the key advantages and limitations that define their current technological landscape. Furthermore, the concept of tandem solar cells was introduced as a pathway to exceed the Shockley–Queisser efficiency limit, with particular attention to the design and performance characteristics of 2T, 3T, and 4T configurations.

Building upon this foundation, the following chapter focuses on the experimental and simulation study of a perovskite single-junction solar cell and the design and performance evaluation of a 2T tandem configuration. These analyses aim to deepen the understanding of material–device relationships and efficiency optimization strategies within advanced perovskite photovoltaic systems.

Chapter 3

Simulation and design of perovskite solar cells using Silvaco ATLAS TCAD

3.1 Introduction

The exponential advancement in photovoltaic technology demands sophisticated computational tools to accelerate device optimization while minimizing experimental costs and development time. Chapter 3 establishes the comprehensive computational framework employed for simulating and optimizing perovskite solar cell architectures, with particular emphasis on single-junction devices and advanced tandem configurations combining perovskite and silicon subcells. This chapter provides the methodological foundation underlying all subsequent analysis and optimization studies presented in this thesis. The primary focus centers on the implementation and validation of Silvaco Atlas TCAD technology computer-aided design (TCAD) software as the core simulation platform, enabling accurate prediction of device performance through rigorous numerical modeling of fundamental semiconductor physics. The computational approach addresses the critical need for reliable virtual prototyping in perovskite photovoltaic research, where experimental parameter optimization is often resource-intensive and time-consuming.

3.2 Presentation of Silvaco

3.2.1 Silvaco TCAD and ATLAS simulator

Silvaco TCAD is a modular suite for semiconductor device simulation, with ATLAS serving as the core engine for solving coupled equations governing carrier transport, recombination, and optical generation in solar cells. From conventional silicon to cutting-edge perovskites, it supports a wide range of materials, enabling virtual prototyping to lower experimental costs and speed up design iterations [231, 232].

Introduction to Silvaco Atlas TCAD

ATLAS is a physically based device simulator that solves Poisson's equation, carrier continuity equations, and drift-diffusion transport to model DC, AC, transient, and optical responses. In order to simulate light absorption under AM1.5G spectra, it incorporates optical modules such as ray-tracing and transfer-matrix techniques for PSCs.

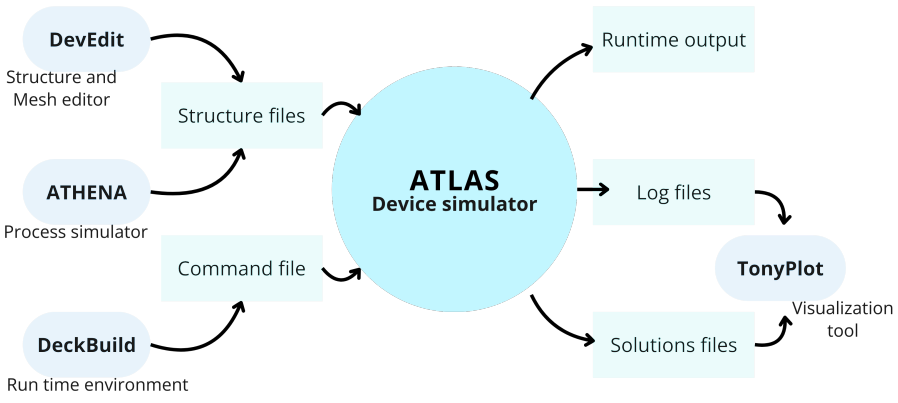


Figure 3.1: Atlas inputs and outputs.

The tool supports batch runs for parameter sweeps and interfaces with TonyPlot for visualization and DeckBuild for input deck creation. ATLAS has been used to model single-junction, tandem, and multi-terminal configurations in PSC simulations, capturing interface recombination and defect states [231, 233].

Advantages and limitations of Silvaco Atlas TCAD

Silvaco Atlas TCAD is an advanced PSC simulator that enables powerful simulations with high precision by virtue of advanced physical models and large material libraries to describe heterojunctions, carrier transport, and quantum effects accurately. It can accommodate intricate device structures such as graded bandgap absorbers, textured surfaces, and tandem devices due to its versatility, while optical solvers like FDTD or TMM can be combined with electrical solvers to enable detailed predictions of EQE, J–V characteristics, and overall output. Nevertheless, these capabilities come with sharp limitations: simulations of 3D structures or fine-resolution grids can be slow and require much computational power; output is strongly sensitive to the precision of input parameters, as bandgap, mobility, and defect density with even minor inaccuracies can warp predictions; and perovskite devices specifically can suffer from poor convergence due to the solvers' sensitivity to meshing strategy and model choice in defect-abundant materials. Nevertheless, Silvaco Atlas TCAD is a powerful yet resource-hungry software that needs to be carefully calibrated to deliver reliable results.

3.2.2 Device structure under Silvaco

The perovskite solar cell is simulated with ATLAS using the DeckBuild interface. The structure is created by a series of commands for both geometry-related parameters (e.g., layer thickness and device length) and material properties with respect to physical characteristics (e.g., bandgap, affinity, permittivity, mobilities, and recombination models). Each layer of the device (FTO, TiO_2, perovskite absorber, and HTM) is added one-by-one in conjunction with their doping levels and optical properties.

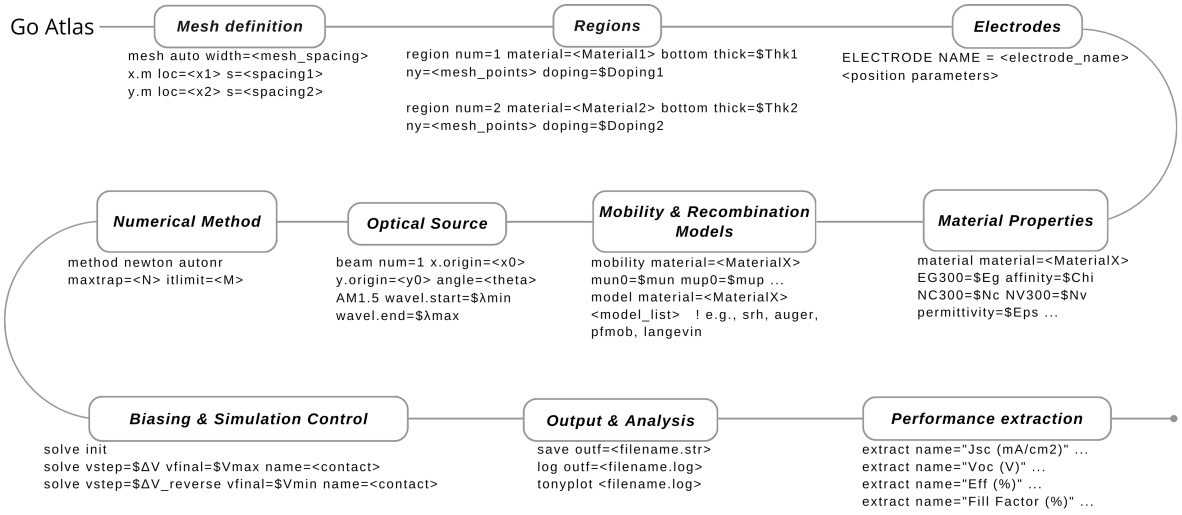


Figure 3.2: General workflow of device simulation using Silvaco Atlas TCAD.

The contacts with the anode and cathode are defined for past electrical configuration. The overall workflow, illustrated in the flow chart of Figure 3.2, illustrates the stepwise flow that builds and produces the results for this simulation.

Mesh definition

In device simulation, the mesh constitutes the numerical discretization of the device geometry into finite elements, over which the coupled semiconductor transport equations are solved. The use of a refined mesh is essential in localized regions characterized by strong spatial gradients in carrier concentration, electric field, and generation-recombination processes, particularly at heterointerfaces and in the vicinity of electrical contacts. Inadequate spatial resolution may lead to numerical inaccuracies and poor convergence, whereas excessive refinement can considerably increase computational cost without a commensurate improvement in physical fidelity. In this work, the meshing strategy was implemented through automatic refinement, with additional resolution imposed along the device boundaries and in the vertical direction to capture the critical electrostatic and transport features with sufficient precision. This selective approach ensures an optimal compromise between numerical accuracy and computational efficiency. Figure 3.3 illustrates the mesh configuration employed in ATLAS. Such targeted refinement is especially important for PSCs, where interfacial charge extraction and recombination processes exert a decisive influence on device performance [231, 232].

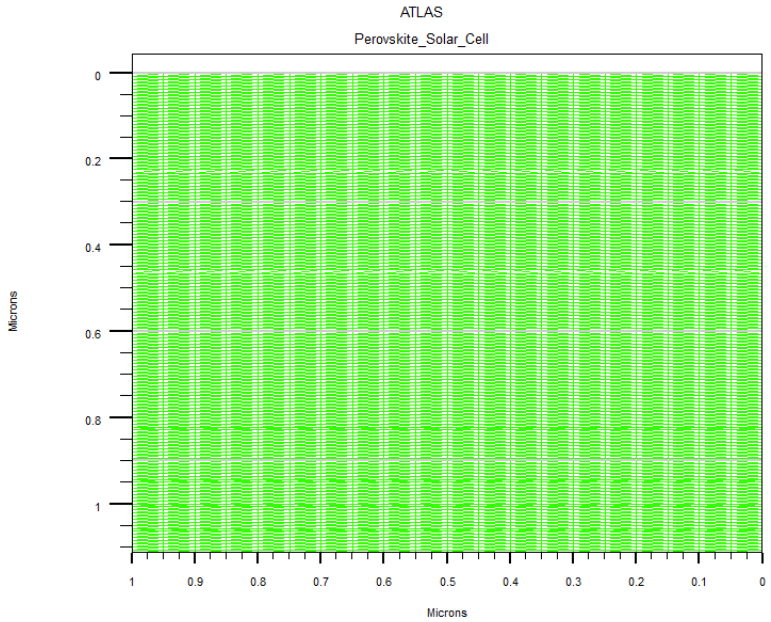


Figure 3.3: ATLAS mesh creation.

Device regions

Regions define the geometry and material identity of each layer in the simulated solar cell. This includes thickness, doping, and the number of vertical divisions for meshing. Accurate region specification is necessary because it determines how carriers are generated, transported, and collected. In the present simulation, four layers are modeled:

- **Region 1:** Fluorine-doped tin oxide (FTO, 0.3 µm) acting as the transparent conductive oxide.
- **Region 2:** Titanium dioxide (TiO_2, 0.3 µm, donor concentration 10^{15} cm^{-3}), serving as the ETL.
- **Region 3:** The perovskite absorber ($MAPbI_3$, 0.3 µm, low doping of 10^9 cm^{-3}), which governs optical absorption and charge generation.
- **Region 4:** Hole transport material (HTM, 0.213 µm, acceptor concentration 2×10^9 cm^{-3}), responsible for hole extraction.

The defined device regions and their corresponding doping profiles in ATLAS are illustrated in Figure 3.4, where each layer is represented with its material properties and net doping concentration. These parameters reproduce a typical n-i-p perovskite solar cell structure widely used in high-efficiency PSC research. Proper region definition enables realistic simulation of band alignment, carrier distribution, and recombination pathways [233].

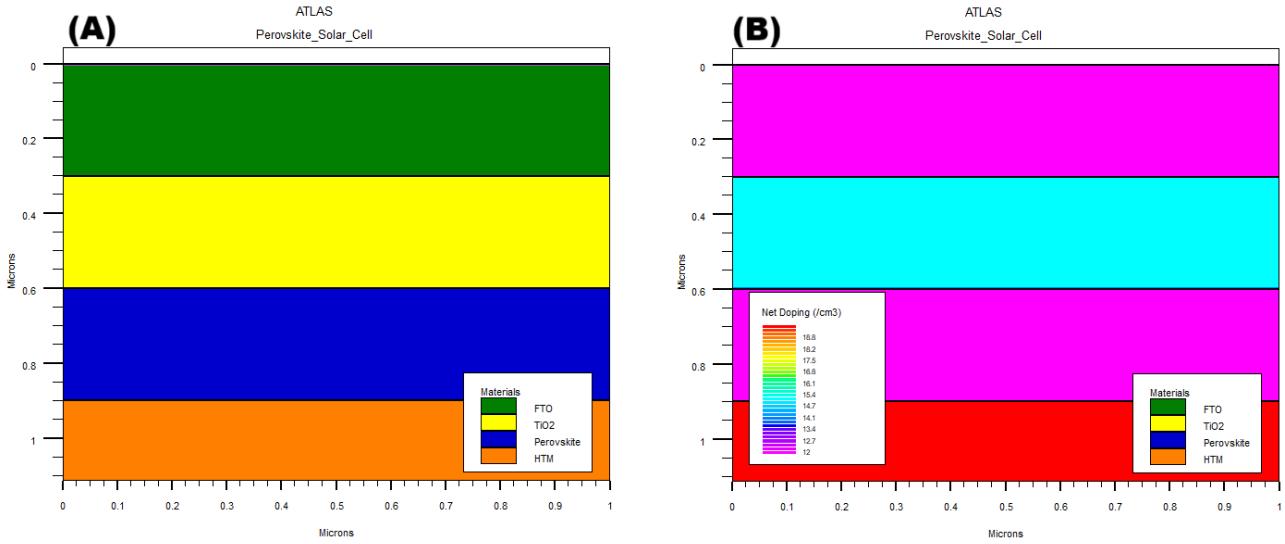


Figure 3.4: Defined device: (A) Regions and (B) Doping profiles.

Electrodes

Electrodes represent the boundary conditions where current flows in and out of the device and where external bias is applied. Proper electrode definitions are particularly important when simulating charge extraction efficiency and minimizing artificial losses. In our simulation, the cathode (`elec num=1 name=cathode top material=FTO`) is chosen at the top of the FTO, and the anode is located at the bottom and has a work function of 5.5 eV (`contact name=anode workf=5.5`), which ensures alignment with the HTM (hole transport material), enabling efficient hole extraction.

The electrode configuration of the simulated perovskite solar cell is shown in Figure 3.5, the FTO acts as the front electrode (cathode), while the back contact is defined as the

anode. These electrodes enable current collection across the device and establish the necessary biasing conditions for accurate electrical simulation in ATLAS. Voltage sweeps between $-1\,\mathrm{V}$ and $1.2\,\mathrm{V}$ are applied to simulate J–V curves in both the forward and reverse direction, allowing the evaluation of device hysteresis. The method of defining electrodes adheres to experimental architectures using transparent conductive oxides and selective contacts [234].

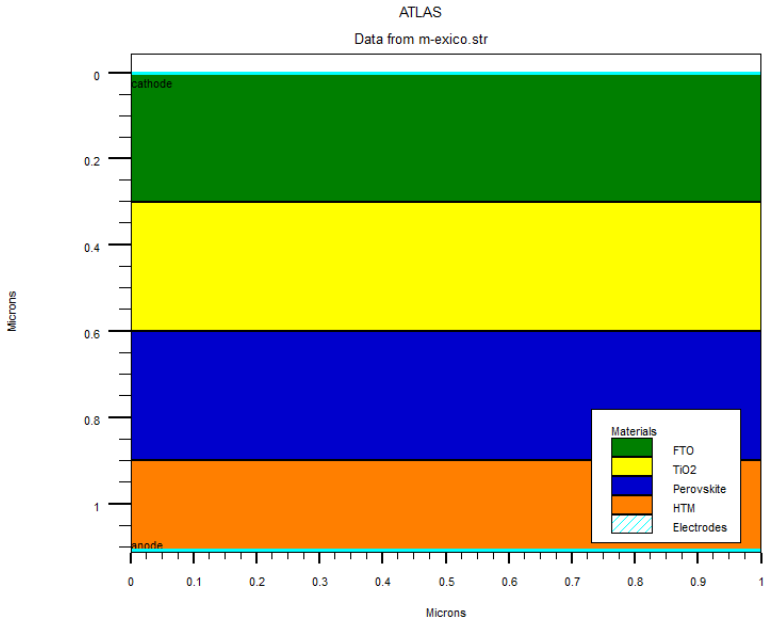


Figure 3.5: Electrode configuration in the perovskite solar cell.

Material properties

Material parameters are fundamental to the predictive accuracy of simulations. They define bandgap energy, electron affinity, permittivity, carrier mobilities, and lifetimes, all of which govern optical absorption, charge transport, and recombination. In this work:

- **FTO** is assigned high resistivity to act primarily as a transparent conductor.
- **$\mathbf{TiO_2}$** has a high bandgap ($3.2\,\mathrm{eV}$), a relatively high dielectric constant (30), and low mobilities ($\mu_n = 0.002\,\mathrm{cm^2/(V\,s)}$, $\mu_p = 0.001\,\mathrm{cm^2/(V\,s)}$), showing its selective electron-transport characteristics.
- **$\mathbf{MAPbI_3}$** perovskite is characterized and modeled with a bandgap of $1.55\,\mathrm{eV}$, affinity of $3.83\,\mathrm{eV}$, permittivity of 150, moderate mobilities ($0.1\,\mathrm{cm^2/(V\,s)}$), and carrier lifetimes of $1\,\mu\mathrm{s}$, permitting efficient light absorption and charge transport.
- **HTM** has a bandgap of $3.0\,\mathrm{eV}$, low permittivity (3), and low mobilities, consistent with organic hole transporters.

Furthermore, wavelength-dependent refractive index (n) and extinction coefficient (k) values are imported from experimental data files (`MAPbI3.nk`, etc.), ensuring realistic

optical absorption modeling. Precise parameterization is necessary because inaccuracies in bandgap, mobility, or permittivity can significantly affect predicted J–V and EQE curves [231].

Physical models

The accuracy of device simulation depends heavily on the physical models activated in ATLAS. These models describe the fundamental processes governing carrier transport, recombination, and light absorption:

- **Mobility Models:** The mobility of charge carriers is described as field-dependent by utilizing the Poole-Frenkel model (`pfmob`), which includes the effects of increased mobility at elevated electric fields frequent in thin layers of perovskite.
- **Recombination Models:** The model includes bulk recombination through SRH trap-assisted states as well as Langevin bimolecular recombination effects, both of which are key non-radiative and radiative loss mechanisms found in PSCs.
- **Field Effects:** Field-dependent transport is vital because the internal field in the perovskite affects charge separation and hysteresis effects. ATLAS incorporates these effects through the self-consistent solution of Poisson's equation.
- **Optical Generation (Light Absorption):** The `beam` command is used to simulate AM1.5G illumination in the solar spectrum (0.3–1.5 µm, 60 wavelength points per spectrum point) through transfer matrix formalism to allow for accurate generation of photogenerated charge which depends on the spectrum.
- **Physical Parameters (Exciton Dynamics):** Exciton dynamics are incorporated through `singlet` and `s.dissoc` parameters which describe the pathways of exciton creation and dissociation at the interfaces which is significant to hybrid organic–inorganic perovskites.

All of these models allow for a realistic description of PSC operation and allow to predict the EQE, J–V curves and transient behavior. However, the precision of these models is subject to the precision of input parameters presented and a description of previous input and model calibration have been reported in Silvaco [231].

Optical simulation

Optical simulation determines how incident sunlight is absorbed within each layer and converted into electron–hole pairs. This is critical in thin-film PSCs, where interference and reflection can significantly modify generation rates. The `beam` definition in ATLAS specifies an AM1.5G spectrum, normal incidence, and 60 discrete wavelengths between 300 nm and 1500 nm. This approach ensures realistic EQE and IQE predictions, consistent with transfer-matrix optical modeling used in literature [232, 233].

Solver settings

The solution of equations of semiconductors is solved using the Newton–Raphson method with automatic damping (`method newton autonr maxtrap=10 itlimit=50`). This will guarantee convergence even in the presence of strong non-linearities in perovskite systems from traps and field dependent effects. The simulation is initiated (`solve init`), biased under preset conditions (`solve vanode=$Vpreset`), and then forwards and reverse sweeps are performed to develop full J–V curves. The scanning speed can be controlled by `scan_time`, which allows for studying hysteresis, which is a well-documented issue in PSCs [231, 234].

Output and analysis

Simulation results are analyzed by extracting photovoltaic performance parameters such as J_{sc}, V_{oc}, FF, P_{max}, and PCE. These are plotted using TonyPlot and calculated using `extract` statements. Wavelength-resolved EQE/IQE spectra are also produced, allowing for direct comparison with experimental characterization. Validating device behavior and improving structure design require such thorough outputs [231–233].

3.3 Validation of the structure

3.3.1 Energy band diagram at equilibrium

The equilibrium energy band diagram (Figure 3.6) shows how the conduction and valence bands align across the different layers of the solar cell, providing a clear picture of the junctions formed at each interface.

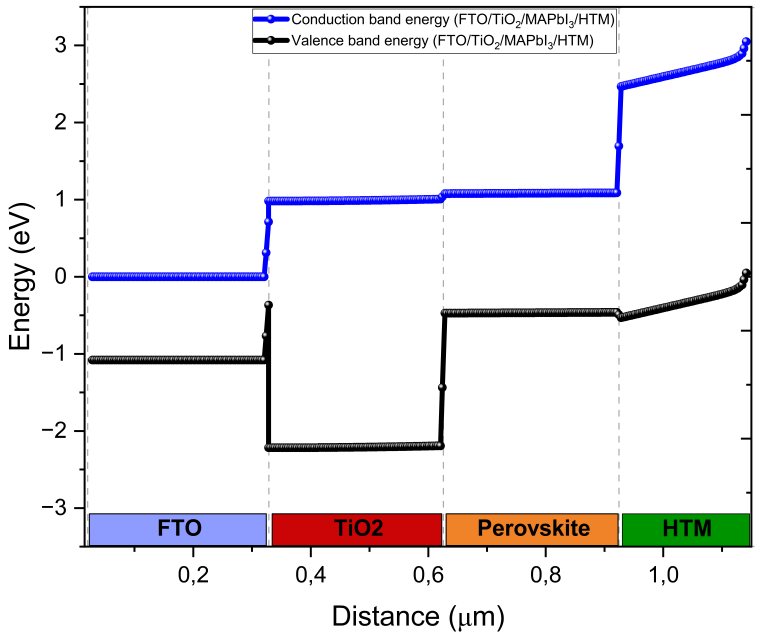


Figure 3.6: Energy band diagram of the FTO/TiO_2/$MAPbI_3$/HTM solar cell at equilibrium.

At this state, the Fermi level is flat, meaning the device is in balance with no external bias applied. The band offsets between layers define the built-in electric field, which is crucial for separating and directing electrons and holes toward their respective transport layers. A smooth alignment at the absorber/transport interfaces supports efficient charge extraction, while minimal barriers at the contacts help reduce recombination. Overall, the diagram confirms that the structure is well designed to support photovoltaic operation by ensuring favorable band alignment and proper carrier flow.

3.3.2 Device under forward bias

When the device is subjected to a forward bias (Figure 3.7), the equilibrium condition is disturbed and the Fermi levels in the different layers split, reducing the built-in electric field across the junction. This leads to a bending of both conduction and valence bands, as can be seen in the diagram. The applied voltage lowers the barrier at the perovskite/transport layer interfaces, facilitating the injection of carriers: electrons from the FTO/TiO_2 side into the perovskite conduction band and holes from the HTM into the perovskite valence band. This condition enhances recombination inside the absorber since carriers are no longer efficiently separated by the built-in field, which explains why forward bias reduces photovoltaic output. The diagram therefore illustrates how external bias directly impacts band alignment, carrier transport, and overall device performance.

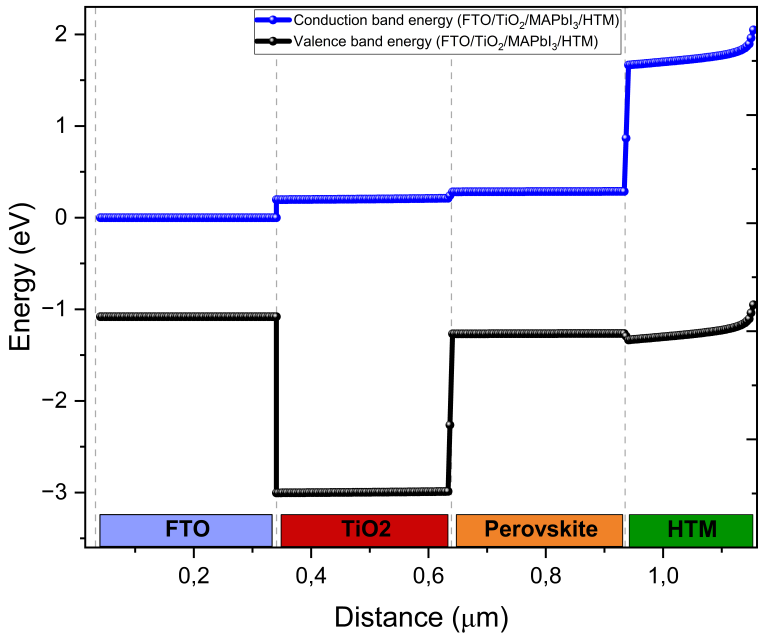


Figure 3.7: Energy band diagram of the FTO/TiO_2/$MAPbI_3$/HTM solar cell under forward bias.

3.3.3 Device under reverse bias

Under reverse bias, the external voltage reinforces the built-in electric field of the device, causing a stronger band bending across the heterojunctions. As shown in the Figure

3.8, the conduction and valence bands separate further at the interfaces, which increases the potential barrier for carrier injection from the contacts. This enhanced electric field significantly improves the drift-driven separation of photogenerated electron–hole pairs in the perovskite layer. Electrons are efficiently swept toward the TiO_2/FTO side, while holes are directed toward the HTM, thereby suppressing recombination losses. Although reverse bias does not contribute to power generation, it is useful for characterizing charge transport and confirming the robustness of carrier extraction pathways in the device.

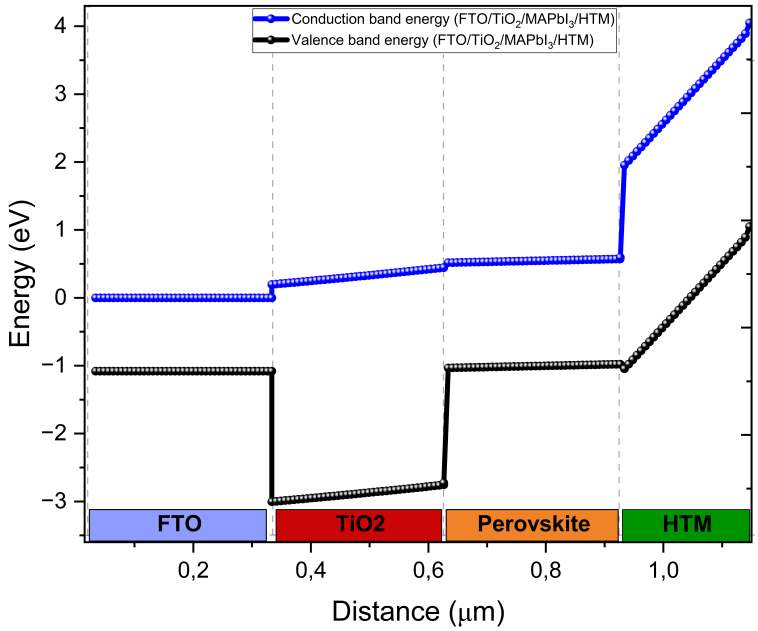


Figure 3.8: Energy band diagram of the FTO/TiO_2/$MAPbI_3$/HTM solar cell under reverse bias.

3.4 Perovskite single-junction cell structure

3.4.1 Methodology

The investigation of the perovskite solar cell based on the FTO/TiO_2/$MAPbI_3$/HTM structure was carried out in two complementary stages. First, an experimental device was fabricated and characterized in order to establish a reliable reference for the photovoltaic parameters of the structure. The current–voltage characteristics and other key performance indicators were measured under standard illumination conditions. In the second stage, the same device architecture was reproduced and simulated using the Silvaco Atlas TCAD platform, allowing a direct comparison between experimental results and numerical predictions. This validation step confirmed the accuracy of the simulation approach and provided confidence for further optimization. Building on this framework, a systematic study of the HTL was performed by replacing the reference HTL with alternative materials. The effect of these substitutions on the photovoltaic performance—such as J_{sc}, V_{oc}, fill factor, and efficiency—was analyzed in order to identify possible improvements and to gain deeper insight into the role of the HTL in perovskite solar cells [235].

3.4.2 Device fabrication

The FTO-TEC 15 substrate was first cleaned through a sequence of preparatory steps, including hot air flow washing, rinsing, and drying, followed by a 20-minute ultraviolet/ozone (UV/O_3) treatment. The deposition of the TiO_2 layer on the FTO substrate was then carried out using a stepwise procedure. A precursor solution was prepared by mixing 10 mL of isopropyl alcohol (ACS, Fermont), 0.6 mL of titanium(IV) isopropoxide (97 %, Sigma-Aldrich), and 0.2 mL of hydrochloric acid (36.5–38.0 %, J.T. Baker). This mixture was subjected to ultrasonic agitation for 30 minutes and then spin-coated onto the FTO substrate at 2000 rpm for 1 minute. The coated substrate was dried in air at 150 °C for 5 minutes and subsequently annealed at 450 °C for 30 minutes to achieve crystallization. The perovskite absorber layer ($CH_3NH_3PbI_3$) was deposited using a two-step method inside a nitrogen-controlled glove box. In the first step, a 1.0 M solution of PbI_2 in 1 mL of N,N-dimethylformamide (DMF) was stirred at 70 °C for 30 minutes and then spin-coated onto the TiO_2 layer at 6000 rpm for 40 seconds. The coated film was annealed at 70 °C for 1 hour to form a PbI_2 layer. In the second step, a 0.314 M solution of CH_3NH_3I in isopropanol was spin-coated at 4000 rpm for 10 seconds, followed by annealing at 140 °C for 30 minutes to complete the perovskite formation.

Finally, the HTM was deposited from a solution containing 60 mg of spiro-OMeTAD dissolved in 498 µL of chlorobenzene, to which 18 µL of 4-tert-butylpyridine and 10 µL of lithium bis(trifluoromethylsulfonyl)imide (50 mg mL^{-1} in acetonitrile) were added. This solution was spin-coated at 5000 rpm for 30 seconds. The HTM film was then left under ambient conditions for 12 hours to improve its conductivity (see Figure 3.9) [236].

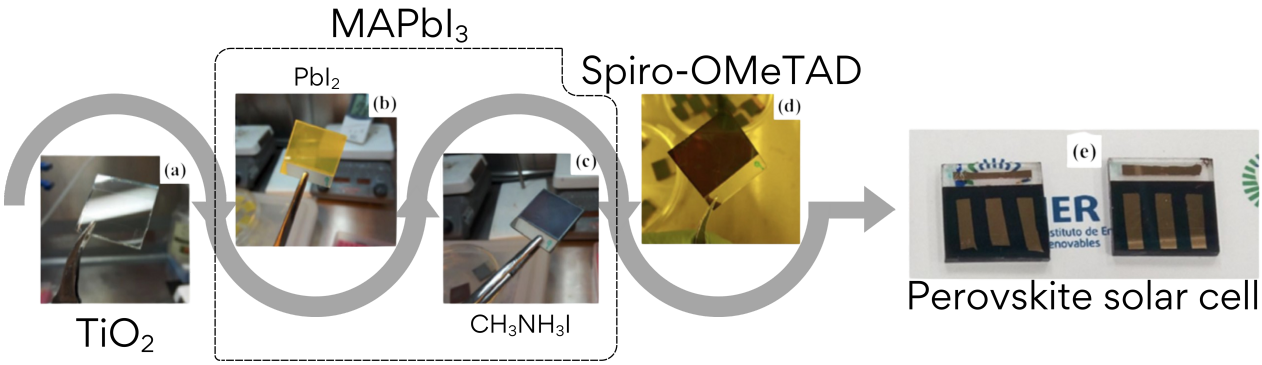


Figure 3.9: Experimental route for each layer of a perovskite solar cell development. Deposition of: (a) compact and mesoporous TiO_2, (b) PbI_2, (c) CH_3NH_3I (formation of perovskite film), (d) Spiro-OMeTAD and (e) final perovskite solar cell [236].

3.4.3 Device structure

Figure 3.10 illustrates the structure of a single-junction perovskite solar cell. The device is composed of four main layers: fluorine-doped tin oxide (FTO) serving as the transparent conductive electrode, titanium dioxide (TiO_2) acting as the electron transport layer, methylammonium lead iodide ($MAPbI_3$) functioning as the light-absorbing layer, and a hole transport material (Spiro-OMeTAD).

The thickness of each layer, except for the HTM, is set to 300 nm, while the HTM layer has a thickness of 213 nm [236].

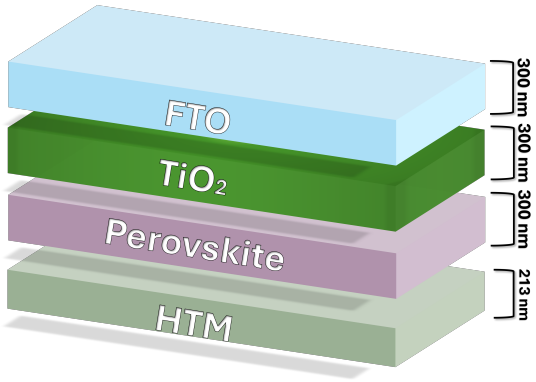


Figure 3.10: Cross-sectional schematic of a solar cell with the FTO/TiO_2/$MAPbI_3$/HTM configuration

The material parameters used in this study are listed in Table 3.1, including values for band gap, electron affinity, dielectric constant, carrier mobilities, and doping concentrations. These parameters serve as the input data for the simulation and performance analysis of the FTO/TiO_2/$MAPbI_3$/HTM solar cell.

Table 3.1: Parameters used for simulating the perovskite solar cell [236].

Parameters	FTO	TiO_2	Perovskite	HTM
Thickness (nm)	300	300	300	213
Band gap (eV)	3.5	3.2	1.5	3
Electron affinity (eV)	4.0	4.1	3.9	2.2
Dielectric permittivity (ε_r)	9	10	6.5	3
Electron mobility ($cm^2/(V\,s)$)	20	20	2	10^{-4}
Hole mobility ($cm^2/(V\,s)$)	10	10	2	10^{-4}
Donor density N_d (cm^{-3})	2×10^{19}	10^{15}	10^9	-
Acceptor density N_A (cm^{-3})	-	-	10^9	2×10^{19}

3.4.4 Device modeling

Modeling of the heterojunction perovskite solar cell was performed using the ATLAS Silvaco simulator [237]. The LUMINOUS module was employed to compute photogeneration through an optical ray-tracing algorithm, where the n determined reflection and transmission at each interface between adjacent layers [238]. The k was used to evaluate absorption and photon generation at each mesh point [157]. Recombination processes in the device included monomolecular, bimolecular, and trimolecular mechanisms, with the dominant pathway depending on the material properties [239]. Charge carrier mobility in the perovskite absorber was modeled using the Pool-Frenkel field model [240], while Langevin recombination was applied to describe carrier–carrier interactions [241].

Trap-assisted recombination was incorporated through the Shockley–Read–Hall model. To enhance simulation accuracy, a structured mesh with non-uniform spacing was used. The device architecture consisted of FTO as the transparent cathode, TiO_2 as the ETL, $MAPbI_3$ perovskite as the light-absorbing layer, and an HTM as the hole transport layer. Each layer was assigned a fixed thickness, with the number of grid points set to 40 for FTO, 40 for TiO_2, 40 for perovskite, and 30 for HTM. Electrical boundary conditions defined FTO as the cathode with a work function of 4.4 eV, while the back contact was modeled as the anode with a work function of 5.5 eV. Material models for TiO_2, perovskite, and HTM were incorporated to accurately describe charge transport, recombination dynamics, and optical behavior [242]. The optical simulation used the AM1.5 solar spectrum in the wavelength range of 300–1500 nm, with optical constants defined by n–k files specific to each material. Electrical simulations were performed through J–V sweeps in both reverse (1.2–−1 V) and forward (−1–1.2 V) directions at a scan rate of 10 mV/s. Hysteresis effects were analyzed by applying a preconditioning voltage of 0.2 V, followed by a backward scan (1.2–−1 V) and a forward scan (−1–1.2 V). Additionally, the EQE and IQE were calculated, with EQE defined as the ratio of collected current to incident photons. This methodology enabled a robust analysis of the single-junction perovskite solar cell, ensuring consistency between simulation outputs and experimental observations.

3.5 Results and discussion

3.5.1 Performance characterization

The J–V characteristics shown in the graph compare the simulated and experimental performance of the FTO/TiO_2/$MAPbI_3$/HTM perovskite solar cell [236]. Both curves follow a very similar behavior, which confirms that the proposed structure is functional and validates the reliability of our design.

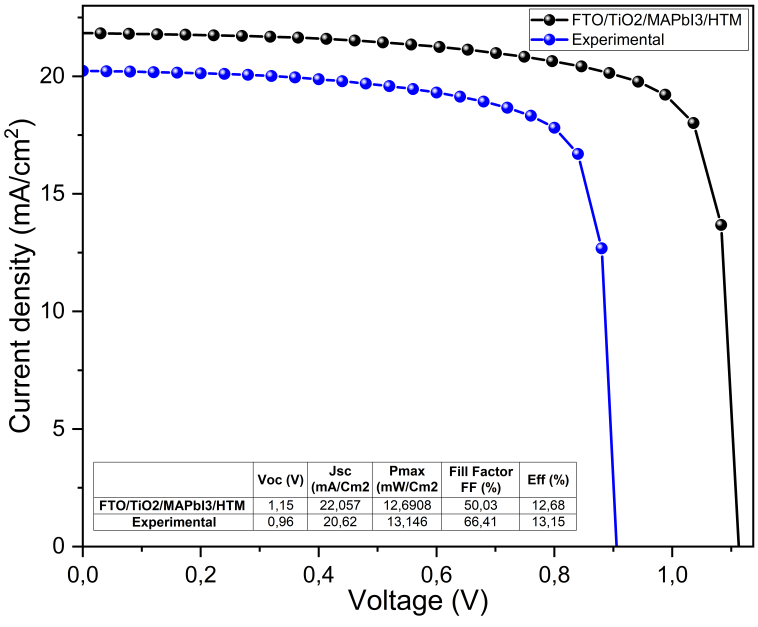


Figure 3.11: J–V characteristics of the FTO/TiO_2/$MAPbI_3$/HTM solar cell (simulated and experimental).

The simulated cell shows a slightly higher $J_{sc} \approx 22.06\,\mathrm{mA/cm^2}$ and $V_{oc} \approx 1.15\,\mathrm{V}$ compared to the experimental values $J_{sc} \approx 20.62\,\mathrm{mA/cm^2}$ and $V_{oc} \approx 0.96\,\mathrm{V}$, reflecting the idealized conditions assumed in the model. On the other hand, the fill factor is higher in the experiment, which compensates for the lower J_{sc} and V_{oc}, leading to an overall experimental efficiency of 13.15 %, very close to the simulated efficiency of 12.68 %. This close agreement between simulated and experimental data demonstrates that our structure not only works effectively in practice but also represents a valid and reliable platform for further optimization of perovskite solar cells.

3.5.2 EQE and IQE spectra of FTO/TiO_2/$MAPbI_3$/HTM single-junction solar sell

Figures 3.12A and 3.12B display the EQE and IQE spectra of the simulated single-junction perovskite solar cell with the structure FTO/TiO_2/$MAPbI_3$/HTM. In Figure 3.12A, the EQE response covers a wide spectral range between approximately 0.3 µm and 0.9 µm, with peak values above 50 %. This broad and relatively high response reflects the strong absorption capability of the $MAPbI_3$ layer in the visible region, allowing efficient conversion of incident photons into electron–hole pairs. The decline in EQE values near 0.9 µm corresponds to the absorption edge of the perovskite, indicating the bandgap limit of the active layer. The fluctuations observed within the visible spectrum are associated with variations in photon absorption and collection efficiency at specific wavelengths.

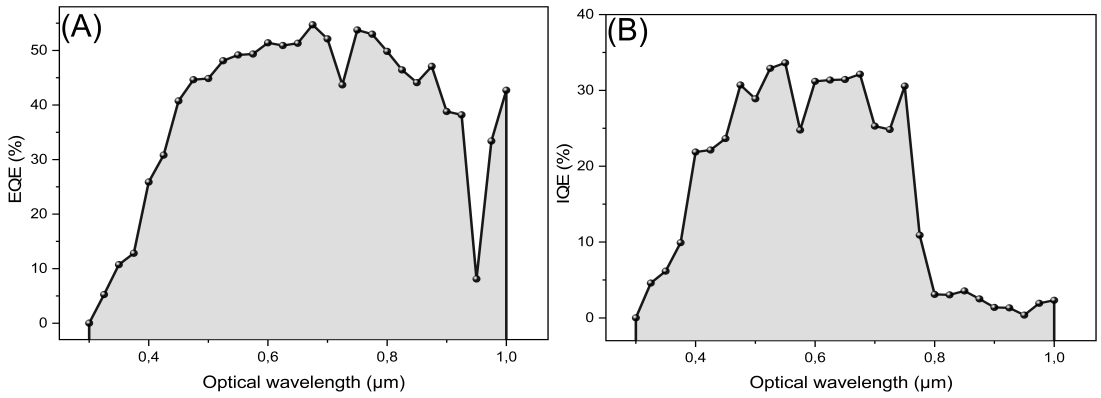


Figure 3.12: (A) EQE (B) IQE spectra of FTO/TiO_2/$MAPbI_3$/HTM solar cell.

In Figure 3.12B, the IQE spectrum exhibits peak values exceeding 30 % across the same optical range. This demonstrates that a significant fraction of the absorbed photons are successfully converted into collected charge carriers, confirming efficient charge generation and transport processes in the device. The relatively high IQE in the central visible region highlights the effectiveness of the TiO_2 electron transport layer and the HTM in facilitating carrier extraction. However, the observed decrease in IQE toward the longer wavelengths points to recombination losses and incomplete carrier collection near the absorption edge of $MAPbI_3$.

Together, the EQE and IQE results validate the good optoelectronic quality of the FTO/TiO_2/$MAPbI_3$/HTM solar cell. The high spectral response in the visible region confirms that this structure can efficiently harvest solar photons, while the reduction near

the band edge illustrates the intrinsic material limitations that constrain the performance at longer wavelengths.

3.5.3 Absorption and transmission spectra of FTO/TiO_2/$MAPbI_3$/HTM single-junction perovskite solar cell

The Figure 3.13 presents the absorption and transmission spectra of the single-junction perovskite solar cell with the architecture FTO/TiO_2/$MAPbI_3$/HTM as a function of the optical wavelength. The absorption spectrum (grey curve) shows strong values across the visible region, with peak absorption exceeding 0.8 A/W in the range between 0.35 µm and 0.55 µm. This behavior highlights the excellent light-harvesting capability of the $MAPbI_3$ perovskite layer, which is known for its high absorption coefficient in the visible range. The absorption remains relatively high and stable across much of the spectrum up to about 0.75 µm, after which it drops sharply as the photon energy approaches the bandgap threshold of $MAPbI_3$. This rapid decline beyond 0.8 µm reflects the intrinsic limitation of the perovskite material, as longer-wavelength photons possess insufficient energy to be absorbed and converted into charge carriers.

In contrast, the transmission spectrum (green curve) exhibits very low values in the visible region, confirming that most incident photons are effectively absorbed rather than transmitted. As the wavelength increases beyond 0.75 µm, the transmission rises significantly, reaching peak values near 1.0 µm. This is consistent with the reduction in absorption beyond the band edge, allowing longer-wavelength photons to pass through the device without contributing to photocurrent generation.

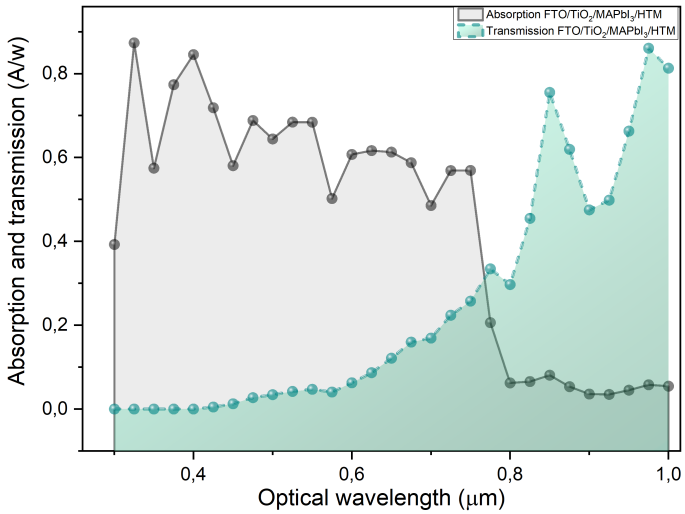


Figure 3.13: Absorption and transmission spectra of the FTO/TiO_2/$MAPbI_3$/HTM configuration.

Overall, the complementary behavior of the absorption and transmission spectra demonstrates the strong optical performance of the FTO/TiO_2/$MAPbI_3$/HTM device. The high absorption in the visible region ensures efficient photon harvesting, while the transmission at longer wavelengths underscores the spectral cutoff dictated by the perovskite bandgap. These results confirm the suitability of the device structure for visible-

light applications, while also illustrating the fundamental limitation of single-junction perovskite cells in capturing near-infrared photons.

3.5.4 Energy band alignment and carrier transport in FTO/TiO_2/$MAPbI_3$/HTM single-junction perovskite solar cell

The energy band diagram in Figure 3.14 illustrates the conduction band (blue) and valence band (black) profiles across the FTO/TiO_2/$MAPbI_3$/HTM device structure. Each interface plays a crucial role in ensuring efficient charge separation and transport. At the FTO/TiO_2 interface, the conduction band of TiO_2 lies slightly below that of the FTO, which provides a favorable energy offset that enables efficient injection of photogenerated electrons into the TiO_2 layer. This makes TiO_2 an effective ETL, as it selectively extracts and guides electrons toward the front electrode while blocking holes. Within the $MAPbI_3$ layer, the conduction band minimum and valence band maximum are positioned in such a way that both electrons and holes can be efficiently generated upon light absorption. The band alignment between TiO_2 and $MAPbI_3$ facilitates electron transfer from the perovskite conduction band into the TiO_2 layer, while the relatively large energy offset at the valence band suppresses hole back-transfer, thus reducing recombination losses at this interface.

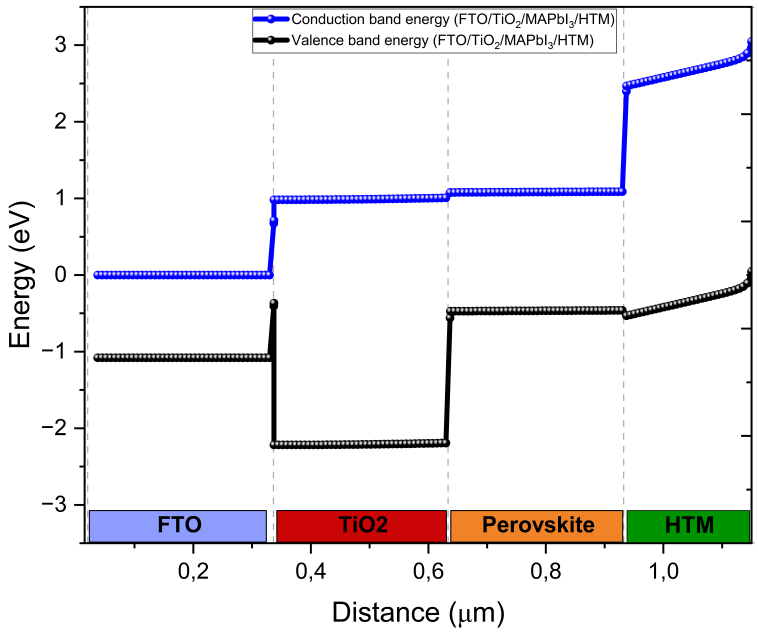


Figure 3.14: Energy band diagram of the FTO/TiO_2/$MAPbI_3$/HTM configuration.

On the other side, at the $MAPbI_3$/HTM interface, the valence band maximum of the HTM is aligned above that of the perovskite. This creates a driving force for hole extraction from the absorber into the HTM, while simultaneously blocking electrons due to the higher conduction band level of the HTM. This selective transport ensures that holes are efficiently collected at the back contact, complementing the electron extraction on the TiO_2 side. Overall, the gradual step-like alignment of conduction and valence bands across the layers provides a built-in potential that supports efficient charge carrier separation. Electrons flow from perovskite to TiO_2 and finally to the FTO contact, while

holes are driven toward the HTM and subsequently collected at the anode [243]. This well-defined band structure minimizes recombination, enhances carrier selectivity, and is key to the effective operation of the single-junction perovskite solar cell.

3.6 Impact of hole transport layer selection on device characteristics

In the baseline perovskite solar cell configuration (FTO/TiO_2/$MAPbI_3$/HTM), Spiro-OMeTAD is employed as the HTM and serves as a reliable reference, providing high PCE due to its favorable alignment with the perovskite absorber and effective hole extraction. To further investigate the potential of other HTLs and evaluate their impact on device behavior, we introduce three alternative materials into the same structure: NiO_x, CuSCN, and CuI.

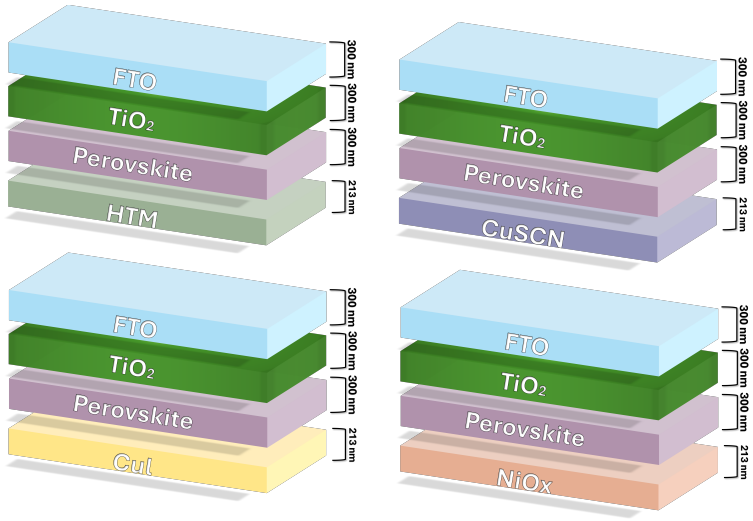


Figure 3.15: Cross-sectional diagram of FTO/TiO_2/$MAPbI_3$ solar cells with different HTLs

These inorganic HTLs have been widely studied for their stability, cost-effectiveness, and compatibility with perovskite absorbers. Each material offers distinct electronic properties, such as bandgap, carrier mobility, and doping concentration, which directly influence charge extraction and transport at the perovskite/HTL interface. For consistency, the device thickness is maintained at 213 nm for all HTLs. The parameters used in the simulation are summarized in Table 3.2.

By comparing these HTLs with Spiro-OMeTAD under identical conditions, the study aims to highlight the differences in energy level alignment, charge extraction efficiency, and photovoltaic performance. The next section will present and analyze the J–V characteristics and spectral responses (EQE/IQE) to identify the most effective HTL candidate.

Table 3.2: Input parameters of different HTLs used in the simulation.

Parameter	Spiro-OMeTAD	NiO_x	CuSCN	CuI
Thickness (nm)	213	213	213	213
Band gap (eV)	3.00	3.60	3.60	3.00
Electron affinity (eV)	2.20	2.00	2.20	2.50
Dielectric permittivity (ε_r)	3	11	8	7
Electron mobility ($cm^2/(V\,s)$)	1×10^{-4}	1×10^{-4}	1×10^{-5}	1.0
Hole mobility ($cm^2/(V\,s)$)	1×10^{-4}	1×10^{-4}	0.05	0.01
Acceptor density N_A (cm^{-3})	2×10^{19}	5×10^{17}	1×10^{9}	1×10^{18}

3.6.1 J–V characteristics of $FTO/TiO_2/MAPbI_3$ with different HTLs

The J–V characteristics of the $FTO/TiO_2/MAPbI_3$/HTM solar cell with different HTLs are shown in Figure 3.16. Four HTLs were considered in this study: Spiro-OMeTAD, CuI, CuSCN, and NiO_x. The comparison highlights the impact of the HTL on charge extraction, recombination dynamics, and overall device efficiency. These results reveal the crucial role of the HTL in balancing interfacial band alignment, carrier mobility, and recombination processes.

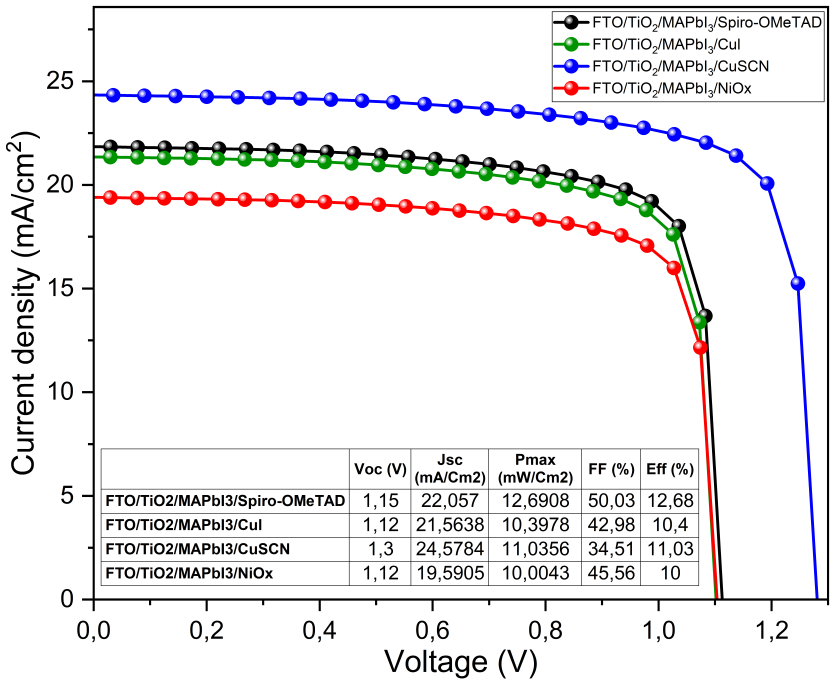


Figure 3.16: J–V characteristics of $FTO/TiO_2/MAPbI_3$ solar cells employing different HTLs (Spiro-OMeTAD, CuI, CuSCN, and NiO_x).

Spiro-OMeTAD was used as the reference HTL and delivered the best overall efficiency of 12.68 %. This performance results from a balanced combination of V_{oc} (1.15 V), J_{sc} (22.06 mA/cm^2), and a relatively high FF (50.03 %). The superior fill factor indicates

efficient charge transport and low resistive losses within the HTM and at its interface with the perovskite absorber. Although Spiro does not yield the highest J_{sc} or V_{oc} among the studied materials, its stability in maintaining efficient extraction with minimal losses allows it to achieve the highest PCE. This demonstrates that the success of Spiro lies not in maximizing individual parameters but in providing a well-balanced device operation with reduced recombination and sufficient conductivity.

The CuSCN-based device exhibited the highest V_{oc} (1.30 V) and the highest J_{sc} (24.58 mA/cm^2), clearly indicating excellent interfacial alignment between the perovskite valence band and the CuSCN layer, which favors hole extraction and reduces recombination under open-circuit and short-circuit conditions. However, despite these favorable characteristics, the fill factor was significantly reduced to 34.52 %, leading to an overall efficiency of 11.03 %. The low FF suggests severe transport limitations caused by high series resistance and/or poor interfacial contact between CuSCN and the back electrode. This behavior indicates that while CuSCN is capable of extracting photogenerated carriers effectively, its bulk conductivity and interfacial transport properties under operating conditions limit the usable output power. Optimization of doping density, conductivity, and interfacial engineering could therefore unlock its high V_{oc}–J_{sc} potential and surpass Spiro in performance.

CuI presented moderate performance, with a V_{oc} of 1.12 V and a J_{sc} of 21.56 mA/cm^2, accompanied by a reduced fill factor of 42.99 %. The resulting efficiency was 10.40 %. Compared to Spiro, the lower J_{sc} and FF suggest that hole extraction is less efficient, likely due to increased interfacial recombination and sub-optimal valence band alignment between CuI and the perovskite. This increases carrier losses during transport and reduces the slope of the J–V curve near the maximum power point. While CuI provides a stable structure and has the potential for cost-effectiveness compared to organic HTLs, its performance here indicates that further optimization is required to minimize recombination pathways and improve conductivity.

NiO_x showed the lowest performance among the tested HTLs, with a V_{oc} of 1.12 V, a J_{sc} of only 19.59 mA/cm^2, and a moderate FF of 45.57 %, resulting in an efficiency of 10.00 %. The significantly reduced J_{sc} highlights poor carrier collection efficiency at the perovskite/NiO_x interface. This could be attributed to either unfavorable band alignment, insufficient hole mobility, or a high density of interface traps that act as recombination centers. Although NiO_x is attractive as an inorganic HTL due to its stability and low cost, the present results indicate that without surface treatments or interfacial passivation layers, its use leads to substantial recombination losses and underutilization of the photogenerated carriers.

Overall, the comparative study reveals that Spiro-OMeTAD remains the most effective HTL for this single-junction FTO/TiO_2/$MAPbI_3$ device configuration due to its balanced transport and minimal resistive losses. However, the results for CuSCN are particularly promising, as the combination of very high V_{oc} and J_{sc} indicates that, if transport bottlenecks can be resolved, it has the potential to outperform Spiro. Both CuI and NiO_x demonstrate acceptable but limited performance, with efficiency losses primarily due to interfacial recombination and lower carrier collection. This comparative analysis highlights the importance of HTL optimization in perovskite solar cells, not only in terms of energy level alignment but also in conductivity, doping, and interfacial quality.

3.6.2 EQE and IQE of FTO/TiO_2/$MAPbI_3$ with different HTLs

The EQE, represented by the blue line in Figure 3.17, remains relatively constant across all HTLs, indicating that the external photon-to-electron conversion efficiency is nearly identical regardless of the HTL material. This suggests that the external processes of charge collection at the electrode interface are unaffected by the choice of HTL, with all materials facilitating similar extraction of photogenerated carriers.

The consistency in EQE signifies that the photon extraction efficiency and charge collection at the electrode are not the limiting factors for device performance across the HTLs, highlighting that the external architecture of the devices operates comparably, independent of the HTL material.

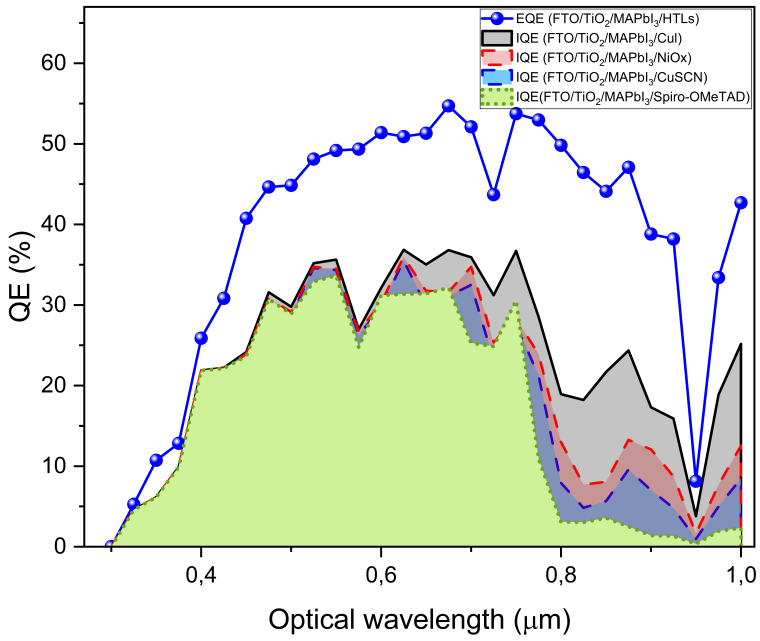


Figure 3.17: EQE and IQE of FTO/TiO_2/$MAPbI_3$ solar cells with HTLs.

Conversely, the IQE data reveals significant variations among the different HTLs, underscoring their impact on the internal charge generation, transport, and recombination processes within the device. For Spiro-OMeTAD (green dashed line), the IQE is notably lower compared to the other HTLs, particularly at longer wavelengths. This indicates that, while Spiro-OMeTAD may be efficient in extracting charges at the external interface, it exhibits less favorable internal charge generation and transport characteristics. Specifically, the lower IQE suggests that the Spiro-OMeTAD layer may experience higher carrier recombination or suboptimal hole extraction, despite the device demonstrating comparable external performance as the other materials.

In contrast, CuSCN (blue dashed line) and CuI (black line) exhibit higher IQE values, particularly at longer wavelengths, which suggests these materials are more efficient at facilitating internal charge generation and transport. This enhanced internal efficiency likely arises from their superior charge mobility and energy alignment with the perovskite layer, leading to reduced recombination losses and more effective hole extraction. NiOx (red dashed line), while demonstrating intermediate IQE performance, still exhibits higher internal efficiency compared to Spiro-OMeTAD, though not as high as CuI and CuSCN.

This suggests that NiOx provides a moderate improvement in internal charge dynamics but does not reach the performance levels of CuI and CuSCN.

While the EQE remains unaffected by the choice of HTL, the variability in IQE emphasizes the crucial role that the HTL material plays in influencing the internal charge dynamics of the device. Specifically, the differing IQE profiles reflect the interplay of material properties such as energy level alignment, charge transport characteristics, and recombination rates, all of which significantly impact the device's internal efficiency. The enhanced internal performance of CuI and CuSCN underscores their potential in optimizing charge carrier dynamics, which are critical to achieving higher overall efficiency in perovskite solar cells.

In summary, the observed consistency in EQE across all HTLs indicates that external carrier collection processes are not the limiting factor in device performance. However, the substantial variation in IQE between the HTLs highlights the significant role of internal charge generation and transport processes in determining overall device efficiency. The different IQE trends underscore the need for careful selection of HTL materials to optimize internal charge dynamics and minimize recombination losses, thereby enhancing the performance of perovskite solar cells.

3.7 Tandem perovskite/silicon solar cell study

This study investigates the performance of a tandem solar cell structure combining a perovskite top cell (FTO/TiO_2/$MAPbI_3$/HTM) with a silicon bottom cell. By adding an intermediate layer between the two cells, we aim to optimize efficiency through enhanced charge transfer. The following section outlines the methodology used to evaluate this tandem configuration, focusing on its overall performance and key design considerations.

3.7.1 Methodology

In the previous part, a single-junction perovskite solar cell was simulated using the FTO/TiO_2/$MAPbI_3$/HTM configuration, where all material properties, including electronic and optical characteristics, were accurately defined to closely match real material behaviors. The physical models used in this simulation were maintained unchanged in the current study. Building on this, a tandem architecture was developed to enhance power conversion efficiency and optimize the configuration. This new design incorporated a three-layer silicon structure—comprising n−Si, i−Si, and p−Si layers—beneath the perovskite absorber. A 3 nm FTO layer was inserted between the single-junction cell and the silicon layers to ensure proper electrical contact. The silicon material properties were optimized by adjusting doping levels to improve charge transport and performance [235].

The characteristics of the tandem structure are then discussed, focusing on efficiency gains and overall improvements compared to the single-junction cell.

3.7.2 Simulation details

The tandem solar cell improves upon the initial single-junction configuration by incorporating a 3 nm thick FTO layer and a silicon-based subcell. This subcell consists of three distinct crystalline silicon layers: an *n*-type silicon layer (n−Si), an intrinsic silicon layer (i−Si), and a *p*-type silicon layer (p−Si). The respective thicknesses of these layers are 10 nm, 15 nm and 10 nm. To optimize charge transport efficiency, the n−Si and p−Si layers are doped, while the i−Si layer remains undoped.

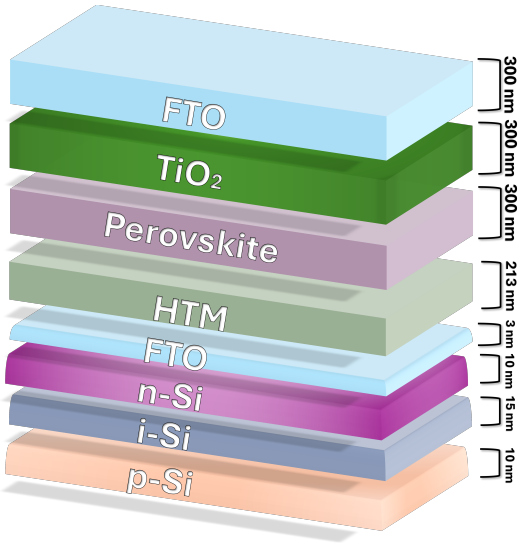


Figure 3.18: A cross-sectional schematic of the tandem solar cell.

The parameters defining the silicon layers and the tandem structure are provided in Table 3.3. The design of the tandem cell aims to leverage the synergy between the light absorption and high photogenerated efficiency of both perovskite and silicon materials, offering enhanced PCE compared to a single-junction device [235, 244].

Table 3.3: Parameters of silicon layers in the tandem solar cell structure.

Parameters	**n−Si**	**i−Si**	**p−Si**
Thickness (nm)	10	15	10
Band gap (eV)	1.12	1.12	1.12
Electron affinity (eV)	4.05	4.05	4.05
Dielectric permittivity (ε_r)	11.9	11.9	11.9
Electron mobility ($cm^2/(V\,s)$)	1350	1350	1350
Hole mobility ($cm^2/(V\,s)$)	450	450	450
Donor density N_D ($1/cm^3$)	1×10^{19}	-	-
Acceptor density N_A ($1/cm^3$)	-	-	6×10^{18}

Optimizing the thickness and doping profiles of the silicon layers is essential for improving efficiency, charge transport, and minimizing recombination losses in tandem solar

cells. Studies have demonstrated that a 15 nm thick i−Si layer strikes the optimal balance between light absorption and charge collection, as thinner layers result in poor absorption, while thicker layers increase recombination losses [245]. Both the n-type and p-type silicon layers, typically 10 nm thick, are heavily doped to generate a strong electric field, thereby enhancing charge separation and transport [246]. Research on GaAs/Si tandem cells indicates that an emitter doping concentration of approximately $5\times10^{18}1/\mathrm{cm}^3$ optimizes carrier injection efficiency, further supported by findings suggesting that controlled dopant diffusion in silicon improves photovoltaic performance [247]. These optimizations are key to achieving high short-circuit current density and PCE, making them crucial for the advancement of next-generation tandem solar cells.

Design consideration and structural choice

The 3 nm FTO interlayer was selected for its high optical transparency (>80 %), low sheet resistance (10–15 Ω/sq), and excellent thermal stability (600 °C), making it superior to alternatives such as ZnO, SnO_2, and MoO_3 in terms of charge transport and compatibility with TiO_2. This enhances carrier extraction and reduces recombination [248]. In comparison to ITO, FTO offers better thermal stability and preserves structural integrity at higher temperatures, making it more suitable for tandem architectures [249]. The 3 nm thickness provides sufficient conductivity without significant optical losses, effectively balancing transparency and charge transport efficiency. Although FTO's surface roughness may affect the quality of the layer, the tandem structure design includes interface optimization to minimize defects and enhance charge extraction [250]. The n-i-p structure was chosen for the silicon subcell because it more effectively facilitates charge separation, reduces recombination losses, and improves charge transport properties. This structure comprises a 10 nm n-type layer, a 15 nm intrinsic silicon layer, and a 10 nm p-type layer, collectively forming a strong built-in electric field for efficient carrier collection [251]. In contrast to the p-i-n structure, which suffers from increased recombination at the perovskite-silicon interface, the n-i-p structure offers better band alignment and overall efficiency [252]. Moreover, the thickness of the i−Si layer was optimized within a range of 5–25 nm, with 15 nm found to be the optimal balance between light absorption and charge transport, thus enhancing the overall efficiency of the tandem solar cell [253].

Models

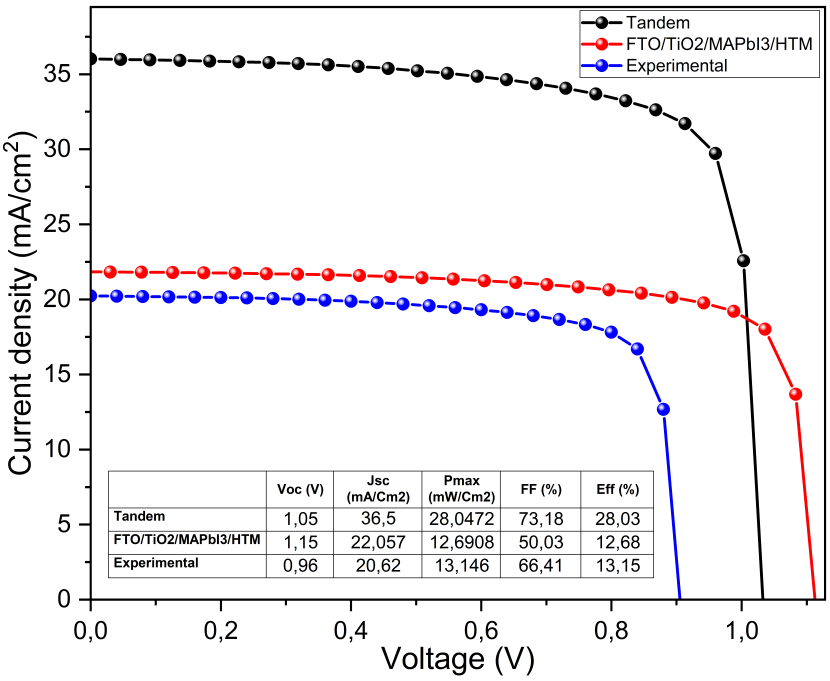
Modeling of the tandem heterojunction perovskite solar cell was conducted using the same ATLAS Silvaco simulator and parameters as the single-junction device. The simulation for the tandem configuration included the addition of a silicon-based subcell, consisting of an n−Si, i−Si, and p−Si structure. The optical ray-tracing algorithm within the LUMINOUS module was retained to compute photogeneration, with the refractive index (n) and extinction coefficient (k) used for reflection, transmission, absorption, and photon generation at each layer interface, as in the single-junction model [157, 238]. The same recombination mechanisms, including monomolecular, bimolecular, and trimolecular processes, were applied, with their dominance determined by material properties [239]. Charge carrier mobility and recombination in the perovskite absorber layer continued to

be modeled using the Poole–Frenkel field model and Langevin recombination, respectively [240, 241], while trap-assisted recombination was incorporated via the SRH model. The simulations for the silicon subcell remained based on the drift–diffusion model, using doping profiles for the n−Si and p−Si layers, with the i−Si layer undoped [254]. A structured mesh with non-uniform spacing was again used to enhance simulation accuracy. The device architecture for the tandem solar cell includes the FTO as the cathode, TiO_2 as the ETL, $MAPbI_3$ perovskite as the absorber layer, HTM as the hole transport layer, and silicon layers as the bottom subcell. The same material models and boundary conditions used in the single-junction simulation were retained for consistency. The optical simulation continued to use the AM1.5 solar spectrum, and electrical simulations were performed with J–V sweeps, hysteresis analysis, and the calculation of EQE and IQE, just as in the single-junction case. This methodology provided a comprehensive and consistent framework for analyzing the performance of the tandem solar cell.

3.8 Results and discussion

3.8.1 J–V characteristics of FTO/TiO_2/$MAPbI_3$/HTM and tandem solar cells

Figure 3.19 illustrates the J–V characteristics of the tandem solar cell compared to the single-junction cell, with the simulated results shown in red and the experimental results in blue.



	Voc (V)	Jsc (mA/Cm2)	Pmax (mW/Cm2)	FF (%)	Eff (%)
Tandem	1,05	36,5	28,0472	73,18	28,03
FTO/TiO2/MAPbI3/HTM	1,15	22,057	12,6908	50,03	12,68
Experimental	0,96	20,62	13,146	66,41	13,15

Figure 3.19: J–V characteristics of tandem and single-junction solar cells (simulated and experimental).

The tandem cell significantly outperforms the single-junction cell, achieving an efficiency of 28.03 % and a current density of 36.5 mA/cm^2. In contrast, the single-junction

cell reaches 12.68 % efficiency in simulation and 13.15 % in the experiment [**16**], with corresponding J_{sc} values of 22.057 mA/cm^2 and 20.62 mA/cm^2, respectively. These results demonstrate the clear efficiency and current density advantages of the tandem structure, attributed to its superior utilization of the solar spectrum compared to single-junction devices [243].

3.8.2 IQE and EQE analysis

Figures 3.20A and 3.20B present the IQE and EQE spectra for both the tandem solar cell and the simulated single-junction FTO/TiO_2/$MAPbI_3$/HTM cell. The results clearly demonstrate that the tandem solar cell achieves superior performance across both IQE and EQE, particularly in the wavelength range of 0.4–0.8 µm.

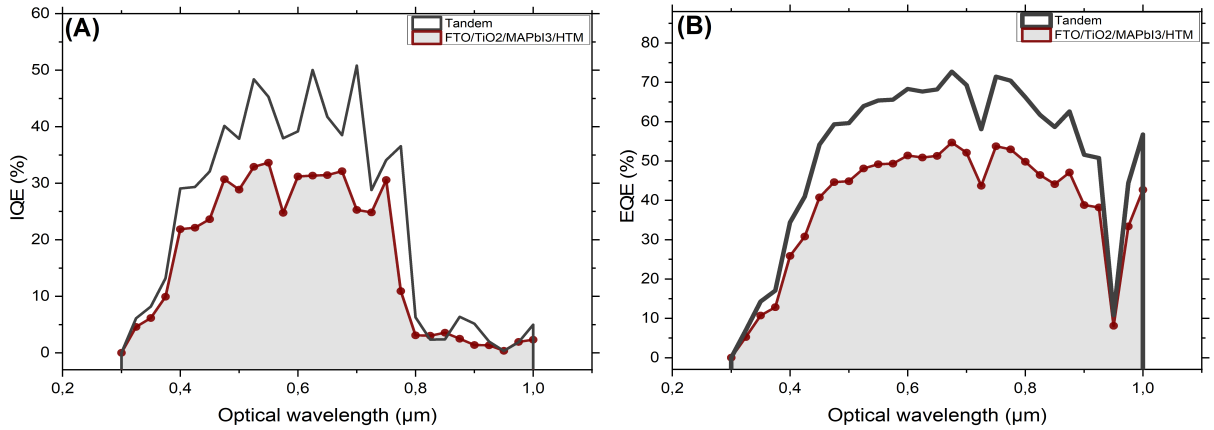


Figure 3.20: (A) IQE, (B) EQE spectra of tandem and FTO/TiO_2/$MAPbI_3$/HTM solar cells.

In Figure 3.20A, the tandem solar cell reaches a peak IQE of 50.81 %, which is significantly higher than the 33 % observed for the single-junction cell. This notable increase in IQE suggests that the tandem structure is more efficient in converting absorbed photons into charge carriers. The tandem configuration benefits from the combined action of the perovskite top cell and the silicon bottom cell, each optimized to absorb and convert light over different parts of the spectrum. While the perovskite top cell captures photons in the visible range, the silicon bottom cell efficiently absorbs light in the infrared region, allowing for more effective carrier generation across a broader spectrum. The higher IQE in the tandem cell reflects improved internal charge generation and transport, with less recombination, especially in the longer-wavelength regions that the single-junction cell cannot effectively capture.

In Figure 3.20B, the tandem cell achieves an EQE of 73 %, compared to around 55 % for the single-junction cell. This difference is particularly striking in the red and near-infrared regions of the spectrum. The higher EQE in the tandem configuration is indicative of the superior ability of the tandem cell to extract photogenerated charge carriers at the electrode interface. The tandem cell's ability to maintain higher EQE values across a wider range of wavelengths suggests it is more efficient at converting photons into useful current. The perovskite top cell in the tandem structure absorbs photons in the visible

range and contributes significantly to the total EQE, while the silicon bottom cell captures photons in the near-infrared, which the perovskite alone would not absorb. This extended spectral coverage enables the tandem solar cell to outperform the single-junction device, which is limited to absorbing a narrower portion of the solar spectrum.

The key reason for the higher IQE and EQE of the tandem cell lies in its ability to exploit a broader range of the solar spectrum. The perovskite layer in the top cell efficiently absorbs visible light, while the silicon layer in the bottom subcell absorbs near-infrared light. The combination of these two materials, with their complementary absorption spectra, allows the tandem cell to utilize more of the incident light, thus achieving higher quantum efficiencies. The interface optimization between the perovskite and silicon layers, facilitated by the thin intermediate layer, also ensures minimal recombination losses and maximizes the extraction of charge carriers. This results in the tandem cell having both higher IQE (indicating better charge generation and transport) and higher EQE (indicating more efficient conversion of photons to electrical current) than the single-junction cell, which is limited in its ability to absorb and convert photons outside the visible range.

Thus, the tandem structure demonstrates a clear advantage in exploiting a larger portion of the solar spectrum, increasing its overall efficiency in both charge generation and extraction, leading to superior IQE and EQE compared to the single-junction device.

3.8.3 Optical absorption and transmission properties

Figure 3.21 compares the absorption and transmission spectra of the FTO/TiO_2/$MAPbI_3$/HTM single-junction device and the tandem configuration as functions of optical wavelength. The results reveal clear differences in light–matter interaction between the two structures.

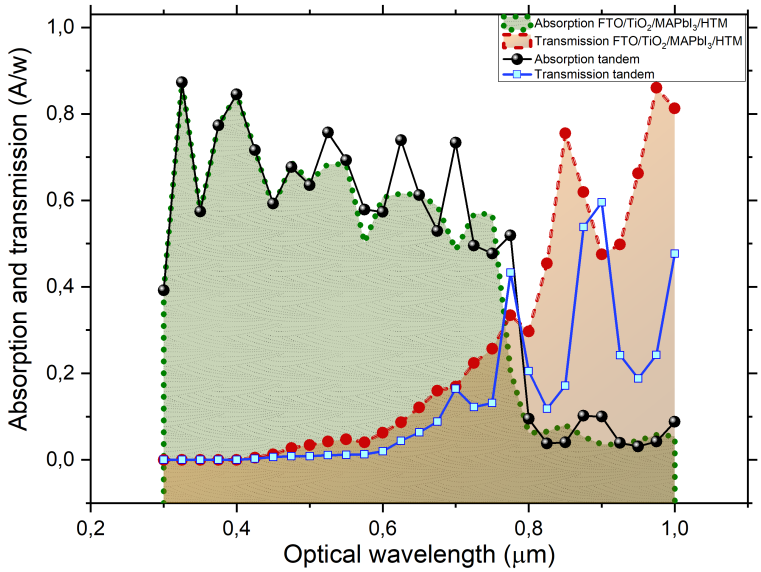


Figure 3.21: Absorption and transmission spectra of the tandem solar cell compared to the FTO/TiO_2/$MAPbI_3$/HTM configuration.

In the wavelength range of 0.3 µm to 0.8 µm, the tandem device shows a markedly higher absorption (black line) than the single-junction perovskite device (green dotted line). This indicates that the tandem structure captures a larger fraction of incident

photons across the visible and near-infrared spectrum, thereby increasing the potential for photogeneration. For example, absorption values in the tandem reach up to approximately 0.9 A/W around 0.45–0.55 µm, whereas the single-junction device remains notably lower. At the same time, the transmission behavior is inversely related. The tandem device (blue line with open squares) exhibits lower transmission compared to the single-junction cell (red dashed line) within the same region, reflecting reduced photon losses. This means that fewer photons pass through the device without being absorbed, highlighting the tandem's superior photon-harvesting capability. Beyond 0.8 µm, both devices exhibit reduced absorption and increasing transmission, which is expected because of the lower energy of near-infrared photons. In this region, the tandem cell still retains slightly better absorption performance than the single-junction, but the overall trend reflects the physical limitation of photon energy relative to the bandgap.

Taken together, the tandem structure demonstrates significantly improved absorption efficiency and reduced transmission losses compared to the FTO/TiO_2/$MAPbI_3$/HTM device. This enhanced spectral utilization confirms the tandem's ability to exploit a broader portion of the solar spectrum, laying the foundation for improved current generation and ultimately higher power conversion efficiency.

3.8.4 Energy band alignment and carrier transport pathways

Figure 3.22 presents the energy band diagram for two different solar cell configurations: the standard perovskite device (FTO/TiO_2/$MAPbI_3$/HTM) and the tandem structure, which includes a silicon bottom cell.

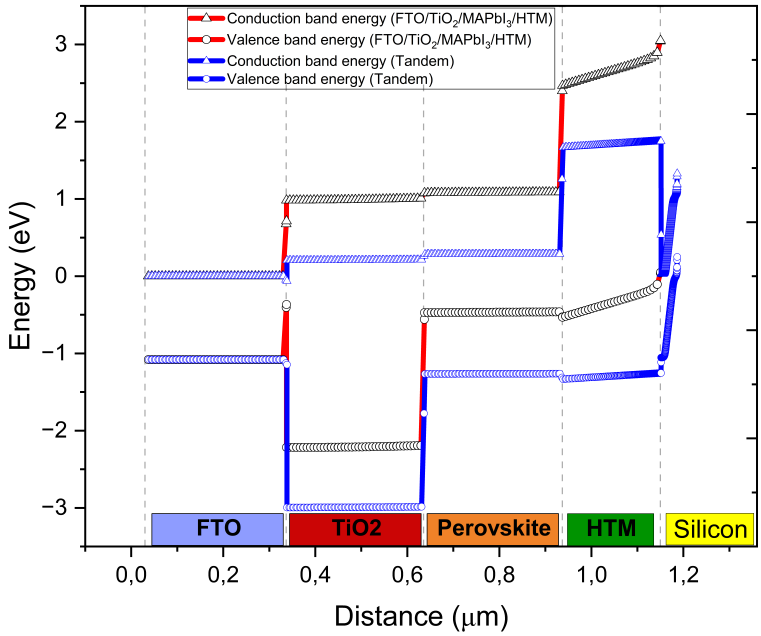


Figure 3.22: Energy band diagram of the tandem solar cell and FTO/TiO_2/$MAPbI_3$/HTM configuration.

In the standard configuration, the conduction and valence bands are aligned gradually across the layers, allowing for efficient charge separation and transport. Specifically, electrons are transferred from the perovskite to the TiO_2 conduction band, where the energy

offset ($\approx 0.3\,\text{eV}$) facilitates electron injection into the TiO_2 layer, while holes are directed from the perovskite to the HTM valence band, ensuring efficient hole collection at the top electrode. This smooth alignment between the layers ensures minimal recombination and effective charge transport within the single-junction perovskite solar cell.

In contrast, the tandem configuration introduces a silicon subcell, which extends the energy band alignment across a broader range, enabling the device to efficiently capture low-energy photons in the infrared spectrum. The addition of silicon enhances the solar cell's overall spectral response, especially in the wavelength range beyond 800 nm, which the perovskite alone cannot efficiently absorb. The conduction band of silicon is aligned with the perovskite conduction band with a relatively small offset ($\approx 0.1\,\text{eV}$), allowing for smooth electron transfer between the two materials, while the valence band alignment of silicon and perovskite is optimized to minimize carrier recombination at the interface. This smooth transition ensures efficient hole transport from the perovskite to the silicon layer. The 3 nm thick FTO interlayer placed between the perovskite and silicon layers plays a critical role in facilitating this seamless band alignment. It serves as a buffer layer, ensuring minimal recombination losses and promoting smooth charge carrier transport across the interface. This layer effectively reduces the potential for energy barriers that could hinder carrier flow, particularly at the perovskite/silicon interface.

Overall, the tandem configuration not only provides a broader spectral absorption range but also enhances charge carrier extraction and transport efficiency due to the well-aligned conduction and valence bands. This improved alignment minimizes recombination losses and ensures more efficient utilization of the absorbed photons, leading to higher overall PCE. By extending the absorption into the infrared spectrum and optimizing the band alignment between the perovskite and silicon subcells, the tandem structure achieves superior performance compared to the standard single-junction perovskite solar cell [80].

3.9 Comprehensive study of tandem solar cell performance: investigating the effects of temperature and intrinsic silicon thickness

3.9.1 Effect of intrinsic silicon thickness on tandem cell efficiency

To investigate the impact of i−Si layer thickness on the performance of the tandem solar cell, we systematically vary the thickness of the i−Si layer. This study aims to observe how changes in i−Si thickness influence key performance parameters such as J_{sc} and P_{max}, and to determine the optimal thickness for achieving the best efficiency in the tandem structure. By examining configurations with different i−Si thicknesses, we can better understand the trade-offs between optical absorption, carrier transport, and recombination losses in the tandem solar cell.

J–V characteristics of tandem solar cells with varying intrinsic silicon thickness

The J–V curve shown in Figure 3.23 illustrates the effect of different i−Si layer thicknesses on the performance of a tandem solar cell. The figure compares the current density as a function of applied voltage for various configurations of the i−Si layer thickness: 5 nm, 10 nm, 15 nm, and 25 nm.

From the curve, it is evident that the performance of the tandem device is highly sensitive to the thickness of the i−Si layer. The 15 nm i−Si layer configuration, represented by the black circles, achieves the highest current density and performs optimally, balancing both light absorption and charge transport efficiency. This thickness strikes an ideal compromise, ensuring that the device efficiently absorbs light without incurring significant recombination losses.

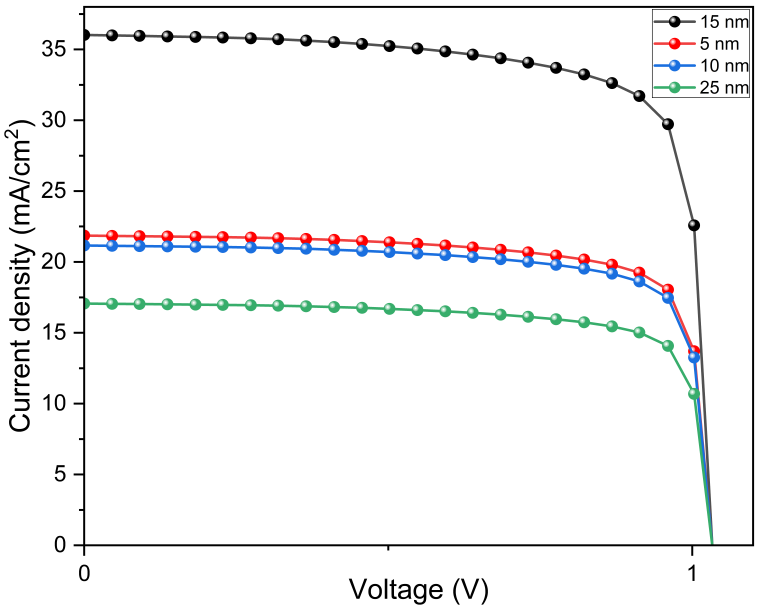


Figure 3.23: J–V characteristics of the tandem solar cell for different intrinsic silicon layer thicknesses.

In contrast, thinner i−Si layers (5 nm and 10 nm, represented by red and blue circles, respectively) result in lower current densities, which can be attributed to poor optical absorption. These thinner layers fail to capture sufficient infrared photons, leading to a reduction in the photocurrent generated by the cell. On the other hand, the 25 nm i−Si layer (green circles) shows a decrease in performance as well, though for a different reason. The increased thickness of the i−Si layer leads to higher recombination rates within the silicon subcell, thus reducing the overall current density.

Overall, the 15 nm i−Si layer configuration in the tandem solar cell provides the best trade-off between enhanced light absorption and minimized recombination, thereby achieving the highest current density and optimal performance. These results indicate that 15 nm is the optimal thickness for the i−Si layer in this tandem structure, maximizing the efficiency of the tandem solar cell.

Effect of intrinsic silicon layer thickness on J_{sc} and P_{max} in tandem solar cells

The results shown in Figure 3.24 demonstrate the nonlinear dependence of the tandem solar cell's performance on the thickness of the i−Si layer. As observed, the J_{sc} and P_{max} exhibit distinct trends as the i−Si layer thickness varies.

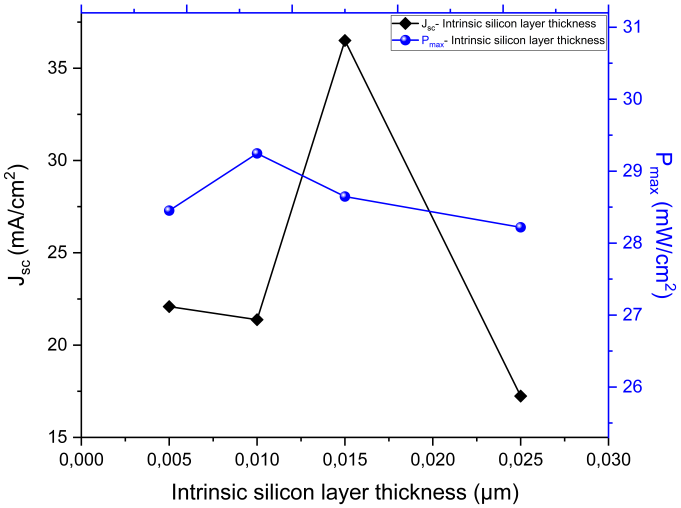


Figure 3.24: Effect of intrinsic silicon layer thickness on short-circuit current density and maximum power in tandem solar cell configuration.

At 15 nm, the tandem solar cell reaches an optimal Pmax of 28.0472 mW/cm^2, which represents the best balance between charge collection and transport efficiency. This thickness is identified as the reference configuration for our tandem cell design, due to its superior performance in terms of both current density and power output. As seen in the graph, increasing the i−Si thickness beyond 15 nm results in a decrease in performance. This indicates that fine-tuning the thickness of the i−Si layer is crucial to maintaining optimal tandem cell performance. The sharp increase in J_{sc} observed at 15 nm corresponds to the point where the intrinsic silicon layer reaches an ideal thickness, optimizing charge collection efficiency. At lower i−Si thicknesses (5 nm and 10 nm), recombination losses dominate, limiting the photocurrent and resulting in lower J_{sc} values. As the i−Si thickness increases to 15 nm, the built-in electric field enhances the drift of charge carriers, leading to a significant increase in J_{sc}. However, beyond this optimal thickness (e.g., 25 nm), the performance starts to degrade due to increased recombination and carrier mobility issues within the silicon layer.

This behavior underscores the importance of precise tuning of the i−Si layer thickness in the tandem solar cell configuration. The ability to balance light absorption and charge transport while minimizing recombination losses is key to optimizing the efficiency of tandem devices.

3.9.2 Temperature dependence of tandem solar cell performance

To further assess the operational stability of the tandem solar cell, we investigate the effect of varying the operating temperature on its performance. Since temperature strongly

influences carrier transport, recombination dynamics, and material properties, this analysis helps to determine how thermal fluctuations impact key performance parameters such as J_{sc} and P_{max}.

J–V characteristics of tandem solar cells at different operating temperatures

The J–V curve shown in Figure 3.25 illustrates the effect of temperature variation on the performance of the tandem solar cell. The simulation was conducted at various temperatures: 10 °C, 25 °C, 35 °C, 45 °C and 55 °C, with 25 °C used as the reference temperature.

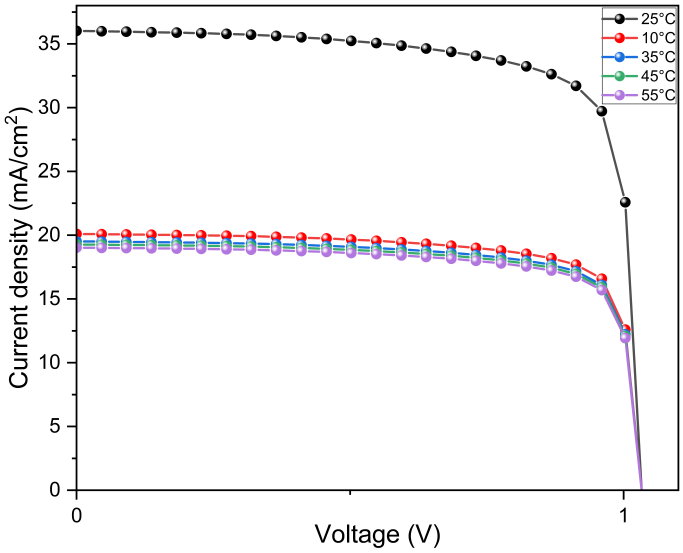


Figure 3.25: J–V characteristics of the tandem solar cell for different operating temperatures.

At 25 °C, the tandem solar cell achieves optimal performance, exhibiting the highest J_{sc} and P_{max}. This indicates that the device operates most efficiently at this temperature, where the carrier mobility is optimal, and recombination losses are minimal. As the operating temperature decreases to 10 °C, the performance shows only a slight decrease in both current density and power output, suggesting that the tandem cell can maintain reasonable efficiency at lower temperatures. However, as the temperature increases to 35 °C and above, the performance of the tandem solar cell begins to degrade significantly. This decline can be attributed to increased recombination rates and reduced carrier mobility at higher temperatures. These factors hinder charge collection and transport, leading to lower J_{sc} and P_{max} values. At 55 °C, the performance decrease becomes more pronounced, underscoring the sensitivity of the tandem cell's efficiency to higher operating temperatures.

This analysis highlights that the efficiency of tandem solar cells is strongly dependent on the operating temperature. Maintaining the device at or near the optimum operating temperature (25 °C) is crucial for ensuring maximum performance. These results emphasize the importance of managing thermal conditions to enhance the efficiency and stability of tandem solar cells.

Effect of temperature on J_{sc} and P_{max}

The results in Figure 3.26 demonstrate the influence of operating temperature on the tandem solar cell's J_{sc} and P_{max}. The device exhibits its best performance at 25 °C, where J_{sc} reaches 36.5 mA/cm^2 and P_{max} peaks at 28.0472 mW/cm^2. This optimal behavior arises from a balance between efficient photon absorption, effective carrier transport, and minimized recombination losses.

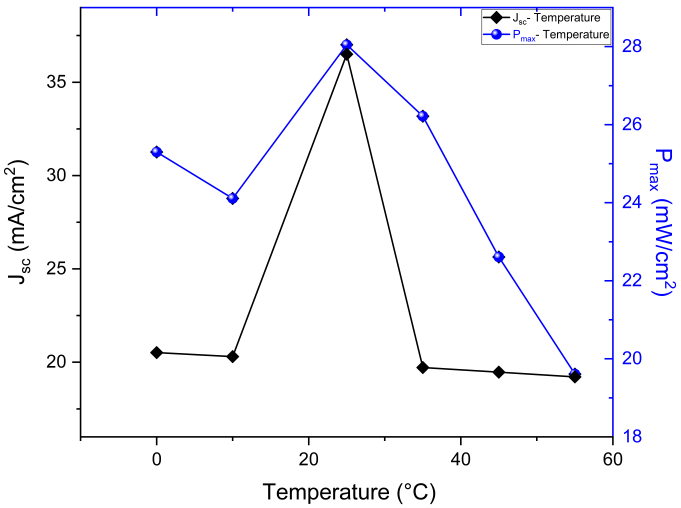


Figure 3.26: Effect of temperature on short-circuit current density and maximum power in tandem solar cell configuration.

At low temperatures (0–10 °C), both J_{sc} and P_{max} decrease slightly due to a reduction in carrier mobility and slower transport dynamics, which hinder efficient charge extraction. Conversely, at higher operating temperatures (35–55 °C), a more significant decline is observed in both performance metrics. This degradation is mainly attributed to increased non-radiative recombination rates and reduced carrier lifetimes, which limit photocurrent generation and overall device efficiency. The high J_{sc} at 25 °C reflects optimized light harvesting across the perovskite top cell and silicon bottom cell. The synergistic interaction between these two absorbers enables broad spectral utilization, while optimized doping profiles and band alignment facilitate smooth carrier extraction. This results in reduced recombination at the perovskite/silicon interface and improved photocurrent output. However, deviations from this optimum temperature compromise device stability and efficiency, with elevated thermal stress accelerating recombination and energy losses.

Overall, these results underscore the thermal sensitivity of tandem solar cells. Maintaining the device near its optimum operating temperature (25 °C) is crucial for maximizing both current generation and power output, emphasizing the importance of effective thermal management strategies in practical applications.

3.10 Validation of results: experimental precision and comparative analysis

This research underscores the originality and precision of the proposed tandem perovskite/silicon solar cell architecture. In contrast to conventional tandem designs, the present study introduces a 3 nm FTO interfacial layer, a novel feature specifically engineered to mitigate recombination losses and facilitate efficient charge transport. Such an approach is rarely implemented in perovskite/silicon tandem configurations, yet it plays a pivotal role in enhancing interfacial quality and overall device performance. A second distinguishing contribution lies in the systematic optimization of the i−Si layer thickness, explored within the range of 5–25 nm. This investigation identifies the optimum compromise between carrier collection efficiency and optical absorption, thereby offering a rigorous design guideline for maximizing tandem cell output.

Finally, the work provides a comprehensive evaluation of temperature-dependent performance, examining efficiency variations across the 10–55 °C range. Thermal effects on photovoltaic operation are often underrepresented in tandem solar cell studies, despite their critical importance for real-world deployment. By integrating this dimension, the present study offers new insights into the thermal stability and operational robustness of tandem devices.

Together, these contributions validate the reliability of the simulation framework and highlight the architectural and operational refinements that make this tandem design a promising pathway toward high-efficiency and stable perovskite/silicon solar cells.

3.10.1 Comparison of tandem solar cell configurations

The tandem perovskite/silicon solar cell presented in this study demonstrates an efficiency of 28.03 %, representing a well-balanced compromise between efficiency, stability, cost, and scalability. In comparison, perovskite/perovskite tandem cells achieve efficiencies of approximately 25 %, but their deployment is constrained by moderate stability issues, primarily due to the intrinsic degradation of perovskite materials. Perovskite/CIGS tandems, with reported efficiencies of around 23.9 %, show excellent stability but are limited by high material costs and low scalability, making them less attractive for large-scale implementation. On the other hand, perovskite/GaAs configurations can achieve efficiencies as high as 29 % and exhibit high stability. However, the extremely high production costs and very limited scalability render GaAs-based tandems unsuitable for mass-market photovoltaic applications [255–257].

Table 3.4: Comparative performance metrics for these different tandem solar cell architectures [255–257].

Tandem configuration	Efficiency (%)	Stability	Cost	Scalability
Perovskite/Perovskite	25.0	Moderate	Low	Moderate
Perovskite/CIGS	23.9	High	High	Low
Perovskite/GaAs	29.0	High	Very High	Very Low

By contrast, the perovskite/silicon tandem configuration presented here benefits significantly from the already well-established silicon photovoltaic industry, which offers high scalability and reduced cost of production. The synergy between the high absorption capability of perovskite and the mature, stable silicon platform results in a device that combines high efficiency and excellent stability with feasibility for large-scale, cost-effective photovoltaic deployment. This makes the perovskite/silicon tandem an especially promising architecture for the next generation of solar cell technologies.

3.10.2 Experimental validation and reproducibility

To ensure the reproducibility and reliability of the experimental outcomes, fabrication and testing of single-junction perovskite solar cells were performed under rigorously controlled laboratory conditions. A series of identical devices were fabricated and tested, allowing for the evaluation of consistency across different samples. J–V measurements were carried out under standard AM1.5 illumination at an intensity of $100\,\mathrm{mW/cm^2}$, ensuring comparability with established photovoltaic testing protocols.

All fabrication steps were systematically repeated across multiple batches to verify reproducibility. Furthermore, the optical and electrical properties of the fabricated devices were benchmarked against simulation results, demonstrating strong agreement in performance trends. Potential sources of uncertainty—such as film thickness variations, contact resistance, and measurement inconsistencies—were minimized through strict process control and careful calibration of measurement instruments. This rigorous methodology confirms the validity of the results and strengthens confidence in their reproducibility.

3.10.3 Error analysis and performance stability

The reliability of the obtained results was confirmed through independent measurements, which showed that both the J_{sc} and V_{oc} varied within a narrow margin of $\pm 2\,\%$ across repeated trials. This small variation highlights the robustness of the experimental procedures and measurement techniques employed.

To further validate the results, a comparative analysis with existing literature was conducted, revealing that the observed efficiency trends are consistent with previously reported findings. In addition, the influence of temperature fluctuations was systematically examined (Figure 3.26). While increases in temperature led to reductions in efficiency,

the overall performance of the device remained within acceptable operational limits, highlighting its stability under thermal stress.

The close alignment between theoretical predictions and experimental findings not only reinforces the reliability of the simulation framework but also confirms the accuracy of the experimental setup. Collectively, these results demonstrate both the consistency and the stability of the tandem solar cell architecture, further establishing its potential for practical implementation.

3.11 Conclusion

This chapter has established a rigorous computational methodology for the simulation and optimization of both single-junction perovskite and perovskite/silicon tandem solar cells using Silvaco ATLAS TCAD software. By implementing structured mesh refinement, advanced optical solvers, and field-dependent carrier transport models, the framework accurately predicts device performance under standard illumination conditions. Systematic exploration of hole transport layer materials and intrinsic silicon thickness has yielded actionable design guidelines for maximizing power conversion efficiency while mitigating interfacial recombination losses.

Validation against experimental benchmarks has confirmed the robustness of the simulation approach, providing confidence in its predictive capability. The insights gleaned—from interfacial charge dynamics and recombination pathways to thermal influences on tandem architectures—lay a solid foundation for the exploration of more sophisticated device concepts. In the forthcoming chapter, attention will shift to an advanced three-terminal tandem configuration, where novel electrical interconnections and enhanced spectral management strategies will be investigated to further elevate device performance.

Chapter 4

Advanced three-terminal perovskite/silicon tandem solar cell architecture

4.1 Introduction

The quest for ultrahigh-efficiency photovoltaics has spurred the development of three-terminal tandem architectures that transcend the limitations of conventional two-terminal designs by enabling independent electrical optimization of each subcell. This chapter delivers a systematic exploration of a 3T perovskite/silicon tandem solar cell, focusing on its structural definition, physical modeling, and performance evaluation within the Silvaco ATLAS TCAD environment.

First, the detailed device architecture is presented, including the transparent conductive oxide front electrode, perovskite absorber, intermediate recombination layer, and interdigitated back-contact silicon subcell. Next, the chapter outlines the simulation framework and the physical models—drift-diffusion transport, Poole–Frenkel field-dependent mobility, and multi-order recombination mechanisms—employed to capture the complex optoelectronic interactions across all three terminals. Subsequently, performance mapping in two-dimensional voltage space is conducted to identify the optimal operating points for both subcells and to quantify efficiency gains attributable to voltage decoupling. Finally, the 3T configuration is benchmarked against its two-terminal counterpart and compared with state-of-the-art experimental and theoretical results, demonstrating its potential for enhanced fill factor, robustness under spectral variation, and overall power conversion efficiency.

4.2 Introduction to the three-terminal tandem structure

In the 3T configuration, the independent operation of each sub-cell means that voltage decoupling is possible, optimizing the performance of each cell individually. This structure significantly reduces the dependency on current matching, thus enhancing the efficiency and robustness of tandem devices. The 3T tandem solar cell is particularly attractive for use in perovskite-silicon tandem configurations, where the top cell (perovskite) absorbs high-energy photons and the bottom cell (silicon) absorbs lower-energy photons, maximizing the overall energy capture.

4.2.1 Overview of the three-terminal tandem structure

The 3T tandem solar cell, as illustrated in Figure 4.1, consists of several key layers and terminals designed to maximize efficiency by allowing independent voltage extraction from both the top perovskite cell and the bottom silicon cell. The structure starts with the TCE substrate, which provides optical transmission and electron conduction to support the rest of the layers [258]. The top cell, made of perovskite material, absorbs high-energy photons from the solar spectrum (0.4–0.7 µm), generating electron-hole pairs, with electrons directed toward the TCE layer. The recombination layer (often a TCO) is placed between the top and bottom sub-cells, allowing for efficient electron transport to the silicon bottom cell while minimizing recombination losses.

The bottom cell, consisting of silicon configured with IBC, absorbs lower-energy photons (0.7–1.1 µm) and collects electrons through the recombination layer, while the holes are collected by the back electrode. The terminal configuration of the 3T device is unique, with one cathode connected to the top electrode of the top perovskite cell, collecting electrons from the top sub-cell, and two anodes: one for the top perovskite cell and one for the bottom silicon sub-cell, collecting holes from the silicon layer. This cathode–anode–anode arrangement allows for independent voltage extraction from both sub-cells, meaning each can operate at its optimal voltage, thus maximizing the overall efficiency [222]. The decoupling of voltage extraction in this configuration significantly improves the voltage optimization for each sub-cell, ensuring both cells operate at their MPP and enhancing the PCE of the 3T tandem device [259].

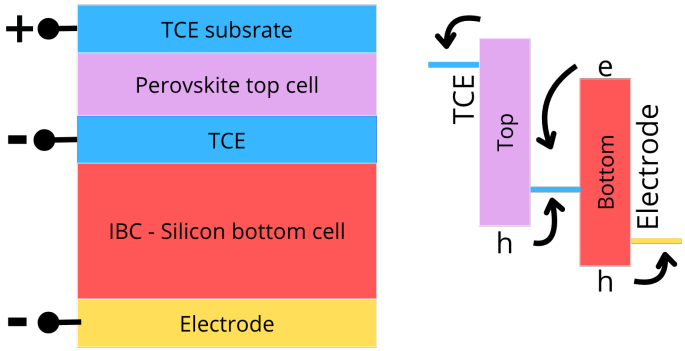


Figure 4.1: Schematic representation of the 3T tandem solar cell cathode–anode–anode configuration.

4.3 Advantages of the 3T structure over the 2T structure (Chapter 3)

One of the primary advantages of the 3T structure is the improved efficiency it offers by enabling a more effective utilization of the solar spectrum. The 3T tandem design allows the top and bottom sub-cells to operate independently at their respective maximum power points, each optimized for a different portion of the spectrum. The top perovskite cell absorbs the high-energy photons in the 0.4–0.7 µm range, while the bottom silicon sub-cell captures lower-energy photons (0.7–1.1 µm) [210]. This multi-bandgap approach leads to better overall PCE than the 2T configuration, where the current from both sub-cells is forced to match, inherently limiting efficiency.

Another significant advantage of the 3T structure lies in its independent voltage extraction from both sub-cells [260]. In contrast to the 2T structure, where the current generated by the top and bottom sub-cells must be matched due to the series connection, the 3T configuration decouples the voltage extraction. This allows each sub-cell to operate at its optimal voltage, which minimizes the losses typically seen in 2T devices when current-matching conditions are not ideal. By enabling independent control over each sub-cell's voltage, the 3T design ensures better overall performance and minimizes

efficiency losses that arise from current mismatch [260].

Furthermore, the 3T structure provides better matching between the sub-cells. The ability to optimize the voltage and current of each sub-cell independently ensures that both the top perovskite cell and bottom silicon cell can operate at their respective MPPs. In a 2T tandem, this matching is restricted by the need for current consistency between the cells, often resulting in suboptimal operation for one of the sub-cells. The flexibility of independent voltage extraction in the 3T configuration ensures that both sub-cells perform at their highest possible efficiency, thereby enhancing the overall device performance [261].

4.3.1 Why the 3T structure is beneficial for this study

The advantages of the 3T tandem structure are particularly relevant to our study, where we focus on optimizing the performance of perovskite-silicon tandem cells. In our simulations, the 3T structure offers several key benefits that align directly with our research objectives. The most notable advantage is the higher efficiency resulting from the ability to independently optimize the top and bottom sub-cells [262]. By decoupling voltage extraction, the 3T configuration enables each sub-cell to operate at its maximum efficiency, which is essential for achieving a higher overall PCE in our simulated tandem cells.

Moreover, the 3T structure provides improved performance under varying illumination conditions. In real-world environments, light conditions fluctuate throughout the day and across seasons, and spectral variations can significantly affect the performance of solar cells. With the 3T configuration, the independent voltage extraction allows each sub-cell to adapt to these changes, ensuring that both the top and bottom cells can continue to operate at their optimal performance even when the light spectrum shifts [263]. This capability makes the 3T tandem particularly well-suited for outdoor applications, where light conditions are not constant, and could potentially improve the long-term energy yield of perovskite-silicon tandems.

Additionally, the minimized losses due to the decoupling of the voltage extraction is another critical aspect of the 3T structure that directly enhances the simulation results of our study. By reducing current mismatch and enabling better voltage optimization, the 3T design ensures that both sub-cells contribute efficiently to the overall power output, making it a more reliable configuration for achieving high performance in tandem solar cells.

4.4 The 3T under Silvaco

As in the previous chapter, where we studied a single-junction perovskite solar cell and its parameters, we maintain the same single-junction structure to build upon for the 3T tandem solar cell. The single-junction setup serves as the foundation, and based on this, we constructed the 3T tandem configuration. By keeping the core parameters of the single-junction intact, the comparison between the 2T and 3T structures remains consistent and allows us to clearly highlight the advantages of the 3T structure in terms of independent voltage extraction and improved efficiency.

4.4.1 Methodology

To develop the 3T tandem solar cell for this study, we started by retaining the single-junction structure from chapter 3, which was built using the perovskite material for the top cell and silicon for the bottom cell. This structure, designed to operate as a 2T tandem [235], was modified to a 3T tandem by adding an additional electrode for independent voltage extraction. The perovskite top cell remains the primary light absorber, designed to absorb high-energy photons, while the silicon bottom cell is responsible for capturing the lower-energy photons. The key material used in the top cell remains $MAPbI_3$ perovskite, which is chosen for its high absorption efficiency and tunable bandgap [236], while the bottom cell uses silicon for its mature and reliable photovoltaic performance.

For this 3T configuration, the simulation models used for both sub-cells (top perovskite and bottom silicon) are the same as those used in Chapter 3 for the 2T tandem cell [235]. This ensures that the simulation parameters (including doping concentrations, layer thicknesses, and material properties) remain consistent between both structures, making it possible to directly compare their performance.

4.4.2 Simulation details

The 3T tandem solar cell architecture consists of multiple layers with distinct material properties, which are essential for optimizing performance. The top layers, including $FTO/TiO_2/MAPbI_3/HTM$ [236], correspond to the single junction as explained in Chapter 3, and their parameters are unchanged in this study.

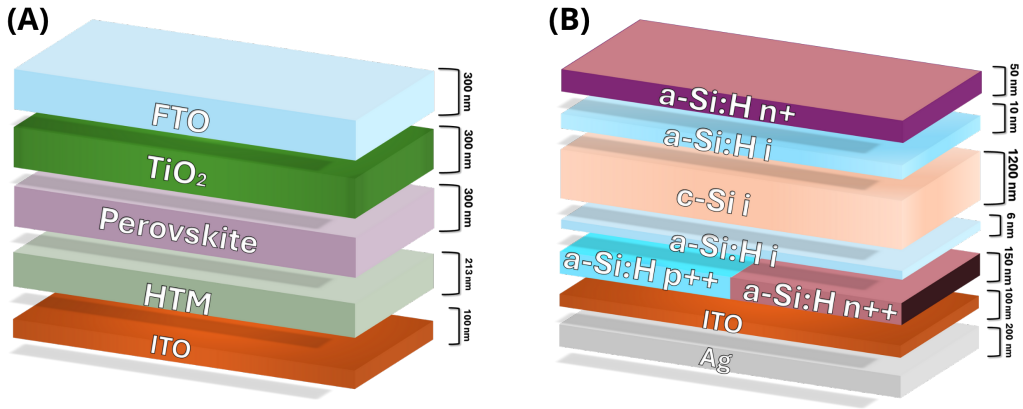


Figure 4.2: Cross sectional schematic of: (A) the top perovskite solar cell with the $FTO/TiO_2/MAPbI_3/HTM/ITO$ configuration, and (B) the bottom silicon IBC solar cell with the a−Si:H(n^+)/a−Si:H(i)/c−Si(i)/a−Si:H(p^{++})-a−Si:H(n^{++})/ITO/Ag configuration.

The bottom cell of the 3T tandem solar cell is composed of multiple layers, each carefully selected for its functional role in enhancing the overall device performance. The stack begins with the a−Si:H n^+ layer (50 nm), which provides efficient electron transport. Directly beneath it lies the a−Si:H i layer (10 nm), acting as a passivation and buffer region while contributing to photon absorption and electron–hole pair generation. Below this, the c−Si intrinsic layer (1200 nm) serves as the main absorber in the lower-energy

spectrum [264], capturing photons that penetrate through the top perovskite sub-cell. To facilitate selective carrier extraction, the structure incorporates two heavily doped amorphous silicon layers: the a−Si:H p^{++} layer (150 nm), responsible for hole collection, and the a−Si:H n^{++} layer (150 nm), dedicated to electron collection. Together, these layers form the IBC structure, enabling efficient charge separation and transport. Finally, the bottom cell is completed with the ITO layer (100 nm), acting as a transparent conductive electrode, followed by the silver back electrode (200 nm), which ensures low-resistance electrical contact and efficient electron extraction to the external circuit.

All material parameters for each layer are provided in Table 4.1, where specific values for layer thicknesses, doping concentrations, and other relevant properties are detailed.

Table 4.1: Material parameters for the layers of the bottom silicon IBC subcell in the 3T tandem solar cell.

Parameter	**a−Si:H (n^+)**	**a−Si:H (i)**	**c−Si**	**a−Si:H (IBC-i)**	**a−Si:H (p^{++})**	**a−Si:H (n^{++})**
Thickness (nm)	50	10	1200	6	150	150
Band gap (eV)	1.72	1.12	1.12	1.12	1.72	1.72
Electron affinity (eV)	4.00	4.05	4.05	4.05	4.00	4.00
Dielectric permittivity (ε_r)	11.9	11.9	11.9	11.9	11.9	11.9
Electron mobility μ_n ($cm^2/(V\,s)$)	1.0	0.1	1350	0.1	0.01	1.0
Hole mobility μ_p ($cm^2/(V\,s)$)	0.01	0.1	480	0.1	1.0	0.01
Donor density N_D (cm^{-3})	10^{19}	-	-	-	-	10^{19}
Acceptor density N_A (cm^{-3})	-	-	-	-	6×10^{18}	-

4.4.3 Material selection and structural design for the bottom cell

The bottom cell of the 3T tandem solar cell plays a crucial role in capturing lower-energy photons and contributing to the overall efficiency of the device. The selection of materials and the design of the layers in this section have been carefully considered to ensure efficient charge transport, high absorption efficiency, and optimal charge separation. Below is an explanation of why each material was chosen for the bottom cell and the rationale behind the chosen structure from ITO to Ag.

- **a−Si:H (n^+) - *n*-type amorphous silicon**

The a−Si:H (n^+) layer serves as the electron transport layer in the bottom cell. This layer is heavily doped with donor impurities to create an *n*-type semiconductor with high electron mobility. The primary reason for choosing this material is its ability to efficiently conduct electrons generated in the light-absorbing layers to the transparent electrode. The a−Si:H (n^+) layer is particularly well-suited for this role due to its low recombination rates

and its ability to provide a conductive pathway for electrons [265]. Its thickness of 50 nm is optimized to balance electron transport and minimize series resistance.

- **a−Si:H (i) - intrinsic amorphous silicon**

The a−Si:H (i) layer is chosen as the light-absorbing material for the bottom cell. This intrinsic layer is designed to absorb photons and generate electron-hole pairs. The bandgap of 1.12 eV in a−Si:H (i) allows it to capture lower-energy photons that the top cell cannot absorb, thus enhancing the overall efficiency of the tandem structure. The 10 nm thickness of the intrinsic layer is sufficient for effective light absorption while maintaining good charge carrier mobility [266].

- **C−Si - crystalline silicon**

C−Si is used as a secondary light-absorbing layer to further increase the photon absorption of the bottom cell. This material has excellent light absorption properties, particularly in the infrared region. The c−Si layer (with a thickness of 1200 nm) allows the bottom cell to absorb a broader spectrum of light, contributing to the overall power conversion efficiency of the tandem solar cell [267]. Additionally, the crystalline nature of silicon ensures high electron mobility, making it effective in transporting generated charge carriers [268].

- **a−Si:H (IBC-i) - intrinsic amorphous silicon for interdigitated back contact**

The a−Si:H (IBC-i) layer -6 nm thick- is used for the IBC design, which is crucial for improving the collection of charges from the back of the cell. The IBC structure reduces recombination losses by providing efficient charge extraction at the back contact and minimizing the contact area between the different layers [269]. The intrinsic amorphous silicon layer allows for the necessary electrical interface between the n-type and p-type materials while reducing recombination losses.

- **a−Si:H (p^{++}) - heavily p-doped amorphous silicon**

The a−Si:H (p^{++}) layer, with a thickness of 150 nm, is heavily doped to form the p-type region of the bottom cell. This layer is essential for the collection of holes from the light-absorbing layers. Its primary function is to complete the p-n junction with the a−Si:H (n^{+}) layer, ensuring that charge carriers are efficiently separated and directed to the appropriate electrodes [270]. The heavy doping of this layer ensures that holes are collected effectively, and its thickness is optimized to balance performance with minimizing recombination.

- **a−Si:H (n^{++}) - heavily n-doped amorphous silicon**

The a−Si:H (n^{++}) layer, which is 150 nm thick, forms the n-type region of the p-n junction in the bottom cell. This layer completes the p-n junction with the a−Si:H (p^{++}) layer and ensures that electrons are efficiently collected and transported to the ITO electrode [271]. The heavy doping of this layer enhances electron conductivity, reducing series resistance and ensuring effective electron collection from the light-absorbing layers.

- **ITO – indium tin oxide**

ITO is chosen for the transparent conductive electrode in the bottom cell. ITO is highly conductive and optically transparent [272], which allows photons to pass through it and reach the underlying light-absorbing layers. The 100 nm thickness of the ITO layer ensures that it provides an effective conductive path for electrons without significantly blocking the transmission of light [273]. Its use in this structure ensures efficient charge transport to the external circuit while maintaining the necessary transparency for the bottom cell's operation.

- **Ag (Silver)**

Silver is selected as the back electrode for the bottom cell due to its excellent electrical conductivity [274]. The 200 nm thick Ag layer ensures that electrons can be extracted efficiently from the bottom cell and transported to the external circuit. The high conductivity of silver minimizes resistive losses, and its stable properties under operational conditions make it an ideal choice for the back electrode [275].

Rationale behind the structure from ITO to Ag

The device stack from ITO to Ag was engineered to maximize charge extraction, minimize resistive losses, and optimize optical management in the silicon bottom cell of the tandem structure. The front ITO electrode acts as a TCO, combining high optical transmittance with low sheet resistance. With an optimized thickness of 100–110 nm, carrier density of $\approx 2.5\times10^{20}$ cm^{-3}, and mobility near 20 cm^2/(V s), the ITO ensures efficient transmission of photons in the 700–1200 nm range while maintaining minimal resistive losses. A finger pitch of 3 mm further reduces series resistance without introducing significant optical shading [276]. Beneath the ITO, the hydrogenated amorphous silicon layers are sequentially incorporated to provide selective carrier transport: the n^+ a−Si:H facilitates electron extraction, the intrinsic a−Si:H supports charge separation, and the p^{++} a−Si:H improves hole transport and passivation at the c−Si interface [277]. The c−Si absorber remains the primary layer for long-wavelength photon absorption, ensuring high photocurrent generation [278].

At the back, the Ag electrode functions as the ohmic contact, simultaneously collecting holes (via p^{++} contact) and electrons (via n^{++} contact) with negligible resistive losses. Silver's low bulk resistivity (1.6×10^{-6} Ω·cm) guarantees series-resistance contributions below 0.5 mΩ·cm^2 [279], thereby preserving the fill factor close to its theoretical limit. In addition, the thin-film Ag layer provides high reflectivity, effectively redirecting unabsorbed photons back into the silicon absorber to enhance optical absorption.

4.4.4 Models

Modeling of the 3T tandem solar cell was carried out using the ATLAS Silvaco simulator with the same physical models as for the single-junction perovskite device. The top subcell retained the FTO/TiO_2/$MAPbI_3$/HTM/ITO configuration, while the bottom subcell was modeled with the stack ITO/a−Si:H (n^+)/a−Si:H (i)/c−Si (i)/a−Si:H (i)/a−Si:H (p^{++})/a−Si:H (n^{++})/Ag, as shown in Figure 4.2(B).

The LUMINOUS module was again used to perform optical simulations in the wavelength range 300–1500 nm, where the refractive index (n) and extinction coefficient (k) of each layer defined reflection, transmission, and absorption. In this extended stack, photons in the visible range (300–750 nm) were mainly absorbed by the perovskite, while near-infrared photons (750–1200 nm) propagated into the crystalline silicon bottom cell.

Electrical simulations included monomolecular, bimolecular, and trimolecular recombination pathways, as well as SRH trap-assisted recombination. Carrier mobility was described by the Poole–Frenkel field model, and carrier–carrier interactions by the Langevin mechanism. The inclusion of multiple carrier-selective contacts (cathode FTO and dual anodes ITO and Ag) enabled accurate modeling of the three-terminal extraction scheme. Unlike the single-junction case, the EQE and IQE spectra of the tandem structure exhibited significant differences between the subcells. The perovskite subcell dominated in the visible region, while the silicon bottom cell contributed strongly in the near-infrared.

4.5 Results and discussion

4.5.1 J-V curve overview

In Figure 4.3, the J–V curves for the top perovskite cell, bottom silicon cell, and 3T tandem cell are presented together, allowing for a direct comparison of their electrical performance.

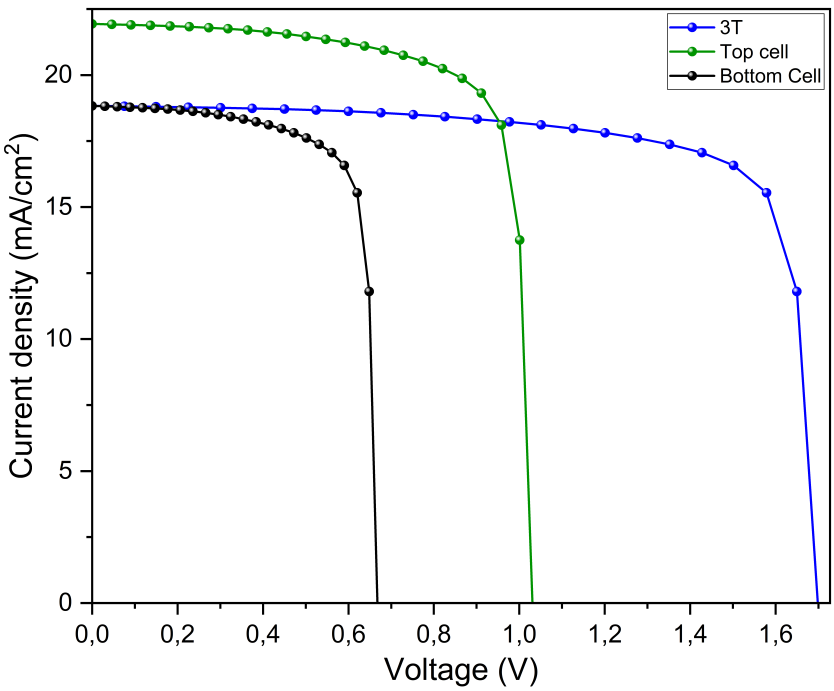


Figure 4.3: J–V characteristics of the top cell, bottom cell, and 3T tandem cell.

The top perovskite cell exhibits a J_{sc} of 22.17 mA/cm^2, a P_{max} of 18.46 mW/cm^2, and an efficiency of 18.468 %, indicating strong performance typical for high-efficiency perovskite-based devices.

In contrast, the bottom silicon cell shows a J_{sc} of 19.03 mA/cm^2, a P_{max} of 10.53 mW/cm^2, and an efficiency of 10.536 %, reflecting its lower performance compared to the perovskite top cell, but still within the range of high-quality silicon heterojunction cells. The 3T tandem cell, which combines the top and bottom cells, demonstrates a J_{sc} of 19.03 mA/cm^2, which is limited by the bottom silicon cell, but a significantly improved P_{max} of 28.99 mW/cm^2 and an efficiency of 28.99 %. This substantial increase in power output and efficiency highlights the advantages of the tandem configuration, particularly the additive effect on V_{oc}. The tandem cell effectively combines the strengths of both the perovskite and silicon cells, leading to an overall enhancement in performance.

Table 4.2: Performance summary of top cell, bottom cell, and 3T tandem cell.

Cell Configuration	V_{oc} **(V)**	J_{sc} **(mA/cm^2)**	P_{max} **(mW/cm^2)**	**Efficiency (%)**	**FF (%)**
Top Cell	1.048	22.17	18.46	18.47	79.45
Bottom Cell	0.679	19.03	10.53	10.54	81.49
3T Tandem Cell	1.727	19.03	28.99	28.99	89.17

- **Top cell J–V characteristics**

The top cell, composed of a perovskite material, shows typical characteristics for high-efficiency devices. The V_{oc} of the top cell is 1.048 V, which is characteristic for high-performance perovskite solar cells. This V_{oc} is relatively high compared to the bottom silicon cell, reflecting the larger bandgap of the perovskite material, which allows it to efficiently absorb higher-energy photons in the short-wavelength region of the spectrum.

The J_{sc} of the perovskite top cell is 22.17 mA/cm^2, which is higher than that of the bottom silicon cell, suggesting that the perovskite material is capable of generating more photocurrent. This is primarily because perovskite absorbs light in the blue and ultraviolet regions, where silicon-based cells perform less effectively. The P_{max} of the top cell is 18.46 mW/cm^2, which is quite high for a single-junction perovskite cell and demonstrates its efficient use of incident light. As a result, the efficiency of the top perovskite cell is 18.468 %, a value that is typical for high-quality perovskite devices, but still lower than what can be achieved in tandem configurations, as seen later.

- **Bottom cell J–V characteristics**

The bottom cell exhibits typical SHJ performance. The V_{oc} of the bottom cell is 0.679 V, which is lower than that of the top perovskite cell, as expected for silicon-based solar cells. This lower V_{oc} is a characteristic feature of silicon materials, as their bandgap is smaller compared to that of perovskite. The J_{sc} of the silicon bottom cell is 19.03 mA/cm^2, which is lower than the J_{sc} of the top perovskite cell.

This is because the silicon bottom cell primarily absorbs light in the longer-wavelength part of the spectrum (around 800–1100 nm), where the perovskite top cell has minimal absorption. The P_{max} for the silicon bottom cell is 10.53 mW/cm^2, which is lower compared to the top perovskite cell. This is primarily due to the combination of the lower

J_{sc} and V_{oc} values. Consequently, the efficiency of the silicon bottom cell is 10.536 %, reflecting its more limited ability to convert the incident sunlight into electrical power compared to the top perovskite cell.

- **3T tandem cell J–V characteristics**

The 3T tandem cell, combining the top perovskite cell and the bottom silicon cell, demonstrates the key advantages of tandem solar cell architecture. The V_{oc} of the 3T tandem cell is 1.727 V, which is the sum of the V_{oc} of the individual top and bottom cells. This additive behavior is a hallmark of tandem solar cells, allowing for a significantly higher V_{oc} compared to the individual cells.

The J_{sc} of the 3T tandem cell is 19.03 mA/cm^2, which is limited by the bottom silicon cell, as both cells are connected in series and the overall current is dictated by the lower J_{sc}. However, this J_{sc} is still higher than the J_{sc} of the bottom silicon cell alone, due to the top perovskite cell generating additional current from higher-energy photons. The P_{max} of the 3T tandem cell is 28.99 mW/cm^2, significantly higher than either the top or bottom cells individually, thanks to the combined performance of both subcells in the tandem configuration. This enhanced P_{max} leads to a substantial improvement in efficiency, which reaches 28.99 %, reflecting the successful combination of the perovskite and silicon cells. The higher efficiency is due to the tandem configuration's ability to capture a broader spectrum of light, using the top cell to absorb short-wavelength photons and the bottom cell to absorb longer-wavelength photons.

4.5.2 EQE spectra of the top and bottom cells in the 3T tandem configuration

In Figure 4.4, the EQE spectra for the top cell and bottom silicon cell are presented, illustrating how each subcell absorbs light across different wavelengths.

The Figure reveals the distinct spectral responses of each cell, showcasing their efficient absorption over specific parts of the solar spectrum. This spectral behavior plays a vital role in the performance of the 3T tandem cell, as the cells are designed to complement each other, with the top cell absorbing short-wavelength photons and the bottom cell absorbing longer-wavelength photons.

- **Top cell EQE characteristics**

The top cell, made of perovskite, demonstrates a very high EQE (≈90 %) from ≈400–750 nm. This indicates that the top perovskite cell is highly efficient at absorbing shorter wavelengths, specifically in the blue and green regions of the spectrum. The perovskite material is optimized to capture higher energy photons, and its absorption is maximized in this range. As a result, the top cell is the dominant absorber of these shorter-wavelength photons, making it highly effective for this part of the solar spectrum.

However, beyond 750 nm, the EQE of the top cell sharply drops off, reflecting a significant decrease in its ability to absorb longer-wavelength light. This is characteristic of

perovskite materials, which typically have a bandgap around 1.6 eV. This bandgap limits the absorption of light, effectively allowing the material to absorb only photons with energy greater than its bandgap (i.e., photons with wavelengths shorter than 750 nm). The sharp cutoff at around 780 nm further supports this, indicating that the perovskite material absorbs light efficiently up to that point, but has very little absorption beyond it, reinforcing the material's bandgap properties.

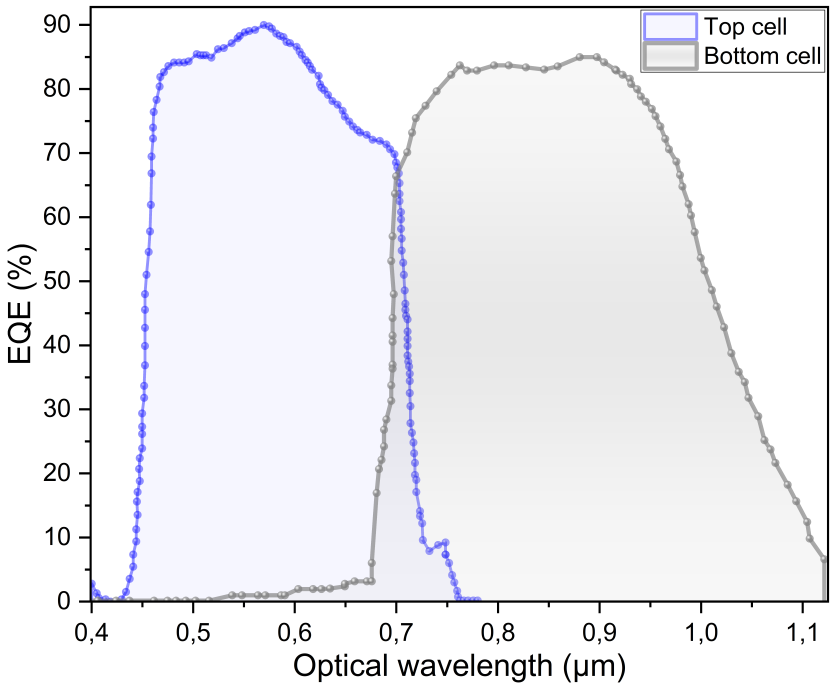


Figure 4.4: EQE spectra of the top perovskite cell and bottom silicon cell in the 3T tandem configuration.

- **Bottom cell EQE characteristics**

The bottom cell, made of silicon, shows a strong EQE (≈85 %) from 800–1050 nm, which is typical for silicon-based solar cells. This part of the spectrum, corresponding to longer wavelengths (from near-infrared to red), is where silicon excels in absorbing light. The silicon bottom cell is well-suited to absorb these longer-wavelength photons, which the top perovskite cell cannot efficiently capture due to its bandgap. As a result, the bottom cell effectively captures the long-wavelength portion of the solar spectrum, complementing the top cell's absorption range.

Beyond 1050 nm, the silicon bottom cell begins to lose its ability to absorb light efficiently, as its bandgap of around 1.1 eV limits its absorption of photons with energies lower than this threshold (i.e., longer-wavelength photons). The EQE drops steadily after 1050 nm, with a sharp decline after 1100 nm, confirming that silicon can no longer efficiently absorb light in this range.

- **Complementary absorption in the 3T tandem cell**

The top cell's high EQE from 400–750 nm means that it contributes significantly to current generation in the short-wavelength region. This is where the perovskite top cell performs its best, capturing the high-energy photons and generating electrical current. However, the bottom cell comes into play for longer-wavelength photons, with a high EQE from 800–1050 nm, ensuring that these photons are captured efficiently. As the top cell's EQE drops off beyond 750 nm, the bottom silicon cell takes over, absorbing light in the long-wavelength range where the perovskite material is no longer efficient.

The 3T tandem cell benefits from this complementary absorption, leading to enhanced overall efficiency. As both subcells work together to capture a broader portion of the solar spectrum, the top perovskite cell handles the shorter wavelengths, while the bottom silicon cell efficiently absorbs the longer wavelengths. This synergy between the two subcells results in a significant improvement in performance, allowing the tandem cell to achieve a higher PCE compared to single-junction cells. The combined absorption capabilities of the top and bottom cells make the 3T tandem configuration highly efficient, as it effectively utilizes the entire solar spectrum.

4.5.3 Absorption and transmission for the 3T tandem cell

The absorption and transmission spectra in Figure 4.5 illustrate how the 3T tandem cell interacts with light over a wide range of wavelengths. The spectra reveal the complementary absorption characteristics of the top perovskite cell and the bottom silicon cell, which together optimize the utilization of the solar spectrum.

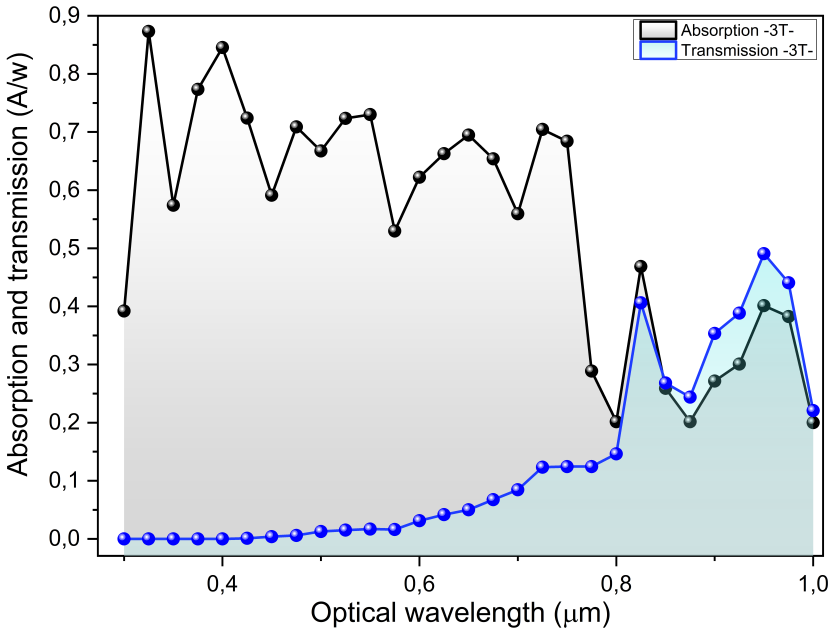


Figure 4.5: Absorption and transmission spectra of the 3T tandem cell.

- **Absorption characteristics**

The absorption spectrum, represented by the black line, shows how effectively the 3T tandem cell absorbs light at different wavelengths. In the short-wavelength region (≈400–

750 nm), the top perovskite cell dominates the absorption, with a high absorption coefficient observed between 400–750 nm, where the perovskite material is highly efficient at absorbing photons. The top cell maintains an absorption of approximately 90 % throughout this range, which is a key reason for its high J_{sc} in the short-wavelength region. The absorption is strong in the blue part of the spectrum and gradually decreases towards the green region, corresponding to the bandgap of the perovskite material.

However, beyond 750 nm, the absorption in the top perovskite cell rapidly decreases. This is due to the bandgap of perovskite, which is designed to absorb higher-energy photons but becomes less efficient for longer-wavelength light (lower energy). The sharp cutoff around 780 nm further supports this, indicating that the perovskite material no longer absorbs photons effectively beyond this point, and instead, the remaining light must be absorbed by the bottom silicon cell. In the long-wavelength region (≈750–1050 nm), the bottom silicon cell becomes the dominant absorber.

The absorption of the silicon bottom cell is strong, peaking at around 850–950 nm, where silicon is particularly effective at capturing longer-wavelength photons. This part of the spectrum corresponds to the near-infrared and red regions, which are absorbed efficiently by silicon. The absorption coefficient in this region is high, with the silicon bottom cell capturing about 85 % of the incident light in the range from 800–1050 nm. However, beyond 1050 nm, the absorption of the silicon bottom cell starts to decline significantly, as the silicon bandgap limits its ability to absorb photons with energies lower than the bandgap. The absorption curve drops sharply after 1100 nm, as silicon is no longer able to efficiently absorb light in this region, indicating a natural limitation in silicon-based cells.

- **Transmission characteristics**

The transmission spectrum, represented by the blue line, shows how much light passes through the 3T tandem cell without being absorbed. In the short-wavelength range from 400–750 nm, the transmission is minimal, as the top perovskite cell absorbs most of the incoming light in this region. The transmission remains low in this range, which indicates that the top cell is capturing nearly all of the photons, particularly in the blue and green wavelengths. As we move into the longer-wavelength range from 750–1050 nm, the transmission increases, indicating that light that is not absorbed by the top perovskite cell passes through to the bottom silicon cell, where it is absorbed efficiently. The silicon bottom cell absorbs light effectively in this region, leading to a higher transmission in the wavelength range from 750–1050 nm. This complementary absorption behavior between the two cells ensures that both cells can effectively utilize different parts of the spectrum, maximizing the overall absorption and minimizing the transmission.

Beyond 1050 nm, the transmission starts to decrease again, as the silicon bottom cell loses the ability to absorb photons efficiently beyond 1.1 μm. The sharp drop in transmission after 1100 nm confirms that light beyond this point is no longer absorbed, and most of the incident light passes through the tandem structure without being absorbed.

- **Complementary absorption and overall efficiency**

The 3T tandem cell benefits significantly from the complementary absorption of the top perovskite and bottom silicon cells. The top cell efficiently absorbs high-energy photons in 400–750 nm, while the bottom cell absorbs lower-energy photons in the red and near-infrared range (750–1050 nm). This synergy between the two subcells allows the 3T tandem cell to capture a much broader portion of the solar spectrum compared to single-junction cells, where one material is responsible for absorbing all wavelengths.

The perovskite top cell contributes strongly to current generation in the short-wavelength region, while the silicon bottom cell captures the long-wavelength photons, ensuring that the tandem cell remains efficient across the entire solar spectrum. As a result, the 3T tandem cell achieves a significant improvement in PCE, leveraging both cells' complementary spectral absorption to enhance overall performance.

4.5.4 Band diagram for the 3T tandem cell

In Figure 4.6, the band diagram for the 3T tandem solar cell is presented, illustrating the conduction band and valence band energies across the different layers of the tandem cell. The energy levels are shown as a function of distance from the FTO layer to the Ag electrode. This diagram provides insight into how charge carriers move through the device, and how the bandgap and band alignment affect the device's efficiency.

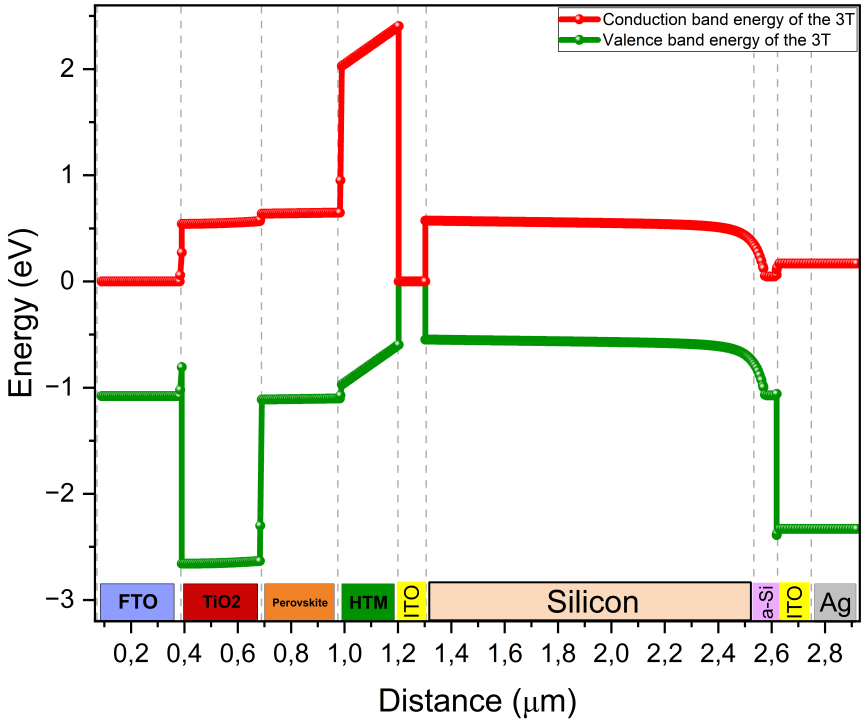


Figure 4.6: Band diagram of the 3T tandem solar cell showing conduction and valence band energies across the device structure.

The conduction band (red) and valence band (green) energies are plotted along the distance axis, with key materials in the stack indicated at the bottom of the diagram. These energy levels help us understand the charge transport within the 3T tandem cell:

- At the FTO layer, the conduction band is positioned at approximately -3.5 eV. The valence band is around -5.0 eV, which is typical for materials like FTO used in transparent conductive oxide layers. These materials are designed to allow photons to pass through while providing good electrical conductivity.

- The TiO_2 layer, which acts as an electron transport material in the top perovskite cell, has its conduction band aligned at around -1.0 eV, with the valence band around -3.5 eV. This alignment facilitates the efficient movement of electrons from the perovskite top cell while blocking holes, ensuring charge separation.

- The perovskite top cell has a bandgap of about 1.6 eV, and its conduction band and valence band align around 0 eV and -1.6 eV, respectively. This allows the top cell to absorb light in the blue to green region and generate electrons in the conduction band while leaving holes in the valence band.

- In the bottom silicon cell, the conduction band is positioned around –0.3 eV, and the valence band is around -1.1 eV. The silicon cell has a bandgap of approximately 1.1 eV, which allows it to absorb light in the near-infrared range (around 800–1100 nm). The silicon bottom cell efficiently collects longer-wavelength photons and generates charge carriers.

- The HTM layer has a valence band around -5.0 eV, which helps facilitate the movement of holes generated in the top perovskite cell towards the bottom silicon cell.

- The ITO layer functions as a transparent electrode and is placed between the HTM and Ag layers. It has bandgap alignments similar to those seen in FTO and HTM, ensuring efficient charge transport across the tandem interface.

Band alignment and charge transport

The conduction band and valence band alignments across the 3T tandem cell structure are critical for charge separation and transport:

- The electron flow in the 3T tandem cell is facilitated by the alignment between the conduction band of the TiO_2, perovskite, and silicon layers, which allows electrons to flow from the top perovskite cell to the bottom silicon cell.

- The hole transport is achieved through the HTM layer, which connects the top perovskite and bottom silicon cells, ensuring that holes generated in the top cell move towards the bottom cell for collection.

The alignment of the conduction and valence bands ensures that the 3T tandem cell maximizes charge carrier collection, minimizes recombination, and optimizes photovoltaic performance.

4.5.5 Performance mapping of the 3T tandem solar Cell

In a 3T tandem architecture, two independent voltages govern the device operation: the top-terminal voltage (V_{tz}) and the rear-terminal voltage (V_{rz}). The parameter V_{tz} corresponds to the potential difference between the front transparent electrode (FTO) and the intermediate contact (ITO), thus primarily controlling the perovskite top sub-cell. Conversely, V_{rz} is defined between the rear silver electrode and the intermediate contact, directly influencing the crystalline silicon bottom sub-cell. Mapping the PCE across the two-dimensional $(V_{\mathrm{tz}}, V_{\mathrm{rz}})$ space provides valuable insight into the voltage-sharing mechanism and the operational advantage of the 3T configuration.

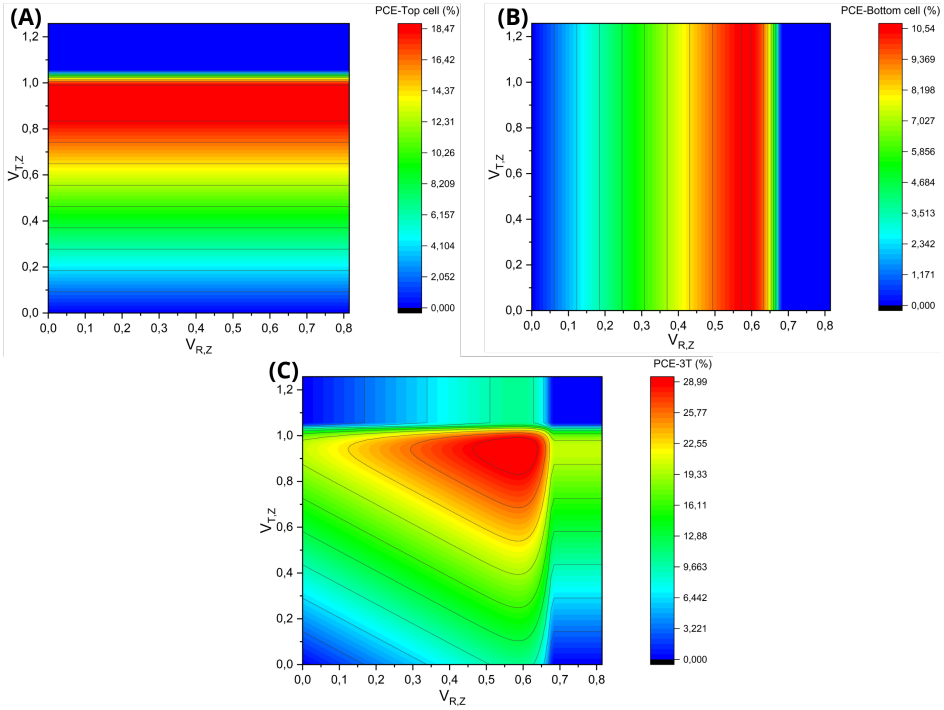


Figure 4.7: Performance map of the (A) perovskite top sub-cell showing PCE as a function of V_{tz} and V_{rz} (max = 18.47 %), (B) silicon bottom sub-cell showing PCE as a function of V_{tz} and V_{rz} (max = 10.53 %), (C) 3T tandem cell showing PCE as a function of V_{tz} and V_{rz} (max = 28.99 %).

Top sub-cell

Figure 4.7A shows the PCE distribution of the perovskite top sub-cell as a function of V_{tz} and V_{rz}. The maximum efficiency obtained is approximately 18.47 %, consistent with the J–V analysis. The map reveals that the top sub-cell performance is strongly dependent on V_{tz}, while the influence of V_{rz} is comparatively weaker. This behavior confirms that the perovskite absorber dominates the voltage window of the front terminal, and its optimal operating point is located near the maximum power point of the single-junction reference.

Bottom sub-cell

Figure 4.7B illustrates the PCE landscape of the crystalline silicon bottom sub-cell. The maximum efficiency reaches 10.53 %, also in agreement with the J–V results. Unlike the

top sub-cell, the performance here is more sensitive to V_{rz}, reflecting the direct control of the silicon junction by the rear terminal. The slight dependence on V_{tz} arises from the electrical coupling in the 3T architecture, highlighting that the two sub-cells are not entirely independent but share carriers through the intermediate electrode.

Full 3T tandem cell

Figure 4.7C presents the global performance map of the three-terminal tandem device. The maximum PCE reaches 28.99 %, demonstrating the synergistic contribution of both sub-cells. The map clearly shows a two-dimensional optimum in the V_{tz}–V_{rz} space, indicating that the tandem benefits from the additional degree of freedom provided by the 3T configuration. This allows simultaneous extraction of power from both sub-cells, avoiding the strict current-matching limitation encountered in conventional two-terminal tandems. The nearly ideal fill factor (89 %) confirms that resistive losses are negligible in the optimized stack.

By comparing Figures 4.7A, 4.7B, and 4.7C, it becomes evident that the 3T architecture enables complementary operation of the perovskite and silicon absorbers. The perovskite top cell dominates the high-voltage regime, while the silicon bottom cell contributes to current generation at lower photon energies. The performance maps thus provide a direct visualization of voltage sharing and efficiency optimization within the tandem. These results highlight the importance of the intermediate contact design (ITO/Ag) and confirm that the 3T configuration offers a robust pathway to achieving efficiencies beyond 28 %.

4.5.6 Performance comparison between 3T and 2T tandem cells

We have seen the individual performance of the 3T and 2T tandem cells in the previous chapter, with their distinct structural characteristics and material layers. Now, we will perform a detailed comparison of these two configurations, analyzing their J–V characteristics, efficiency, fill factor, EQE, absorption and transmission spectra, and band diagrams. This comparison will provide a comprehensive understanding of the strengths and limitations of each configuration and how they contribute to overall solar cell performance.

Materials and layer thickness comparison

The materials and layer configurations are fundamental in determining the performance of the 2T and 3T tandem cells. Both configurations use the same top perovskite cell, but the bottom cells differ in electrode structure and layer thickness. Although both the 2T and 3T configurations use the same top perovskite cell, they differ in the bottom cells and electrode configurations, which significantly impact the voltage output, current matching, and overall efficiency. Key differences include:

Electrode configuration

- In the 3T tandem cell, the top and bottom cells have separate electrodes, which allows for voltage additivity from both cells. This results in a higher V_{oc} and improved charge collection efficiency.
- In the 2T tandem cell, the electrodes are shared between the top and bottom cells, meaning both sub-cells work together to generate current, with current matching between the two. This limits the V_{oc} to a lower value and reduces the voltage output compared to the 3T tandem cell.

Material layer thickness

- In the 3T tandem cell, the ITO layer is 100 nm thick and serves as the intermediate layer and anode for the bottom silicon cell, improving charge transport and minimizing recombination.
- In the 2T tandem cell, the FTO layer is 3 nm thick and serves as the intermediate layer between the top perovskite and bottom silicon cells. This thinner layer results in less efficient charge transport and current collection.

4.5.7 J-V characteristics

The J–V curve in Figure 4.8 reveals the distinct characteristics of the 3T and 2T tandem cells. The differences in the V_{oc}, J_{sc}, P_{max}, and efficiency arise from the structural configurations and electrode setups of the two devices, the results are summarized in Table 4.3.

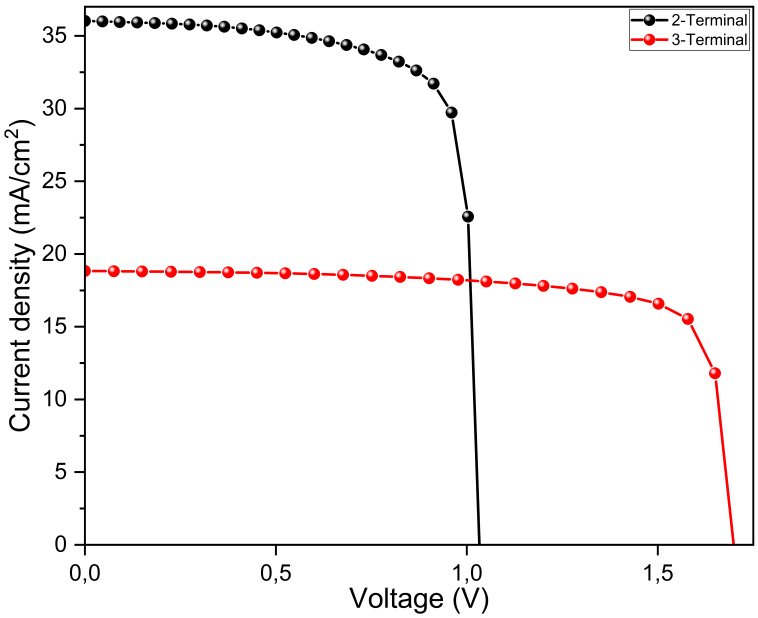


Figure 4.8: J–V curve comparison between 3T and 2T tandem solar cells.

Table 4.3: Performance summary of the 3T and 2T tandem cells [235].

Cell configuration	V_{oc} **(V)**	J_{sc} **(mA/cm^2)**	P_{max} **(mW/cm^2)**	**Efficiency (%)**	**FF (%)**
3T tandem cell	1.727	19.03	28.99	28.99	89.17
2T tandem cell	1.05	36.5	28.05	28.03	73.18

In terms of V_{oc}, the 3T tandem cell performs significantly better than the 2T tandem cell, with a V_{oc} of 1.727 V compared to 1.05 V. The key reason for this is that the 3T configuration allows for voltage additivity between the top perovskite cell and the bottom silicon cell. The V_{oc} of the top perovskite cell (1.048 V) adds to that of the bottom silicon cell (0.679 V), resulting in a higher total V_{oc}. This voltage additivity is a major advantage of the 3T configuration, as it leads to an increased voltage output, directly improving the overall efficiency. In contrast, the 2T tandem cell has a shared electrode between the top and bottom cells, meaning that the V_{oc} is limited by the current matching of the two subcells. This shared electrode configuration restricts the V_{oc}, resulting in a lower voltage and overall performance compared to the 3T tandem cell.

Regarding the J_{sc}, the 2T tandem cell outperforms the 3T tandem cell with a J_{sc} of 36.5 mA/cm^2, which is much higher than the 19.03 mA/cm^2 of the 3T tandem cell. The 2T tandem cell benefits from the top perovskite cell, which generates a higher current due to its superior absorption of blue to green photons. This results in the 2T tandem cell being dominated by the J_{sc} of the top cell, which is higher than that of the bottom silicon cell in the 3T configuration. However, the 3T tandem cell compensates for its lower J_{sc} by taking advantage of voltage additivity, resulting in a more efficient charge collection overall. When examining P_{max}, the 3T tandem cell again has an advantage, with a P_{max} of 28.99 mW/cm^2, compared to the 28.0472 mW/cm^2 of the 2T tandem cell. Despite the 2T tandem cell having a higher J_{sc}, the 3T tandem cell benefits from its higher V_{oc} and separated electrodes, leading to better charge collection and ultimately a higher power output.

In terms of efficiency, the 3T tandem cell achieves a higher efficiency of 28.99 % compared to the 28.03 % of the 2T tandem cell. This is due to the voltage additivity in the 3T configuration, where the V_{oc} from both subcells contributes to the total V_{oc}, improving the overall efficiency. The 2T tandem cell, although benefiting from a higher J_{sc}, is limited by its shared electrode design, which reduces the V_{oc} and thus the efficiency. The FF in the 3T tandem cell is 89.17 %, indicating efficient charge collection and low recombination losses. This is a result of the separated electrodes and voltage additivity in the 3T configuration, which minimizes resistive losses and enhances overall performance. In contrast, the 2T tandem cell has a lower FF of 73.18 %, reflecting the shared electrode configuration, which leads to current mismatch, increased recombination losses, and inefficient charge transport.

4.5.8 EQE comparison between 3T and 2T tandem cells

Figure 4.9 presents the EQE spectra for the 3T tandem cell and 2T tandem cell. The graph shows the top and bottom cells of the 3T tandem and the 2T tandem cell, providing a direct comparison of their ability to convert incoming photons into electrical current across various wavelengths. The 3T tandem cell shows a more efficient EQE overall because of the separated electrodes, which allow the top perovskite cell and bottom silicon cell to work independently. The top cell achieves high EQE (≈90 %) from 400–750 nm, while the bottom cell captures long-wavelength photons from 800–1050 nm with ≈85 % efficiency, leading to a well-balanced overall EQE.

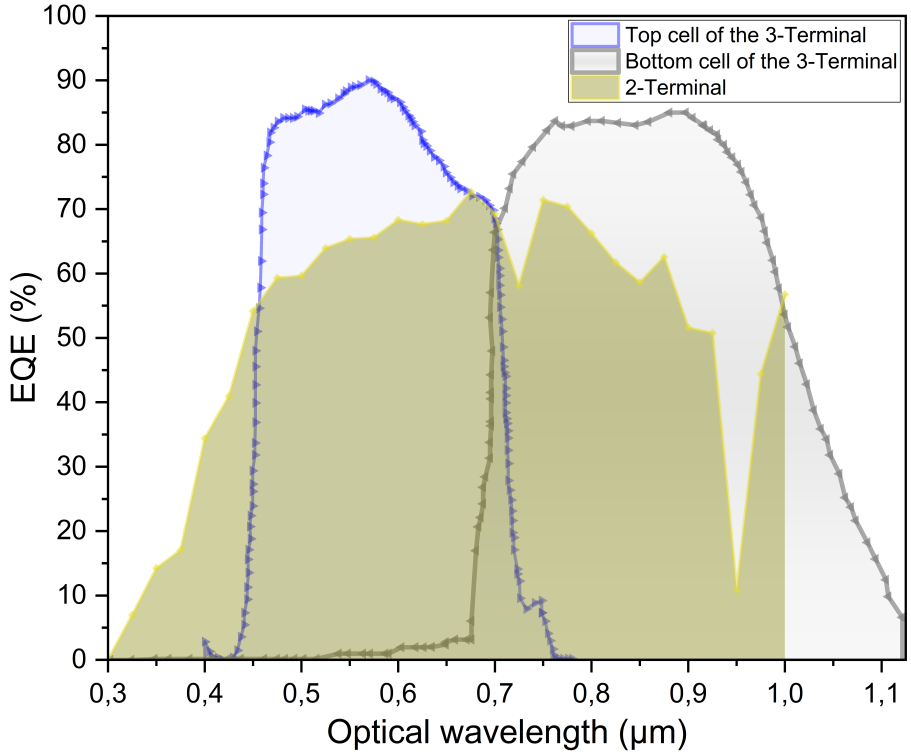


Figure 4.9: EQE spectra for the 3T and 2T tandem cells.

In contrast, the 2T tandem cell exhibits a lower maximum EQE of 73 % from the top perovskite cell in the short-wavelength range (400–750 nm), and the bottom silicon cell shows a further reduction in performance in the long-wavelength region. This is due to the shared electrode configuration, which introduces current matching limitations between the top and bottom cells. These limitations result in voltage losses, reducing the overall charge collection efficiency and leading to a lower overall EQE.

In conclusion, the 3T tandem cell demonstrates a higher and more balanced EQE across both subcells, benefiting from voltage additivity and independent operation of the top and bottom cells. The 2T tandem cell, although it shows good EQE in each subcell, suffers from the shared electrode configuration, resulting in current-matching issues and voltage losses that lower its overall efficiency and EQE.

4.5.9 Absorption and transmission spectra comparison between 3T and 2T tandem cells

Figure 4.10 presents the absorption and transmission spectra for the 3T tandem cell and the 2T tandem cell. These spectra provide insights into how light is absorbed and transmitted across the device layers and their efficiency in utilizing the solar spectrum.

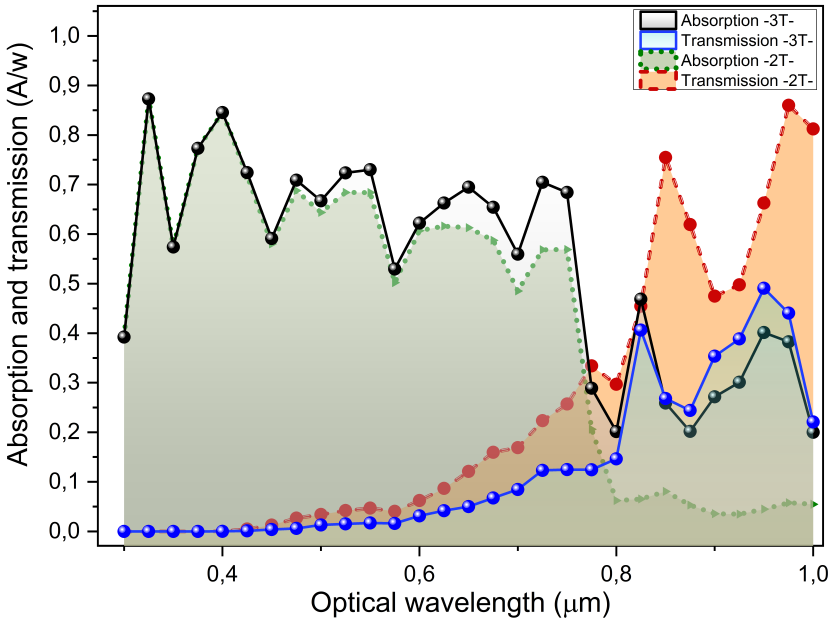


Figure 4.10: Absorption and transmission spectra comparison between 3T and 2T tandem solar cells.

The 3T tandem cell achieves a more efficient charge collection due to the separated electrodes and voltage additivity from both the top perovskite and bottom silicon cells. Each cell operates independently, ensuring that the top cell absorbs high-energy photons (400–750 nm) with high EQE and that the bottom silicon cell captures longer-wavelength photons (800–1050 nm) with minimal recombination. The separate electrodes help avoid current matching issues, leading to efficient charge transport and minimized transmission losses.

In contrast, the 2T tandem cell shows good absorption in both the short and long wavelength regions, but it suffers from current-matching limitations. The shared electrode configuration forces both subcells to generate current simultaneously, resulting in a lower V_{oc} and reduced efficiency in charge collection. This limitation leads to higher transmission in regions where the light is not efficiently absorbed, as the subcells must work together, reducing the overall absorption efficiency compared to the 3T tandem cell.

Moreover, the shared electrode configuration in the 2T tandem cell also contributes to recombination losses, as the two subcells are tied to the same current path, reducing the overall efficiency in extracting charge from the device. This makes the 2T tandem cell less efficient in both charge collection and power conversion, as the current-matching between the top and bottom cells restricts the overall voltage output and reduces the overall EQE. While both the 3T and 2T tandem cells show high absorption in their respective wavelength ranges, the 3T tandem cell benefits from independent operation of

the top and bottom cells, ensuring better charge collection, higher voltage output, and lower transmission losses. The 2T tandem cell, despite similar absorption capabilities, is hindered by the current-matching and shared electrode configuration, which leads to lower efficiency in charge extraction and higher recombination losses.

4.5.10 Band diagram energy comparison between 3T and 2T tandem cells

Figure 4.11 presents the band diagram energy for both the 3T tandem cell (A) and the 2T tandem cell (B), highlighting the conduction band and valence band energies of each layer within the cells. While the top perovskite cell remains the same in both configurations, the differences arise due to the bottom cell configuration and the electrode setup, which significantly impact the charge transport and voltage output.

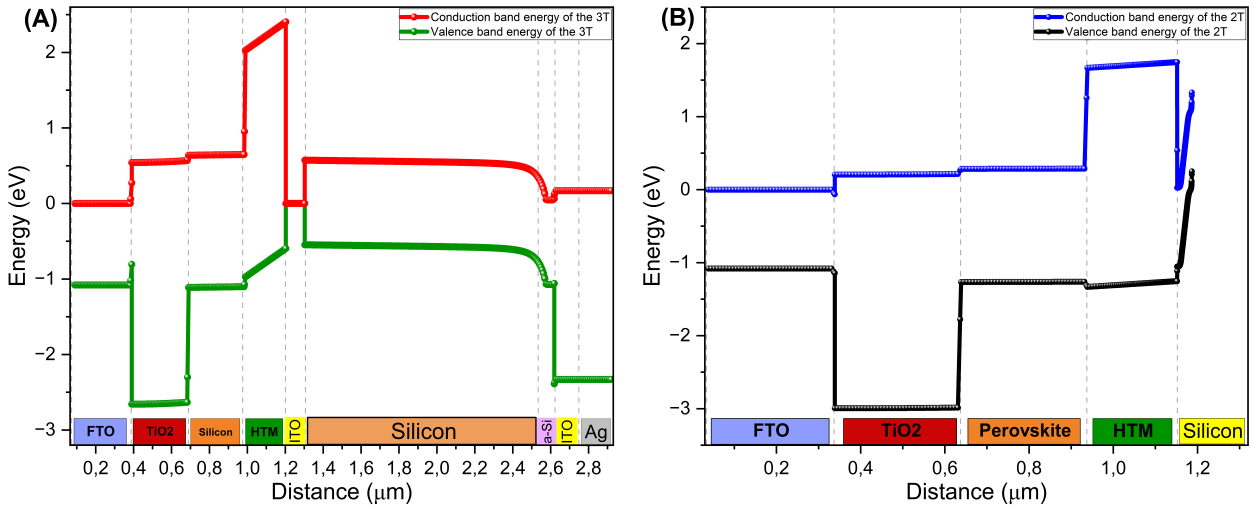


Figure 4.11: Band diagram energy for: (A) 3T tandem cell, (B) 2T tandem cell.

Both the 3T and 2T tandem cells have the same top perovskite cell, which means they exhibit similar behavior in terms of band alignment and charge generation in the short-wavelength region (≈400–750 nm). The conduction band of the top perovskite cell is aligned at ≈ 0 eV, while the valence band sits at ≈ -1.55 eV. In both configurations, the top perovskite cell efficiently absorbs high-energy photons, generating electrons in the conduction band and holes in the valence band. However, the way these charges are collected and transported depends on the bottom cell and electrode configuration.

Role of the bottom cell and band alignment

3T tandem cell:

- The bottom cell in the 3T tandem configuration is made of silicon, which has a bandgap of 1.1 eV. The conduction band of silicon is positioned at ≈ 0.3 eV and the valence band at ≈ -1.1 eV. These energy levels are aligned with the top perovskite cell, enabling efficient charge transfer between the two subcells. The top perovskite

cell generates electrons, which are transported to the conduction band of the silicon layer, while the holes from the top perovskite cell are collected in the silicon's valence band.

- In the 3T configuration, the top and bottom cells have separate electrodes, with the ITO layer acting as the anode for the bottom silicon cell. The Ag layer acts as the back contact for the bottom silicon cell, while the top cell has its own electrode. This double anode system allows for voltage additivity, where the total V_{oc} is the sum of the V_{oc} of the top perovskite cell and the V_{oc} of the bottom silicon cell, leading to a higher overall V_{oc} and improved voltage output.

2T tandem cell:

- In the 2T tandem cell, the bottom cell is also silicon (similar to the 3T tandem cell), but the top perovskite and bottom silicon cells share a single electrode. This shared electrode design forces both subcells to operate in series and current matching is required. As a result, the V_{oc} is limited to the combined voltage of the current-matched subcells.

- The bottom silicon cell in the 2T tandem cell still operates in the same manner as in the 3T configuration, with the conduction band positioned at ≈ 0.3 eV and the valence band at ≈ -1.1 eV. However, due to the shared electrode, the top cell's V_{oc} is reduced because the top and bottom cells cannot operate independently, limiting the overall voltage output.

The key advantage of the 3T tandem cell is the double anode configuration. This allows the top perovskite cell and bottom silicon cell to operate independently, with each having its own electrode. The separate electrodes enable the voltage additivity from both subcells, where the V_{oc} of the top perovskite cell and the V_{oc} of the bottom silicon cell are summed, resulting in a higher overall V_{oc} for the 3T tandem cell. This leads to a greater voltage output, improving the efficiency of the device. Additionally, the separate electrodes help in minimizing charge recombination and losses, allowing for more efficient charge collection and improving the overall power conversion efficiency. In contrast, the 2T tandem cell suffers from current-matching issues and voltage losses due to the shared electrode, which leads to reduced V_{oc} and lower overall efficiency.

4.6 Comparative analysis with reported literature

To evaluate the validity and performance of our simulated devices, both 2T and 3T structures were benchmarked against recent state-of-the-art tandem solar cells reported in the literature. Table 4.4 summarizes key photovoltaic parameters – V_{oc}, J_{sc}, fill factor, and PCE – obtained in our study and compared with those of various reported works.

Table 4.4: Comparison of simulated 2T and 3T tandem solar cells with reported literature.

Device Structure Configuration	V_{oc} **(V)**	J_{sc} **(mA/cm²)**	**FF (%)**	**PCE (%)**	**Reference**
2T perovskite/silicon tandem solar cell consisting of a FTO/TiO_2/$MAPbI_3$/HTM top sub-cell and a SHJ (c−Si) bottom sub-cell.	1.05	36.5	73.18	28.03	[235]
2T monolithic perovskite-silicon heterojunction (*p-i-n* triple-halide perovskite on *n*-type SHJ Si, with SiO_x passivation and Ag grid).	1.983	20.24	81.96	32.9	[280]
2T flexible perovskite/silicon monolithic (Ag/ITO/a−Si(p)/a−Si(i)/n-Si/a−Si(i)/a−Si(n)/ITO/NiO_x/2PACz/perovskite/C_{60}/SnO_2/IZO/Ag/LiF, ≈70 µm Si).	1.89	19.51	80.9	29.83	[212]
2T perovskite–organic (wide-bandgap perovskite top with PM6:P2EH-1V organic bottom, transparent oxide interconnector).	1.37	28.60	85.5	26.7	[213]
2T monolithic perovskite/TOPCon silicon (with additive and substrate engineering).	1.931	19.89	81.54	31.32	[281]
3T quasi-interdigitated back-contact all-perovskite ($CsPbI_2Br$ top/inverted, $MASn_{0.5}Pb_{0.5}I_3$ bottom) – simulation.	2.19	16.75	83.9	30.3	[282]
3T all-perovskite triple-tandem medium-bandgap optimized (rational design for middle cell) – simulation.	2.88	11.00	78.9	24.96	[283]
3T perovskite–perovskite–silicon device comprising a $Cs_{0.2}FA_{0.8}Pb(I_{0.5}Br_{0.5})_3$ top cell, an $FAPbI_3$ middle cell, and a POLO–Si bottom cell.	2.75	16.45	83.40	24.40	[284]
Monolithic 3T perovskite/silicon tandem solar cell consisting of a perovskite top cell (FTO/TiO_2/$MAPbI_3$/HTM) and a silicon IBC-based bottom cell.	1.727	19.03	89.17	28.99	This study

The simulated results of both 2T and 3T perovskite/silicon tandem architectures confirm the high potential of these configurations for next-generation photovoltaic applications. The obtained characteristics demonstrate a strong alignment with state-of-the-art experimental findings and theoretical predictions reported for perovskite/silicon tandem

cells. The 2T configuration, composed of FTO/TiO_2/$MAPbI_3$/HTM/c−Si, achieves a PCE of 28.03 %, with a V_{oc} of 1.05 V and a J_{sc} of 36.5 mA/cm^2. These values fall within the typical range of 26–33 % reported for monolithic tandem solar cells using $MAPbI_3$-based perovskites as the top absorber. Such performance reflects efficient optical coupling between the top and bottom sub-cells, minimal parasitic absorption in the transport layers, and effective energy level alignment across interfaces. The relatively high short-circuit current indicates that photon transmission through the perovskite is sufficient to feed the crystalline silicon bottom cell, while the V_{oc} confirms a low interface recombination rate. However, the slightly moderate fill factor (73.18 %) compared to the best-reported 2T devices (typically 80–85 %) suggests the presence of non-ideal carrier extraction, likely associated with series resistance or limited charge selectivity in the HTM or recombination interface.

In contrast, the 3T tandem structure reveals clear advantages in charge collection and recombination management. The device exhibits a remarkably high fill factor of 89.17 % and an enhanced PCE of 28.99 %, which indicates superior charge extraction efficiency due to the partial electrical decoupling of the sub-cells. The V_{oc} of 1.727 V — approximately the sum of the two individual sub-cell voltages — arises from the quasi-independent operation of the top and bottom junctions. This decoupled behavior significantly reduces the current-matching constraint inherent to the 2T design. Consequently, both sub-cells operate near their respective maximum power points, improving the overall tandem performance. Furthermore, the improved FF and enhanced V_{oc} observed in the 3T simulation confirm the critical role of the intermediate recombination layer (Z interface). Proper energy-level alignment and high optical transparency of this layer enable efficient charge recombination without introducing additional resistive losses. The simultaneous improvement of PCE and V_{oc} indicates that the recombination interface maintains a low density of interface traps, ensuring fast and radiative recombination processes rather than non-radiative pathways.

Overall, our simulated results show that the 3T architecture can achieve performance comparable to or surpassing current high-efficiency tandem reports, while maintaining realistic and physically consistent device parameters. The accuracy of the simulated data relative to experimental trends underscores the reliability of the ATLAS Silvaco modeling framework and validates the chosen material properties, boundary conditions, and recombination models. In essence, the 3T architecture combines the optical benefits of the monolithic 2T tandem with the electrical flexibility of multi-terminal designs, offering a balanced trade-off between complexity and efficiency. This configuration thus represents a promising route toward stable, high-efficiency perovskite/silicon tandems suitable for large-scale and outdoor applications.

4.6.1 Key insights

- **Current matching mitigation:** The 3T configuration effectively mitigates the current-matching constraint of 2T tandems by allowing each sub-cell to operate independently. This ensures that both the perovskite and silicon cells contribute near their optimal operating points, maximizing power extraction under varying illumination or spectral conditions.

- **Strong agreement with literature:** The simulated metrics (V_{oc}, J_{sc}, FF, PCE) closely match experimental and theoretical reports for advanced perovskite/silicon tandem systems, confirming that the adopted physical models and interface assumptions are realistic.
- **Efficiency approaching the 30 % threshold:** Both the 2T and 3T designs deliver efficiencies approaching 30 %, placing them within the competitive range of the best-performing tandem cells reported to date. The 3T structure, in particular, shows potential for surpassing this limit with optimized layer properties.
- **High fill factor and low recombination losses:** The FF enhancement in the 3T structure (up to 89 %) reflects low series resistance and efficient charge collection due to the intermediate electrode's proper band alignment and conductivity. This high FF is often a signature of minimized resistive and recombination losses.
- **Role of the intermediate contact (Z layer):** The transparent conductive layer plays a central role in ensuring efficient carrier recombination and charge transfer between the sub-cells. Its optical and electrical optimization directly influences both V_{oc} and FF.
- **Pathways for future optimization:**
  1. Engineering advanced charge transport layers (e.g., SnO_2-based ETL, NiO_x HTL) with better mobility and stability.
  2. Applying interface passivation to suppress defect-assisted recombination at critical junctions.
  3. Enhancing optical coupling using anti-reflective coatings, light-trapping textures, or graded refractive index layers.
  4. Incorporating wide-bandgap perovskites (1.7–1.8 eV) to increase V_{oc} without compromising current in the bottom cell.
  5. Evaluating long-term stability and thermal robustness of the 3T design under operational conditions.

4.7 Conclusion

This chapter has presented a comprehensive investigation of a three-terminal perovskite/silicon tandem solar cell, demonstrating its structural blueprint, detailed physical modeling, and performance optimization within a TCAD framework. By decoupling the voltages of the perovskite top cell and silicon bottom cell, the 3T design achieves independent optimization of each subcell's operating point, yielding significant enhancements in fill factor and overall efficiency compared to traditional two-terminal tandems. Two-dimensional voltage mapping has elucidated the synergistic interplay between subcell biases, identifying optimal operating conditions that maximize power output under standard illumination. Benchmarking against established two-terminal architectures and state-of-the-art literature underscores the 3T configuration's superior robustness to spectral variations

and its potential to push photovoltaic efficiencies beyond current limits. These findings establish the three-terminal tandem as a promising pathway for next-generation high-performance photovoltaics and pave the way for subsequent exploration of advanced interconnect strategies, stability enhancement, and scale-up considerations.

Conclusion

This thesis has comprehensively explored the design, simulation, and optimization of perovskite-based photovoltaic devices, focusing on single-junction cells and advanced two- and three-terminal perovskite/silicon tandem architectures. Using Silvaco Atlas TCAD, supported by experimental validation, a robust modeling framework was established to accurately predict and enhance device performance.

The results confirm the strong potential of perovskite photovoltaics as a next-generation alternative to conventional silicon technology.

The single-junction FTO/TiO_2/$MAPbI_3$/HTM cell achieved a simulated efficiency of 12.68 %, closely matching the experimental 13.15 %, validating the adopted physical models, including Poole–Frenkel field-dependent mobility, SRH and Langevin recombination. Comparative analysis of hole transport layers (Spiro−OMeTAD, NiO_x, CuSCN, CuI) showed that while Spiro−OMeTAD provided the best overall performance, CuSCN exhibited the highest open-circuit voltage and short-circuit current density, indicating strong potential with improved conductivity and interface engineering.

Building on this, the two-terminal perovskite–silicon tandem reached an efficiency of 28.03 %, leveraging the complementary absorption spectra of both subcells. The inclusion of a 3 nm FTO recombination layer enabled efficient charge transfer with minimal optical loss. Optimal performance was achieved with a 15 nm intrinsic silicon layer and an operating temperature of 25 °C, balancing absorption and carrier collection.

The three-terminal tandem further enhanced performance, achieving 28.99 % efficiency and a fill factor of 89 %. By independently extracting voltages from each subcell, the 3T design eliminated current-matching constraints and allowed both subcells to operate near their maximum power points. Voltage mapping confirmed superior charge collection and resilience to spectral variations, aligning closely with state-of-the-art experimental results.

Beyond specific architectures, this work offers a validated numerical methodology and clear design guidelines for optimizing perovskite photovoltaics—covering layer thickness, doping, passivation, and thermal management. Efficiencies approaching 29 % demonstrate that perovskite–silicon tandems can surpass the Shockley–Queisser limit and achieve cost-effective, high-efficiency solar conversion suitable for large-scale deployment.

Remaining challenges include stability, lead toxicity, and scalability. Environmental degradation, phase instability, and fabrication complexity–particularly for 3T architectures–require continued material and process innovation.

Overall, this research establishes a coherent path from fundamental modeling to advanced device design, contributing valuable insights toward the realization of efficient, stable, and scalable perovskite-based solar technologies.

Bibliographie

[1] C. Yang, W. Hu, J. Liu, et al. "Achievements, challenges, and future prospects for industrialization of perovskite solar cells". en. In: *Light: Science & Applications* 13.1 (2024), p. 227. DOI: 10.1038/s41377-024-01461-x.

[2] A. Machín and F. Márquez. "Advancements in Photovoltaic Cell Materials: Silicon, Organic, and Perovskite Solar Cells". en. In: *Materials* 17.5 (2024), p. 1165. DOI: 10.3390/ma17051165.

[3] W. Shockley and H. J. Queisser. "Detailed Balance Limit of Efficiency of *p-n* Junction Solar Cells". en. In: *Journal of Applied Physics* 32.3 (1961), pp. 510–519. DOI: 10.1063/1.1736034.

[4] W. Fidel, I. Bel-Hadj, N. Doumit, G. Ferblantier, J. Botsoa, and E. Ntsoenzok. "SnOx-doped TiOx Thin Films by Reactive Magnetron Sputtering: A Promising Electron Transport Layer for Perovskite Solar Cells". In: *2025 IEEE 53rd Photovoltaic Specialists Conference (PVSC)*. Montreal, QC, Canada: IEEE, 2025, pp. 0956–0956. DOI: 10.1109/PVSC59419.2025.11132581.

[5] H. Chen, C. Liu, J. Xu, et al. "Improved charge extraction in inverted perovskite solar cells with dual-site-binding ligands". en. In: *Science* 384.6692 (2024), pp. 189–193. DOI: 10.1126/science.adm9474.

[6] T. Nakamura, Y. Kondo, N. Ohashi, et al. "Materials chemistry for metal halide perovskite photovoltaics". en. In: *Bulletin of the Chemical Society of Japan* 97.3 (2024), uoad025. DOI: 10.1093/bulcsj/uoad025.

[7] A. Harter, K. Artuk, F. Mathies, et al. "Perovskite/Silicon Tandem Solar Cells Above 30% Conversion Efficiency on Submicron-Sized Textured Czochralski-Silicon Bottom Cells with Improved Hole-Transport Layers". en. In: *ACS Applied Materials & Interfaces* 16.45 (2024), pp. 62817–62826. DOI: 10.1021/acsami.4c09264.

[8] D. Xu, M. Wu, Y. Bai, et al. "Record-Efficiency Inverted $CsPbI_3$ Perovskite Solar Cells Enabled by Rearrangement and Hydrophilic Modification of SAMs". en. In: *Advanced Functional Materials* 35.2 (2025), p. 2412946. DOI: 10.1002/adfm.202412946.

[9] S. Wang, H. Sun, P. Wang, et al. "Small Molecule Regulatory Strategy for Inorganic Perovskite Solar Cells with 368 mV of V_{OC} Deficit and its Application in Tandem Devices". en. In: *Advanced Energy Materials* 14.26 (2024), p. 2400151. DOI: 10.1002/aenm.202400151.

[10] M. Azhar, Y. Yalcinkaya, D. T. Cuzzupè, Y. Abebe Temitmie, M. I. Haider, and L. Schmidt-Mende. "Perovskite Thin Films Solar Cells: The Gas Quenching Method". In: *Materials and Sustainability* (2025), p. 5. DOI: 10.53941/matsus.2025.100005.

[11] L. Arunagiri and F. Gao. "Molecule doping enables high-quality perovskite junctions for all-perovskite tandem solar cells". en. In: *National Science Review* 11.7 (2024), nwae170. DOI: 10.1093/nsr/nwae170.

[12] B. P. Singh, S. K. Goyal, and P. Kumar. "Solar PV cell materials and technologies: Analyzing the recent developments". en. In: *Materials Today: Proceedings* 43 (2021), pp. 2843–2849. DOI: 10.1016/j.matpr.2021.01.003.

[13] A. Allisy. "Henri Becquerel: The Discovery of Radioactivity". en. In: *Radiation Protection Dosimetry* 68.1 (1996), pp. 3–10. DOI: 10.1093/oxfordjournals.rpd.a031848.

[14] "Effect of Light on Selenium During the Passage of An Electric Current*". In: *Nature* 7.173 (1873), pp. 303–303. DOI: 10.1038/007303e0.

[15] X. Li, Q. Zhang, Y. Chen, X. Liu, S. Braun, and M. Fahlman. "Fermi Level Shifts of Organic Semiconductor Films in Ambient Air". en. In: *ACS Applied Materials & Interfaces* 17.3 (2025), pp. 5153–5164. DOI: 10.1021/acsami.4c13674.

[16] J. Perlin. *Let it shine: the 6,000-year story of solar energy*. eng. Fully revised and expanded. Novato, California: New World library, 2013.

[17] D. Lincot. "The new paradigm of photovoltaics: From powering satellites to powering humanity". en. In: *Comptes Rendus. Physique* 18.7-8 (2017), pp. 381–390. DOI: 10.1016/j.crhy.2017.09.003.

[18] J. Liu, Y. He, L. Ding, et al. "Perovskite/silicon tandem solar cells with bilayer interface passivation". en. In: *Nature* 635.8039 (2024), pp. 596–603. DOI: 10.1038/s41586-024-07997-7.

[19] A. S. Subbiah, A. Razzaq, T. G. Allen, and S. De Wolf. "Outlook on monolithic perovskite/silicon tandem photovoltaics". en. In: *MRS Bulletin* 49.12 (2024), pp. 1251–1264. DOI: 10.1557/s43577-024-00826-2.

[20] V. John. "Possibility of Seawater Desalination Using Reverse Osmosis Powered by Solar Photovoltaic Electricity on the Island of Crete, Greece". In: *International Journal of Advanced Multidisciplinary Research and Studies* 5.3 (2025), pp. 851–858. DOI: 10.62225/2583049X.2025.5.3.4367.

[21] U. R. Qureshi, A. Rashid, N. Altini, V. Bevilacqua, and M. La Scala. "Explainable Intelligent Inspection of Solar Photovoltaic Systems with Deep Transfer Learning: Considering Warmer Weather Effects Using Aerial Radiometric Infrared Thermography". en. In: *Electronics* 14.4 (2025), p. 755. DOI: 10.3390/electronics14040755.

[22] NCERT. *Physics: Textbook for class XII Part - II*. eng. OCLC: 1144575996. New Delhi: National Council of Educational Research and Training, 2018.

[23] P. Y. Yu and M. Cardona. "Electronic Band Structures". en. In: *Fundamentals of Semiconductors*. Berlin, Heidelberg: Springer Berlin Heidelberg, 2010, pp. 17–106. DOI: 10.1007/978-3-642-00710-1_2.

[24] P. Y. Yu and M. Cardona. "Electronic Properties of Defects". en. In: *Fundamentals of Semiconductors*. Berlin, Heidelberg: Springer Berlin Heidelberg, 2010, pp. 159–202. DOI: 10.1007/978-3-642-00710-1_4.

[25] A. D. Terna, E. E. Elemike, J. I. Mbonu, O. E. Osafile, and R. O. Ezeani. "The future of semiconductors nanoparticles: Synthesis, properties and applications". en. In: *Materials Science and Engineering: B* 272 (2021), p. 115363. DOI: 10.1016/j.mseb.2021.115363.

[26] J. B. Marion. "THE STRUCTURE OF MATTER". en. In: *Physics in the Modern World*. Elsevier, 1981, pp. 529–552. DOI: 10.1016/B978-0-12-472280-4.50022-8.

[27] "Photocatalysis by inorganic solid materials". en. In: *Advances in Inorganic Chemistry*. Vol. 63. Elsevier, 2011, pp. 395–430. DOI: 10.1016/B978-0-12-385904-4.00001-9.

[28] J. Jasieniak, M. Califano, and S. E. Watkins. "Size-Dependent Valence and Conduction Band-Edge Energies of Semiconductor Nanocrystals". en. In: *ACS Nano* 5.7 (2011), pp. 5888–5902. DOI: 10.1021/nn201681s.

[29] B. G. Streetman. "Semiconductors and Transistors". en. In: *Reference Data for Engineers*. Elsevier, 2002, pp. 18–1–18–27. DOI: 10.1016/B978-075067291-7/50020-0.

[30] R. F. Pierret. *Semiconductor device fundamentals*. Reading, Mass: Addison-Wesley, 1996.

[31] H. Jouhara, A. Żabnieńska-Góra, N. Khordehgah, et al. "Thermoelectric generator (TEG) technologies and applications". en. In: *International Journal of Thermofluids* 9 (2021), p. 100063. DOI: 10.1016/j.ijft.2021.100063.

[32] L. Hirst. "Principles of Solar Energy Conversion". en. In: *Comprehensive Renewable Energy*. Elsevier, 2022, pp. 234–255. DOI: 10.1016/B978-0-12-819727-1.00112-6.

[33] J. Demas and S. Demas. "Luminescence". en. In: *Encyclopedia of Physical Science and Technology*. Elsevier, 2003, pp. 799–823. DOI: 10.1016/B0-12-227410-5/00389-6.

[34] S. M. Sze. *Physics of semiconductor devices*. 2nd ed. New York: Wiley, 1981.

[35] E. Spain and A. Venkatanarayanan. "Review of Physical Principles of Sensing and Types of Sensing Materials". en. In: *Comprehensive Materials Processing*. Elsevier, 2014, pp. 5–46. DOI: 10.1016/B978-0-08-096532-1.01302-9.

[36] "Design of active photocatalysts and visible light photocatalysis". en. In: *Interface Science and Technology*. Vol. 32. Elsevier, 2021, pp. 557–623. DOI: 10.1016/B978-0-12-818806-4.00012-7.

[37] H. J. Jenniches. "Basic Semiconductor Physics". en. In: *Spin Electronics*. Ed. by R. Beig, J. Ehlers, U. Frisch, et al. Vol. 569. Series Title: Lecture Notes in Physics. Berlin, Heidelberg: Springer Berlin Heidelberg, 2001, pp. 172–198. DOI: 10.1007/3-540-45258-3_8.

[38] M. S. Silberberg and P. Amateis. *Chemistry: the molecular nature of matter and change*. Ninth edition. Dubuque: McGraw-Hill Education, 2021.

[39] Y. Yin, Z. Cheng, L. Wang, K. Jin, and W. Wang. "Graphene, a material for high temperature devices – intrinsic carrier density, carrier drift velocity and lattice energy". en. In: *Scientific Reports* 4.1 (2014), p. 5758. DOI: 10.1038/srep05758.

[40] T. T. Mnatsakanov, M. E. Levinshtein, A. G. Tandoev, and S. N. Yurkov. "Transport phenomena in intrinsic semiconductors and insulators at high current densities: Suppression of the broken neutrality drift". en. In: *Journal of Applied Physics* 114.6 (2013), p. 064503. DOI: 10.1063/1.4817657.

[41] N. P. The, D. N. Thao, and H. K. Hieu. "Effects of electric field and device size on the electron velocity in p-i-n GaAs semiconductor". en. In: *Physics Letters A* 490 (2023), p. 129174. DOI: 10.1016/j.physleta.2023.129174.

[42] B. G. Streetman and S. K. Banerjee. *Solid state electronic devices*. eng. 7. ed., global ed. Always learning. Boston Munich: Pearson, 2016.

[43] S. M. Sze and K. K. Ng. *Physics of semiconductor devices*. eng. 3. ed. Wiley-Interscience online books. Hoboken, N.J: Wiley-Interscience, 2007.

[44] B. G. Streetman and S. Banerjee. *Solid state electronic devices*. eng. 6th ed., [eastern economy ed.] OCLC: 1116729508. Dehli: PHI Learning, 2013.

[45] T. Kita, Y. Harada, and S. Asahi. "Fundamentals of Semiconductors". en. In: *Energy Conversion Efficiency of Solar Cells*. Singapore: Springer Singapore, 2019, pp. 157–202. DOI: 10.1007/978-981-13-9089-0_8.

[46] S. M. Sze. *Physics of semiconductor devices*. eng. 2. ed., [Nachdr.] A Wiley-Interscience publication. New York, N.Y.: Wiley, 2003.

[47] C. M. Wolfe, N. Holonyak, and G. E. Stillman. *Physical properties of semiconductors*. eng. International ed. Prentice Hall series in solid state physical electronics. Englewood Cliffs, N. J.: Prentice Hall, 1989.

[48] N. W. Ashcroft and N. D. Mermin. *Solid state physics*. eng. Fort Worth Philadelphia San Diego [etc.]: Saunders college publ, 1976.

[49] C. Hilsum. "Semiconductors (2nd edn)". In: *Physics Bulletin* 30.12 (1979), pp. 528–528. DOI: 10.1088/0031-9112/30/12/049.

[50] N. Arora. "Review of Basic Semiconductor and pn Junction Theory". In: *MOSFET Models for VLSI Circuit Simulation*. Ed. by S. Selberherr. Vienna: Springer Vienna, 1993, pp. 15–68. DOI: 10.1007/978-3-7091-9247-4_2.

[51] S. S. Li. "p-n Junction Diodes". en. In: *Semiconductor Physical Electronics*. Ed. by S. S. Li. New York, NY: Springer New York, 2006, pp. 334–380. DOI: 10.1007/0-387-37766-2_11.

[52] T. Soga. "Fundamentals of Solar Cell". en. In: *Nanostructured Materials for Solar Energy Conversion*. Elsevier, 2006, pp. 3–43. DOI: 10.1016/B978-044452844-5/50002-0.

[53] P. Fulay and J.-K. Lee. *Electronic, Magnetic, and Optical Materials*. en. 0th ed. CRC Press, 2016. DOI: 10.1201/9781439882603.

[54] R. Hui and M. O'sullivan. "Fundamentals of optical devices". en. In: *Fiber-Optic Measurement Techniques*. Elsevier, 2023, pp. 1–135. DOI: 10.1016/B978-0-323-90957-0.00002-3.

[55] Y. Pan, T. Jian, P. Gu, et al. "Precise p-type and n-type doping of two-dimensional semiconductors for monolithic integrated circuits". en. In: *Nature Communications* 15.1 (2024), p. 9631. DOI: 10.1038/s41467-024-54050-2.

[56] S.-M. Kang and Y. Leblebici. *CMOS digital integrated circuits: analysis and design*. eng. 3. Aufl. Boston: McGraw-Hill, 2003.

[57] H. Geng, ed. *Semiconductor manufacturing handbook*. eng. Second edition. McGraw-Hill handbooks. New York Chicago San Francisco: McGraw-Hill Education, 2018.

[58] P. Berger and A. Ramesh. "Negative Differential Resistance Devices and Circuits". en. In: *Comprehensive Semiconductor Science and Technology*. Elsevier, 2011, pp. 176–241. DOI: 10.1016/B978-0-44-453153-7.00013-4.

[59] M. T. Thompson. "Review of Diode Physics and the Ideal (and Later, Nonideal) Diode". en. In: *Intuitive Analog Circuit Design*. Elsevier, 2014, pp. 53–86. DOI: 10.1016/B978-0-12-405866-8.00003-6.

[60] M. Kubát. "Properties of a pn Junction in a Semiconductor; Semiconductor—Metal Contact". en. In: *Power Semiconductors*. Berlin, Heidelberg: Springer Berlin Heidelberg, 1984, pp. 54–142. DOI: 10.1007/978-3-662-02418-8_3.

[61] B. M. E. "Memoire sur les Effets Electriques Produits sous l'Influence des Rayons Solaires". In: *Comptes Rendus Hebdomadaires des Seances de L'Academie des Sciences* 9 (1839), pp. 561–567.

[62] S. Hubbard. "Recombination". en. In: *Photovoltaic Solar Energy*. Ed. by A. Reinders, P. Verlinden, W. Sark, and A. Freundlich. 1st ed. Wiley, 2016, pp. 39–46. DOI: 10.1002/9781118927496.ch5.

[63] A. P. French and E. F. Taylor. *An introduction to quantum physics*. eng. Reprint. The M.I.T. introductory physics series. Cheltenham: Nelson Thornes, 2001.

[64] S. Boyer-Richard, F. Fan, A. Beck, et al. "Investigation of III-V GaP solar cell on silicon substrate". In: *EPJ Photovoltaics* 14 (2023), p. 31. DOI: 10.1051/epjpv/2023020.

[65] D. Luo, R. Su, W. Zhang, Q. Gong, and R. Zhu. "Minimizing non-radiative recombination losses in perovskite solar cells". en. In: *Nature Reviews Materials* 5.1 (2019), pp. 44–60. DOI: 10.1038/s41578-019-0151-y.

[66] T. Markvart. "Shockley: Queisser detailed balance limit after 60 years". en. In: *WIREs Energy and Environment* 11.4 (2022), e430. DOI: 10.1002/wene.430.

[67] T. Tiedje, E. Yablonovich, G. Cody, and B. Brooks. "Limiting efficiency of silicon solar cells". In: *IEEE TRANSACTIONS ON ELECTRON DEVICES* ED-31 (1984).

[68] A. Zanatta. "The Shockley–Queisser limit and the conversion efficiency of silicon-based solar cells". en. In: *Results in Optics* 9 (2022), p. 100320. DOI: 10.1016/j.rio.2022.100320.

[69] S. J. Fonash. "Material Properties and Device Physics Basic to Photovoltaics". en. In: *Solar Cell Device Physics*. Elsevier, 2010, pp. 9–65. DOI: 10.1016/B978-0-12-374774-7.00002-9.

[70] T. Goudon, V. Miljanović, and C. Schmeiser. "On the Shockley–Read–Hall Model: Generation-Recombination in Semiconductors". en. In: *SIAM Journal on Applied Mathematics* 67.4 (2007), pp. 1183–1201. DOI: 10.1137/060650751.

[71] K. T. Delaney, P. Rinke, and C. G. Van De Walle. "Auger recombination rates in nitrides from first principles". en. In: *Applied Physics Letters* 94.19 (2009), p. 191109. DOI: 10.1063/1.3133359.

[72] L. C. Hirst and N. J. Ekins-Daukes. "Fundamental losses in solar cells". en. In: *Progress in Photovoltaics: Research and Applications* 19.3 (2011), pp. 286–293. DOI: 10.1002/pip.1024.

[73] M. Wright and A. Uddin. "Organic—inorganic hybrid solar cells: A comparative review". en. In: *Solar Energy Materials and Solar Cells* 107 (2012), pp. 87–111. DOI: 10.1016/j.solmat.2012.07.006.

[74] M. J. Heredia-Rios, L. Hernandez-Martinez, M. Linares-Aranda, M. Moreno-Moreno, and J. F. Méndez. "Analysis of Losses Associated with Series Resistance (Rs) in Simple-Structured c-Si Solar Cells". en. In: *Energies* 17.7 (2024), p. 1520. DOI: 10.3390/en17071520.

[75] Gius Uddin. "Development of Simplified In Situ Processing Routes for Rear-Side Patterning of Silicon Heterojunction Interdigitated Back Contact (SHJ-IBC) Solar Cells". en. In: (2018). DOI: 10.13140/RG.2.2.11514.13767.

[76] A. O. Ali, A. T. Elgohr, M. H. El-Mahdy, et al. "Advancements in photovoltaic technology: A comprehensive review of recent advances and future prospects". en. In: *Energy Conversion and Management: X* 26 (2025), p. 100952. DOI: 10.1016/j.ecmx.2025.100952.

[77] M. Schmid. "Revisiting the Definition of Solar Cell Generations". en. In: *Advanced Optical Materials* 11.20 (2023), p. 2300697. DOI: 10.1002/adom.202300697.

[78] Z. Wang, F. Lang, L. Yin, Y. Zhang, J. Shi, and W. Zhang. "Low-light response performance analysis of crystalline silicon solar cells and modules". en. In: *Journal of Renewable and Sustainable Energy* 17.5 (2025), p. 053705. DOI: 10.1063/5.0288470.

[79] S. Mohammadi, N. Kaur, and D. R. Radu. "Nanoscale Cu2ZnSnSxSe(4—x) (CZTS/Se) for Sustainable Solutions in Renewable Energy, Sensing, and Nanomedicine". en. In: *Crystals* 14.5 (2024), p. 479. DOI: 10.3390/cryst14050479.

[80] J. Lim, N.-G. Park, S. Il Seok, and M. Saliba. "All-perovskite tandem solar cells: from fundamentals to technological progress". en. In: *Energy & Environmental Science* 17.13 (2024), pp. 4390–4425. DOI: 10.1039/D3EE03638C.

[81] A. B. Obisesan. "Recent Developments in Solar Energy (2023–2025)". In: *International Journal of Technology, Management and Humanities* 11.03 (2025), pp. 11–13. DOI: 10.21590/ijtmh.11.03.02.

[83] X. Tao, X. Yang, Q. Zeng, et al. "Interface Engineering with Oxygen-Doped Amorphous Silicon for Stabilizing Light Soaking Gains in Silicon Solar Cells". en. In: *Advanced Functional Materials* (2025), e16753. DOI: 10.1002/adfm.202516753.

[84] Y. Fu. "The Road to Breaking Through Limits: Improving Photoelectric Conversion Efficiency of Perovskite Solar Cells". In: *Highlights in Science, Engineering and Technology* 147 (2025), pp. 265–275. DOI: 10.54097/n3tsj743.

[85] C. Battaglia, A. Cuevas, and S. De Wolf. "High-efficiency crystalline silicon solar cells: status and perspectives". en. In: *Energy & Environmental Science* 9.5 (2016), pp. 1552–1576. DOI: 10.1039/C5EE03380B.

[86] R. Dallaev, T. Pisarenko, N. Papež, and V. Holcman. "Overview of the Current State of Flexible Solar Panels and Photovoltaic Materials". en. In: *Materials* 16.17 (2023), p. 5839. DOI: 10.3390/ma16175839.

[87] A. M. H. Saad. "Next-Generation Solar Cells: Advancements in Materials, Architectures, and System Integration for A Sustainable Energy Future." In: *American Journal of Innovation in Science and Engineering* 4.2 (2025), pp. 23–30. DOI: 10.54536/ajise.v4i2.3832.

[88] A. Bosio, S. Pasini, and N. Romeo. "The History of Photovoltaics with Emphasis on CdTe Solar Cells and Modules". en. In: *Coatings* 10.4 (2020), p. 344. DOI: 10.3390/coatings10040344.

[89] I. Dharmadasa and A. Alam. "How to Achieve Efficiencies beyond 22.1% for CdTe-Based Thin-Film Solar Cells". en. In: *Energies* 15.24 (2022), p. 9510. DOI: 10.3390/en15249510.

[90] K. Makita, Y. Kamikawa, H. Mizuno, et al. "GaAs//CuInGaSe-Based Multijunction Solar Cells with 30% Efficiency Under Low Concentrated Sunlight". en. In: *Solar RRL* 8.19 (2024), p. 2400351. DOI: 10.1002/solr.202400351.

[91] J. Yan and B. R. Saunders. "Third-generation solar cells: a review and comparison of polymer:fullerene, hybrid polymer and perovskite solar cells". en. In: *RSC Adv.* 4.82 (2014), pp. 43286–43314. DOI: 10.1039/C4RA07064J.

[92] M. W. Aziz, N. A. Ahmad, and H. W. Hamed. "An Overview of High-Efficiency Perovskite and Perovskite-Based Tandem Solar Cells: Progress in 2025". In: *Scientific Journal of Engineering, and Technology* 2.2 (2025), pp. 114–118. DOI: 10.69739/sjet.v2i2.946.

[93] J. Suo, H. Pettersson, and B. Yang. "Sustainable Approaches to Address Lead Toxicity in Halide Perovskite Solar Cells: A Review of Lead Encapsulation and Recycling Solutions". en. In: *EcoMat* 7.1 (2025), e12511. DOI: 10.1002/eom2.12511.

[94] C. Ding, D. Wang, D. Liu, et al. "Over 15% Efficiency PbS Quantum-Dot Solar Cells by Synergistic Effects of Three Interface Engineering: Reducing Nonradiative Recombination and Balancing Charge Carrier Extraction". en. In: *Advanced Energy Materials* 12.35 (2022), p. 2201676. DOI: 10.1002/aenm.202201676.

[95] P. Zhang, M. Li, and W.-C. Chen. "A Perspective on Perovskite Solar Cells: Emergence, Progress, and Commercialization". In: *Frontiers in Chemistry* 10 (2022), p. 802890. DOI: 10.3389/fchem.2022.802890.

[96] M. T. Hasan, M. M. Hasan, M. A. Jafor, M. C. Barmon, and M. Abrar. "Photovoltaic Technology in Industrial and Building Applications: A Path Toward Sustainable Energy". In: *European Journal of Theoretical and Applied Sciences* 3.2 (2025), pp. 236–248. DOI: 10.59324/ejtas.2025.3(2).18.

[97] G. Rose. "Beschreibung einiger neuen Mineralien des Urals". en. In: *Annalen der Physik* 126.8 (1840), pp. 652–656. DOI: 10.1002/andp.18401260807.

[98] O. Tschauner, C. Ma, J. R. Beckett, C. Prescher, V. B. Prakapenka, and G. R. Rossman. "Discovery of bridgmanite, the most abundant mineral in Earth, in a shocked meteorite". en. In: *Science* 346.6213 (2014), pp. 1100–1102. DOI: 10.1126/science.1259369.

[99] V. M. Goldschmidt. "Die Gesetze der Krystallochemie". de. In: *Die Naturwissenschaften* 14.21 (1926), pp. 477–485. DOI: 10.1007/BF01507527.

[100] C. J. Bartel, C. Sutton, B. R. Goldsmith, et al. "New tolerance factor to predict the stability of perovskite oxides and halides". en. In: *Science Advances* 5.2 (2019), eaav0693. DOI: 10.1126/sciadv.aav0693.

[101] A. M. Glazer. "The classification of tilted octahedra in perovskites". In: *Acta Crystallographica Section B Structural Crystallography and Crystal Chemistry* 28.11 (1972), pp. 3384–3392. DOI: 10.1107/S0567740872007976.

[102] H. L. Wells. "Über die Cäsium- und Kalium-Bleihalogenide". en. In: *Zeitschrift für anorganische Chemie* 3.1 (1893), pp. 195–210. DOI: 10.1002/zaac.18930030124.

[103] A. Marstrander, C. Møller, and K. D. v. selskab. *The structure of white cesium lead (II) bromide, CsPbBr3*. Mathematisk-fysiske meddelelser. tex.lccn: 67107784. Munksgaard, 1966.

[104] D. Weber. "CH_3 NH_3 $SnBr_x$ I_{3-x} (x = 0-3), ein Sn(II)-System mit kubischer Perowskitstruktur / CH_3 NH_3 $SnBr_x$ I_{3-x} (x = 0-3), a Sn(II)-System with Cubic Perovskite Structure". en. In: *Zeitschrift für Naturforschung B* 33.8 (1978), pp. 862–865. DOI: 10.1515/znb-1978-0809.

[105] D. B. Mitzi, C. A. Feild, W. T. A. Harrison, and A. M. Guloy. "Conducting tin halides with a layered organic-based perovskite structure". en. In: *Nature* 369.6480 (1994), pp. 467–469. DOI: 10.1038/369467a0.

[106] D. Mitzi, C. Feild, Z. Schlesinger, and R. Laibowitz. "Transport, Optical, and Magnetic Properties of the Conducting Halide Perovskite CH3NH3SnI3". en. In: *Journal of Solid State Chemistry* 114.1 (1995), pp. 159–163. DOI: 10.1006/jssc.1995.1023.

[107] K. Liang, D. B. Mitzi, and M. T. Prikas. "Synthesis and Characterization of Organic−Inorganic Perovskite Thin Films Prepared Using a Versatile Two-Step Dipping Technique". en. In: *Chemistry of Materials* 10.1 (1998), pp. 403–411. DOI: 10.1021/cm970568f.

[108] D. B. Mitzi. "Templating and structural engineering in organic–inorganic perovskites". In: *Journal of the Chemical Society, Dalton Transactions* 1 (2001), pp. 1–12. DOI: 10.1039/b007070j.

[109] D. B. Mitzi, K. Chondroudis, and C. R. Kagan. "Organic-inorganic electronics". In: *IBM Journal of Research and Development* 45.1 (2001), pp. 29–45. DOI: 10.1147/rd.451.0029.

[110] K. D. Karlin, ed. *Progress in Inorganic Chemistry*. en. 1st ed. Vol. 57. Progress in Inorganic Chemistry. Wiley, 2011. DOI: 10.1002/9781118148235.

[111] J. Breternitz, F. Lehmann, S. A. Barnett, H. Nowell, and S. Schorr. "Role of the Iodide–Methylammonium Interaction in the Ferroelectricity of CH_3 NH_3 PbI_3". en. In: *Angewandte Chemie International Edition* 59.1 (2020), pp. 424–428. DOI: 10.1002/anie.201910599.

[112] K. T. Butler. "The chemical forces underlying octahedral tilting in halide perovskites". en. In: *Journal of Materials Chemistry C* 6.44 (2018), pp. 12045–12051. DOI: 10.1039/C8TC02976H.

[113] M. R. Filip and F. Giustino. "The geometric blueprint of perovskites". en. In: *Proceedings of the National Academy of Sciences* 115.21 (2018), pp. 5397–5402. DOI: 10.1073/pnas.1719179115.

[114] R. D. Shannon. "Revised effective ionic radii and systematic studies of interatomic distances in halides and chalcogenides". In: *Acta Crystallographica Section A* 32.5 (1976), pp. 751–767. DOI: 10.1107/S0567739476001551.

[115] W. Travis, E. N. K. Glover, H. Bronstein, D. O. Scanlon, and R. G. Palgrave. "On the application of the tolerance factor to inorganic and hybrid halide perovskites: a revised system". en. In: *Chemical Science* 7.7 (2016), pp. 4548–4556. DOI: 10.1039/C5SC04845A.

[116] E. I. Marchenko, S. A. Fateev, A. A. Petrov, et al. "Database of Two-Dimensional Hybrid Perovskite Materials: Open-Access Collection of Crystal Structures, Band Gaps, and Atomic Partial Charges Predicted by Machine Learning". en. In: *Chemistry of Materials* 32.17 (2020), pp. 7383–7388. DOI: 10.1021/acs.chemmater.0c02290.

[117] Y. Yan, W.-J. Yin, T. Shi, W. Meng, and C. Feng. "Defect Physics of CH3NH3PbX3 (X = I, Br, Cl) Perovskites". en. In: *Organic-Inorganic Halide Perovskite Photovoltaics*. Ed. by N.-G. Park, M. Grätzel, and T. Miyasaka. Cham: Springer International Publishing, 2016, pp. 79–105. DOI: 10.1007/978-3-319-35114-8_4.

[118] C. C. Stoumpos, D. H. Cao, D. J. Clark, et al. "Ruddlesden–Popper Hybrid Lead Iodide Perovskite 2D Homologous Semiconductors". en. In: *Chemistry of Materials* 28.8 (2016), pp. 2852–2867. DOI: 10.1021/acs.chemmater.6b00847.

[119] C. C. Stoumpos, C. D. Malliakas, and M. G. Kanatzidis. "Semiconducting Tin and Lead Iodide Perovskites with Organic Cations: Phase Transitions, High Mobilities, and Near-Infrared Photoluminescent Properties". en. In: *Inorganic Chemistry* 52.15 (2013), pp. 9019–9038. DOI: 10.1021/ic401215x.

[120] M. Seitz, A. J. Magdaleno, N. Alcázar-Cano, et al. "Exciton diffusion in two-dimensional metal-halide perovskites". en. In: *Nature Communications* 11.1 (2020), p. 2035. DOI: 10.1038/s41467-020-15882-w.

[121] J. Tong, Z. Song, D. H. Kim, et al. “Carrier lifetimes of >1 s in Sn-Pb perovskites enable efficient all-perovskite tandem solar cells”. en. In: *Science* 364.6439 (2019), pp. 475–479. DOI: 10.1126/science.aav7911.

[122] G. Kim, H. Min, K. S. Lee, D. Y. Lee, S. M. Yoon, and S. I. Seok. “Impact of strain relaxation on performance of -formamidinium lead iodide perovskite solar cells”. en. In: *Science* 370.6512 (2020), pp. 108–112. DOI: 10.1126/science.abc4417.

[123] D. G. Billing and A. Lemmerer. “Synthesis, characterization and phase transitions in the inorganic–organic layered perovskite-type hybrids $[(C_n H_{2n+1} NH_3)_2 PbI_4]$, $n = 4$, 5 and 6”. In: *Acta Crystallographica Section B Structural Science* 63.5 (2007), pp. 735–747. DOI: 10.1107/S0108768107031758.

[124] W. Paritmongkol, N. S. Dahod, A. Stollmann, et al. “Synthetic Variation and Structural Trends in Layered Two-Dimensional Alkylammonium Lead Halide Perovskites”. en. In: *Chemistry of Materials* 31.15 (2019), pp. 5592–5607. DOI: 10.1021/acs.chemmater.9b01318.

[125] P. Gratia, I. Zimmermann, P. Schouwink, et al. “The Many Faces of Mixed Ion Perovskites: Unraveling and Understanding the Crystallization Process”. en. In: *ACS Energy Letters* 2.12 (2017), pp. 2686–2693. DOI: 10.1021/acsenergylett.7b00981.

[126] U.-G. Jong, C.-J. Yu, G.-C. Ri, et al. “Influence of water intercalation and hydration on chemical decomposition and ion transport in methylammonium lead halide perovskites”. en. In: *Journal of Materials Chemistry A* 6.3 (2018), pp. 1067–1074. DOI: 10.1039/C7TA09112E.

[127] P. E. Marchezi, E. M. Therézio, R. Szostak, et al. “Degradation mechanisms in mixed-cation and mixed-halide $Cs_x FA_{1-x} Pb(Br_y I_{1-y})_3$ perovskite films under ambient conditions”. en. In: *Journal of Materials Chemistry A* 8.18 (2020), pp. 9302–9312. DOI: 10.1039/D0TA01201G.

[128] L. E. Mundt and L. T. Schelhas. “Structural Evolution During Perovskite Crystal Formation and Degradation: In Situ and Operando X-Ray Diffraction Studies”. en. In: *Advanced Energy Materials* 10.26 (2020), p. 1903074. DOI: 10.1002/aenm.201903074.

[129] J. Cao, X. Jing, J. Yan, et al. “Identifying the Molecular Structures of Intermediates for Optimizing the Fabrication of High-Quality Perovskite Films”. en. In: *Journal of the American Chemical Society* 138.31 (2016), pp. 9919–9926. DOI: 10.1021/jacs.6b04924.

[130] A. A. Petrov, I. P. Sokolova, N. A. Belich, et al. “Crystal Structure of DMF-Intermediate Phases Uncovers the Link Between $CH_3 NH_3 PbI_3$ Morphology and Precursor Stoichiometry”. en. In: *The Journal of Physical Chemistry C* 121.38 (2017), pp. 20739–20743. DOI: 10.1021/acs.jpcc.7b08468.

[131] A. S. Thind, X. Huang, J. Sun, and R. Mishra. “First-Principles Prediction of a Stable Hexagonal Phase of $CH_3 NH_3 PbI_3$”. en. In: *Chemistry of Materials* 29.14 (2017), pp. 6003–6011. DOI: 10.1021/acs.chemmater.7b01781.

[132] M. Szafrański and A. Katrusiak. "Phase transitions in the layered structure of diguanidinium tetraiodoplumbate". en. In: *Physical Review B* 61.2 (2000), pp. 1026–1035. DOI: 10.1103/PhysRevB.61.1026.

[133] G. H. Imler, X. Li, B. Xu, et al. "Solid state transformation of the crystalline monohydrate (CH_3 NH_3)PbI_3 (H_2 O) to the (CH_3 NH_3)PbI_3 perovskite". en. In: *Chemical Communications* 51.56 (2015), pp. 11290–11292. DOI: 10.1039/C5CC03741G.

[134] D. A. Egger, A. M. Rappe, and L. Kronik. "Hybrid Organic–Inorganic Perovskites on the Move". en. In: *Accounts of Chemical Research* 49.3 (2016), pp. 573–581. DOI: 10.1021/acs.accounts.5b00540.

[135] F. V. Maziviero, D. M. A. Melo, R. L. B. A. Medeiros, et al. "Advancements and Prospects in Perovskite Solar Cells: From Hybrid to All-Inorganic Materials". en. In: *Nanomaterials* 14.4 (2024), p. 332. DOI: 10.3390/nano14040332.

[136] X. Zhang, M. E. Turiansky, and C. G. Van De Walle. "All-inorganic halide perovskites as candidates for efficient solar cells". en. In: *Cell Reports Physical Science* 2.10 (2021), p. 100604. DOI: 10.1016/j.xcrp.2021.100604.

[137] L. Schmidt-Mende, V. Dyakonov, S. Olthof, et al. "Roadmap on organic–inorganic hybrid perovskite semiconductors and devices". en. In: *APL Materials* 9.10 (2021), p. 109202. DOI: 10.1063/5.0047616.

[138] Y. Li, C. Yang, W. Guo, T. Duan, Z. Zhou, and Y. Zhou. "All-inorganic perovskite solar cells featuring mixed group IVA cations". en. In: *Nanoscale* 15.16 (2023), pp. 7249–7260. DOI: 10.1039/D3NR00133D.

[139] H. Wu, Z. Sun, H. Li, et al. "Review of all-inorganic perovskites and their tandem solar cells with crystalline silicon". en. In: *Energy Materials and Devices* 2.3 (2024), p. 9370045. DOI: 10.26599/EMD.2024.9370045.

[140] C. Shen, T. Ye, P. Yang, and G. Chen. "All–Inorganic Perovskite Solar Cells: Defect Regulation and Emerging Applications in Extreme Environments". en. In: *Advanced Materials* 36.25 (2024), p. 2401498. DOI: 10.1002/adma.202401498.

[141] R. He, S. Ren, C. Chen, et al. "Wide-bandgap organic–inorganic hybrid and all-inorganic perovskite solar cells and their application in all-perovskite tandem solar cells". en. In: *Energy & Environmental Science* 14.11 (2021), pp. 5723–5759. DOI: 10.1039/D1EE01562A.

[142] I. M. Maafa. "All-Inorganic Perovskite Solar Cells: Recent Advancements and Challenges". eng. In: *Nanomaterials (Basel, Switzerland)* 12.10 (2022), p. 1651. DOI: 10.3390/nano12101651.

[143] J. Wang, J. Zhang, Y. Zhou, et al. "Highly efficient all-inorganic perovskite solar cells with suppressed non-radiative recombination by a Lewis base". en. In: *Nature Communications* 11.1 (2020), p. 177. DOI: 10.1038/s41467-019-13909-5.

[144] T. D. Raju, V. Murugadoss, K. A. Nirmal, T. D. Dongale, A. V. Kesavan, and T. G. Kim. "Advancements in perovskites for solar cell commercialization: A review". en. In: *Advanced Powder Materials* 4.2 (2025), p. 100275. DOI: 10.1016/j.apmate.2025.100275.

[145] N. Kaur, J. Madan, A. Perumal, and R. Pandey. "Current matched all perovskite tandem solar cells with low lead perovskites achieving 31.9% efficiency and enhanced stability". en. In: *Scientific Reports* 15.1 (2025), p. 29724. DOI: 10.1038/s41598-025-99575-8.

[146] Z. Kuang, B. Liang, T. Huang, T. Shi, and W. Xie. "Theoretical advances and future perspectives of all-inorganic germanium-based perovskites". en. In: *Journal of Materials Chemistry C* 13.35 (2025), pp. 18043–18059. DOI: 10.1039/D5TC01917F.

[147] Y. Li, Z. Zheng, X. Zheng, et al. "Mutual stabilization of hybrid and inorganic perovskites for photovoltaics". en. In: *eScience* (2025), p. 100449. DOI: 10.1016/j.esci.2025.100449.

[148] Q. Chen, Y. Shen, R. Cai, Z. Zhao, and G. Dong. "The impact of antimony on all-inorganic lead-free perovskites: progress in optical advancement and applications". en. In: *Nanoscale* 17.9 (2025), pp. 4892–4905. DOI: 10.1039/D4NR04102J.

[149] X. Zhang, D. Zhang, Z. Wang, Y. Zhao, and H. Chen. "All-Inorganic Tin-Containing Perovskite Solar Cells: An Emerging Eco-Friendly Photovoltaic Technology". en. In: *Advanced Materials* 37.29 (2025), p. 2505543. DOI: 10.1002/adma.202505543.

[150] R. Jono and H. Segawa. "Theoretical Study of the Band-gap Differences among Lead Triiodide Perovskite Materials: $CsPbI_3$, $MAPbI_3$, and $FAPbI_3$". en. In: *Chemistry Letters* 48.8 (2019), pp. 877–880. DOI: 10.1246/cl.190256.

[151] Y. Yuan, G. Yan, R. Hong, Z. Liang, and T. Kirchartz. "Quantifying Efficiency Limitations in All-Inorganic Halide Perovskite Solar Cells". en. In: *Advanced Materials* 34.21 (2022), p. 2108132. DOI: 10.1002/adma.202108132.

[152] S. Jekal, H. Choi, Z. Otgonbayar, et al. "Comparative Study of the Electrorheological Properties of Various Halide Perovskites". en. In: *ACS Omega* 10.13 (2025), pp. 13327–13338. DOI: 10.1021/acsomega.4c11212.

[153] S. Kim, M. Adnan, Z. Irshad, et al. "Recent advancements and challenges in highly stable all-inorganic perovskite solar cells". en. In: *Materials Today Electronics* 10 (2024), p. 100127. DOI: 10.1016/j.mtelec.2024.100127.

[154] F. Igbari, M. Bilal, and Z. Li. "Strategies for performance and stability advancement in multicomponent perovskite photovoltaics". en. In: *Journal of Materials Chemistry A* 13.39 (2025), pp. 32964–33011. DOI: 10.1039/D5TA04375A.

[155] P. T. Mokabane, V. T. Lukong, and T.-C. Jen. "A review of the effect of stability issues and wide-bandgap in the application of perovskite solar cells". en. In: *Materials for Renewable and Sustainable Energy* 14.2 (2025), p. 34. DOI: 10.1007/s40243-025-00307-9.

[156] H. Jin, Y.-J. Zeng, J. A. Steele, M. B. J. Roeffaers, J. Hofkens, and E. Debroye. "Phase stabilization of cesium lead iodide perovskites for use in efficient optoelectronic devices". en. In: *NPG Asia Materials* 16.1 (2024), p. 24. DOI: 10.1038/s41427-024-00540-0.

[157] K. Gamal, M. Gamal, A. Okaz, N. Shehata, and I. Kandas. "Comprehensive performance analysis of perovskite solar cells based on different crystalline structures of MAPbI3". en. In: *Optical and Quantum Electronics* 56.5 (2024), p. 827. DOI: 10.1007/s11082-024-06655-6.

[158] S. Y. Hong, D. S. Lee, H. J. Lee, K.-H. Hong, and S. H. Im. "Recent progress in Pb-, Sn-, and Pb–Sn-based inorganic perovskite solar cells: toward enhanced stability and efficiency". en. In: *EES Solar* 1.4 (2025), pp. 441–481. DOI: 10.1039/D5EL00065C.

[159] M. J. Seol, S. Hwang, and S. Y. Kim. "Enhanced Structural and Chemical Stability of New Inorganic Halide Perovskite Solar Cell Structures via Nickel Doping and Silicon Dioxide Encapsulation". en. In: *International Journal of Energy Research* 2025.1 (2025). Ed. by D. Fathi, p. 7589178. DOI: 10.1155/er/7589178.

[161] L. Wang, B. Fan, B. Zheng, Z. Yang, P. Yin, and L. Huo. "Organic functional materials: recent advances in all-inorganic perovskite solar cells". en. In: *Sustainable Energy & Fuels* 4.5 (2020), pp. 2134–2148. DOI: 10.1039/D0SE00214C.

[162] P. Pandey and D.-W. Kang. "Vapor-Deposited Inorganic Perovskite Solar Cells from Fundamentals to Scalable Commercial Pathways". en. In: *Electronics* 14.16 (2025), p. 3171. DOI: 10.3390/electronics14163171.

[163] Y. Wang, Y. Zhang, Z. Shi, et al. "Performance analysis of CsFAMAPbIBr perovskite cells compared with MAPbI3 perovskite cells". en. In: *Chemical Physics Letters* 857 (2024), p. 141724. DOI: 10.1016/j.cplett.2024.141724.

[164] A. Hossain, H. AlMohamadi, B. Wang, M. Akhtaruzzaman, and M. M. Uddin. "Structural, electronic, optical, mechanical, and thermal properties of A3MCl3 (A = Mg, Ca; M = N, Bi) halide perovskites: A first-principles study". In: *Computational Condensed Matter* 45 (2025), e01116. DOI: 10.1016/j.cocom.2025.e01116.

[165] U.-G. Jong, C.-J. Yu, Y.-H. Kye, Y.-G. Choe, W. Hao, and S. Li. "First-Principles Study on Structural, Electronic, and Optical Properties of Inorganic Ge-Based Halide Perovskites". en. In: *Inorganic Chemistry* 58.7 (2019), pp. 4134–4140. DOI: 10.1021/acs.inorgchem.8b03095.

[166] M. M. Hasan, M. A. Sarker, M. B. Mansur, M. R. Islam, and S. Ahmad. "Pressure-induced structural, electronic, optical, and mechanical properties of lead-free GaGeX3 (X = Cl, Br and, I) perovskites: First-principles calculation". eng. In: *Heliyon* 10.15 (2024), e34824. DOI: 10.1016/j.heliyon.2024.e34824.

[167] A. Alsaad, A. Telfah, H. Baaziz, et al. "Ab initio investigation of mechanical, electronic and optical properties in the orthorhombic CsPbI3 inorganic perovskite". In: *Materials Science in Semiconductor Processing* 177 (2024), p. 108375. DOI: 10.1016/j.mssp.2024.108375.

[168] M. A. Ul Islam, O. Das, D. B. Khadka, et al. "Effect of Low to High Pressure on the Structural, Mechanical, Electrical, and Optical Properties of Inorganic Material Ca_3 $AsBr_3$: An Ab Initio Investigation". en. In: *ACS Omega* (2024), acsomega.3c08131. DOI: 10.1021/acsomega.3c08131.

[169] X. Li, Y. Shang, X. Wang, et al. "Understanding ion migration suppression in all-inorganic mixed halide perovskites via tin-lead alloying". en. In: *Nano Research Energy* 4.2 (2025), e9120166. DOI: 10.26599/NRE.2025.9120166.

[170] Y. Liang, F. Li, X. Cui, et al. "Multiple B-site doping suppresses ion migration in halide perovskites". en. In: *Science Advances* 11.11 (2025), eads7054. DOI: 10.1126/sciadv.ads7054.

[171] Y. Liu, C. Fang, S. Lin, et al. "Calculation of Mechanical Properties, Electronic Structure and Optical Properties of CsPbX3 (X = F, Cl, Br, I)". en. In: *Molecules* 28.22 (2023), p. 7643. DOI: 10.3390/molecules28227643.

[172] C. Mi, G. C. Gee, C. W. Lander, et al. "Towards non-blinking and photostable perovskite quantum dots". en. In: *Nature Communications* 16.1 (2025), p. 204. DOI: 10.1038/s41467-024-55619-7.

[173] H. Wang, B. Li, F. Liu, et al. "2D Capping Layer Passivation toward Inorganic $CsPbI_3$ Perovskite Minimodule". en. In: *Advanced Functional Materials* 35.35 (2025), p. 2423397. DOI: 10.1002/adfm.202423397.

[174] A. Swarnkar, A. R. Marshall, E. M. Sanehira, et al. "Quantum dot-induced phase stabilization of -CsPbI3 perovskite for high-efficiency photovoltaics". eng. In: *Science (New York, N.Y.)* 354.6308 (2016), pp. 92–95. DOI: 10.1126/science.aag2700.

[175] I. Khan, A. Ullah, W. M. Almalki, et al. "Probing the physical properties of LiSbX3 (X = Cl, F) halides perovskites for optoelectronic applications". en. In: *Scientific Reports* 15.1 (2025), p. 18837. DOI: 10.1038/s41598-025-03320-0.

[176] F. Tayari, S. S. Teixeira, M. P. F. Graca, and K. I. Nassar. "A Comprehensive Review of Recent Advances in Perovskite Materials: Electrical, Dielectric, and Magnetic Properties". en. In: *Inorganics* 13.3 (2025), p. 67. DOI: 10.3390/inorganics13030067.

[177] P. Kumar, G. Shankar, A. Kumar, A. Najar, and B. Pradhan. "Recent progress in all-perovskite tandem solar cells and modules: redefining limits". In: *Progress in Materials Science* 156 (2026), p. 101560. DOI: 10.1016/j.pmatsci.2025.101560.

[178] Q. Zhang, X. Chen, E. L. Lim, L. Shi, and Z. Wei. "Advancing all-perovskite two-terminal tandem solar cells: optimization of wide- and narrow-bandgap perovskites and interconnecting layers". en. In: *Energy & Environmental Science* 18.7 (2025), pp. 3060–3084. DOI: 10.1039/D4EE06027J.

[179] A. Kojima, K. Teshima, Y. Shirai, and T. Miyasaka. "Organometal Halide Perovskites as Visible-Light Sensitizers for Photovoltaic Cells". en. In: *Journal of the American Chemical Society* 131.17 (2009), pp. 6050–6051. DOI: 10.1021/ja809598r.

[180] F. M. Rombach, S. A. Haque, and T. J. Macdonald. "Lessons learned from spiro-OMeTAD and PTAA in perovskite solar cells". en. In: *Energy & Environmental Science* 14.10 (2021), pp. 5161–5190. DOI: 10.1039/D1EE02095A.

[181] C. Luo, H. Gu, B. Zhang, S. M. Park, M. Wei, and Y. Hou. "Perovskite Tandems: the Next Big Leap in Photovoltaic Technology". en. In: *Advanced Materials* (2025), e08331. DOI: 10.1002/adma.202508331.

[182] M. Afroz, R. K. Ratnesh, S. Srivastava, and J. Singh. "Perovskite solar cells: Progress, challenges, and future avenues to clean energy". In: *Solar Energy* 287 (2025), p. 113205. DOI: 10.1016/j.solener.2024.113205.

[183] F. De Angelis. "Celebrating 10 Years of Perovskite Photovoltaics". en. In: *ACS Energy Letters* 4.4 (2019), pp. 853–854. DOI: 10.1021/acsenergylett.9b00500.

[186] Y. Yu, J. Xia, and Y. Liang. "Basic understanding of perovskite solar cells and passivation mechanism". en. In: *AIP Advances* 12.5 (2022), p. 055307. DOI: 10.1063/5.0058441.

[187] T. Hellmann, C. Das, T. Abzieher, et al. "The Electronic Structure of MAPI-Based Perovskite Solar Cells: Detailed Band Diagram Determination by Photoemission Spectroscopy Comparing Classical and Inverted Device Stacks". en. In: *Advanced Energy Materials* 10.42 (2020), p. 2002129. DOI: 10.1002/aenm.202002129.

[188] E. Gutierrez-Partida, M. Rusu, F. Zu, et al. "Toward Understanding the Built-in Field in Perovskite Solar Cells through Layer-by-Layer Surface Photovoltage Measurements". en. In: *ACS Applied Materials & Interfaces* 17.7 (2025), pp. 11176–11186. DOI: 10.1021/acsami.4c14194.

[189] S. Mariotti. "Hybrid and inorganic plumbo-halide perovskites for solar cells". In: (2019). DOI: 10.17638/03031053.

[190] F. De Angelis. "Tandem Perovskite Solar Cells: Where Academic Challenges Meet Industrial Requirements". en. In: *ACS Energy Letters* 9.4 (2024), pp. 1759–1760. DOI: 10.1021/acsenergylett.4c00806.

[191] H.-L. Yip and A. K.-Y. Jen. "Recent advances in solution-processed interfacial materials for efficient and stable polymer solar cells". en. In: *Energy & Environmental Science* 5.3 (2012), p. 5994. DOI: 10.1039/c2ee02806a.

[192] M.-I. Jamesh, H. Tong, M. Du, et al. "Advancement of technology towards developing perovskite-based solar cells for renewable energy harvesting and energy transformation applications". en. In: *npj Materials Sustainability* 3.1 (2025), p. 29. DOI: 10.1038/s44296-025-00073-9.

[193] N. Tsvetkov, M. Lee, Y. Kim, D. Kim, J. S. Yun, and H. Min. "Advancements in perovskite solar cell concentrators and future prospects". en. In: *Journal of Materials Chemistry A* 13.11 (2025), pp. 7656–7681. DOI: 10.1039/D4TA08688K.

[194] J. Huang and L. Mao. "A Review on Perovskite/Silicon Tandem Solar Cells: Current Status and Future Challenges". en. In: *Energies* 18.16 (2025), p. 4327. DOI: 10.3390/en18164327.

[195] J. A. Aguiar, S. Wozny, T. G. Holesinger, et al. "In situ investigation of the formation and metastability of formamidinium lead tri-iodide perovskite solar cells". en. In: *Energy & Environmental Science* 9.7 (2016), pp. 2372–2382. DOI: 10.1039/C6EE01079B.

[196] E. M. Miller, Y. Zhao, C. C. Mercado, et al. "Substrate-controlled band positions in CH_3 NH_3 PbI_3 perovskite films". en. In: *Phys. Chem. Chem. Phys.* 16.40 (2014), pp. 22122–22130. DOI: 10.1039/C4CP03533J.

[197] Y. Liu, Z. Zhang, T. Wu, et al. "Cost Effectivities Analysis of Perovskite Solar Cells: Will it Outperform Crystalline Silicon Ones?" en. In: *Nano-Micro Letters* 17.1 (2025), p. 219. DOI: 10.1007/s40820-025-01744-x.

[198] A. Mdallal, A. Yasin, M. Mahmoud, M. A. Abdelkareem, A. H. Alami, and A. G. Olabi. "A comprehensive review on solar photovoltaics: Navigating generational shifts, innovations, and sustainability". In: *Sustainable Horizons* 13 (2025), p. 100137. DOI: 10.1016/j.horiz.2025.100137.

[199] Y. Yang, Y. Yan, M. Yang, et al. "Low surface recombination velocity in solution-grown CH3NH3PbBr3 perovskite single crystal". en. In: *Nature Communications* 6.1 (2015), p. 7961. DOI: 10.1038/ncomms8961.

[200] Department of Physics, Bowen University, Iwo, 232101, Nigeria, I. Salami, M. E. Emetere, Department of Physics, Bowen University, Iwo, 232101, Nigeria, and Department of Electrical Engineering Technology, University of Johannesburg, APK, Johannesburg, 2006, South Africa. "A Review of the Significance of Perovskite Solar Cell Architecture for the Optimization of Photovoltaic Parameters". In: *ES Energy & Environment* (2025). DOI: 10.30919/ee1600.

[201] M. H. Tonmoy, S. N. Shiddique, A. T. Abir, and J. Hossain. "Design and optimization of a high efficiency CdTe–FeSi2 based double-junction two-terminal tandem solar cell". In: *Heliyon* 10.6 (2024), e27994. DOI: 10.1016/j.heliyon.2024.e27994.

[202] O. Er-raji, C. Messmer, R. R. Pradhan, et al. "Electron accumulation across the perovskite layer enhances tandem solar cells with textured silicon". en. In: *Science* (2025), eadx1745. DOI: 10.1126/science.adx1745.

[203] M. L. Yu, A. Los, and G. Xiong. "Thin film absorbers for tandem solar cells: an industrial perspective". In: *Journal of Physics: Energy* 5.4 (2023), p. 042002. DOI: 10.1088/2515-7655/acff18.

[204] W. Li, S. Buddhiraju, and S. Fan. "Thermodynamic limits for simultaneous energy harvesting from the hot sun and cold outer space". en. In: *Light: Science & Applications* 9.1 (2020), p. 68. DOI: 10.1038/s41377-020-0296-x.

[205] S. Akhil, S. Akash, A. Pasha, et al. "Review on perovskite silicon tandem solar cells: Status and prospects 2T, 3T and 4T for real world conditions". In: *Materials & Design* 211 (2021), p. 110138. DOI: 10.1016/j.matdes.2021.110138.

[206] Y. Yao, F. Lv, X. Zhao, et al. "A monolithic all-perovskite tandem solar cell with 2-T, 3-T and 4-T architecture integrated". In: *Solar Energy Materials and Solar Cells* 259 (2023), p. 112376. DOI: 10.1016/j.solmat.2023.112376.

[207] G. Coletti, S. L. Luxembourg, L. J. Geerligs, et al. "Bifacial Four-Terminal Perovskite/Silicon Tandem Solar Cells and Modules". en. In: *ACS Energy Letters* 5.5 (2020), pp. 1676–1680. DOI: 10.1021/acsenergylett.0c00682.

[208] K. Alberi, J. J. Berry, J. J. Cordell, et al. "A roadmap for tandem photovoltaics". In: *Joule* 8.3 (2024), pp. 658–692. DOI: 10.1016/j.joule.2024.01.017.

[209] J. H. Park, S. K. Hwang, S. G. Ji, and J. Y. Kim. "Characterization of various tandem solar cells: Protocols, issues, and precautions". In: *Exploration* 3.2 (2023), p. 20220029. DOI: 10.1002/EXP.20220029.

[210] M. Singh, R. Santbergen, I. Syifai, A. Weeber, M. Zeman, and O. Isabella. "Comparing optical performance of a wide range of perovskite/silicon tandem architectures under real-world conditions". en. In: *Nanophotonics* 10.8 (2021), pp. 2043–2057. DOI: 10.1515/nanoph-2020-0643.

[211] G. E. Eperon, M. T. Hörantner, and H. J. Snaith. "Metal halide perovskite tandem and multiple-junction photovoltaics". en. In: *Nature Reviews Chemistry* 1.12 (2017), pp. 1–18. DOI: 10.1038/s41570-017-0095.

[212] Y. Sun, F. Li, H. Zhang, et al. "Flexible perovskite/silicon monolithic tandem solar cells approaching 30% efficiency". en. In: *Nature Communications* 16.1 (2025), p. 5733. DOI: 10.1038/s41467-025-61081-w.

[213] Z. Jia, X. Guo, X. Yin, et al. "Efficient near-infrared harvesting in perovskite–organic tandem solar cells". en. In: *Nature* 643.8070 (2025), pp. 104–110. DOI: 10.1038/s41586-025-09181-x.

[215] T. Todorov, O. Gunawan, and S. Guha. "A road towards 25% efficiency and beyond: perovskite tandem solar cells". en. In: *Molecular Systems Design & Engineering* 1.4 (2016), pp. 370–376. DOI: 10.1039/C6ME00041J.

[216] N. Ito, T. Uesugi, S. Sakai, M. Umeno, and S. Hattori. "InGaAsP/InP Wavelength Division Solar Cells". In: *Japanese Journal of Applied Physics* 20.S2 (1981), p. 121. DOI: 10.7567/JJAPS.20S2.121.

[217] I. J. Park, J. H. Park, S. G. Ji, M.-A. Park, J. H. Jang, and J. Y. Kim. "A Three-Terminal Monolithic Perovskite/Si Tandem Solar Cell Characterization Platform". en. In: *Joule* 3.3 (2019), pp. 807–818. DOI: 10.1016/j.joule.2018.11.017.

[218] T. Soga, M. Yang, T. Jimbo, and M. Umeno. "High-Efficiency Monolithic Three-Terminal GaAs/Si Tandem Solar Cells Fabricated by Metalorganic Chemical Vapor Deposition". In: *Japanese Journal of Applied Physics* 35.2S (1996), p. 1401. DOI: 10.1143/JJAP.35.1401.

[219] T. Nagashima, K. Okumura, K. Murata, and Y. Kimura. "Three-terminal tandem solar cells with a back-contact type bottom cell". In: *Conference Record of the Twenty-Eighth IEEE Photovoltaic Specialists Conference - 2000 (Cat. No.00CH37036)*. Anchorage, AK, USA: IEEE, 2000, pp. 1193–1196. DOI: 10.1109/PVSC.2000.916102.

[220] F. Khan, B. D. Rezgui, M. T. Khan, and F. Al-Sulaiman. "Perovskite-based tandem solar cells: Device architecture, stability, and economic perspectives". In: *Renewable and Sustainable Energy Reviews* 165 (2022), p. 112553. DOI: 10.1016/j.rser.2022.112553.

[221] S. Moeini, M. Noori, and A. Abbasiyan. "Efficiency enhancement in 4T perovskite/Si tandem solar cell by charge extraction management". In: *Solar Energy Materials and Solar Cells* 285 (2025), p. 113510. DOI: 10.1016/j.solmat.2025.113510.

[222] P. Tockhorn, P. Wagner, L. Kegelmann, et al. "Three-Terminal Perovskite/Silicon Tandem Solar Cells with Top and Interdigitated Rear Contacts". en. In: *ACS Applied Energy Materials* 3.2 (2020), pp. 1381–1392. DOI: 10.1021/acsaem.9b01800.

[223] E. L. Warren, M. G. Deceglie, M. Rienäcker, R. Peibst, A. C. Tamboli, and P. Stradins. "Maximizing tandem solar cell power extraction using a three-terminal design". en. In: *Sustainable Energy & Fuels* 2.6 (2018), pp. 1141–1147. DOI: 10.1039/C8SE00133B.

[224] M. Schnabel, H. Schulte-Huxel, M. Rienäcker, et al. "Three-terminal III–V/Si tandem solar cells enabled by a transparent conductive adhesive". en. In: *Sustainable Energy & Fuels* 4.2 (2020), pp. 549–558. DOI: 10.1039/C9SE00893D.

[226] D. Turkay, K. Artuk, X.-Y. Chin, et al. “Synergetic substrate and additive engineering for over 30%-efficient perovskite-Si tandem solar cells”. In: *Joule* 8.6 (2024), pp. 1735–1753. DOI: 10.1016/j.joule.2024.04.015.

[228] X. Jia, D. Yang, D. Zheng, et al. “The progress and challenges of tin-lead alloyed perovskites: Toward the development of large-scale all-perovskite tandem solar cells”. In: *Chem* 11.1 (2025), p. 102384. DOI: 10.1016/j.chempr.2024.12.002.

[229] T. Song, H. K. Jeswani, and A. Azapagic. “Assessing the environmental and economic sustainability of emerging tandem photovoltaic technologies in China”. In: *Energy Conversion and Management* 318 (2024), p. 118890. DOI: 10.1016/j.enconman.2024.118890.

[230] C. Geng, K. Zhang, C. Wang, et al. “Crystallization Modulation and Holistic Passivation Enables Efficient Two-Terminal Perovskite/CuIn(Ga)Se2 Tandem Solar Cells”. en. In: *Nano-Micro Letters* 17.1 (2025), p. 8. DOI: 10.1007/s40820-024-01514-1.

[231] N. Fakhri, M. Salay Naderi, S. Gholami Farkoush, S. SaeidNahaei, S.-N. Park, and S.-B. Rhee. “Simulation of Perovskite Solar Cells Optimized by the Inverse Planar Method in SILVACO: 3D Electrical and Optical Models”. en. In: *Energies* 14.18 (2021), p. 5944. DOI: 10.3390/en14185944.

[232] M. Bacha, A. Saadoune, I. Youcef, and O. terghini. “Design and numerical investigation of Perovskite/Silicon tandem solar cell”. In: *Optical Materials* 131 (2022), p. 112671. DOI: 10.1016/j.optmat.2022.112671.

[233] M. Mehrabian and S. Dalir. “11.73% efficient perovskite heterojunction solar cell simulated by SILVACO ATLAS software”. In: *Optik* 139 (2017), pp. 44–47. DOI: 10.1016/j.ijleo.2017.03.077.

[234] S. Wang, T. Sakurai, W. Wen, and Y. Qi. “Energy Level Alignment at Interfaces in Metal Halide Perovskite Solar Cells”. en. In: *Advanced Materials Interfaces* 5.22 (2018), p. 1800260. DOI: 10.1002/admi.201800260.

[235] M. A. Belbachir, A. Z. Djennati, S. Kerai, M. Khaouani, and H. Rouigueb. “Simulation Validation and Performance Optimization of Tandem Perovskite/Silicon Solar Cells Based on Experimental Single-Junction Perovskite Solar Cell”. en. In: *Journal of Electronic Materials* 54.10 (2025), pp. 8618–8627. DOI: 10.1007/s11664-025-12173-2.

[236] I. Montoya De Los Santos, H. J. Cortina-Marrero, M. Ruíz-Sánchez, et al. “Optimization of CH3NH3PbI3 perovskite solar cells: A theoretical and experimental study”. en. In: *Solar Energy* 199 (2020), pp. 198–205. DOI: 10.1016/j.solener.2020.02.026.

[238] V. Vähänissi, H. S. Laine, Z. Liu, M. Yli-Koski, A. Haarahiltunen, and H. Savin. “Full recovery of red zone in p-type high-performance multicrystalline silicon”. en. In: *Solar Energy Materials and Solar Cells* 173 (2017), pp. 120–127. DOI: 10.1016/j.solmat.2017.05.016.

[240] S. D. Ganichev, E. Ziemann, W. Prettl, I. N. Yassievich, A. A. Istratov, and E. R. Weber. "Distinction between the Poole-Frenkel and tunneling models of electric-field-stimulated carrier emission from deep levels in semiconductors". en. In: *Physical Review B* 61.15 (2000), pp. 10361–10365. DOI: 10.1103/PhysRevB.61.10361.

[241] T. M. Burke, S. Sweetnam, K. Vandewal, and M. D. McGehee. "Beyond Langevin Recombination: How Equilibrium Between Free Carriers and Charge Transfer States Determines the Open-Circuit Voltage of Organic Solar Cells". en. In: *Advanced Energy Materials* 5.11 (2015), p. 1500123. DOI: 10.1002/aenm.201500123.

[242] H. Rouigueb, M. Khaouani, S. Kerai, A. Z. Djennati, and M. A. Belbachir. "Comprehensive analytical modeling of perovskite (MAPbI3) solar cells: A rigorous validation via simulations and experiments". In: *Solar Energy* 302 (2025), p. 113996. DOI: 10.1016/j.solener.2025.113996.

[243] A. Nozik, G. Conibeer, and M. C. Beard, eds. *Advanced Concepts in Photovoltaics*. en. The Royal Society of Chemistry, 2014. DOI: 10.1039/9781849739955.

[244] H. Rouigueb, M. Khaouani, S. Kerai, A. Z. Djennati, and M. A. Belbachir. "Numerical Optimization of Hybrid 2D/3D and Tandem Perovskite/Silicon HTJ Solar Cells, Based on an Experimentally Validated $MAPbI_3$ Cell: Influence of HTL Doping and Temperature". In: *Semiconductor Science and Technology* 41.2 (2026), p. 025020. DOI: 10.1088/1361-6641/ae44c4.

[245] E. Akoto, V. Isahi, V. Odari, C. Maghanga, and F. Nyongesa. "Monolith Cs1-xRbxSnI3 perovskite – silicon 2T tandem solar cell using SCAPS-1D". en. In: *Results in Optics* 12 (2023), p. 100470. DOI: 10.1016/j.rio.2023.100470.

[246] D. P. Pham, S. Lee, and J. Yi. "Optimisation of four-terminal GaAs//Si tandem solar cells using numerical simulation". en. In: *Materials Science in Semiconductor Processing* 139 (2022), p. 106365. DOI: 10.1016/j.mssp.2021.106365.

[247] I. S. Mohamad, P. J. Ker, P. Chelvanathan, et al. "An experimental investigation of spin-on doping optimization for enhanced electrical characteristics in silicon homojunction solar cells: Proof of concept". en. In: *Heliyon* 10.11 (2024), e31193. DOI: 10.1016/j.heliyon.2024.e31193.

[248] D. Chen, J. Yang, Y. Zhou, H. Xie, H. Zhang, and H. Lai. "Divalent-Doped Li1.3Al0.3Ti1.7(PO4)3 Ceramics with Enhanced Microwave Absorption Properties in the X-band". en. In: *Journal of Electronic Materials* 51.5 (2022), pp. 2663–2672. DOI: 10.1007/s11664-022-09522-w.

[249] G. Chen, C. Ji, T. Fan, et al. "Effects of Sintering Method and BaTiO3 Dopant on the Microstructure and Electric Properties of Bi (Fe0.9Al0.05Yb0.05) O3-Based Ceramics". en. In: *Journal of Electronic Materials* 49.4 (2020), pp. 2608–2616. DOI: 10.1007/s11664-020-07968-4.

[250] Q. Zhang, J. Guo, H. Li, S. Chu, and Q. Ma. "ZIF-8-Induced CeO2/ZnO Nanobelts with Curled Edges Accelerating Cycling Efficiency of Ce3+/Ce4+ for Superior Photocatalytic Performance". en. In: *Journal of Electronic Materials* 51.5 (2022), pp. 1940–1945. DOI: 10.1007/s11664-022-09473-2.

[251] K. Yoshikawa, H. Kawasaki, W. Yoshida, et al. "Silicon heterojunction solar cell with interdigitated back contacts for a photoconversion efficiency over 26%". en. In: *Nature Energy* 2.5 (2017), p. 17032. DOI: 10.1038/nenergy.2017.32.

[252] F. Luo and Q. Yang. "Flower-Like Nanostructured CuCo2O4 Grown on the Surface of Conductively-Treated Filter Paper as a Flexible Anode for Lithium-Ion Batteries". en. In: *Journal of Electronic Materials* 49.9 (2020), pp. 5488–5497. DOI: 10.1007/s11664-020-08290-9.

[253] J. Liao, R. Qian, G. Wang, et al. "High performances multilayer transparent conductive films with manipulated Ag growth and layer thickness". en. In: *Journal of Materials Science: Materials in Electronics* 34.9 (2023), p. 795. DOI: 10.1007/s10854-023-10221-3.

[254] S. Sze and K. K. Ng. *Physics of Semiconductor Devices*. en. 1st ed. Wiley, 2006. DOI: 10.1002/0470068329.

[255] M. I. Hossain, A. M. Saleque, S. Ahmed, et al. "Perovskite/perovskite planar tandem solar cells: A comprehensive guideline for reaching energy conversion efficiency beyond 30%". en. In: *Nano Energy* 79 (2021), p. 105400. DOI: 10.1016/j.nanoen.2020.105400.

[256] H. Shen, T. Duong, J. Peng, et al. "Mechanically-stacked perovskite/CIGS tandem solar cells with efficiency of 23.9% and reduced oxygen sensitivity". en. In: *Energy & Environmental Science* 11.2 (2018), pp. 394–406. DOI: 10.1039/C7EE02627G.

[257] Z. Fang, Q. Zeng, C. Zuo, et al. "Perovskite-based tandem solar cells". en. In: *Science Bulletin* 66.6 (2021), pp. 621–636. DOI: 10.1016/j.scib.2020.11.006.

[258] A. Chandrakar and A. Khare. "A comprehensive review of flexible perovskite solar cells: Materials, mechanisms, properties, applications, and commercialization status". In: *Solar Energy* 298 (2025), p. 113649. DOI: 10.1016/j.solener.2025.113649.

[259] I. AL-Wesabi, F. Zhijian, H. M. H. Farh, et al. "Hybrid SSA-PSO based intelligent direct sliding-mode control for extracting maximum photovoltaic output power and regulating the DC-bus voltage". en. In: *International Journal of Hydrogen Energy* 51 (2024), pp. 348–370. DOI: 10.1016/j.ijhydene.2023.10.034.

[260] M. Kikelj, L.-L. Senaud, J. Geissbühler, et al. "Do all good things really come in threes? The true potential of 3-terminal perovskite-silicon tandem solar cell strings". en. In: *Joule* 8.3 (2024), pp. 852–871. DOI: 10.1016/j.joule.2024.01.009.

[261] F. Gota, M. Langenhorst, R. Schmager, J. Lehr, and U. W. Paetzold. "Energy Yield Advantages of Three-Terminal Perovskite-Silicon Tandem Photovoltaics". en. In: *Joule* 4.11 (2020), pp. 2387–2403. DOI: 10.1016/j.joule.2020.08.021.

[262] J. P. Connolly, J. Kleider, M. Gueunier-Farret, et al. "Designing Carrier Selective Perovskite on Silicon 3T Tandems". In: 2023.

[263] M. Rienäcker, E. L. Warren, T. F. Wietler, P. Stradins, A. C. Tamboli, and R. Peibst. "Three-Terminal Bipolar Junction Bottom Cell as Simple as PERC: Towards Lean Tandem Cell Processing". In: *2019 IEEE 46th Photovoltaic Specialists Conference (PVSC)* (2019), pp. 2169–2175. DOI: 10.1109/PVSC40753.2019.8980645.

[264] R. Santbergen and R. Van Zolingen. "The absorption factor of crystalline silicon PV cells: A numerical and experimental study". en. In: *Solar Energy Materials and Solar Cells* 92.4 (2008), pp. 432–444. DOI: 10.1016/j.solmat.2007.10.005.

[265] S. Kirner, L. Mazzarella, L. Korte, B. Stannowski, B. Rech, and R. Schlatmann. "Silicon Heterojunction Solar Cells With Nanocrystalline Silicon Oxide Emitter: Insights Into Charge Carrier Transport". In: *IEEE Journal of Photovoltaics* 5.6 (2015), pp. 1601–1605. DOI: 10.1109/JPHOTOV.2015.2479461.

[266] M. Stuckelberger, R. Biron, N. Wyrsch, F.-J. Haug, and C. Ballif. "Review: Progress in solar cells from hydrogenated amorphous silicon". en. In: *Renewable and Sustainable Energy Reviews* 76 (2017), pp. 1497–1523. DOI: 10.1016/j.rser.2016.11.190.

[267] S. B. Mallick, M. Agrawal, and P. Peumans. "Optimal light trapping in ultra-thin photonic crystal crystalline silicon solar cells". en. In: *Optics Express* 18.6 (2010), p. 5691. DOI: 10.1364/OE.18.005691.

[268] K. Lee, N. Kim, K. Kim, et al. "Neutral-Colored Transparent Crystalline Silicon Photovoltaics". In: *Joule* 4.1 (2020), pp. 235–246. DOI: 10.1016/j.joule.2019.11.008.

[269] J. Wang, H. Lin, Z. Wang, W. Shen, J. Ye, and P. Gao. "Hard mask processing of 20% efficiency back-contacted silicon solar cells with dopant-free heterojunctions". In: *Nano Energy* 66 (2019), p. 104116. DOI: 10.1016/j.nanoen.2019.104116.

[270] Santosh Kumar Srivastava and Jitendra Singh. "The Impact of P-Type Layer on Performance and Stability of Thin Film Silicon Solar Cells in Relation to Third Generation: A review Analysis". In: *International Journal of Scientific Research in Modern Science and Technology* 2.10 (2023), pp. 38–49. DOI: 10.59828/ijsrmst.v2i10.154.

[271] J. Panigrahi and V. K. Komarala. "Progress on the intrinsic a-Si:H films for interface passivation of silicon heterojunction solar cells: A review". en. In: *Journal of Non-Crystalline Solids* 574 (2021), p. 121166. DOI: 10.1016/j.jnoncrysol.2021.121166.

[272] X. Guo, X. Liu, F. Lin, H. Li, Y. Fan, and N. Zhang. "Highly Conductive Transparent Organic Electrodes with Multilayer Structures for Rigid and Flexible Optoelectronics". en. In: *Scientific Reports* 5.1 (2015), p. 10569. DOI: 10.1038/srep10569.

[273] N. Singh and M. Taunk. "3 - Transparent metal oxides in OLED devices". In: *Metal Oxides for Next-Generation Optoelectronic, Photonic, and Photovoltaic Applications*. Ed. by V. Kumar, V. Sharma, H. C. Swart, and S. Das. Metal Oxides. Elsevier, 2024, pp. 77–106. DOI: 10.1016/B978-0-323-99143-8.00006-7.

[274] Y. Shi, L. He, Q. Deng, et al. "Synthesis and Applications of Silver Nanowires for Transparent Conductive Films". en. In: *Micromachines* 10.5 (2019), p. 330. DOI: 10.3390/mi10050330.

[275] H. Wang, H. Shi, H. Lu, et al. "From wasted nonwoven fabrics to conductive flexible substrates, composited with electrospun porous carbon nanofibers for supercapacitor electrodes and electromagnetic interference shielding materials". In: *Diamond and Related Materials* 155 (2025), p. 112280. DOI: 10.1016/j.diamond.2025.112280.

[276] M. A. Leilaeioun, A. Onno, S. Manzoor, et al. "Power Losses in the Front Transparent Conductive Oxide Layer of Silicon Heterojunction Solar Cells: Design Guide for Single-Junction and Four-Terminal Tandem Applications". In: *IEEE Journal of Photovoltaics* 10.2 (2020), pp. 326–334. DOI: 10.1109/JPHOTOV.2019.2954765.

[277] Y. Zhao, L. Mazzarella, P. Procel, et al. "Ultra-thin electron collectors based on nc-Si:H for high-efficiency silicon heterojunction solar cells". en. In: *Progress in Photovoltaics: Research and Applications* 30.8 (2022), pp. 809–822. DOI: 10.1002/pip.3502.

[278] G. Wang, Q. Su, H. Tang, et al. "27.09%-efficiency silicon heterojunction back contact solar cell and going beyond". en. In: *Nature Communications* 15.1 (2024), p. 8931. DOI: 10.1038/s41467-024-53275-5.

[279] D. Chen, S. Pang, W. Zhu, et al. "Efficient Semitransparent Perovskite Solar Cells Using a Transparent Silver Electrode and Four-Terminal Perovskite/Silicon Tandem Device Exploration". en. In: *Journal of Nanomaterials* 2018 (2018), pp. 1–8. DOI: 10.1155/2018/4012850.

[280] K. Artuk, A. Oranskaia, D. Turkay, et al. "60 cm2 perovskite-silicon tandem solar cells with an efficiency of 28.9% by homogeneous passivation". en. In: *Nature Communications* 16.1 (2025), p. 8672. DOI: 10.1038/s41467-025-63673-y.

[281] L. Wang, N. Wang, X. Wu, et al. "Highly Efficient Monolithic Perovskite/TOPCon Silicon Tandem Solar Cells Enabled by "Halide Locking"". en. In: *Advanced Materials* 37.7 (2025), p. 2416150. DOI: 10.1002/adma.202416150.

[282] L. Lin, L. Jiang, P. Li, et al. "Exploring pathways to achieve 30 % efficiency in three-terminal back-contact all-perovskite tandem solar cells". en. In: *Journal of Alloys and Compounds* 1022 (2025), p. 179760. DOI: 10.1016/j.jallcom.2025.179760.

[283] S. Y. Lim, Y. J. Choi, S. J. Park, G. P. Hong, and J. Y. Kim. "Rational Design of Medium-Bandgap Perovskite Solar Cells for Triple-Junction Si Tandems". en. In: *ACS Applied Materials & Interfaces* 17.16 (2025), pp. 23885–23891. DOI: 10.1021/acsami.4c22601.

[284] H. Hu, S. X. An, Y. Li, et al. "Triple-junction perovskite–perovskite–silicon solar cells with power conversion efficiency of 24.4%". en. In: *Energy & Environmental Science* 17.8 (2024), pp. 2800–2814. DOI: 10.1039/D3EE03687A.

Webographie

[82] *Solar Market Insight Report Q2 2025*. en-US.

[160] N. A. Koshi, K. Thekkepat, D.-K. Lee, S.-C. Lee, and S. Bhattacharjee. *Multi-site mixing and entropy stabilization of CsPbI$_{3}$ with potential application in photovoltaics*. arXiv:2504.18272. 2025. DOI: 10.48550/arXiv.2504.18272.

[184] *Perovskite Solar Cells*. en.

[185] *Best Research-Cell Efficiency Chart | Photovoltaic Research | NREL*.

[214] INES. *Le CEA et 3SUN battent un nouveau record de rendement d'une cellule photovoltaïque*. en.

[225] *34.85%! LONGi Breaks World Record for Crystalline Silicon-Perovskite Tandem Solar Cell Efficiency Again*. en.

[227] *https://us.qcells.com/blog/qcells-tandem-cell-world-record-efficiency/*. en-US. 2024.

[237] *Silvaco Inc.* en-US.

[239] K. Hossain, D. Sivadas, D. Kabra, and P. R. Nair. *Perovskite solar cells dominated by bimolecular recombination – how far is the radiative limit?* 2023. DOI: 10.48550/ARXIV.2308.05369.